Molecular Simulations for Hydrogen Storage and Production

From quantum to force field-based methods

Molecular Simulations for Hydrogen Storage and Production

From quantum to force field-based methods

Proefschrift

ter verkrijging van de graad van doctor
aan de Technische Universiteit Delft,
op gezag van de Rector Magnificus, Prof. dr. ir. T. H. J. J. van der Hagen,
voorzitter van het College voor Promoties,
in het openbaar te verdedigen op
dinsdag 4 maart 2025 om 12:30 uur

door

Parsa HABIBI

Master of Science in Chemical Engineering
Technische Universiteit Delft, Nederland
geboren te Teheran, Iran

Dit proefschrift is goedgekeurd door de promotoren.

Samenstelling promotiecommissie bestaat uit:

Rector Magnificus,	voorzitter
Prof. dr. ir. T. J. H. Vlugt,	Technische Universiteit Delft, *promotor*
Dr. O. A. Moultos,	Technische Universiteit Delft, *promotor*
Dr. P. Dey,	Technische Universiteit Delft, *copromotor*
Onafhankelijke leden:	
Prof. dr. ir. M. T. Kreutzer,	Technische Universiteit Delft
Prof. dr. M. van der Elst,	Technische Universiteit Delft
Prof. dr. D. N. Theodorou,	National Technical University of Athens
Dr. B. Sanyal,	Uppsala University

This work was sponsored by NWO Domain Science for the use of supercomputer facilities.

Keywords: Hydrogen, Storage and Production, Molecular Dynamics, Monte Carlo, Density Functional Theory, Thermodynamic and Transport Properties

ISBN XXX-XX-XXXX-XXX-X

Life is like riding a bike.
To keep your balance, you must keep moving.

Einstein

Contents

1

Introduction

1.1. Hydrogen

Hydrogen (H_2) is a crucial molecule in industry [1–4]. It is widely used to produce chemicals such as ammonia and pharmaceuticals [2, 4]. H_2 is also a promising energy carrier to tackle the intermittency of renewable energy sources, such as solar and wind [5, 6]. However, less than 1% of the H_2 produced is used for this purpose [5]. This is because large-scale implementation of H_2 as an energy carrier is hindered by several major challenges. Two of the main challenges are developing cost-effective and non-polluting production methods for H_2, and designing storage systems with both high volumetric and gravimetric energy densities [5, 6].

For production of H_2 using renewable electricity (i.e., the so-called "Green" H_2), water molecules are split into H_2 and O_2 via water electrolysis [5, 7, 8]. Different water electrolysis systems include alkaline, proton-exchange, and solid-oxide electrolyzers [7–9]. Alkaline water electrolyzers are the most mature green H_2 production technology [7, 8], and operate at ca. 30 wt% KOH, 353 K, and pressures ranging from 1 to 100 bar [10–14]. A schematic of alkaline water electrolyzers is shown in Figure 1.1.

Large-scale production and reduction of the cost (i.e., with respect to fossil-based production methods) of green H_2 are significant hurdles [5]. The high production cost of green H_2 is mainly driven by expensive electricity and regulatory barriers for safe operation [5, 8]. To design an efficient and safe production process for H_2, knowledge of the thermodynamic properties (e.g., densities, H_2 storage capacities, and product compositions), and transport coefficients (e.g., diffusion coefficients and shear viscosities) of H_2 in aqueous electrolyte systems is essential [7, 9]. The solubilities and self-diffusivities of H_2 in aqueous KOH solutions influence the H_2 bubble formation rates, which in turn, influence the ohmic resistance of the aqueous electrolyte and reduce the active electrode area [15, 16]. The Vapor-Liquid Equilibria (VLE) of H_2 in aqueous electrolyte solutions (e.g., the maximum water content in H_2

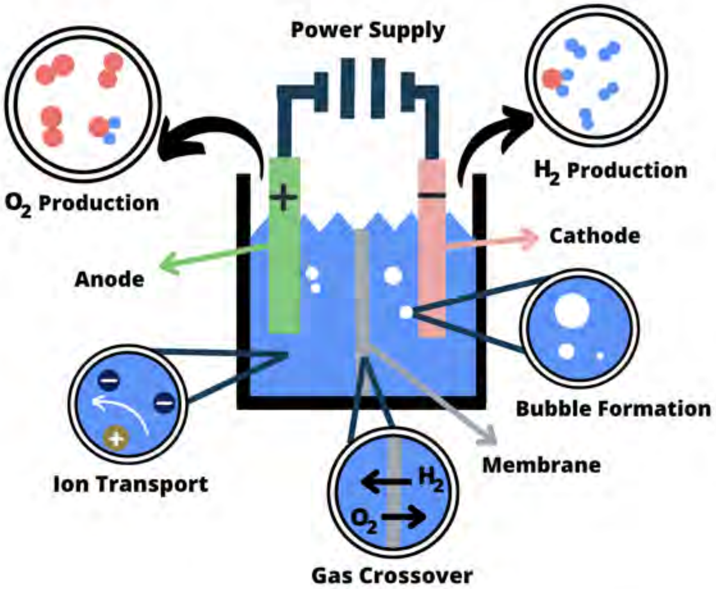

Figure 1.1. Schematic representation of H_2 production using alkaline water electrolysis. In alkaline water electrolysis, water molecules (H_2O) are split using an electric current to produce H_2 (at the cathode) and O_2 (at the anode) in aqueous electrolyte solutions (typically aqueous KOH solutions) [7, 8]. The cathode and the anode departments are separated by a membrane that allows the transport of hydroxide ions from the anode to the cathode, and prevents the direct mixing of H_2 and O_2 [8]. Examples of phenomena that influence H_2 and O_2 production are shown in the schematic, i.e., ion transport in alkaline electrolyte solutions, gas crossover (i.e., the unintended migration H_2 or O_2 from one electrode to the other through the electrolyte and membrane), and H_2 and O_2 gas bubble formation near the cathode and the anode, respectively [7, 9].

gas) influence the purity of the product gas [7, 9]. The thermophysical properties of H_2 and O_2 in alkaline electrolyzers significantly influence gas crossover (i.e., the unintended migration H_2 and O_2 from one electrode to the other through the electrolyte and membrane), as shown in Figure 1.1. This crossover poses a serious safety concern because hydrogen has a broad explosive concentration range, spanning from approximately 4% to 94% H_2 in O_2 [9].

Storage of H_2 is another major engineering challenge [17–19]. The volumetric energy capacity of H_2 is significantly lower than the conventional fuels, such as gasoline, at standard conditions (i.e., H_2 is ca. 3000 times less energy dense than gasoline on a volume basis) [20]. To have a compact source of energy, H_2 is compressed to pressures up to 700 bar or cooled to cryogenic conditions of ca. 20 K [17, 18]. However, the storage of H_2 at high pressures or low temperatures is not energy efficient (ca. 10-40 % of the stored energy of H_2 is lost [21]) and raises safety concerns, such as H_2 embrittlement of the storage medium and potential for leaks and explosions [17]. Underground H_2 storage (i.e., in geological formations such as depleted reservoirs and salt caverns) is also being explored as it provides vast volumes of space [22–24]. Hydrogen stored underground is not meant for immediate use but rather for seasonal or large-scale energy storage needs [22, 24]. Storage of H_2 in materials is another alternative [19, 25]. The interaction of H_2 with materials allows for storage at conditions closer to ambient temperature and pressure compared to H_2 compression or cryogenic cooling [19, 25]. However, none of the existing storage materials have met the conditions set by the US Department of Energy (DOE) [26] for the price (300 \$ / kg H_2), the necessary volumetric (40 g H_2 / L system) and gravimetric capacities (5.5 wt% H_2), and the required kinetics for uptake/release of H_2 for onboard storage [25, 26].

Materials store H_2 through physical (physisorption, i.e., via weak electrostatic or Van der Waals interactions) or chemical adsorption (chemisorption, i.e., via formation of chemical bonds) [17, 25, 27]. Physisorption on porous materials such as Metal Organic Frameworks (MOFs, i.e., materials consisting of metal clusters linked with organic ligands [38]), and zeolites generally results in fast H_2 release and capture kinetics, but suffers from low gravimetric and volumetric H_2 capacities [17, 25]. Chemisorption on materials such as metal hydrides, allows for larger H_2 capacities but the release of H_2 (i.e., the dehydrogenation reaction) is energy intensive and has slow kinetics [39–41]. To make H_2 economy feasible, designing a suitable and cost-effective material that has a high H_2 capacity and fast release/capture kinetics is essential [25, 26]. The number of possible new materials that can be potentially synthesized and used for hydrogen storage is virtually unlimited [25, 42, 43]. Even when considering specific classes of materials, such as MOFs, the number of materials that has been theoretically predicted to date reaches up to half a million [42]. In Figure 1.2, three characteristic examples of different types of materials for H_2 storage are shown. Two-dimensional (2D) materials and porous structures, such as MOFs and zeolites (as shown in Figure 1.2), are frequently studied for hydrogen storage [25, 30, 38] and separation [35, 36] due to their high surface-to-volume ratio and chemical tunability, which allows for optimizing adsorption capacities and efficiencies [17, 25, 27]. New classes of materials are also being discovered and synthesized at a rapid rate and investigated for H_2 storage (as an example 2D borophene hydride, which was synthesized in 2017 [28] is shown in Figure 1.2(a) [28]) [44, 45].

The vast number of materials and conditions (i.e., temperatures,

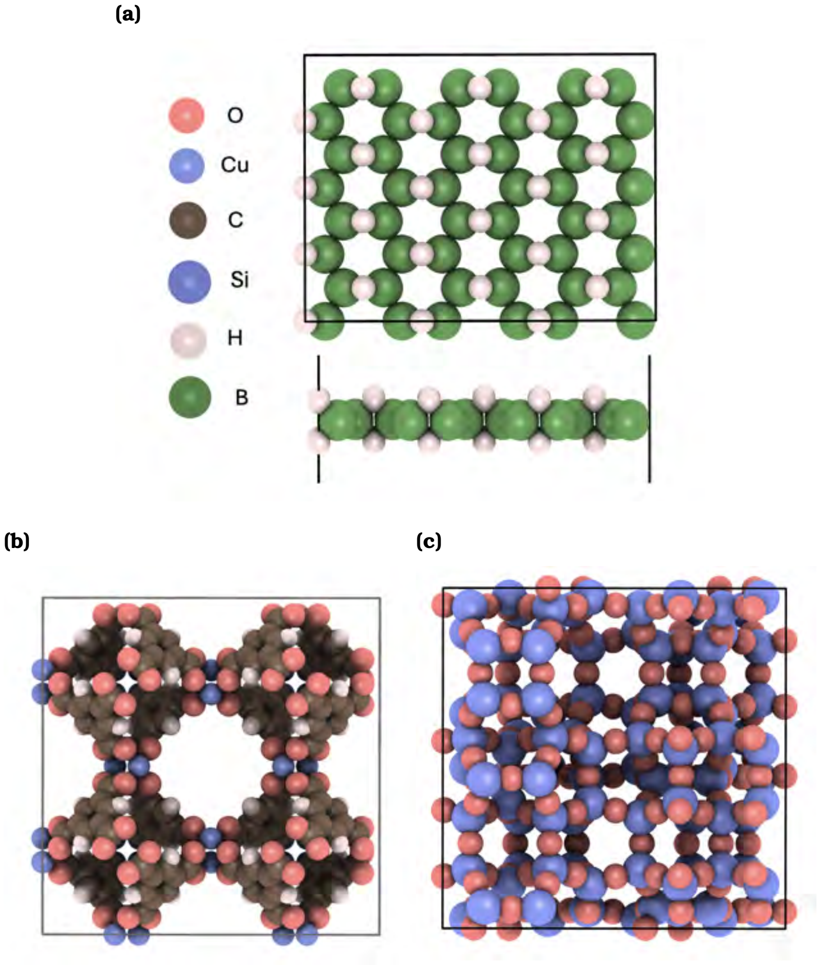

Figure 1.2. 2D materials and porous structures such as MOFs and zeolites are often studied for hydrogen storage and separation due to their high surface to volume ratio [17, 25, 27]. In (a), the front and side view of 2D borophene hydride, which was synthesized in 2017 [28], is shown. This material has been shown by both molecular simulations and experiments to be a promising H_2 storage medium [29, 30]. In (b), the Cu-BTC (MOF) [31, 32] and (c) the MFI-type zeolite structures [33] are shown. The Cu-BTC MOF structure and MFI-type zeolite structures are widely investigated for storage [31, 32, 34] and seperation of H_2 (from CO, CO_2, and water mixtures) [35, 36], respectively. All structures are rendered using iRASPA [37].

pressures, and compositions) relevant to H_2 storage and production makes it costly and time-consuming to rely solely on experiments. Also, experimental measurements involving H_2 require strict adherence to safety standards [46]. These safety standards involve protocols to prevent leaks (especially at high-pressures), explosions, contamination, and to ensure safe handling and storage of H_2 [26, 46]. These challenges render computer simulations (such as molecular simulations) an attractive complementary tool to experiments in terms of time, budget, and safety [47, 48] for computing the thermophysical properties and storage capacities of H_2 in materials.

1.2. Molecular simulations of hydrogen

Molecular simulations [49, 50] are a broad class of computational techniques that predict the macroscopic behavior of materials and fluids by modeling a system of interacting atoms and molecules (schematic representation shown in Figure 1.3). These simulations [49, 50] can in principle be used to discover new catalysts for H_2 production, design materials for H_2 storage and seperation, predict thermophysical properties of H_2 mixtures, and optimize production conditions [42, 51–53]. In this thesis, the emphasis is placed on using molecular simulations to screen and design materials for H_2 storage and to predict the thermodynamic and transport properties of H_2 in aqueous electrolyte solutions, which are relevant to storage and production of H_2 via alkaline water electrolyzers.

Macroscopic properties, such as densities of H_2, can be computed from microscopic configurations (i.e., microstates) [54]. A microstate defines all positions, velocities, and quantum numbers of all the atoms in the systems, and can be related to macroscopic properties using the concept of ensemble averaging [50]. An ensemble refers to the collection of all microstates of a system, subject to different control parameters or constraints that define the system (e.g., temperature, volume, and number of atoms) [50]. The ensemble average of given property $\langle A \rangle$ is defined as [49, 50]:

$$\langle A \rangle = \sum_i P_i A_i \tag{1.1}$$

where P_i refers to the probability of occurrence of microstate i and A_i is the value of variable A at microstate i [49, 50]. P_i depends on parameters such as the energy, temperature, and volume of the microstate. For systems of interacting atoms and molecules, P_i is very close to 0 for the vast majority of microstates [50]. As the total number of microstates i is very large (with majority having a $P_i \approx 0$), it is inefficient and usually impossible to obtain $\langle A \rangle$ directly based on Eq. 1.1 [50, 54]. Various approaches are used to approximate $\langle A \rangle$, depending on the type of molecular simulation technique [50].

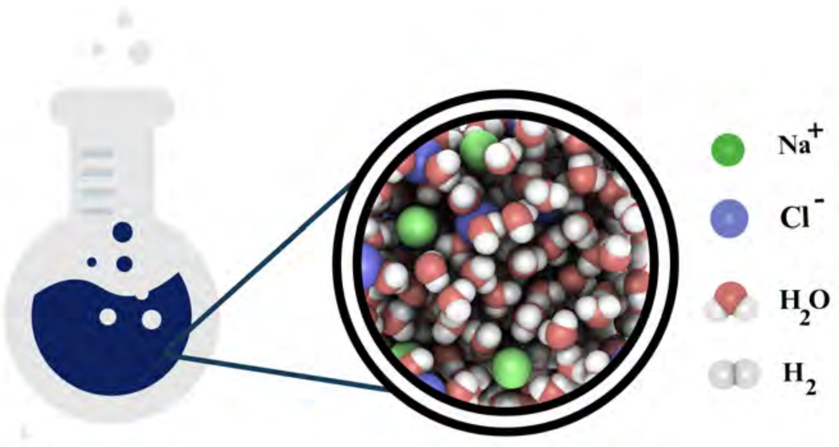

Figure 1.3. Given accurate modeling of the interactions between atoms and molecules, molecular simulations (a snapshot is shown on the right for an aqueous NaCl solution) can be used to complement experiments. Molecular simulations can predict thermophysical properties of materials and fluids for a wide range of temperatures, pressures, and compositions [49, 50].

1.2.1. Molecular dynamics and Monte Carlo simulations

The two most common molecular simulation techniques are Molecular Dynamics (MD) and Monte Carlo (MC) simulations [49, 50]. In MD simulations, the time-evolution of an interacting molecular system is obtained (i.e., trajectories) by numerically integrating Newton's second law of motion [49]. MD simulations are usually deterministic, i.e., given the same particle positions and velocities, the same trajectories will be obtained [49, 50]. Time averages are often used as approximations of ensemble averages in MD simulations due to the ergodicity hypothesis, which states that for long periods of time, the time spent by a system in each microstate is proportional to the probability of the microstate [50]. To accurately compute the ensemble average $\langle A \rangle$, sufficiently long MD trajectories are required [49, 50]. The length of the trajectories depends on: (1) the necessary simulation time needed to compute the property of interest (e.g., transport properties typically require nanosecond time scales), (2) the system size, and (3) the complexity of the underlying model used to compute interactions between different atoms and molecules [49, 50]. The choice of the time scale for numerical integration in MD simulations also depends on the interaction model [49]. Interaction models with sharper gradients with respect to positions of atoms and molecules require smaller time steps to accurately capture the rapid changes in forces and velocities [49, 50].

Unlike the deterministic approach of MD simulations, MC simulations

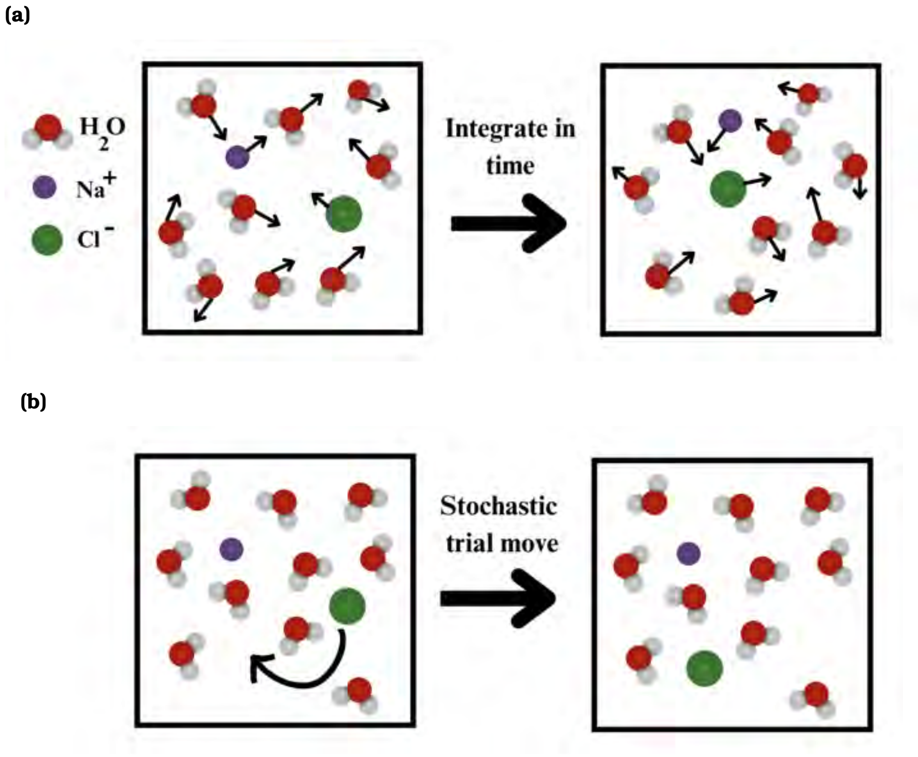

Figure 1.4. Schematic representations of (a) MD and (b) MC simulations for an aqueous NaCl solution. In MD simulations, atoms and molecules are displaced collectively under the influence of interatomic forces, by numerically integrating Newton's equations of motion as a function of time [49, 50]. In MC simulations, a representative collection of microstates is sampled for computing ensemble averages (Eq. 1.1). Microstates are sampled using trial moves. Trial moves attempt to change the configuration of the system so that the system evolves from one microstate to another. Examples of trial moves include translation or reinsertion, applied to randomly selected molecules, ions (shown in (b)), or groups of molecules [50, 55, 56]. In a typical MC simulation (i.e., Metropolis algorithm [57]), the probability of acceptance of a trial move is proportional the probability of occurrence of the microstate [50, 57]. MC simulations can also include collective trial moves [56].

use a stochastic algorithm [50]. In MC simulations, we consider a representative collection of microstates, i, where P_i is much larger than the majority of microstates, which have a $P_i \approx 0$ [50]. Sampling of microstates is achieved using the so-called "trial moves". Trial moves attempt to change the configuration of the system so that the system evolves from one microstate to another [49, 50]. Examples of common trial moves are displacements of molecules, volume changes, or particle insertions (or deletions) [49, 50]. Trial moves do not have to be physical, and can include moves such as identity swaps (switching one atom species by another). The type of trial moves that is used depends on the ensemble and the interaction model that is used [50]. In a typical MC simulation (i.e., Metropolis algorithm), the probability of acceptance of a trial move is often proportional the probability of occurrence of the microstate (i.e., P_i) [50, 57]. This ensures efficient sampling of microstates with high statistical weights (P_i), which contribute most significantly to the summation in Eq. 1.1 [49, 50]. To compute $\langle A \rangle$ accurately, typically thousands to millions of MC cycles are performed, with each cycle referring to N number of trial moves. In MC simulations, the number of cycles required depends on the property of interest, the system size, and the complexity of the interaction model (similar to the length of the trajectories in MD simulations) [49, 50].

The most computationally intensive task in both MC and MD simulations is computing the interactions between different atoms and molecules in the system (especially when dealing with long-range interactions such as electrostatics) [50]. Considering that computational resources (i.e., number of cores/nodes and computing time) are limited, there is always a trade-off between the interaction model complexity, the system size, and the number of MC cycles or the length of the trajectories in MD simulations [50]. It is often necessary to find a balance between accuracy and computationally efficiency (e.g., simplifying the interaction model or reducing the system size) to complete the simulations within a reasonable time [49, 50].

MC simulations are effective for studying thermodynamic equilibrium properties and phase transitions [50, 57], while MD simulations are particularly effective for investigating dynamic properties such as diffusion coefficients, viscosities, and thermal conductivities [50, 58]. Dynamic properties such as transport properties cannot be computed using MC, as the dimension of time is not introduced in these simulations [49, 50]. To perform MD simulations, different software packages, such as LAMMPS [59, 60], GROMACS [61, 62], and AMBER [63, 64] are available. For MC simulations, popular software packages include RASPA [65, 66], BRICK-CFCMC [55, 56], GOMC [67], and Cassandra [68]. A thorough description of MD, MC, and other molecular simulation techniques can be found in Refs. [49, 50, 54, 69, 70].

1.2.2. Ab-initio simulations

The accuracy and reliability of molecular simulations depend on the underlying model that is used to compute the interactions between different atoms and molecules in the system [49, 50]. Ab-initio based methods use quantum chemical calculations, such as Density Functional Theory (DFT), to compute the total energy of the system and the forces between different atoms [71–73]. Ab initio calculations are often limited to small system sizes (ranging from 10s to 100s of atoms) and time-scales (typically ranging from 1 to 100 ps) depending on the properties of the system (e.g., magnetic or non-magnetic) [71, 72]. The accuracy of these calculations is also strongly influenced by the properties of the system and the computational approximations that are used (e.g., the choice of exchange-correlation functional) [73].

DFT is a popular ab-initio technique due to its accuracy and low computational expense compared to alternative techniques such as the Hartree Fock (HF) method [73]. DFT can be used to optimize molecular structures, calculate adsorption energies of H_2, and identify material instability (using phonon dispersion curves) at 0 K [73–75]. Energy barriers (which influence kinetics) for chemical reactions can be determined using ab-initio techniques such as Nudged Elastic Band (NEB) calculations [76–79]. The finite-temperature stability and adsorption/desorption of H_2 can also be simulated using techniques such as Born-Oppenheimer Molecular Dynamics (BOMD) or Car-Parrinello MD simulations [27, 75]. These computations are essential for early detection of unsuitable materials for hydrogen storage and can be used to design novel materials from the molecular level. This helps avoid unnecessary experiments by providing early insights, and saves time in the material development process. Popular software packages for ab-initio simulations are VASP [71, 72], Quantum-espresso [80, 81], WIEN2k [82], and Gaussian [83].

Ab-initio calculations can be used to model quantum effects (i.e., properties that are not described by classical mechanics) [84] in H_2 systems. Quantum effects are crucial for light atoms like hydrogen (H), as the small mass of the H-atom makes its thermal wavelength comparable to the size of the atom itself (i.e., H-atom can easily exhibit both wave and particle-like behavior) [54, 84]. At temperatures below ca. 100 K ignoring quantum effects of H_2 can lead to significant errors [38, 85]. As an example, Bobbitt and Snurr [38] have discussed that at low temperatures (i.e., ca. 70 K), classical simulations of H_2 adsorption in MOFs can overestimate storage capacities of H_2 by up to 20%. Quantum effects become less significant at higher temperatures (ca. 100 K), as the thermal wavelength of H_2 (and other molecules) is inversely proportional to the square root of temperature [54, 84]. Also, as temperature increases, the thermal energy of the system exceeds the energy differences between discrete quantum states [84]. In this regime, the classical description becomes an appropriate approximation because the behavior of the system can be described by averaging over many quantum states, thereby smoothing out the quantum effects [54].

Ab-initio calculations are also important when modeling chemical reactions, as formation and breaking of chemical bonds cannot be modeled using classical mechanics [70, 84]. Thus, properties that are dependent on chemical reactions, such as the pH of aqueous systems (which depends on the self-ionization of water) [86] and self-diffusivities of H^+ or OH^- in water (which depend on the proton transfer reaction mechanism) [87, 88] cannot be simulated classically. For non-reactive systems at temperatures above ca. 100 K, classical molecular simulations can often provide an accurate description of the properties of the system (e.g., densities and self-diffusivities of H_2 in water at room temperature [51]) using simple semi-empirical interaction models [89, 90].

1.2.3. Classical force fields

MD and MC simulations using semi-empirical interaction models, i.e., force fields, can be used to simulate larger system sizes (typically ca. 500-10000 atoms) and time scales (ca. 1-100 ns) compared to ab-initio calculations [49, 50]. These length and time scales are needed for accurate calculation of thermodynamic and transport properties of H_2 systems. A force field refers to a predefined functional form that is used to approximate atomic interactions, unlike ab-initio approaches, which compute interactions from fundamental quantum mechanical calculations. Force fields differ depending on the experimental or ab-initio parameters that are used for their training [49, 50, 89–91]. Even for a diatomic molecule such as H_2, many different force fields have been developed for different applications and systems [89–93]. Examples of H_2 force fields are the force fields developed by Wang *et al.* [94], which are trained on properties such as the vaporization energy and the hydration free energy of H_2, and the force field of Hirschfelder *et al.* [89] which is parameterized based on the second-virial coefficient of H_2 gas.

Classical force fields can be categorized as polarizable or non-polarizable [95–101]. In polarizable force fields, the atomic or molecular charges or distributions vary depending on the local electrostatic environment [96, 97, 102]. The physical origin of polarizability in molecular systems arises from the distortion of the electron clouds within molecules by nearby charges or electric fields [50, 70]. In non-polarizable force fields, fixed point charges are used, which do not account for environmental variations [98, 100, 101, 103, 104]. Despite this simplification, non-polarizable force fields are capable of accurately predicting many properties of H_2 and aqueous electrolyte systems such as densities, transport properties, and radial distribution functions (RDFs) [51, 98, 100, 103, 104]. Non-polarizable force fields are simpler and often more transferable (i.e., the ability to use the same force field parameters across different systems) compared to polarizable force fields [95–97, 99, 101]. The simplicity of non-polarizable force fields also allows for a significantly higher computational efficiency (typically by a factor of ca. 3 to 10) compared to polarizable force fields [95–97]. For these reasons, non-polarizable force fields are expected to continue being widely used in large-scale classical molecular simulations [105].

The transferability and computational efficiency of non-polarizable force fields enables the generation of large data sets of thermophysical properties of H_2 mixtures (e.g., with aqueous systems or gasses such as N_2) for a wide temperature and pressure range [51, 90, 106, 107]. As an example, Köster *et al.* [90] have used non-polarizable force fields to compute isothermal fluid phase diagrams and densities of binary and tertiary H_2 mixtures (with water, N_2, O_2, and Ar). Mixtures of H_2 and water are commonly considered, due to industrial applications such as water electrolysis [16, 106] and supercritical water gasification [108]. The thermodynamic (e.g., densities and solubilities) and transport properties (e.g., self-diffusivities) of H_2 and water mixtures are extensively covered in Refs. [90, 106–110]. Gas molecules such as H_2 are sparsely soluble in liquid water (i.e., mole fractions of ca. 10^{-5} at 298 K and a H_2 pressure of 1 bar [47]), as such, H_2 is often simulated at near infinite dilution [107–109]. Therefore, the choice of the water force field is crucial in these studies, as the force field needs to model the properties and molecular structure of liquid water for a wide temperature/pressure range [51]. Many different non-polarizable water force fields are available and have been reviewed in Ref. [99]. The TIP4P/2005 and the SPC/E force fields of water are particularly popular as these rigid force fields (i.e., with fixed bond lengths and angle) are computationally efficient and result in accurate predictions for densities, viscosities, and self-diffusivities of liquid water [98, 100, 109].

Despite prior studies on thermophysical properties of H_2 in liquid water [51, 107, 108], properties of H_2 in aqueous electrolyte solutions (e.g., KOH, NaOH, and NaCl) have not been modeled using molecular simulations. This is mainly because there are no appropriate non-polarizable force fields for aqueous ions that have been parameterized based on the transport properties of the concentrated (above 3 mol salt / kg water) electrolyte solution [47, 111]. Salts such as NaCl and KOH are highly soluble in water (solubilities of NaCl and KOH in water at 298 K is ca. 6 mol NaCl / kg water and 20 mol NaCl / kg water, respectively), and significantly alter the thermophysical properties of the solution (e.g., densities, viscosities, and self-diffusivities) [112–114]. To model the transport properties of H_2 in aqueous electrolyte solutions, it is essential to accurately model the densities and viscosities of aqueous electrolyte solution, as this ensures that the drag force (i.e., the resistance that H_2 experiences when it moves through the fluid) is well-described [115]. Despite this, existing force fields for aqueous salts (such as the Madrid-2019 [103] and Joung-Cheatam [104] force fields) are not parameterized based on viscosities of concentrated aqueous electrolyte solutions. As a result, these force fields significantly overestimate fluid viscosities at higher salt molalities with respect to the pure solvent (i.e., at 298 K and 4 mol NaCl / kg water, the viscosity computed using the Joung-Cheatam NaCl force field combined with TIP4P/2005 [100] deviates by ca. 100% from experiments). Development of new non-polarizable force fields for salts such as KOH in water (relevant to alkaline water electrolyzers), is essential for molecular modeling of H_2 in aqueous electrolyte solutions [47, 116].

Using non-polarizable force fields, not all thermodynamic or transport properties of aqueous electrolyte solutions can be simultaneously captured accurately [98, 99]. Non-polarizable force fields of water such as SPC/E [98] and TIP4P/2005 [100], which are parameterized based on liquid densities and transport properties [105], cannot be used to accurately predict the free energies of liquid water. Already in 1987, Berendsen *et al.* [98] discovered a fundamental issue when parameterizing the non-polarizable SPC/E force field of water, i.e., fitting force fields to the vaporization energies of water results in excluding the self-polarization energy of water (i.e., the "missing term" mentioned in the title of the famous paper by Berendsen *et al.* [98]). Berendsen *et al.* [98] showed that the inclusion of the self-polarization energy of liquid water by enhancing the dipole moment of water significantly improves predictions of transport properties, densities, and RDFs, at the cost of less accurate predictions for the vaporization energy of water (ca. by 10%). Accurate modeling of free energies is crucial for obtaining the VLE of H_2 and aqueous electrolyte solutions [106]. As such, new methods need to be developed to accurately model the free energies of aqueous systems without compromising the liquid phase properties.

1.3. Outline of this thesis

In this thesis, molecular simulations based on ab-initio calculations are used to assess the suitability of novel 2D materials for hydrogen storage, and new semi-empirical classical force fields and methodologies are introduced to obtain thermodynamic and transport property data for H_2 in aqueous electrolyte solutions (relevant to both hydrogen storage and production).

In chapter 2, the suitability of a novel 2D material, namely borophene oxide [117], as a hydrogen storage medium is assessed using dispersion corrected Density Functional Theory (DFT-D2) calculations [71, 72, 118]. To enhance the physical adsorption energy of H_2 on the 2D structure and to allow for higher H_2 capacities compared to the pristine 2D structure, different metal atoms such as Li, Na, and K are introduced to the surface of borophene oxide. The Li decorated 2D borophene oxide system is shown to have a high H_2 gravimetric capacity of 8.3 wt% H_2, which exceeds the US DOE target of 5.5 wt% H_2. The stability of the Li decorated

2D borophene oxide system and the reversibility of H_2 adsorption is demonstrated using BOMD simulations at 100 K, 300 K, and 500 K. Using semi-empirical equations, a practical gravimetric capacity of 5.2 wt% H_2 is computed for the Li decorated 2D borophene oxide system at adsorption conditions of 298 K and 30 atm, and desorption conditions of 373 K and 3 atm. These findings indicate that 2D borophene oxide can be a promising material for reversible storage of H_2.

In chapter 3, two different 2D materials, namely borophene [44] and borophene hydride [28], are considered for hydrogen storage. In this chapter, the focus is on chemical adsorption of H_2 [25]. Chemical adsorption of hydrogen is usually a highly exothermic reaction with large energy barriers (i.e., exceeding 1.5 eV) for desorption of H_2 [39–41]. This leads to low desorption kinetics and additional cooling or heating when capturing or releasing H_2 from the system [39]. Using DFT and Nudged Elastic Band (NEB) calculations [77, 119], the hydrogenation and dehydrogenation reaction of H_2 on borophene and borophene hydride are assessed. It is found introducing Li decorating atoms significantly lowers the energy barriers for hydrogen desorption compared to the pristine structure. BOMD simulations at 300 K also demonstrate the weakening of the chemical bonds with the H atoms in borophene hydride in presence of Li atoms. A promising Li decorated borophene hydride structure is found for chemical adsorption of H_2, with low energy barriers (below 1 eV) and enthalpy of hydrogenation (below -0.05 eV / H_2).

Classical force fields are more computationally efficient compared to ab-initio simulations and allow for calculation of thermophysical properties at a vast number of conditions (i.e., temperatures, pressures, and compositions). In chapters 4-8, classical force fields are used instead of DFT interactions to compute thermodynamic and transport properties of H_2 in aqueous electrolyte systems. In chapter 4, the interfacial tensions, self-diffusivities, and solubilities of $H_2/H_2O/NaCl$ system are computed using classical MD and MC simulations for a wide temperature (up to 723 K) and pressure (up to 1000 bar) range. The thermodynamic and transport properties of $H_2/H_2O/NaCl$ systems are relevant to underground storage of H_2 and water electrolysis. All the generated data are fitted to engineering equations, which can be used for modeling underground hydrogen storage reservoirs or for water electrolysis. In chapter 5, the thermophysical properties of H_2 and O_2 in aqueous alkaline (i.e., KOH and NaOH) solutions are computed. Alkaline water electrolyzers often use aqueous KOH solutions due to the high electrical conductivity of the solution [7]. A new non-polarizable force field for OH^- is developed to accurately model (within 2% of experiments) the densities and viscosities of aqueous KOH and NaOH solutions. The diffusivities and solubilities of H_2 and O_2 in aqueous KOH and NaOH solutions are computed at 298-353 K and 1-100 bar and fitted to engineering equations for easy retrieval. In chapter 6, the diffusivities and solubilities of H_2 in aqueous $NaB(OH)_4$ solutions are computed. Aqueous $NaB(OH)_4$ solutions are relevant to storage of H_2 in sodium borohydride (i.e., $NaBH_4$). $NaBH_4$ is considered as a promising H_2 storage medium for maritime applications [120–122]. The hydrolysis reaction of $NaBH_4$ forms H_2 and aqueous $NaB(OH)_4$ [120–122]. A new non-polarizable force field for $B(OH)_4^-$ is developed to accurately model (within 2% from experiments) the densities and viscosities of aqueous $NaB(OH)_4$ solutions. Using this force field, the activities of water and self-diffusivities and solubilities of H_2 in aqueous $NaB(OH)_4$ solutions are computed at 0-5 mol $NaB(OH)_4$/kg water at 298-353 K and 1 bar. These thermophysical data can be used to model $NaBH_4$ hydrolysis reactors and to improve reactor efficiency.

A new method is devised to accurately model the VLE of aqueous electrolyte solutions using non-polarizable force fields (chapter 7). Non-polarizable force fields struggle to accurately model the free energies (and thereby the VLE) of water and salt systems, without compromising the predictive ability for densities and transport properties in the liquid phase [98, 99]. In the new method, (1) the TIP4P/2005 water force field is used to describe the effective interactions in the liquid phase, and (2) an additional effective charge surface is used to sample the infinite salt dilution excess chemical potentials of water and salts. For finite-salt dilutions a free energy correction term is added to the partition function of the system. Using this approach, the VLE of water and the free energies of hydration of salts (i.e., NaCl, KCl, LiCl, $MgCl_2$, and $NaCl_2$) are accurately computed, without compromising the liquid phase properties such as densities and viscosities of the solution. In chapter 8, the method that is devised in chapter 7 is used to compute the VLE of H_2 and aqueous KOH and NaCl solutions. The compositions of H_2 and water are computed from the liquid phase excess chemical potentials using an iterative scheme in which the gas phase fugacity coefficients are calculated using the GERG-2008 equation of state [123]. Extensive data are obtained for the solubility of water in H_2 at 298-423 K, 10-400 bar, 0-6 mol NaCl/kg water, and 0-8 mol KOH/kg water. The VLE data presented in this chapter can be used for modeling the water content in the H_2 stream of alkaline electrolyzers (for aqueous KOH solutions) and in underground hydrogen storage systems (for aqueous NaCl solutions). This is essential for ensuring the purity of hydrogen in these processes.

The results obtained in this thesis show that molecular simulation can be a powerful tool for predicting the thermophysical properties of H_2 in solid materials and aqueous solutions for wide temperature and pressure ranges which are relevant to storage and production of H_2. For each chapter, the simulation inputs and outputs are shared in an online repository. All details and links are provided in appendix A.1. The conclusions and outlook for this thesis are discussed in chapter 9.

2

Hydrogen Storage in Metal-Decorated Borophene-Oxide

This chapter is based on the following publication: P. Habibi, T. J. H. Vlugt, P. Dey, and O. A. Moultos. “Reversible Hydrogen Storage in Metal-Decorated Honeycomb Borophene Oxide”. *ACS Applied Materials & Interfaces* 13 (2021), 43233–43240.

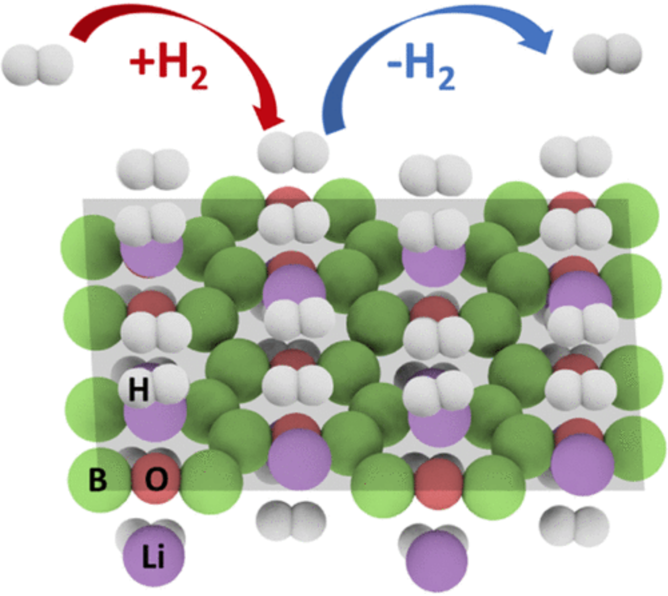

2.1. Introduction

Within physisorption based H_2 storage materials, 2D structures exhibit a great potential in reaching high H_2 capacities due to their large surface to volume ratios [79, 124, 125]. To have reversible H_2 storage, the binding of H_2 on the 2D substrate generally needs to be enhanced. Several adjustments have been proposed to enhance the binding of H_2 with 2D substrates [52, 75, 125–128]. Examples of such adjustments include external charge modulation [126, 127] and introduction of decorating atoms (mainly metals such as Li), which enhance interactions by polarizing H_2 [52, 125, 128]. 2D boron sheets (borophene), which have been recently synthesized [129–131], have shown a favorable affinity with different metal decorating atoms, in contrast to graphene for which clustering of metal atoms can occur [132, 133]. Using a variety of metal decorations, such as Li [52, 128, 132], Na [134], Ca [135], and Ti [136] on different borophene polymorphs, impressive H_2 gravimetric densities have been obtained ranging from 6 to 15 wt%, exceeding the US department of energy (DOE) requirement for onboard storage of 6.5 wt% H_2 [26].

Experimental and theoretical studies on borophene have indicated that borophene is prone to oxidation when exposed to air [44, 129, 137, 138]. For this reason, the protection of borophene polymorphs from air can be crucial for applications such as H_2 storage [138]. Although uncontrolled oxidation is undesirable, one can intentionally use the oxidation process to produce structures that are more chemically stable [117, 139]. For this reason, researchers have been actively looking into a variety of 2D boron oxide structures [139, 140]. Inspired by the recent synthesis of honeycomb borophene on an Al substrate [117, 130], a 2D honeycomb borophene oxide (B_2O) structure has been theoretically proposed [117]. Phonon dispersion and ab-initio molecular dynamics simulations have shown that the 2D honeycomb B_2O structure is stable for temperatures up to 1000 K [117]. 2D honeycomb B_2O has a high capacity for Li/Na functionalization, thereby being a promising anodic material [141]. In particular, B_2O has been shown to have one of the highest capacities for Li storage [141]. The high affinity of 2D B_2O for metal decorating atoms, with its high stability hints at the suitability of this material for H_2 storage applications. To the best of our knowledge, despite the potential of this material, its use for H_2 storage has not yet been explored. Similar to other 2D boron-based structures, such as borophene [142], 2D boron-oxides can form different structural polymorphs [139, 140, 143]. Honeycomb B_2O has a lower formation energy compared to other 2D allotropes such as B_4O, B_{50}, B_6O, , B_7O, and B_8O indicating its stability [117, 139]. Other 2D polymorphs of boron-oxide such as the recently reported B_2O_3 [143] may also be suitable for H_2 storage applications, however, the study of these materials is beyond the scope of this chapter.

In this chapter, the use of 2D B_2O as an efficient H_2 storage material is investigated using first principles calculations. Three different alkali metals (i.e., Li, Na, and K) are considered for enhancing the interactions of 2D B_2O with H_2. The addition of these metal decorating atoms is found to be favorable as evident by negative adsorption energies. All three metal atom types increase the binding energy of H_2 compared to the pristine structure, and result in binding energies suitable for reversible H_2 storage. Our DFT calculations with the Li decorated 2D B_2O structure clearly show that a notable gravimetric density of 8.3 wt% H_2 can be achieved. By performing BOMD simulations we show that the Li-decorated structure is stable at 100, 300 and 500 K. Finally, we used semi-empirical calculations to show that at adsorption conditions of 298 K and 30 atm, and desorption conditions of 373 K and 3 atm, a practical gravimetric density of 5.2 wt% H_2 can be attained. Our findings strongly recommend further experimental investigation of 2D honeycomb B_2O as a potential H_2 storage medium.

2.2. Methodology

2.2.1. Density Functional Theory

DFT calculations are carried out using plane wave basis sets, as implemented in Vienna *ab-initio* simulation package (VASP 5.3.5) [71, 72]. The projected augmented wave method (PAW) is used and the generalized gradient approximation (GGA) is applied with the Perdew-Burke-Ernzerhof (PBE) exchange-correlation functional [144]. Van der Waals forces are accounted for by using a dispersion corrected framework (DFT-D2) [118]. This approach is commonly used in other studies of H_2 storage on 2D metal-decorated substrates [52, 75, 125, 136, 145]. An inter-layer separation of more than 30 Å is used, to prohibit inter-layer interactions [128]. Nevertheless, a smaller inter-layer spacing may also be applicable [52, 75, 145]. The cut-off energy is set to 700 eV for the plane-wave basis set and a Gamma-centered Monkhorts-Pack k-point mesh of $3 \times 9 \times 1$ is used for the structural relaxations and binding energy calculations. The energy convergence criteria for the self-consistent electronic loop is set to 10^{-6} eV. All lattice parameters and atomic positions are relaxed until the residual forces acting on each atom are below 1 meV/Å. Gaussian smearing with a sigma of 0.02 eV is used for Brillouin-zone integration. A 2×2 conventional unit cell of borophene oxide, containing 16 B atoms and 8 O atoms, is used for the DFT simulations. The H_2 adsorption energies are calculated from [52, 74, 146–148]

$$E_\mathrm{b} = (E_{\mathrm{S}+q\mathrm{H}_2} - E_\mathrm{S} - qE_{\mathrm{H}_2})/q \tag{2.1}$$

where E_b is the average binding energy of H_2 with the 2D substrate, $E_{\mathrm{S}+q\mathrm{H}_2}$ and E_S are the energies of the substrate with and without H_2 molecules, E_{H_2} is the energy of a H_2 molecule in vacuum, and q is the number of H_2 molecules. All energies in equation 2.1 are computed using DFT. For simulations in which the 2D structure is functionalized with metals atoms, the average H_2 binding energy is calculated using [52, 74, 146–148]

$$E_{\mathrm{b}} = (E_{\mathrm{S+M+}q\mathrm{H_2}} - E_{\mathrm{S+M}} - qE_{\mathrm{H_2}})/q \tag{2.2}$$

where $E_{\mathrm{S+M+}q\mathrm{H_2}}$, and $E_{\mathrm{S+M}}$ represent the energy of the 2D metal decorated substrate with and without H_2, respectively. The single H_2 removal energy, E_{r}, is calculated according to [149]

$$E_{\mathrm{r}} = E_{\mathrm{S+M+}q\mathrm{H_2}} - E_{\mathrm{S+M+(q-1)H_2}} - E_{\mathrm{H_2}} \tag{2.3}$$

where $E_{\mathrm{S+M+}q\mathrm{H_2}}$, and $E_{\mathrm{S+M+}(q-1)\mathrm{H_2}}$ represent the energies of a 2D metal decorated substrate containing q and $(q-1)$ H_2 molecules, respectively. In the case of metal-decorated 2D B_2O there is an intrinsic dipole in the direction normal to the 2D plane. For this reason calculations are carried out to examine if there is a need for dipole corrections in this system. It is found that for single-metal (Li, Na, and K) decorated B_2O dipole corrections change the total energies by less than 0.02% and the metal adsorption energies on B_2O by less than 2.5 % (most difference for K-decorated and least for Li-decorated B_2O). As the results do not show considerable change, dipole-corrections were not accounted for the rest of the computations.

2.2.2. Born-Oppenheimer Molecular Dynamics

To investigate the finite temperature stability of the structure, BOMD simulations are carried out using VASP [71, 72]. To create the BOMD simulation box, the DFT supercell is multiplied by a factor of 2 along its smallest side, thereby creating a 2×4 supercell. The stability of the H_2 saturated, and Li decorated B_2O structure is examined at three different temperatures (i.e., 100, 300 and 500 K) using a Nosé-Hoover thermostat [150, 151]. These simulations are performed in the canonical ensemble (NVT), and include only the Γ-point. Alternatively, the NPT-ensemble can be used for the simulations. As the number of H_2 molecules is relatively small (32 in total), large pressure fluctuations are expected upon adsorption/desorption of H_2. Due to this when using the NPT ensemble caution must be taken to only adjust the volume normal to the 2D plane, to avoid creating artefacts (e.g. artificial wrinkles) on the 2D structure. For this reason, the NVT ensemble is chosen. The same cut-off energy and smearing as in the DFT calculations are used. The 'normal' precision mode is used for the BOMD simulations and the 'accurate' precision mode is used for the DFT simulations. The BOMD simulations are carried out with a time-step of 1 fs, for a total time of 10 ps. The Verlet algorithm is used for integrating the equations of motion [152]. The variation of free energy (as defined by Kresse et.al [72]) as a function of simulation time is shown in Figure S1 of the Supporting Information of Ref. [27]. In all BOMD simulations, an equilibration period of 5 ps is initially performed. Production runs of 5 ps are used for sampling the property of interest. VESTA is used for all atomic visualizations [153].

2.3. Results and discussion

2.3.1. Pristine B_2O structure

The planar 2D structure of honeycomb B_2O is shown in Figure 2.1. Our results indicate that the relaxed lattice constants for the conventional unit cell are 2.76 and 7.37 Å, while the lattice constant for the primitive cell is 3.93 Å (both sides are equal). The optimal B−O and B−B bond lengths in our simulations are computed to be 1.34 and 1.71 Å, respectively. These results agree well with other DFT results from literature [117, 139]. A single H_2 molecule is then added to the system to compute the binding to the 2D B_2O structure. According to equation 2.1, a single H_2 adsorbs with a binding energy of -0.10 eV/H_2 to the 2D B_2O structure. Figure S2 of the Supporting Information of Ref. [27] shows different initial configurations that are probed and the final relaxed configuration of H_2 on 2D B_2O. All the different initial configurations converged to the same final configuration after relaxing all atomic positions and the structural parameters. Although the binding energy of H_2 with the pristine borophene oxide structure is higher than that of striped borophene (c.a. -0.05 eV/H_2) [52], this binding energy is not adequate for reversible storage of H_2 [154–157]. This illustrates the necessity for the addition of metal decorating atoms.

2.3.2. Metal decoration

Three different alkali metal decorating atoms have been probed, i.e., Li, Na and K. These alkali metal atoms have shown to be particularly adept at enhancing the interaction with H_2, for other 2D structures such as striped borophene [52], boron-phosphide [75] and boron-hydride [145]. Other metal decorations such as Ca, and Ti have also shown to be suitable for H_2 storage applications on 2D borophene structures [135, 136], but examining the applicability of these or other metal atoms as dopants on 2D B_2O for H_2 storage is beyond the scope of this chapter. Before assessing the influence of the decorating atoms on the binding of H_2, the adsorption energy of these metal atoms is calculated on the B_2O surface according to [141]:

$$E_{\mathrm{ads}} = E_{\mathrm{S+M}} - E_{\mathrm{S}} - E_{\mathrm{M,C}} \tag{2.4}$$

where E_{ads}, $E_{\mathrm{S+M}}$, $E_{\mathrm{M,C}}$, and E_{S} are the energy of adsorption, energy of the substrate plus the metal atom, the cohesive energy of the bulk crystalline metal, and the energy of the substrate, respectively. A negative

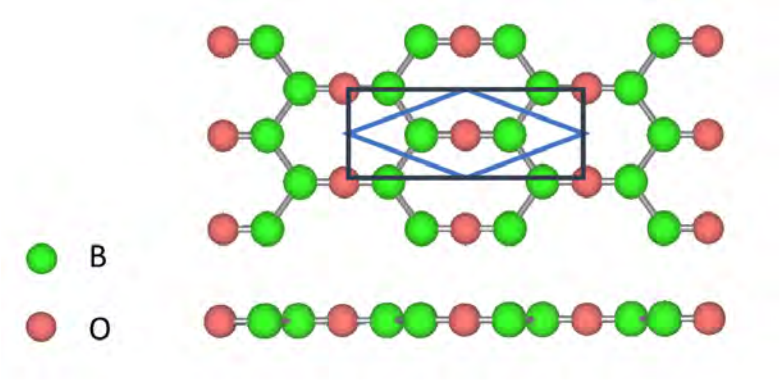

Figure 2.1. Top and side view of the 2D honeycomb borophene oxide structure. The lattice constant for the primitive cell (shown with blue lines) is 3.93 Å, and the lattice constants for the conventional cell (shown with black lines) are 2.76 Å, and 7.37 Å.

adsorption energy signifies the favorable adsorption of the metal atom on the 2D substrate, and a positive energy means that the metal atoms would preferentially cluster together [75]. The results for E_{ads} are -1.00, -0.71, and -1.11 eV for a single Li, Na and K decorated 2D B_2O structure, respectively. All three metal decorating atoms i.e., Li, Na, and K prefer the hollow position in the ring of honeycomb B_2O (see Figure 2.2a for Li) and are situated at a distance of 1.40, 2.02 and 2.41 Å, respectively (see Figure S3 of the Supporting Information of Ref. [27] for different configurations). The charge density difference plot of a Li decorated system is shown in Figure 2.2b. This charge density difference plot is calculated using [75]:

$$\Delta\rho = \rho_{\mathrm{S+M}} - \rho_{\mathrm{S}} - \rho_{\mathrm{M}} \tag{2.5}$$

where $\Delta\rho$, ρ_{S}, ρ_{M}, and $\rho_{\mathrm{S+M}}$ represent the charge density difference, charge density of the substrate, the metal atom, and the combined structure, respectively.

In Figure 2.2b, it can be seen that the addition of the Li atom to the B_2O substrate leads to the formation of a charge depleted region on top of Li (blue region as indicated in Figure 2.2b), while there is enhancement of charge density for the boron and oxygen atoms in the vicinity of Li (yellow region in Figure 2.2b). The Bader charge analysis carried out on Li, Na and K decorated B_2O (see Table S1 of the Supporting Information of Ref. [27]) illustrates the loss of electronic charge by the decorating alkali metals to the 2D substrate. A H_2 molecule that is added to this system interacts with the metal atom, and is adsorbed in the charge depleted region as shown in Figure 2.2c. Figure S4 of the Supporting Information of Ref. [27] shows different configurations that are considered for H_2 adsorption on Li, Na and K-decorated 2D B_2O. For the Li-decorated

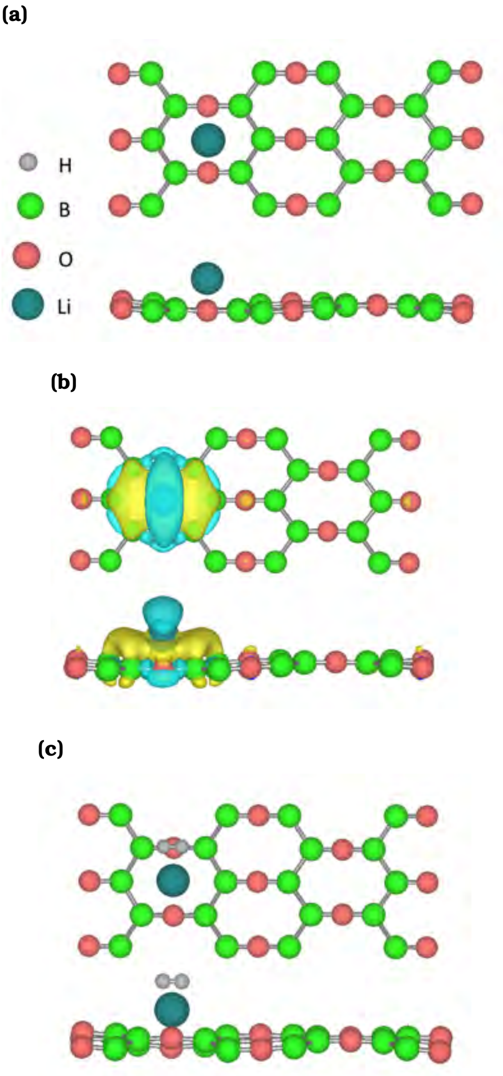

Figure 2.2. Top and side views of (a) a single Li-decorated 2D honeycomb B_2O structure, (b) the charge density difference of the Li-decorated structure, the isosurface value is set to 0.0015 e Å^{-3} (blue areas represent charge density depletion, while yellow areas represent gain), (c) an adsorbed H_2 on the Li-decorated structure, with an H_2 orientation parallel to the B-O-B bond.

structure, H_2 preferentially adsorbs on top of the O-atom, in the vicinity (top edge) of the Li atom (as seen in Figure 2.2c). The favourability of this position is attributed to H_2 maximizing its attractive interaction with the Li atom (and its periodic image) and the 2D B_2O sheet. Similarly, for the Na and K-decorated system (see Figure S4) this site is found to be the most favourable, although the exact positioning of H_2 differs due to the different atomic sizes of Na and K compared to Li. The results for the adsorption of a single H_2 indicate a binding energy of -0.34 eV/H_2 in the case of the Li-decorated structure, and a binding energy of -0.25 and -0.28 eV/H_2 for Na and K decorated structures, respectively. These calculations show that all the alkali metal (i.e., Li, Na, K) decorated B_2O structures have resulted in an interaction energy in the range suitable for reversible H_2 storage (above -0.10 and below -0.60 eV/H_2) [154–157]. For further calculations of the H_2 gravimetric density, the Li-decorated structure is investigated in more detail because of its higher interaction energy with H_2 and the lower atomic mass of Li compared to Na and K.

2.3.3. H_2 gravimetric density

To investigate the suitability of Li decorated honeycomb B_2O for H_2 storage, it is important to estimate the maximum theoretical gravimetric density of H_2 in this structure. For this, both the number of H_2 and Li atoms need to be systematically increased. Before increasing the number of Li atoms it is useful obtain an estimate of the number of H_2 molecules one Li atom can bind to, and how the average binding energy between H_2 and the metal-decorated structure changes with the addition of H_2.

To visualise how H_2 molecules disperse around the Li atom, a structure containing five H_2 surrounding one Li atom is shown in Figure 2.3a. Out of the five H_2 that are shown in this figure, two H_2 have a distance lower than 2.5 Å from Li, while the other three are positioned at a distance of more than 2.5 Å away from the Li atom. In Figure 2.3b the average binding energy per H_2 and the H_2 removal energy is shown as a function of the number of H_2 molecules per Li atom. In a single Li-decorated system, when increasing the number of H_2 molecules from 2 to 3, a large decrease in the magnitude of the H_2 removal energy is observed from -0.27 eV/H_2 to around -0.10 eV/H_2. Considering that -0.10 eV/H_2 is approximately the interaction energy of H_2 with borophene oxide in the absence of Li, it can be concluded that the 3rd to 5th H_2 molecules interact very weakly with Li. Based on the findings shown in Figure 2.3, it is evident that each Li atom can optimally interact with two H_2 molecules, with an average binding energy of -0.30 eV/H_2. Considering that H_2 preferentially binds to the top sides of the Li atom, parallel to the B-O-B bond, it is not suitable to fully cover the structure with Li atoms (i.e., two Li atoms in each hexagonal hole, one at the top and the other at the bottom). Overloading the structure with Li atoms will reduce the number of H_2 that can be adsorbed per Li atom, and thus, lead to a lower H_2 gravimetric density.

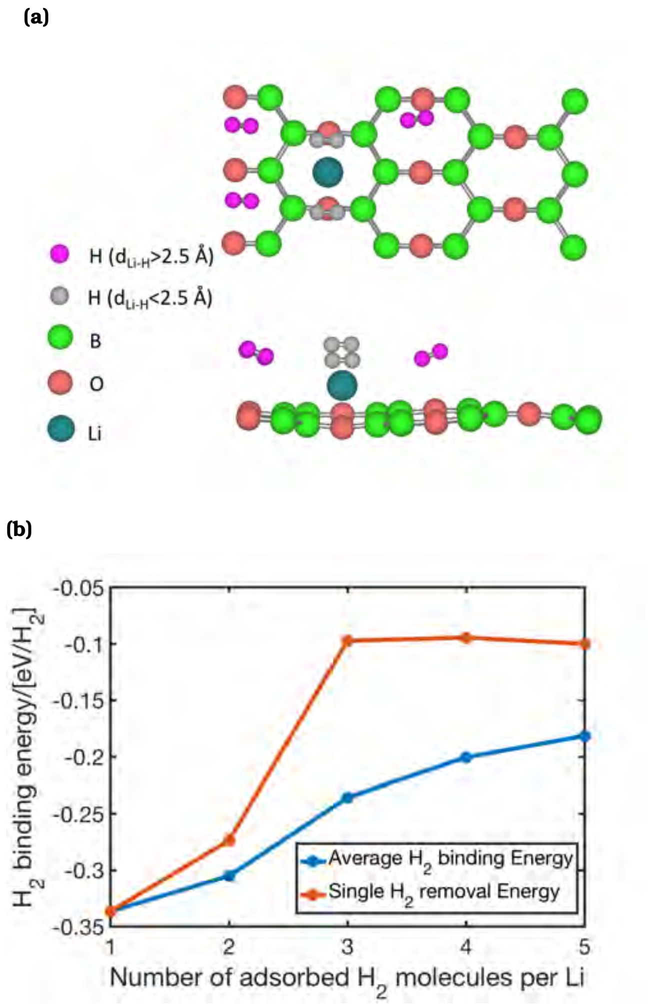

Figure 2.3. (a) Top and side views of a structure containing 5 H_2 surrounding one Li atom. Two H_2 are within a 2.5 Å radius from Li (shown in grey), while the other three are further away due to repulsive forces (shown in pink). (b) The variation of the average H_2 binding energy (E_b) and H_2 removal energy (E_r) as a function of the number of adsorbed H_2 molecules per Li. The lines connecting the points are used to guide the eye.

For this reason, a "half-covered" structure of Li atoms (i.e., a structure containing half as many Li atoms as a fully covered structure) is deemed optimal.

Different "half-covered" Li configurations are shown in Figure 2.4a-c. From the three structures shown, structure 2.4a is the most energetically stable, while structure 2.4b has the highest energy (with a relative difference of 1.5 % compared to the energy of structure 2.4a). Structure 2.4c has a relative energy difference of only 0.3 % with respect to structure 2.4a. Considering that structure 2.4a is the most energetically stable configuration, it is used for further calculations on H_2 adsorption. The addition of two H_2 on the top side of each Li atom (as depicted in Figure 2.4d) resulted in an average binding energy of -0.24 eV/H_2. The weakest H_2 binding energy (H_2 removal energy from the fully H_2 saturated structure shown in Figure 2.4d) is calculated to be -0.21 eV/H_2, while the strongest H_2 binding energy (H_2 binding energy for the first H_2 added to structure shown in Figure 2.4a) is -0.27 eV/H_2. Each H_2 in this structure is located at a distance lower than 2 Å from a Li atom. The gravimetric density (GD) of H_2 can be calculated using [52]

$$GD = \frac{qM_{\mathrm{H_2}}}{qM_{\mathrm{H_2}} + nM_{\mathrm{B}} + lM_{\mathrm{O}} + kM_{\mathrm{m}}} \tag{2.6}$$

where q, n, l and k represent the number of H_2 molecules, B, O and metal decorating atoms in the simulation box, respectively, while M denotes their respective molar masses. Using equation 2.6, the H_2 gravimetric density of this structure equals 8.3 wt%, which exceeds the 6.5 wt% target set by the DOE [26].

2.3.4. Finite temperature stability

To further check the stability and desorption of H_2 at finite temperatures, BOMD simulations are carried out at target temperatures of 100, 300 and 500 K. The results are shown in Figure 2.5. Figure 2.5a-c depict the BOMD snapshots after 10 ps. From these sub-figures, it can be seen that at 100 K, all the H_2 molecules are bound to the Li-decorated B_2O structure, at 300 K 50%, and at 500 K approximately 85% of the H_2 molecules have distances larger than 2.5 Å from a Li atom. To obtain a more quantitative measure of the desorption process, the H-atom distribution in the simulation box is plotted as a function of the distance perpendicular to the 2D surface. The distribution plot is normalized such that the area under the curve equates to the number of H-atoms in the simulation. Figure 2.5d shows two peaks, both at a distance approximately 3 Å away from the 2D structure, which corresponds to the perpendicular distance of the H_2 adsorption sites (above and below) from the 2D structure. The adsorption peak gradually decreases with the increase in the temperature, as H_2 molecules begin to distribute evenly in

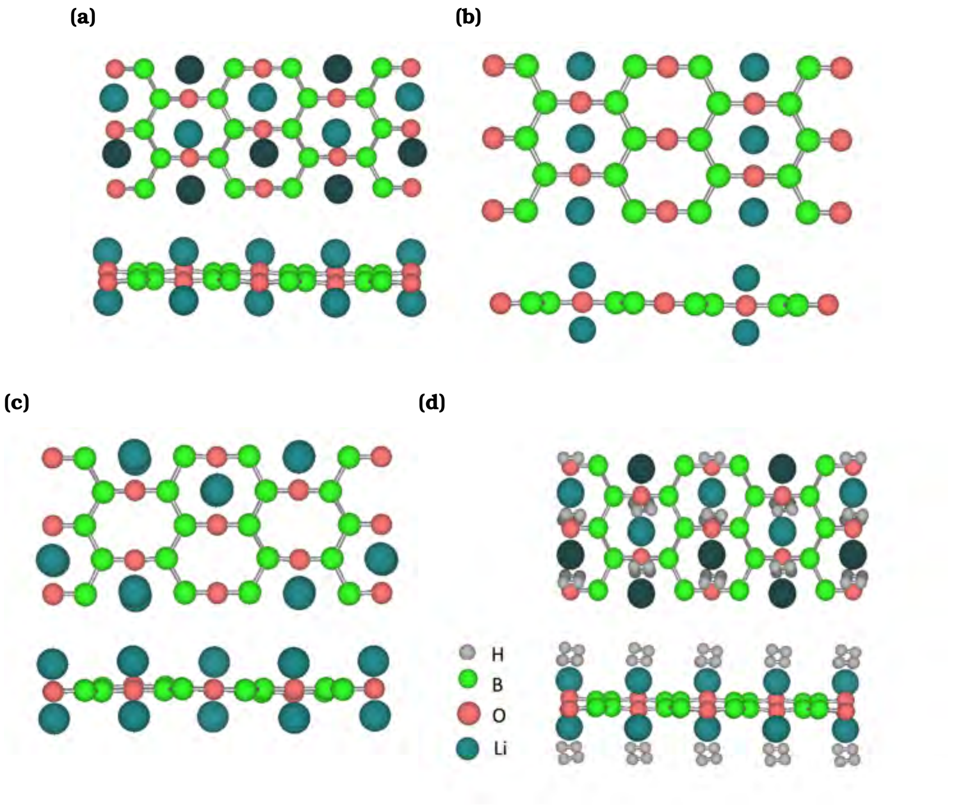

Figure 2.4. (a-c) Different configurations of the "half-covered" Li structures shown from the top and the side. (d) Top and side view of H_2 adsorption in structure 4a. Each Li atom can successfully bind to two H_2 leading to a gravimetric density of 8.3 wt% H_2. In the top view, the Li and H atoms that are on the bottom are given a darker shade for better readability of the figure.

the simulation box. The BOMD simulations also demonstrate that even at 500K, no clustering of Li-atoms is observed in the 10 ps simulation time-frame, and the metal-decorated structure is found to be stable. This confirms the favorable Li adsorption energy as discussed in section 2.3.2. No chemical reactions have occurred between H_2 molecules and the 2D substrate, so the structure does not undergo irreversible changes and H_2 molecules can be released without having to overcome a significant energy barrier (covalent bond making/breaking). Therefore, the findings from the BOMD simulations indicate the stability of Li-decorated B_2O for H_2 storage in the temperature range of 100 to 500 K.

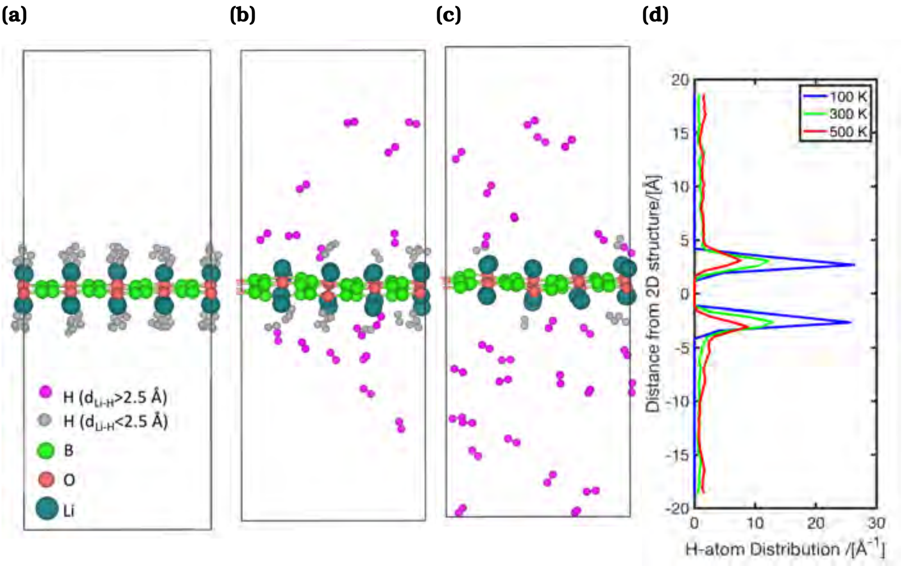

Figure 2.5. BOMD simulation snapshots of Li decorated B_2O structure at three different temperatures of (a) 100, (b) 300 and (c) 500K. H_2 molecules that are at a distance exceeding 2.5 Å from the closest neighboring Li atom are colored in purple while the ones within this range are colored in grey. The average H-atom distribution is calculated over the last 5 ps of the BOMD simulations as a function of the distance perpendicular to the surface as shown in (d).

2.3.5. Adsorption and desorption conditions

In the BOMD simulations the pressure is not controlled and can vary considerably at different temperatures. In this section, semi-empirical calculations are used to estimate the practical H_2 storage capacity at finite temperatures and pressures. The occupation number (F), which represents the expected number of H_2 molecules that can be adsorbed on the structure, can be calculated using [54]

$$F = \frac{\sum_{n=0}^{N_{\text{max}}} n g_n \exp\left[\frac{n(\mu - E_{\text{b}})}{k_{\text{B}}T}\right]}{\sum_{n=0}^{N_{\text{max}}} g_n \exp\left[\frac{n(\mu - E_{\text{b}})}{k_{\text{B}}T}\right]} \tag{2.7}$$

where N_{max} is the maximum number of H_2 molecules that can be adsorbed, g_n is the degeneracy of the state containing n H_2. E_{b}, T, k_B, and μ represent the average H_2 binding energy (function of n), the temperature, Boltzmann constant, and the chemical potential of H_2 in gas phase, respectively. To simplify the expression, it is assumed that each adsorption site on the structure is independent of its neighboring sites. In this case, the situation simplifies to finding the occupation number of a single site (f), on which at most a single H_2 can be adsorbed. In this case, the degeneracy of the occupied and unoccupied state are both 1 and the single site occupation number equates to [125, 149, 156, 158]

$$f = \frac{1}{1 + \exp\left[\frac{-(\mu - E_\mathrm{b})}{k_\mathrm{B} T}\right]} \tag{2.8}$$

where the chemical potential of H_2 in the gas phase μ is a function of temperature and pressure. The total occupation number F and the single site occupation number f are related by $F = M_\mathrm{sites} f$, in which M_sites refers to the total number of H_2 adsorption sites on the structure [156]. The chemical potential μ in our calculations is obtained using the following empirical relation [149, 156, 158, 159]

$$\begin{aligned} \mu(T,P)/[\mathrm{eV}] = \mu_\mathrm{ref}(\mathrm{T},\mathrm{P}) + 0.00015(\mathrm{T} - 186.5) \\ + 0.00065\left[(\log_{10}\frac{P}{P_0} - 0.5)^2 - 0.25\right] \end{aligned} \tag{2.9}$$

where the temperature (T) is in the unit of K, pressure (P) is in the unit of atm, and the reference pressure (P_0) is 1 atm. μ_ref is the reference chemical potential and is calculated using [54]

$$\mu_\mathrm{ref}(T,P) = -k_B T \ln\left[\left(\frac{2\pi m_{\mathrm{H}_2} k_B T}{h^2}\right)^{\frac{3}{2}} \frac{k_B T}{P}\right] \tag{2.10}$$

In our calculations, adsorption takes place at a temperature of 298 K and a pressure of 30 atm, while desorption occurs at 373 K and 3 atm. These adsorption/desorption conditions are often used in literature for calculating the practical gravimetric density [125, 145, 149, 156, 158]. At these conditions, the chemical potential (as calculated by equation 2.9) and the reference chemical potential are similar in value [158]. At adsorption conditions, the reference chemical potential is -0.21 eV, while a value of -0.22 eV is obtained using equation 2.9. At desorption conditions, the reference chemical potential gives a value of -0.36 eV, while μ is obtained as -0.38 eV using equation 2.9 [158]. Calculating f at the adsorption conditions yields a value of 0.64, while at the desorption condition f becomes 0.01. This gives a practical gravimetric density of around 5.2 wt% H_2 for the Li-decorated B_2O under these capture/release conditions. Lowering the adsorption temperature and/or increasing the adsorption pressure can lead to higher gravimetric capacities. These findings indicate that the Li-decorated B_2O structure can be used for reversible H_2 storage, at near-ambient conditions. To obtain the optimal release/capture conditions and more accurate calculations of H_2

capacity at various temperatures and pressures, further simulations are encouraged.

2.4. Conclusions

The capability of 2D honeycomb borophene oxide for H_2 storage applications is assessed using DFT and BOMD simulations. This 2D structure has a favorable affinity with alkali metal atoms such as Li, Na and K, as indicated by the negative adsorption energy of these metals. These alkali metal decorated B_2O structures have enhanced H_2 binding energies with respect to the pristine B_2O structure. In particular, the Li decorated structure reaches a gravimetric density of 8.3 wt% H_2 with an average binding energy of -0.24 eV/H_2, which exceeds the gravimetric density requirement set by DOE for onboard H_2 storage applications [26]. BOMD simulations at 100, 300, and 500 K and calculations of the occupation number show both the stability and reversible binding of H_2 on the Li-decorated borophene oxide structure. Our simulations strongly encourage experiments on borophene oxide and further simulations to accurately find the H_2 capacity at various pressures and temperatures.

3

Hydrogen Dissociation in Borophene and Borophene Hydride

This chapter is based on the following publication: P. Habibi, T. H. G. Saji, T. J. H. Vlugt, O. A. Moultos, and P. Dey. “Hydrogen dissociation in Li-decorated borophene and borophene hydride: An ab-initio study”. *Applied Surface Science* 603 (2022), 154323.

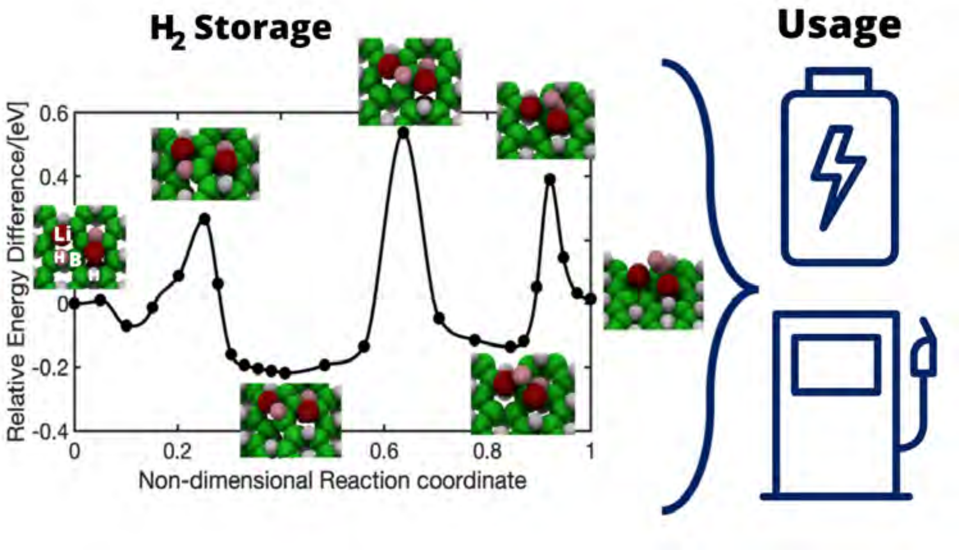

3.1. Introduction

Chemisorption of H_2 can lead to high volumetric capacities, but suffers from slow kinetics due to large energy barriers that have to be overcome to build/break H_2 bonds [79, 160–165]. The hydrogenation reaction in chemisorption based materials, such as in metal hydrides, is usually a highly exothermic reaction [39–41]. Insufficient cooling can lead to high temperatures at which materials can degrade (e.g. sintering in metal hydrides), resulting in a lower H_2 capacity [39]. For these reasons, it is important to design materials in which the hydrogenation (dehydrogenation) reaction can occur reversibly, with little to no heat release (uptake), and with low energy barriers [160].

2D materials are suitable for both chemisorption or physisorption alike. The large surface to volume ratio of these materials provides a large number of adsorption sites, which helps in reaching high H_2 capacities [27, 125]. The electronic properties of these materials and their interaction with H_2 can also be tuned in various ways such as strain-engineering [166–168], addition of dopants [27, 128, 169–171], vacancy creation [79, 172], or by inducing charge, [126, 127] or curvature [173, 174]. The tuning of these electronic properties can assist in enhancing the adsorption/desorption kinetics, or the H_2 capacity. Galvanized by the synthesis of borophene (2D boron-sheets) by molecular epitaxy, the field of 2D boron-based materials has rapidly expanded [129–131]. The elaborate chemistry of boron allows for many different structural allotropes [142], anisotropic mechanical properties, electrical conductivity and favorable affinity with metal dopants [132, 133]. Borophene-hydride (also referred to as 2D hydrogen boride), which has been recently synthesized by a more facile route of cation-exchange and exfoliation [28, 29], shares many of these interesting physical and chemical properties [175–177]. Due to the favorable affinity of 2D boron-based materials with metal dopants, the addition of metal decorating atoms has been a prominent method for enhancing the interaction and capacity of H_2 for physisorption storage [27, 52, 75, 145]. Li dopants have been extensively considered for this application, due to their large adsorption energy with 2D boron-based materials and the low atomic mass of Li, which allows for reaching high H_2 gravimetric densities. Remarkable gravimetric densities in the range of 7-12 wt% have been reported for Li-doped borophene and borophene-hydride for H_2 physisorption-based storage [52, 128, 145, 178]. The structural stability (including the phonon spectrum) and physical properties of various borophene-hydride and borophene structures are discussed in previous studies [176, 179–181].

Prior studies with borophene-hydride have shown that the addition of charge (by doping or applying a current) to the structure can destabilize the 3 center 2 electron B–H–B bonds [30, 182]. As metal decorating atoms lose part of their electronic charge density to the borophene-hydride structure [145], a similar effect on the B–H–B bond may be observed. In other studies, Li has been used at high loadings on borophene-hydride and borophene structures for Li-anode batteries [175, 177, 183] and for H_2 physisorptive storage applications [128, 145]. Despite these existing works, the influence of Li dopants on H_2 chemisorption is not apparent in DFT [27, 75], or in time-scales accessible by quantum molecular dynamics methods (order of 10 ps) [27], even though it may be present in time scales relevant experimentally. To the best of our knowledge, the influence of Li dopants on the reversibility and activation energy barriers associated with H_2 chemisorption and dissociation has not yet been studied for borophene-hydride and striped borophene. In particular borophene-hydride could serve as a suitable H_2 storage medium, as the structure has ca. 8.5 wt % H-atoms [29], provided that the chemisorbed H-atoms can recombine with little heat uptake (reversibly) and low energy barriers (preferably below 1.5 eV [45, 79]).

In this chapter, the H_2 chemisorption and dehydrogenation reaction pathways for Li-doped borophene-hydride and striped borophene are investigated by DFT calculations and the NEB method [76, 77]. It is shown that for the pristine borophene-hydride and striped borophene structures, dehydrogenation reaction is highly endothermic, exceeding 1.5 eV/H_2, and has large energy barriers (i.e., exceeding 2.0 eV). Li-dopants are shown to significantly reduce the relative energy difference between the chemisorbed and physisorbed state, thereby leading to more reversible hydrogenation/dehydrogenation reactions. The Born-Oppenheimer molecular dynamics (BOMD) simulations at 300 K show that the 3-center-2-electron bond in borophene-hydride weakens in the presence of Li dopants. The dehydrogenation energy barriers for H_2 formation are reduced by over 30% for Li doped striped-borophene and borophene-hydride. In the case of Li doped borophene-hydride, a reversible dehydrogenation reaction has been observed with low desorption/adsorption barriers. This suggests the suitability of this material for H_2 chemisorptive storage. Our findings strongly encourage further experimental study on Li-doped 2D boron-based materials to elucidate their influence on dehydrogenation/hydrogenation.

3.2. Methodology

3.2.1. Density Functional Theory

DFT calculations are performed using the VASP 5.3.5 software package [71, 72]. The PAW method and the PBE exchange correlation functional are used along with the DFT-D2 dispersion corrected framework [118]. The more recent DFT-D3 approach [184], accounts for the variations in the local environment of the atoms by considering the coordination number of each atom. Table S1 of the Supplementary Information of Ref. [78] shows a comparison between the heats of dehydrogenation computed using the DFT-D2 and DFT-D3 methods. An inter-layer separation of more than 20 Å is used [52, 145]. The cut-off energy is set to 550 eV for the plane-wave basis set and a Gamma-centered Monkhorst-Pack k-point mesh of $4 \times 4 \times 1$ is used for the structural relaxations and adsorption energy calculations. The convergence test for the k-point mesh is shown in Figure S1 of the Supplementary Information of Ref. [78]. The energy convergence criteria for the self-consistent electronic loop is set to 10^{-6} eV. All lattice parameters and atomic positions are relaxed until the residual forces acting on each atom are below 1 meV/Å. Gaussian smearing with a sigma of 0.05 eV is used for Brillouin-zone integration. A 3×4 conventional unit cell of borophene-hydride, containing 48 B atoms and 48 H atoms, and a 3×6 conventional supercell of striped borophene, containing 36 B atoms, are used for the DFT simulations. The choice of the system sizes is justified in tables S2 and S3 of the Supplementary Information of Ref. [78]. The system size is chosen to limit interactions between periodic images, while ensuring that the computations do not become too expensive. For a single Li-decorated borophene hydride and striped borophene structure, spin-polarized calculations are used, which converged to their non-magnetic counterparts. As both systems are found to be non-magnetic, spin-polarized calculations are not further considered for the rest of the systems studied. The Bader charges are calculated using the algorithm developed by Henkelman et al. [185–188].

3.2.2. Nudged Elastic Band method

To obtain the energy barrier for formation or dissociation of H_2, the minimum energy path (MEP) is computed using the NEB method, as implemented in VASP (5.3.5) [71, 72, 77, 119]. The energies and structures of the initial (chemisorbed) and final (physisorbed) states are calculated using DFT calculations. For the cases where the physisorbed and chemisorbed states are separated by a single transition state (no stationary states present along the reaction pathway), 5 different images are used to sample the MEP. In cases where stationary states are present in between the physisorbed and chemisorbed states, the NEB calculation is broken down into multiple segments with 5 different images connecting each stationary state. The climbing image method is used to drive the image with the highest energy towards the saddle point [76]. The same cut-off energy and k-point mesh is used for the NEB calculations as for the DFT calculations. For each image, all lattice parameters and atomic positions are relaxed until the residual forces acting on each atom are below 10 meV/Å.

3.2.3. Born-Oppenheimer Molecular Dynamics

To investigate finite-temperature (at 300 K) stability of borophene-hydride (with and without Li-dopants), BOMD simulations are carried out using VASP (5.3.5) [71, 72]. The simulations include only the Γ-point, and are performed in the canonical ensemble (*NVT*). The same cut-off energy and smearing as in the DFT calculations are used. The BOMD simulations are carried out with a time-step of 1 fs. In all simulations, an initial equilibration period of 2 ps is performed, in which the temperature is increased from 0 K to 300 K. This is followed by a 10 ps production run. The variation of free energy (as defined by Kresse et al. [72]) and temperature for the BOMD simulations, as a function of simulation time is shown in Figure S2 of the Supplementary Information of Ref. [78]. A Nosé-Hoover thermostat is used [150, 151]. The choice for the Nosé-Hoover mass parameter is explained in Figure S2 of the Supplementary Information of Ref. [78]. For the initial structures, the relaxed (using DFT) borophene-hydride structures (with and without Li dopants) are used. The Verlet algorithm is used for integrating the equations of motion [152]. iRASPA is used for all atomic visualizations [37].

3.3. Results and discussion

3.3.1. Borophene-hydride and striped borophene structures

The pristine borophene-hydride and striped borophene structures are shown in Figure 3.1. Borophene-hydride is a planar structure with a unit cell with dimensions of 3.04 Å by 3.04 Å. For this structure the B−H, B−B (with H at bridge site), and B−B (without H at bridge site) bonds have lengths of 1.33, 1.82, and 1.72 Å, respectively. For striped borophene, a corrugated structure with a conventional/unit cell of 2.86 Å by 1.61 Å is obtained. The corrugation height of the striped borophene structure corresponds to 0.89 Å. Our structural results show a great agreement with other DFT and experimental findings for both structures [29, 52, 129, 145].

3.3.2. H_2 desorption on borophene-hydride (2D BH)

The pristine structure of 2D BH stores 8.5 wt% chemisorbed H atoms [29]. To investigate the desorption of these H-atoms, different paths for H_2 formation are considered. Three different H_2 formation routes are shown in Figure 3.2. To form a H_2 molecule, a H-atom can react with its adjacent (V1), and opposing (up/down (V2), and across the hollow site (V3)) neighboring H-atoms. Our DFT results indicate that the V1 reaction route (see Figure 3.2(a)) is the most energetically favorable route with a heat of dehydrogenation of 1.92 eV/H_2, while the V2 and V3 formation route have a heat of dehydrogenation of 2.11, and 1.94 eV/H_2, respectively. Based on these results, it can be concluded that the physisorbed state is significantly less energetically stable than the chemisorbed state, leading to a strongly endothermic dehydrogenation reaction (ca. 2.0 eV/H_2).

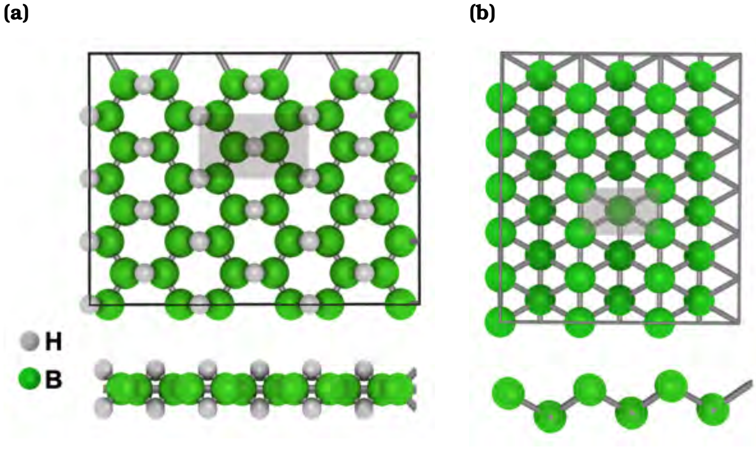

Figure 3.1. Top and side views of relaxed (a) borophene-hydride with a conventional cell of 5.29 Å by 3.01 Å, and (b) striped Borophene with a conventional/unit cell of 2.86 Å by 1.61 Å. The conventional cells are indicated by a grey area for both structures.

In the MEP shown in Figure 3.3, a two-step H_2 formation mechanism is shown for the V1 formation route (see Figure 3.2(a)), with one stationary state in between the initial (chemisorbed) and final (physisorbed) states. In the first step, a H-atom initially diffuses from a bridge site towards a B atom. Subsequently, it forms an H_2 molecule by reacting with its closest neighboring H-atom. The MEP, as obtained from the NEB calculations, is shown in Figure 3.3(b). For dehydrogenation to occur, two energy barriers have to be overcome, with an overall barrier (summation of the two barriers) of 2.87 eV. Other reaction reaction pathways (with a single-step process) for dehydrogenation have also been investigated (see Figure S3 of the Supplementary Information of Ref. [78]. It is found that the two step process as shown in Figure 3.3 has a 12.5% lower overall energy barrier with respect to the single step process. Overall, It can be seen that in the pristine 2D BH structure, dehydrogenation is endothermic, with large activation energy barriers. This finding shows the necessity for addition of dopants to make 2D BH suitable for H_2 chemisorption.

3.3.3. H_2 adsorption/desorption on striped-borophene

As striped borophene does not intrinsically contain any H-atoms, unlike 2D BH, a H_2 molecule is inserted to assess H_2 chemisorption. To examine the energetic stability of different possible configurations for H-atoms (for the initial chemisorbed state) and a H_2 molecule (for the final physisorbed state), three different configurations are probed for both the initial and

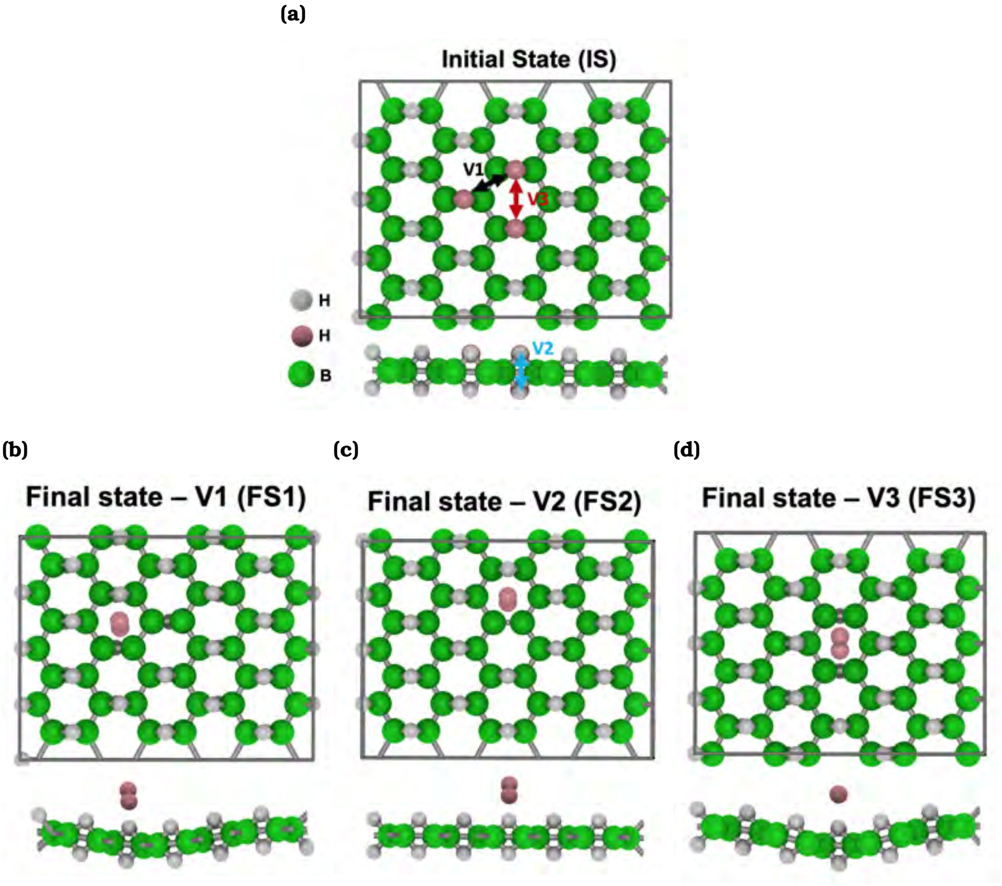

Figure 3.2. Different H_2 dissociation/desorption paths on 2D BH are shown in structure (a). In the first variation (V1), two adjacent H atoms react, while in the second (V2) and third (V3) variation, two up/down and opposing H neighbors react to form H_2, respectively. The different variations, V1, V2 and V3, lead to the H_2 physisorbed states, (b), (c) and (d), respectively. The H atoms that are undergoing reaction are shown in pink while the rest of H-atoms are colored grey.

final states. These different configurations are shown in Figure S4 of the Supplementary Information of Ref. [78]. The most energetically stable configurations are then used to calculate the H_2 chemisorption/desorption energy barrier. Figure 3.4 shows the configurations and the minimum energy path of H_2 desorption or chemisorption for striped borophene. The hydrogenated state is found to be more energetically favorable than the dehydrogenated state, leading to an endothermic hydrogen release of 1.41 eV/H_2. The energy barrier for H_2 release (dehydrogenation) is 2.04 eV,

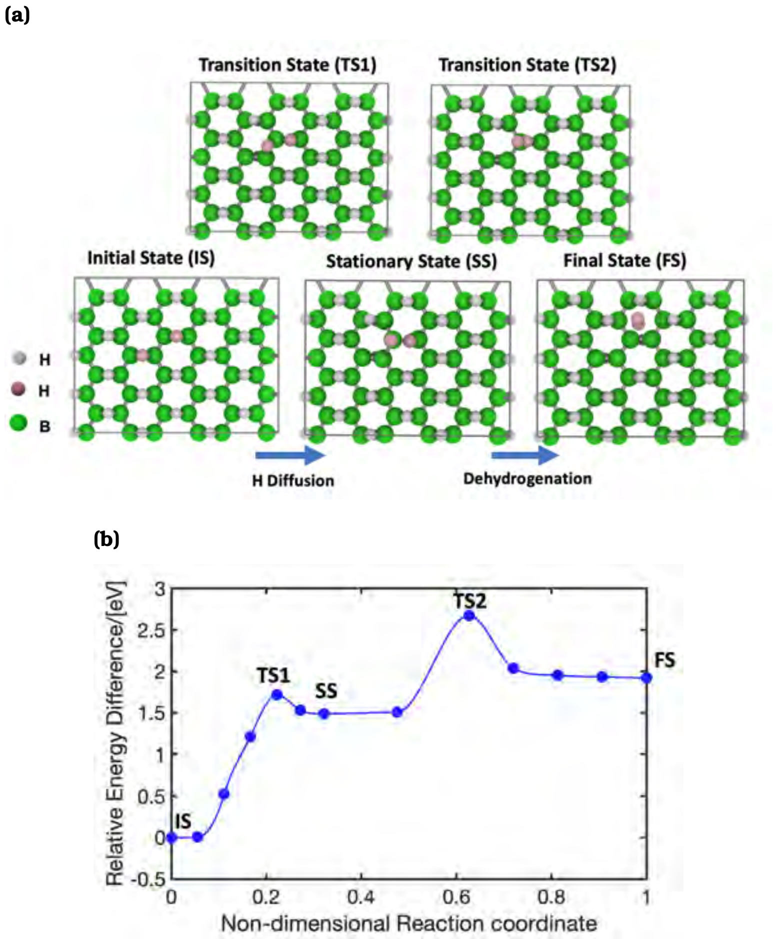

Figure 3.3. (a) The structural configurations corresponding to the minimum energy pathway for a single H_2 release on 2D BH. The H atoms that are undergoing reaction are shown in pink while the rest of H-atoms are colored grey. To reach the final state from the initial state, one of the H-atoms initially hops to a neighboring boron atom (stationary state) and consequently the two H-atoms react to form a H_2 molecule. The transition states for each of the two processes are shown. (b) The minimum energy pathway for a single H_2 release for the path depicted in (a) as a function of a non-dimensional reaction coordinate. The TS1, SS, TS2, and FS states have energy differences of 1.72, 1.53, 2.68, and 1.92 eV with respect to the IS state, respectively. The lines connecting the NEB images (constructed using forced-based cubic splines) are to guide the eye.

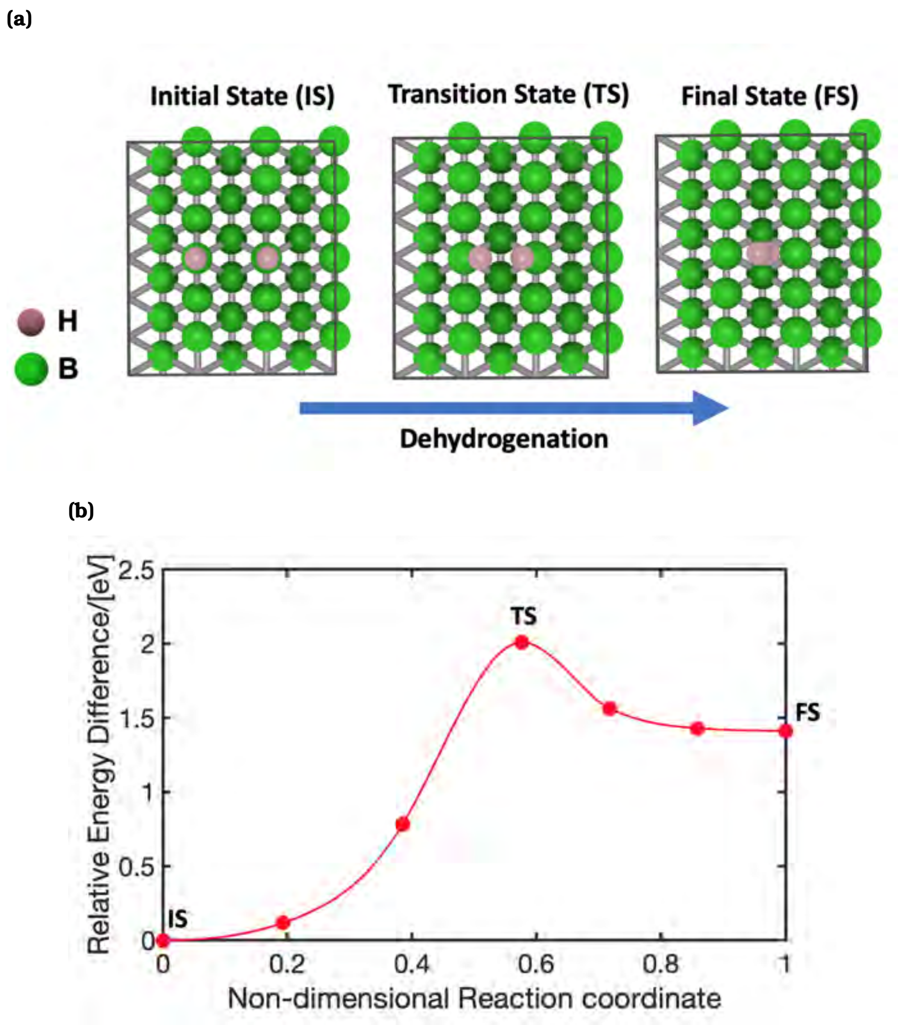

Figure 3.4. (a) The minimum energy path for the release of a single H_2 on striped-borophene. The H atoms that are undergoing reaction are shown in pink. H_2 release occurs in an one-step reaction process from the chemisorbed (initial) state to the released (final) state. The transition state for the process is shown. (b) The minimum energy path for a single H_2 release for the path depicted in (a) as a function of the non-dimensional reaction coordinate. The TS, and FS states have energy differences of 2.04, and 1.41 eV with respect to the IS state, respectively.

which is lower than in 2D BH, but larger compared to graphene based H_2 chemisorption materials reported (usually ca. 1.5 eV [45, 79]). The results obtained for the energy barrier of H_2 release on striped borophene shows adequate agreement to similar calculations reported in literature (ranging from 1.89 eV [189] to 2.21 eV [190]).

3.3.4. Doping with Li

After having established a benchmark for H_2 chemisorption and desorption on the pristine 2D structures, the influence of Li-dopants on the dehydrogenation reaction has been considered. To assess the stability of Li-dopants on the 2D structures, the Li-adsorption energy (E_{ads}) is calculated using Eq. 2.4. Based on prior findings in the literature, Li-dopants have a higher affinity for borophene-hydride compared to dopants such as Na, K, Ca and Mg [145, 177]. For this reason, only Li adatoms are considered here. The study of the influence of other dopants on the dehydrogenation barriers in borophene and borophene hydride is beyond the scope of this chapter.

For a single Li-dopant on 2D BH, three different adsorption sites are considered, namely on top of the B or H atom, or on the vacant site. It is found that the vacant site is the most favorable position, with an adsorption energy of -0.66 eV (see Figure S5 of the Supplementary Information of Ref. [78]. Higher Li-loadings up to 4 Li-atoms are probed, and their influence on the dehydrogenation of 2D BH is investigated. As we are interested in the influence of Li-atoms on the dehydrogenation reaction shown in Figure 3.3(a), the Li-atoms are placed in the proximity of the H-atoms that take part in the reaction. The different configurations of Li-doped 2D BH considered (at various Li loadings) are shown in Figure S6 in the Supplementary Information of Ref. [78]. The initial chemisorbed configuration for the 3-Li decorated 2D BH is shown in Figure 3.5(a).

Table 3.1 shows for each of the configurations the respective Li adsorption energies, the average Bader [185] net charge state of the Li-atoms in the chemisorbed state, and the relative energy difference of the final (physisorbed) state with respect to the initial (chemisorbed) state ($\Delta E_{\text{FS}-\text{IS}}$). The mechanism for Li charge transfer on borophene-hydride, including the electronic structure and charge density difference, is elaborated in prior studies [145, 175]. The average Bader net charge state represents the net gain or loss of electronic charge density of an atom [185] due to its environment, and shows the degree of charge density loss by the Li-dopant onto the 2D substrate at various Li-loadings. Our results indicate that the addition of Li-dopants increases the energetic stability of the final state (physisorbed) with respect to the initial state (chemisorbed), leading to a transition from endothermic to exothermic dehydrogenation on 2D BH. Specifically for the structures shown in Figure 3.5(a) and (c) (3Li-2D BH configuration), the initial and final state are close in energy, thereby making dehydrogenation a much more reversible

Table 3.1. The Li-adsorption energy ($E_{\mathrm{ads,Li}}$), and the average Li-Bader net charge state on 2D BH at different loadings of Li. For the Bader net charge state, the plus sign indicates a gain of electronic charge density and a minus sign indicates a loss of electronic charge density with respect to the atomic charge of respective elements (net charge 0). The energy difference between the final (physisorbed) and initial (chemisorbed) state ($\Delta E_{\mathrm{FS-IS}}$) is shown at different Li-doped configuration (see Figure S6 of the Supplementary Information of Ref. [78] for the structures).

Configuration	$E_{\mathrm{ads,Li}}$ / [eV]	Li Bader net charge / [e]	$\Delta E_{\mathrm{FS-IS}}$ / [eV]
2D BH	-	-	1.94
Li-2D BH	-0.66	-0.88	1.11
2Li-2D BH	-0.53	-0.87	0.58
3Li-2D BH	-0.45	-0.87	0.02
4Li-2D BH	-0.30	-0.87	-0.50

reaction when compared to the pristine case. The minimum energy path for the dehydrogenation reaction on the 3Li-2D BH configuration is shown in Figure 3.5(d) as a function of the non-dimensional reaction coordinate. The full schematic of this minimum energy path, including all the stationary and transition states, is shown in Figure S7 in the Supplementary Information of Ref. [78]. In the case of pristine 2D BH, 3 center 2 electron bonds (B−H−B) provided the most stable state along the reaction path way (see Figure 3.3(b)), but in the presence of few Li-dopants, the state with the minimum energy is a stationary state in which two B−H bonds have replaced two B−H−B bonds. This may be due to the charge donating nature of Li-atoms (as shown by the negative Bader net charges in Table 3.1), which weakens the electron deficient 3-center-2 electron bonds present in B−H−B. This result is supported by our BOMD simulations at 300 K (simulation snapshots are shown in Figure 3.6), which show that upon addition of Li, the H atoms in the vicinity of Li-atoms can escape the bridge site of B-atoms, while in the pristine case, H-atoms only exhibit vibrations around the bridge site. By subtracting the energy of the final H_2 physisorbed state (see Figure 3.5(c)) from the most stable stationary state (see Figure 3.5(b)), a heat of reaction (dehydrogenation) of 0.24 eV/H_2 can be obtained. This value of heat of dehydrogenation is 88% lower than for pristine 2D BH (i.e., 1.92 eV/H_2). Based on the results of Figure 3.5, it can be concluded that the energy barriers for dehydrogenation have reduced significantly in the presence of Li-atoms. The magnitude of the largest activation barrier for the dehydrogenation reaction (ca. 0.8 eV) is significantly lower than the activation energy for the pristine case (i.e., 2.86 eV), and the number of stationary states present along the reaction pathway has considerably increased in the presence of Li-dopants. Excluding the initial and final

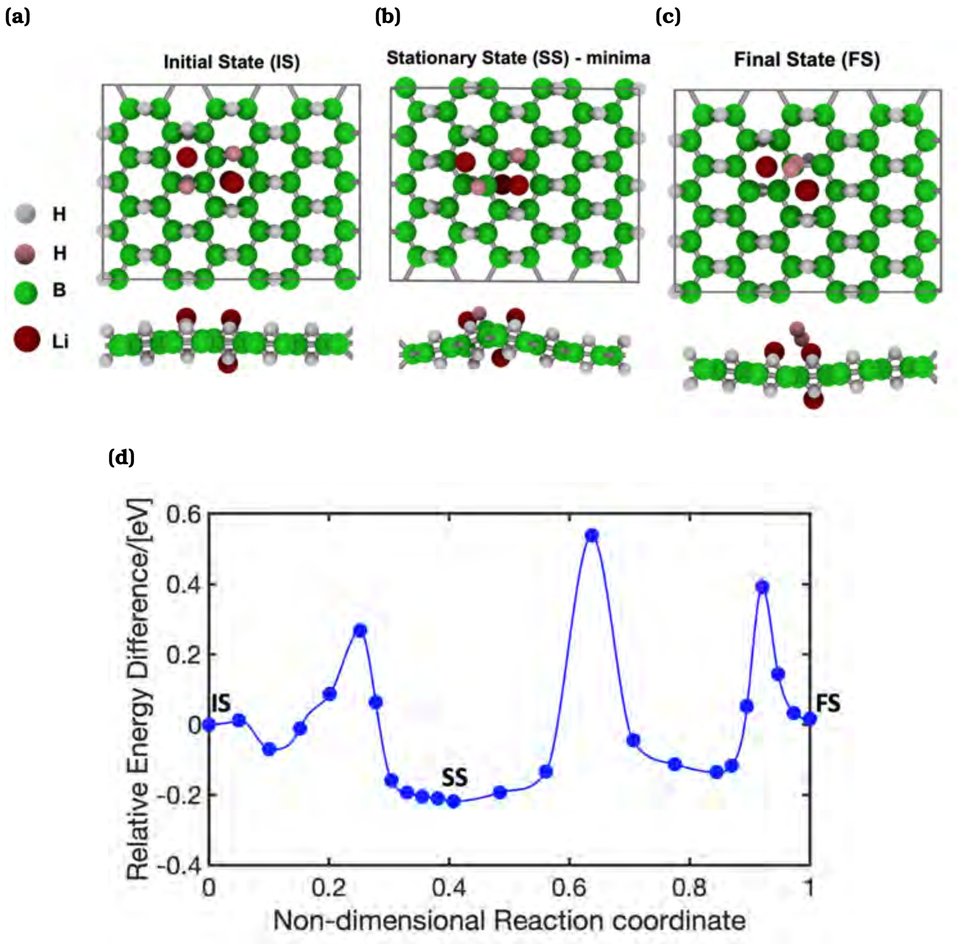

Figure 3.5. Top and side views of the (a) initial state, (b) most stable stationary state (minima), and (c) final state of 3Li-2D BH. The H atoms that are undergoing reaction are shown in pink while the rest of H-atoms are colored grey. (d) The minimum energy path for a single H_2 dehydrogenation on 3Li-2D BH. The relative energy with respect to the initial state is shown as a function of the non-dimensional reaction coordinate. The SS, and FS states have energy differences of -0.22, and 0.02 eV with respect to the IS state, respectively.

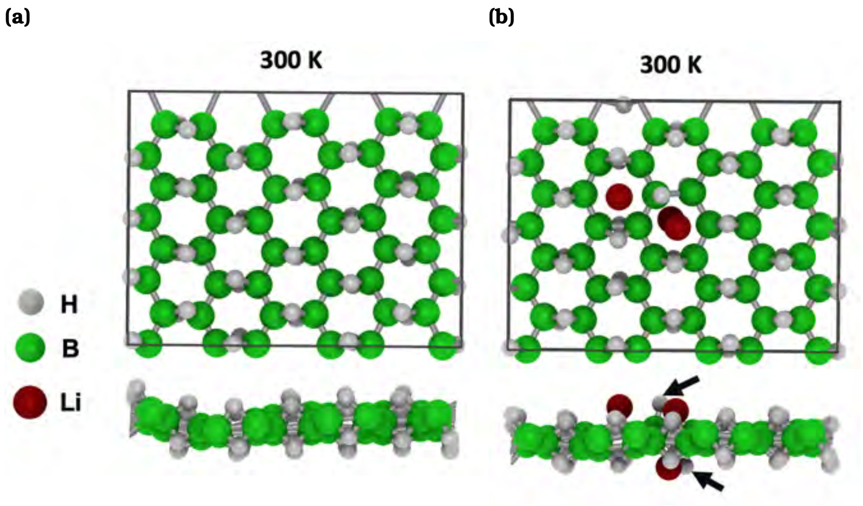

Figure 3.6. Top and side views of BOMD simulation snapshots after a 12 ps run at 300 K for (a) borophene-hydride, (b) 3Li - doped borophene-hydride. For borophene-hydride, the H-atoms exhibit vibrations around the bridge site of the boron atoms (3-center-2 electron bonds). In the 3Li-2D BH configuration two H-atoms (indicated by the black arrows) escape the bridge bond (one at the top and one at the bottom of the layer).

state, there are 3 stationary states along the reaction pathway for 3Li-2D BH compared to 1 in the pristine case. This can be attributed to the more complex potential energy landscape that forms due to the addition of Li.

Overall, it can be seen that Li-dopants can have a significant influence on both the energy barriers and favorability of the dehydrogenation reaction on 2D BH. This means that for applications that require large loadings of Li on 2D BH, such as for Li anode batteries, and physisorptive storage of H_2 by means of Li dopants, both the reconfiguration of the B−H−B bond and the possibility for dehydrogenation needs to be considered. Our results further entail that by tuning the Li-loading it may be possible to release the chemisorbed H-atoms in a reversible manner with enhanced adsorption/desorption kinetics (lower energy barriers).

Similarly for the case of striped-borophene, Li-dopants are added to examine their influence on H_2 chemisorption and dehydrogenation. The Li-atoms are positioned in the proximity of (to the sides and below) the H-atom adsorption sites (shown in Figure 3.7(a) for the 3-Li doped striped borophene configuration). All different Li configurations that are probed are shown in Figure S8 in the Supplementary Information of Ref. [78]. Table 3.2 shows the Li adsorption energies, the average Bader net charge state of Li, and the energetic difference between the final (physisorbed)

Table 3.2. The Li-adsorption energy ($E_{\mathrm{ads,Li}}$), and the average Li-Bader net charge state on striped borophene at different loadings of Li. For the Bader net charge state, the plus sign indicates a gain of electronic charge density and a minus sign indicates a loss of electronic charge density with respect to the atomic charge of respective elements (net charge 0). The energy difference between the final (physisorbed) and initial (chemisorbed) state ($\Delta E_{\mathrm{FS-IS}}$) is shown at different Li-doped configurations (see Figure S9 of the Supplementary Information of Ref. [78] for the structures).

Configuration	$E_{\mathrm{ads,Li}}$ / [eV]	Li Bader net charge / [e]	$\Delta E_{\mathrm{FS-IS}}$ / [eV]
B Striped	-	-	1.41
Li-B striped	-1.54	-0.89	1.02
2Li-B striped	-1.12	-0.89	0.83
3Li-B striped	-1.56	-0.88	0.73
4Li-B striped	-1.32	-0.88	0.84

and initial (chemisorbed) state ($\Delta E_{\mathrm{FS-IS}}$). The mechanism for Li charge transfer on striped-borophene is elaborated in prior studies [157, 191].

In striped-borophene, Li-dopants have reduced the energy difference between the chemisorbed (hydrogenated) and physisorbed state by ca. 50% compared to the pristine striped-borophene (1.41 eV). Based on the minimum energy path shown in Figure 3.7(d), it can be seen that the dehydrogenation barriers have been reduced by ca. 30 % (1.34 eV) with respect to the dehydrogenation barrier of the pristine case (2.04 eV based on Figure 3.3). The full schematic of this minimum energy path, including all the stationary and transition states is shown in Figure S10 in the Supplementary Information of Ref. [78]. The reason why in 2D BH, the influence of Li-dopants on the endothermicity of dehydrogenation is larger than in striped borophene, may be due to the different bonding type of H-atoms in the two structures. Overall, it can be seen that Li-dopants have a significant effect on the chemisorption and dehydrogenation properties of striped-borophene as well. Further study is needed to optimize the dopant loadings and to observe these effects experimentally. In a realistic H_2 storage material, the 2D layers have to be stacked on each other forming a layered 3D structure. The calculation of the optimum layering distance, gravimetric or volumetric capacity of H_2 in these materials is beyond the scope of our work.

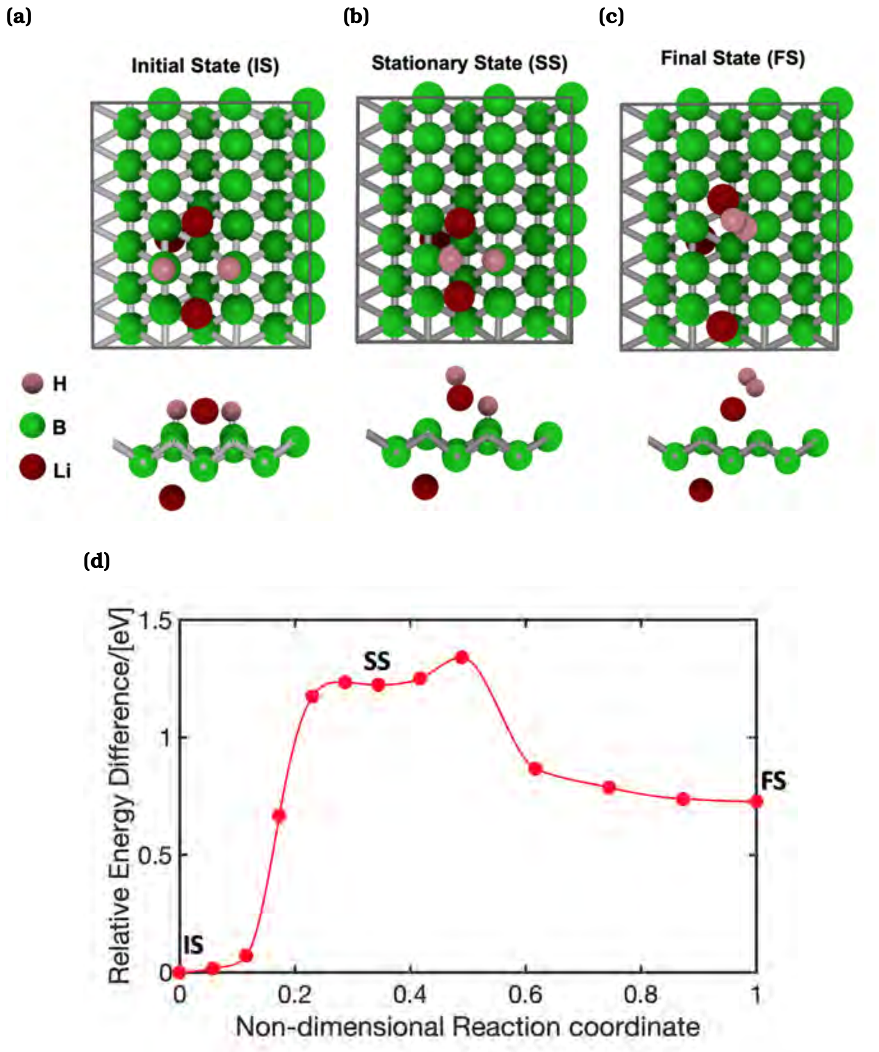

Figure 3.7. Top and side views of the (a) initial state, (b) stationary state, and (c) final state of 3 Li doped striped borophene. The H atoms that are undergoing reaction are shown in pink. (d) The minimum energy path for single H_2 dehydrogenation on 3-Li doped striped borophene. The relative energy with respect to the initial state is shown as a function of the non-dimensional reaction coordinate for the dehydrogenation reaction. The SS, and FS states have energy differences of 1.22, and 0.73 eV with respect to the IS state, respectively.

3.4. Conclusions

The influence of Li-dopants at various loadings on H_2 chemisorption and desorption barriers of borophene-hydride and striped-borophene are assessed using first-principle calculations. In the pristine case, it is found that dehydrogenation of borophene-hydride and striped-borophene is highly endothermic. The energy barriers for H_2 desorption are also large (2.04 eV for striped-borophene and 2.87 eV for borophene-hydride). Both of these factors limit the application of this material for H_2 chemisorption applications. With the addition of Li, the relative energy difference between the chemisorbed and physisorbed states is significantly decreased. In 3-Li doped borophene-hydride and striped borophene, there is ca. 90% and 50% decrease in the endothermicity of the dehydrogenation reaction, respectively, with respect to the pristine 2D structures. The BOMD simulations for 2D BH at 300 K show that the 3-center-2-electron bond weakens in the presence of Li dopants. The dehydrogenation barriers are also reduced by more than 30% for both structures in the presence of Li-dopants. Our findings show that Li-dopants (especially at high loadings) strongly influence the hydrogenation/dehydrogenation reaction of borophene-hydride and striped borophene, and may encourage experimental studies on Li-doped borophene-hydride as a potential H_2 chemisorptive storage medium.

4

Thermodynamic and Transport Properties of Hydrogen in Aqueous NaCl solutions

This chapter is based on the following publication: W. A. van Rooijen[1], P. Habibi[1], K. Xu, P. Dey, T. J. H. Vlugt, H. Hajibeygi, O. A. Moultos, "Interfacial Tensions, Solubilities, and Transport Properties of the $H_2/H_2O/NaCl$ system stems: A Molecular Simulation Study". *Journal of Chemical & Engineering Data* 69 (2024) 307-319.

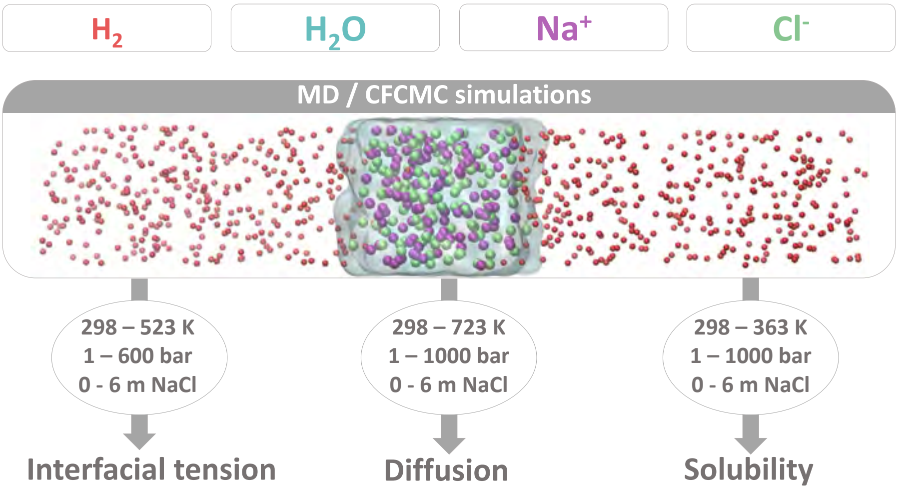

---

[1] These authors contributed equally to this work.

4.1. Introduction

Important technologies in the H_2 value chain include underground H_2 storage [24, 192–194] and H_2O electrolysis [8, 195]. To enable the design and optimization of these technologies, accurate knowledge of thermodynamic, interfacial, and transport properties of H_2 is essential [7, 16, 22, 194, 196]. More specifically, the diffusivities and solubilities of H_2 in aqueous solutions, and the interfacial tensions of H_2 gas in contact with aqueous electrolyte solutions are crucial properties. The interplay of these properties determine the efficiency of the technologies, and allow for accurate predictions of the processes involved, which are e.g., required for safety. These properties depend on pressure, temperature, and salt concentration [197]. H_2 technologies cover a wide range of operational conditions. For example, in underground H_2 storage sites, the pressure, temperature, and salt molality can be as high as 300 bar, 333 K, and 5 mol NaCl/kg H_2O, respectively [192]. Typically, H_2O electrolysers operate at atmospheric pressure, temperatures of ca. (348 to 372) K, and molalities of ca (3 to 4) electrolyte/kg H_2O [198]. Other types of electrolysis require much higher pressures and temperatures, i.e., up to 700 bar and 1400 K, respectively [199–201]. Thus, to cover the conditions for important H_2 applications, the interfacial tensions, self-diffusivities, and solubilities need to be available for a very wide range of pressures, temperatures, and salt concentrations.

Traditionally, these thermophysical properties are measured experimentally [202–204]. Nevertheless, only a small number of experimental studies on the interfacial tension of H_2/pure H_2O [202, 205–208] is available, while only two studies report measurements of interfacial tension of H_2/aqueous solutions (with NaCl and NaCl+KCl) [207, 208]. These experiments are performed by using the capillary rise [209] and the pendant drop [205, 207, 208, 210] techniques. Interfacial tensions of H_2/aqueous solutions are reported for temperatures up to 423 K, pressures up to 345 bar, and molalities of up to 5 mol (NaCl + KCl)/kg H_2O. As far as the solubility of H_2 in aqueous NaCl solutions is concerned, for an overview of the available experimental data the reader is referred to the works of Chabab *et al.* [211], Torín-Ollarves *et al.* [212], and Ansari *et al.* [213]. Although a lot of experimental data are available for H_2 in pure H_2O, solubility measurements of H_2 in aqueous NaCl solutions are scarce, and in many cases conflicting [203, 211, 214–218]. The two main sources of experimental data of solubilities of H_2 in aqueous solutions at concentrations above 1 mol NaCl/kg H_2O, at temperatures above 300 K, and at pressures above 10 bar by Torín-Ollarves *et al.* [212], and Chabab *et al.* [211] show conflicting results as the measured solubilities differ by ca. 30%. For the self-diffusivity of H_2 in H_2O, experimental data are available [204, 219–226] but mostly at atmospheric pressure and for limited temperatures below 340 K. Similarly to the solubilities, the experimental measurements also differ by up to 70 %. To the best of our knowledge, no experimental data are available for the self-diffusivity of H_2 in aqueous NaCl solutions.

Based on the available experimental data, it is evident that only a limited range of the required interfacial tensions, solubilities, and self-diffusivities of the $H_2/H_2O/NaCl$ system has been measured, while in some cases, there are significant discrepancies between the data reported from different sources. The reason for the scarcity of and deviation in the data may be that experimental measurements are rather challenging and expensive to perform, especially at high pressures and temperatures. To this end, a widely used complementary approach for obtaining thermophysical data is molecular simulation, especially at conditions which are challenging for experimental measurements.

Numerous studies have used MD to compute the interfacial tension of gases (e.g., CO_2, CH_4) and liquids (e.g., hydrocarbons) in contact with H_2O (pure or saline) [227–236]. However, no molecular simulation studies on the interfacial tension of H_2 and aqueous solutions are available. MD simulations have also been performed to compute self-diffusivities of H_2 in pure H_2O [107–109, 237, 238]. Recently, Tsimpanogiannis *et al.* [109] reported such data for pressures in the range of (1 to 2000) bar and temperatures in the range of (275 to 975) K spanning vapor, liquid, and supercritical H_2O. The Marx [91], Vrabec [90], Buch [93], Hirschenfelder [89], Cracknell [239], and Silvera-Goldman [240] H_2 force fields were used in combination with the TIP4P/2005 [100] H_2O force field. The Buch [93] and Vrabec [90] H_2 force fields were shown to yield the best agreement with experimental data. In contrast, self-diffusivities of H_2 in aqueous NaCl solutions computed from MD simulations have not yet been reported, while there are a few studies available reporting computations of self-diffusivities of CO_2 in aqueous NaCl solutions [241–244]. Lopez-Lazaro *et al.* [245] have computed solubilities of H_2 in aqueous NaCl solutions using MC simulations for molalities up to a maximum of 2 mol NaCl/kg H_2O. To the best of the authors knowledge, this was the only molecular simulation study on H_2 solubilities in aqueous NaCl solutions. Molecular simulations have been used for computing solubilities of other gases (e.g., CO_2, CH_4) in water and aqueous NaCl solutions [47, 231, 236, 246, 247].

Despite the urgency and importance of reliable data of interfacial tension of H_2 in contact with aqueous NaCl solutions, self-diffusivity of H_2 in aqueous NaCl solutions, and solubility of H_2 in aqueous NaCl solutions, only very limited experimental and simulation studies are available. The objective of this chapter is to generate reliable data for these properties for a wide range of conditions relevant to H_2 technologies, such as underground H_2 storage and H_2O electrolysis. We present new data sets of (a) interfacial tensions of H_2 and aqueous NaCl solutions for temperatures, pressures, and molalities of (298 to 523) K, (1 to 600) bar, and (0 to 6) mol NaCl/kg H_2O, respectively, (b) self-diffusivities of H_2 in aqueous NaCl solutions for temperatures, pressures, and molalities of

(298 to 723) K, (1 to 1000) bar and (0 to 6) mol NaCl/kg H_2O, respectively, and (c) solubilities of H_2 in aqueous NaCl solutions for temperatures, pressures, and molalities of (298 to 363) K, (1 to 1000) bar and (0 to 6) mol NaCl/kg H_2O, respectively. The interfacial tensions and self-diffusivities are computed using MD simulations, and the solubilities are computed using Continuous Fractional Component Monte Carlo (CFCMC) [248–250] simulations. Densities and viscosities of the aqueous NaCl solutions are also computed for a wide range of conditions and are compared to available experimental data. The TIP4P/2005 [100] force field is used for H_2O, the Madrid-2019 [103] force field for NaCl, and the Vrabec [90] and Marx [91] force fields are used for H_2. A modified version of the Madrid-2019 force field by Vega and co-workers [111] (i.e., the Madrid-Transport [47, 111]), optimized for viscosities of aqueous NaCl solutions for salinities up to the experimental solubility limit, is also used.

The chapter is structured as follows. Details of the force fields used and the molecular simulation techniques are given in section 4.2. In section 4.3, the computed interfacial tensions, viscosities, densities, self-diffusivities, and solubilities obtained are presented and compared with experimental data when possible. Finally, concluding remarks are presented in section 4.4. All data computed in this study are provided in a tabulated format as Supporting Information of Ref. [48].

4.2. Methodology

4.2.1. Force fields

The four-site TIP4P/2005 [100] force field is used to model H_2O. Previous studies have shown that this force field can accurately capture thermodynamic, transport, and interfacial properties of pure H_2O and H_2O/NaCl solutions in contact with gases for a wide range of conditions [51, 109, 227, 247, 251–255]. For the Na^+ and Cl^- ions, the Madrid-2019 [103] force field is used, which is parameterized for the TIP4P/2005 H_2O model [256]. A new version of the Madrid-2019 force field (i.e., Madrid-Transport force field [47, 111]) is currently being developed by Vega and co-workers [111], which performs better for transport properties, especially at high NaCl molalities. The difference of Madrid-Tranport from Madrid-2019 is that ion charges are scaled by 0.75 instead of 0.85, and the Lennard-Jones (LJ) parameters are slightly altered. Interfacial tensions and self-diffusivities are computed using the single-site Vrabec [90] H_2 force field, while for the solubilities of H_2 in the aqueous NaCl solutions the three-site Marx [91] model is used. Tsimpanogiannis *et al.* [51] showed that the Vrabec [90] H_2 force field yields very accurate self-diffusivities of H_2 in pure TIP4P/2005 H_2O. The solubilities computed using the Vrabec [90] force field deviate from experimental data of H_2 in pure water by ca. 50%. In sharp contrast, the solubilities computed using the Marx [91] force field show excellent agreement with experimental data.

A comparison of the solubilities computed using the Marx and Vrabec force fields in pure TIP4P/2005 H_2O are listed in Table S1 and shown in Figure S1 of the Supporting Information of Ref. [48]. All force field parameters are listed in Tables A.1-A.4 of the Appendix A.2.

4.2.2. MD simulations

The MD simulations are used to calculate (a) the interfacial tensions of H_2 in contact with aqueous NaCl solutions, (b) self-diffusivities of H_2 in aqueous NaCl solutions, (c) densities, and (d) viscosities of aqueous NaCl solutions. For all MD simulations, the LAMMPS [59] software package is used (version 29 Sep 2021). For the integration of the equations of motion, the velocity-Verlet algorithm is used with a time step of 1 fs. The bond length and bending angle of H_2O are fixed using the SHAKE algorithm [59, 257]. The intermolecular interactions are described by Lennard-Jones and Coulombic interaction potentials. The Lorentz-Berthelot combining rules [49] are used for interactions between different types of molecules, with the exception of $\mathrm{Na^+ - H_2O}$, $\mathrm{Na^+ - Cl^-}$, and $\mathrm{Cl^- - H_2O}$ LJ interactions as specified in Table S5 of the Supporting Information of Ref. [48]. Long-range electrostatic energies are computed using the particle-particle particle-mesh (PPPM) method [50, 258] with a relative error [60] of 10^{-5}. The temperature and pressure are regulated by the Nosé-Hoover thermostat and barostat [50]. Initial configurations are created using the PACKMOL software [259]. Periodic boundary conditions are imposed in all directions. All MD simulations for a specific set of conditions are repeated 5 times using different initial velocity distributions from which the average quantities are calculated. The reported uncertainties are standard deviations from the results of these 5 simulations.

4.2.3. Computation of interfacial tensions

The following procedure is used for computing the interfacial tensions: An initial configuration is created by combining separately equilibrated bulk phases of aqueous sodium chloride solutions and H_2 gas. An equilibration run of 5 ns is carried out in the NPT ensemble using anisotropic pressure coupling, i.e., only the z-direction of the simulation box is allowed to fluctuate. The last 2 ns of the equilibration run are used to calculate the average simulation box dimensions, which are used for an equilibration run of 3 ns in the NVT ensemble. Next, production runs of 2 ns are carried out for computing the interfacial tension. In all simulations, 2088 H_2O molecules are used. Depending on the pressure, the number of H_2 molecules varied between 64 - 640. 0 - 188 Na^+ and Cl^- ions are used, depending on the molality. The exact numbers of species along with the simulation box sizes for all simulations are listed in Table S6 of the Supporting Information of Ref. [48]. A cutoff radius of 12 Å is used for the short-range LJ and short-range electrostatic energies. Because the

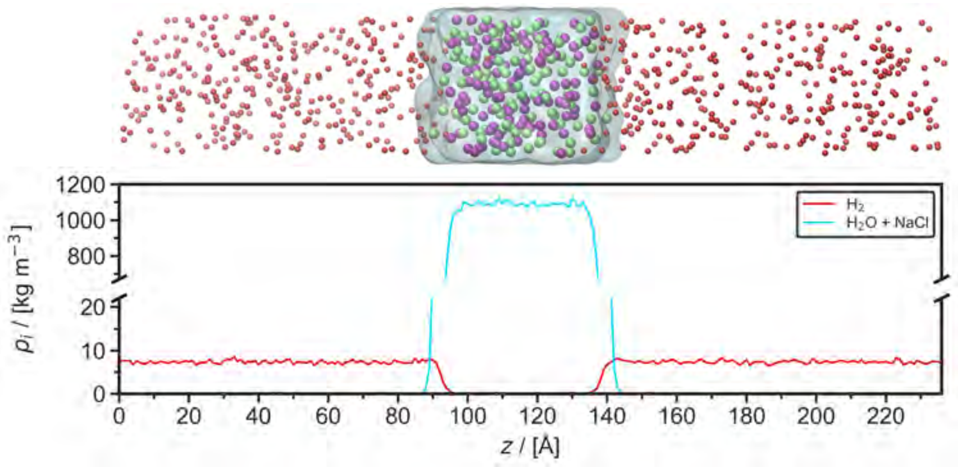

Figure 4.1. Top: Typical snapshot from a Molecular Dynamics simulation used to calculate the interfacial tension of H_2 and an aqueous NaCl solution (3 mol NaCl/kg H_2O) at 343 K and 100 bar. H_2 molecules are represented by red spheres, Na^+ and Cl^- are represented by purple and green spheres, respectively, H_2O is represented by the transparent blue surface. Bottom: Density profile in the z-direction of H_2 and the aqueous NaCl solution of the same simulation, averaged over 1 ns. z is the direction perpendicular to the interface.

system is inhomogeneous, analytic corrections were not used. Instead, Long-range LJ and electrostatic interactions are computed using the Particle-Particle Particle-Mesh (PPPM) method [50, 258, 260]. For the real and reciprocal space computations for the dispersion part of the PPPM method the desired accuracies are set to 0.0001 and 0.002, respectively. A relative error of 10^{-5} is used for the long-range electrostatic energies. The adequacy of the PPPM method for computing the LJ interactions has been recently validated by Salehi *et al.* [261] in interfacial MD simulations of deep eutectic solvents with water.

Figure 4.1 (top panel) shows a typical MD simulation snapshot at T = 343 K, P = 100 bar, and m = 3 mol NaCl/kg H_2O. The bulk liquid H_2O phase containing the Na^+ and Cl^- ions, which is shown as the transparent blue surface, occupies a domain of ca. 40 × 40 × 40 Å in the middle of the simulation box. H_2 gas is in contact with the liquid phase from both sides, in the z-direction. This creates two H_2/H_2O interfaces perpendicular to the z-direction. The density profile of this system, averaged over 1 ns, is shown in Figure 4.1 bottom panel. The interfacial tension γ is calculated from the principal components of the diagonal elements of the stress tensor (P_{zz}, P_{xx}, and P_{yy}) [262]:

$$\gamma = \frac{1}{2} h_z \left[P_{zz} - \frac{1}{2} \left(P_{xx} + P_{yy} \right) \right], \tag{4.1}$$

where h_z is the simulation cell length in z-direction.

4.2.4. Computation of self-diffusivities and viscosities

The scheme used for computing self-diffusivities and viscosities follows from Ref. [263]. Initially, energy minimizion of the system is performed, followed by equilibration runs in the NPT and NVT ensembles for 1 – 2 ns. Next, production runs in the NVT ensemble for 10 ns are carried out. The system consists of 700 H_2O molecules, 2 H_2 molecules, and 0 – 76 Na^+ and Cl^- ions, depending on the molality. The exact numbers of species used for every state point are provided in Table S7 of the Supporting Information of Ref. [48]. A cutoff radius of 10 Å is used for Lennard-Jones and electrostatic interactions. Analytic tail corrections for energies and pressures are applied.

To compute the self-diffusivities and the shear viscosities, the OCTP plugin [263] in LAMMPS is used. In this plugin, the Einstein relations are used in combination with the order-n algorithm [50] as implemented by Dubbeldam *et al.* [264]. The self-diffusivity D_i of species i is computed from [53]:

$$D_i = \lim_{t \to \infty} \frac{1}{6 N_i t} \left\langle \sum_{j=1}^{N_i} \left(\boldsymbol{r}_{j,i}(t) - \boldsymbol{r}_{j,i}(0) \right)^2 \right\rangle, \tag{4.2}$$

where $\boldsymbol{r}_{j,i(t)}$ is the position vector of the j-th molecule of species i at time t and N_i is the number of molecules of species i. All self-diffusivities in this chapter are corrected for finite size effects using the Yeh-Hummer equation [265–267]:

$$D = D_i + \frac{k_B T \xi}{6 \pi \eta L}, \tag{4.3}$$

where D is the finite size corrected self-diffusivity, T is the temperature in K, ξ is a dimensionless constant equal to 2.837298, η is the shear viscosity from Equation 4.4, and L is the simulation box length. In this chapter, the finite size correction magnitude was ca. 5-10 % of the computed self-diffusivities.

The shear viscosity η is computed from [53]:

$$\eta = \lim_{t \to \infty} \frac{1}{10 \cdot 2t} \frac{V}{k_B T} \left\langle \sum_{\alpha\beta} \left(\int_0^t P^{\mathrm{os}}_{\alpha\beta} \left(t' \right) \mathrm{d}t' \right)^2 \right\rangle, \tag{4.4}$$

where

$$P^{\mathrm{os}}_{\alpha\beta} = \frac{P_{\alpha\beta} + P_{\beta\alpha}}{2} - \delta_{\alpha\beta}\left(\frac{1}{3}\sum_{k} P_{kk}\right), \tag{4.5}$$

where V is the volume of the system, k_B is the Boltzmann constant, $P^{\mathrm{os}}_{\alpha\beta}$ denotes the components of the traceless pressure tensor, $\delta_{\alpha\beta}$ is the Kronecker delta, and $\langle ..\rangle$ indicates an ensemble average. The computaion of η does not depend on the size of the system [268–270].

4.2.5. Computation of solubilities

Continuous Fractional Component Monte Carlo [248–250] simulations in the isobaric-isothermal (CFCNPT) ensemble are used to compute solubilities and excess chemical potentials of H_2 in NaCl solutions. The open-source Brick-CFCMC software [55, 56, 248] is used for all simulations. A 10 Å cutoff radius is used for both the LJ and Coulombic interactions. The Ewald summation with a relative precision of 10^{-6} is used for the electrostatics. Analytic tail corrections for energies and pressures are applied [50]. The infinite dilution excess chemical potential of H_2 can be computed using a single "fractional" molecule of H_2. Fractional molecules have their interactions with surrounding molecules scaled with a continuous order parameter λ [106, 248]. In CFCNPT simulations, λ ranges from 0 to 1. $\lambda = 0$ indicates that the fractional molecule does not interact with the surrounding molecules/atoms (i.e., the fractional molecule behaves as an ideal gas molecule), and $\lambda = 1$ corresponds to full interactions. For the specifics regarding the scaling of the interactions the reader is referred elsewhere [271–273]. To improve the sampling in the λ-space, a biasing weight function ($W(\lambda)$) is created using the Wang-Landau algorithm [274, 275]. This biasing weight function is used to ensure a flat probability distribution in the λ-space ($p_{\mathrm{obs}}(\lambda)$). To compute the probability of occurrence of each λ value, a histogram with 100 bins is used. The Boltzmann averaged probability distributions of λ ($p(\lambda)$) can be computed using [47, 276]

$$p(\lambda) = \frac{\langle p_{\mathrm{obs}}(\lambda)\exp[-W(\lambda)]\rangle}{\langle \exp[-W(\lambda)]\rangle}. \tag{4.6}$$

The Boltzmann sampled probability distribution of λ ($p(\lambda)$) can be related to the infinite dilution chemical potential (μ^{ex}) using [47, 248, 276]

$$\mu^{\mathrm{ex}} = -k_\mathrm{B} T \ln \frac{p(\lambda = 1)}{p(\lambda = 0)}, \tag{4.7}$$

where $p(\lambda = 1)$ and $p(\lambda = 0)$ are the Boltzmann averaged probability distributions of λ at 1 and 0, respectively.

For all simulations, 5×10^5 equilibration cycles, and 5×10^5 production cycles are performed. A cycle contains N number of trial moves, with N

being the total number of molecules, with a minimum of 20. The following probabilities are used for selecting the trial moves: 35% translations, 29% rotations, 1% volume changes, 25% λ changes, and 10% reinsertions of the fractional molecules at random locations inside the simulation box. The maximum displacements for molecule translations, volume changes, rotations, and λ changes are adjusted to obtain ca. 50% acceptance. Another method that can be used to compute μ^{ex} is the Widom's Test Particle Insertion method (WTPI) [49, 50, 277, 278]. In dense fluid phases WTPI yields inaccurate results compared to the CFCMC method as successful insertion of test particles is a highly unlikely event due to the significant potential energy increase in case of overlap with other particles [248, 279].

The solubilities of H_2 in aqueous NaCl solutions are computed at temperatures in the range (298 to 363) K and at H_2 partial pressures of 1, 10, 100, 400, and 1000 bar. At H_2 partial pressures of 1 bar and 10 bar, the H_2 solubilities are computed using Henry coefficients (H) [47, 276]:

$$H = \lim_{f_i \to 0} \frac{f_i}{\rho_{\text{H}_2,\text{L}}/\rho_0}, \tag{4.8}$$

where f_i is the fugacity of H_2 in the gas phase, $\rho_{\text{H}_2,\text{L}}$ is the number density of H_2 in the aqueous solution in units of $1/\text{m}^3$, and ρ_0 is a reference number density in the same unit as $\rho_{\text{H}_2,\text{L}}$ (set to 1 molecule per m^3) [276]. At H_2 partial pressures of 1 bar and 10 bar, the fugacity coefficient of H_2 is assumed to be 1 (i.e., the fugacity of H_2 is equal to the partial pressure of H_2). From the MC simulations, H can be computed using [276]

$$H = \rho_0 k_\text{B} T \exp\left[\frac{\mu^{\text{ex}}_{\text{H}_2,\text{L}}}{k_\text{B} T}\right], \tag{4.9}$$

where $\mu^{\text{ex}}_{\text{H}_2,\text{L}}$ is the infinite dilution chemical potential of H_2 in the aqueous solution. A single fractional molecule of H_2, 300 H_2O molecules, and varying number of NaCl molecules depending on the molality (ranging from 0 to 6 mol NaCl/kg H_2O) are used to compute $\mu^{\text{ex}}_{\text{H}_2,\text{L}}$. The exact numbers of ions used for each molality are listed in Table S8 of the Supporting Information of Ref. [48]. To calculate solubilities of H_2 in aqueous NaCl solutions at pressures of 100, 400, and 1000 bar, the chemical potentials of H_2 in the liquid and in the gas phase are equated at constant pressure and temperature. The chemical potential of H_2 in the gas phase ($\mu_{\text{H}_2,\text{G}}$) is equal to [50]

$$\mu_{\text{H}_2,\text{G}} = \mu^0_{\text{H}_2} + k_\text{B} T \ln\left(\frac{\rho_{\text{H}_2,\text{G}}}{\rho_0}\right) + \mu^{\text{ex}}_{\text{H}_2,\text{G}}, \tag{4.10}$$

where $\mu^0_{\text{H}_2}$ is the reference state of the chemical potential, $\rho_{\text{H}_2,\text{G}}$ is the number density of H_2 in the gas phase in units of $1/\text{m}^3$, and $\mu^{\text{ex}}_{\text{H}_2,\text{G}}$ is the excess chemical potential of H_2 in the gas phase. At pressures above 100 bar and at temperatures between (298 to 363) K, the gas phase contains very few H_2O molecules (a H_2O mole fraction below 0.01) [106]. $\mu^{\text{ex}}_{\text{H}_2,\text{G}}$ is calculated in separate CFCNPT simulations, containing a single fractional molecule of H_2, and 300 H_2 molecules in the gas phase. The chemical potential of H_2 in the liquid phase ($\mu_{\text{H}_2,\text{L}}$) is equal to [50]

$$\mu_{\text{H}_2,\text{L}} = \mu^0_{\text{H}_2} + k_\text{B}T\ln\left(\frac{\rho_{\text{H}_2,\text{L}}}{\rho_0}\right) + \mu^{\text{ex}}_{\text{H}_2,\text{L}}. \tag{4.11}$$

$\rho_{\text{H}_2,\text{L}}$ can be computed by equating Eq. 4.10 and Eq. 4.11. The mole fractions of H_2 (x_{H_2}) in aqueous NaCl solutions are computed using

$$x_{\text{H}_2} = \frac{\rho_{\text{H}_2,\text{L}}\langle V\rangle}{N_{\text{H}_2\text{O}} + N_{\text{NaCl}} + \rho_{\text{H}_2,\text{L}}\langle V\rangle}, \tag{4.12}$$

where $\langle V\rangle$ is the average volume of the simulation box, computed in the CFCNPT ensemble. $N_{\text{H}_2\text{O}}$ and N_{NaCl} are the numbers of H_2O and NaCl molecules in the simulation box, respectively. For each condition (concentration, temperature, and pressure), 20 independent simulations are performed. These 20 simulations are divided into 5 blocks from which the Boltzmann sampled probability distribution of λ ($p(\lambda)$) are averaged. The averaged distributions ($p(\lambda)$) of all blocks are used to compute mean values and standard deviations for the excess chemical potentials and solubilities of H_2.

4.3. Results and discussion

4.3.1. Interfacial tensions

Figure 4.2 shows the computed interfacial tensions of $H_2/H_2O/NaCl$ as a function of pressure (Figure 4.2(a)), molality (Figure 4.2(b)) at temperatures in the range of (298 to 523) K, and as a function of temperature (Figure 4.2(c)) for molalities in the range of (0 to 6) mol NaCl/kg H_2O. Tabulated raw data of the interfacial tension along with their statistical uncertainties are listed in Table S9 of the Supporting Information of Ref. [48]. Figure 4.2(a) and 4.2(c) also show the available experimental data from Hosseini *et al.* [207]. For the whole range of conditions a close agreement with the experimental results is found. The MD results differ on average 6.4 % from the experimental values.

The interfacial tensions computed in this chapter are fitted to an engineering equation:

$$\gamma = c_1 + c_2 m + c_3 T^{c_4}, \tag{4.13}$$

where c_1, c_2, c_3 and c_4 are fitting parameters, which are listed in Table 4.1. Eq. 4.13 is valid for temperatures, pressures, and molalities of (298 to 523) K, (1 to 600) bar, and (0 to 6) mol NaCl/kg H_2O, respectively.

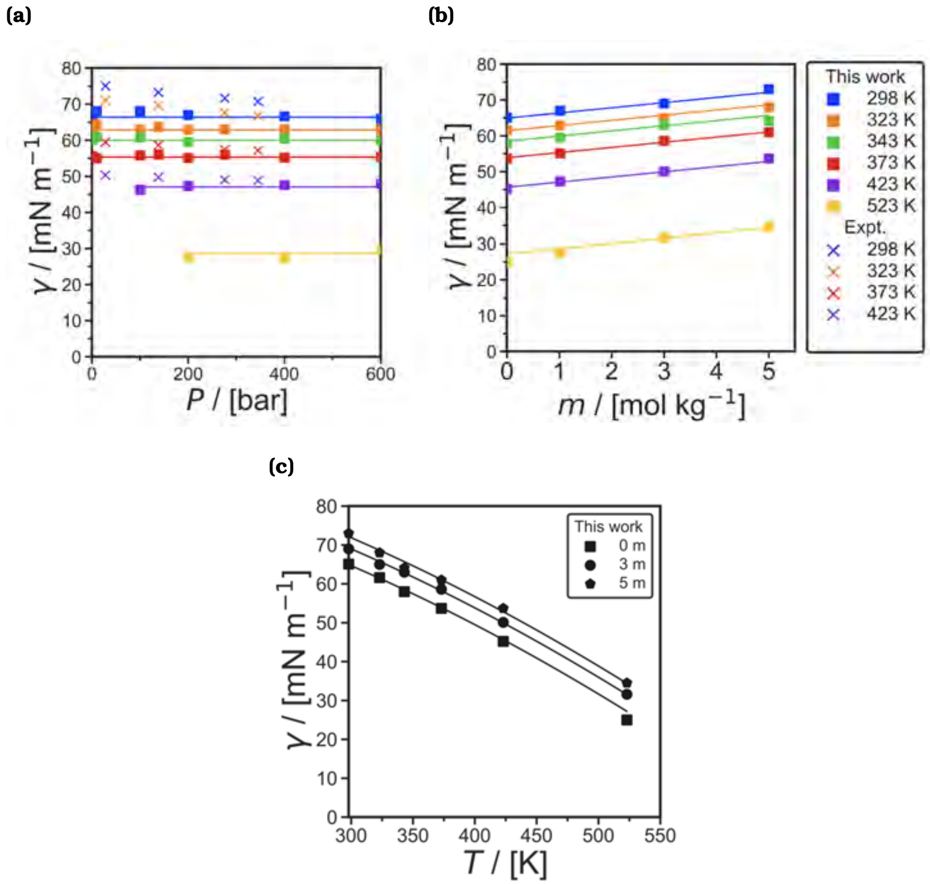

Figure 4.2. MD results of interfacial tension γ of H_2 and aqueous NaCl solutions using the NaCl Madrid-2019 [103] force fields, the TIP4P/2005 [100] H_2O force field, and the Vrabec [90] H_2 force field (a) as functions of pressure P for temperatures in a range of (298 to 523) K with a molality m of 1 mol NaCl/kg H_2O in combination with the experimental results of Hosseini *et al.* [207], (b) as functions of molality at a pressure of 200 bar of the solution for similar temperatures, and (c) as functions of temperature at a pressure of 200 bar and molalities of (0 to 6) mol NaCl/kg H_2O. The statistical uncertainties are comparable to or smaller than the symbols and can be found in Table S9 of the Supporting Information of Ref. [48]. The error bars have been omitted for clarity. The solid lines represent fits using Eq. 4.13 for temperatures in the range of (298 to 523) K.

Table 4.1. Parameters of Eq. 4.13 for predicting interfacial tension of H_2 in contact with aqueous NaCl solutions obtained using the NaCl Madrid-2019 [103] force fields, TIP4P/2005 [100] H_2O force field and Vrabec [90] H_2 force field. These parameters are valid for NaCl molalities of (0 to 6) mol NaCl/kg H_2O, temperatures of (298 to 523) K, and pressures of (1 to 600) bar.

c_1 / [mN/m]	89.6
c_2 / [(mN·kg$_{\mathrm{H_2O}}$)/(m·mol$_{\mathrm{NaCl}}$)]	1.44
c_3 / [mN/(m·K$^{1.65}$)]	-2.04×10^{-3}
c_4 / [-]	1.65

The results of this engineering equation are shown as solid lines in Figure 4.2. Eq. 4.13 is a very good fit to MD results, and can be used for calculating values at a specific combination of conditions in a fast and reliable way.

As shown in Figure 4.2(a), no significant pressure dependence of interfacial tension is observed, which is in line with experimental studies [202, 205, 207, 208]. In particular, Higgs *et al.* [208] did not observe a significant pressure dependence for H_2 in contact with aqueous NaCl solutions, while other studies observed a small decrease in interfacial tension of H_2 and pure H_2O [202, 205, 207] and H_2 and aqueous (NaCl+KCl) solutions [207]. Interestingly, the pressure dependence of H_2/H_2O interfacial tension is small compared to the CO_2/H_2O [280–282] and CH_4/H_2O [230, 283, 284] systems. This is because the interfacial tension is related to the density difference between the two phases [197]. The change in density difference between H_2 and H_2O is very small at varying pressures because the density of H_2 is very low in comparison to H_2O, and H_2O is almost incompressible at these pressures.

As shown in Figure 4.2(b), the interfacial tension increases linearly with solution molalities, in agreement with the available experimental data [207]. This behavior is also observed for other gases such as CO_2 and CH_4 [285–287]. This increase is mainly due to the increased density of saline H_2O compared to pure H_2O as well as the arrangement of cations and anions at the interface [286, 288–292]. The hydrogen bond network of H_2O is strengthened by cations [289–291], while anions cause the opposite effect [289–291]. Therefore, cations are absorbed into the bulk phase while anions are depleted from the bulk phase. This phenomenon can be observed in Figure S2 of the Supporting Information of Ref. [48], where it is shown that the number density of Cl^- ions at the interface is higher than Na^+ ions, and Na^+ ions are drawn into the bulk phase. The strengthening of the hydrogen bond network of H_2O leads to an increase in interfacial tension [286, 288].

In Figure 4.2(c), a non-linear decrease of interfacial tension with temperature can be observed. This is in line with the experimental data of Chow *et al.* [205]. In sharp contrast, Hosseini *et al.* [207] reported a linear decrease of interfacial tension with temperature. The fact that interfacial tension depends non-linearly on the density difference between the two phases in contact [197] combined with the non-linear effect of temperature on the density difference between H_2 and H_2O, results in the expectation that the interfacial tension is also non-linearly related to temperature. Therefore, the observed non-linear relationship between interfacial tension and temperature in our results is expected.

4.3.2. Densities and viscosities

Figure 4.3 shows the computed densities and viscosities of aqueous NaCl solutions as functions of NaCl molalities at 298 and 343 K. Densities and viscosities of aqueous NaCl solutions have a weaker dependence on pressure (in the range of 0 – 1000 bar) compared to temperature and NaCl molalities. Figure S3 and S4 in the Supporting Information of Ref. [48]. show the densities, and viscosities as functions of pressure. The results for the Madrid-2019 [103] and the Madrid-Transport [47, 111] NaCl force fields are shown in Figure 4.3. The fits to experimental data for viscosities (Figure 4.3(a)) and densities (Figure 4.3(b)) are obtained from Laliberté. [113] and Laliberté *et al.* [112], respectively. The raw data of these properties, as well as their statistical uncertainties, are listed in Table S10 of the Supporting Information of Ref. [48]. Both the Madrid-2019 [103] and Madrid-Transport [47, 111] capture the experimental data of density very accurately (within 1%). As shown in Figure 4.3(a), the Madrid-Transport [47, 111] force field yields a better agreement with the experimental data of viscosity compared to the Madrid-2019 [103] force field. The discrepancy between the two force fields starts at molalities above 2 mol NaCl/kg H_2O. The viscosities computed using the Madrid-2019 force field deviate on average ca. 20 % from the experimental data, while this deviation is is only ca. 3% when the Madrid-Transport force field is used. Based on the excellent performance of Madrid-Transport in reproducing experimental viscosities, which is necessary for reliable diffusivity predictions [115], only this force field was used for computing the self-diffusivities of H_2 in NaCl solutions.

4.3.3. Self-diffusivities of H_2

Figure 4.4 shows the computed finite size corrected self-diffusivities of H_2 in aqueous NaCl solutions as a function of (a) pressure, (b) NaCl molality, and (c) temperature. These simulation are performed with the Madrid-Transport [47, 111] force field for NaCl, the TIP4P/2005 [100] H_2O, and the Vrabec [90] force field for H_2. All the self-diffusivities of H_2 computed in this chapter are listed in Tables S11 and S12 of the Supporting Information of Ref. [48]. Simulations using the Madrid-2019 [103] NaCl

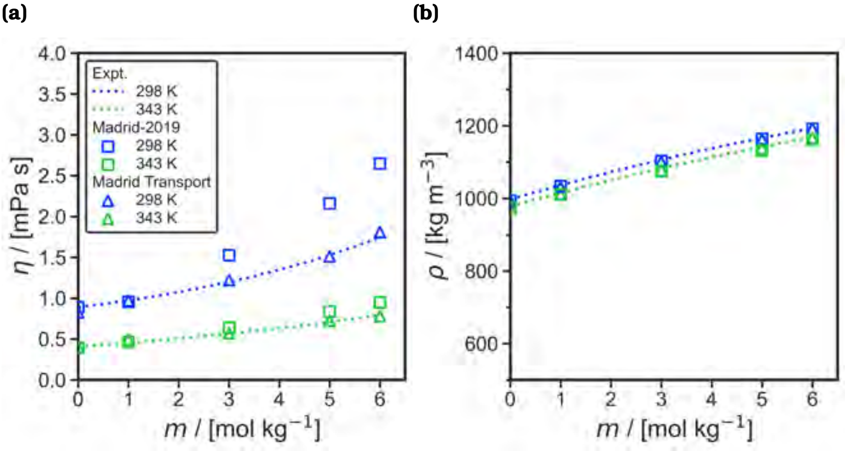

Figure 4.3. Computed (a) viscosities η and (b) densities ρ of aqueous NaCl solutions as a function of molality m (mol NaCl/kg H_2O) at a pressure of 1 bar and temperatures of 298 and 343 K. The fit to the experimental data is created by (a) Laliberté. [113] and (b) Laliberté *et al.* [112]. The statistical uncertainties can be found in Table S10 of the Supporting Information of Ref. [48]. The error bars are smaller or comparable to the symbol size and have been omitted for clarity.

force field are performed for comparison. These data are shown in Table S12 of the Supporting Information of Ref. [48]. The self-diffusivities of H_2 shown in Figure 4.4 are fitted to an engineering correlation:

$$D = c_1 \exp\left[c_2 m + c_3 \left(\frac{1}{T}\right) + c_4 P\right], \tag{4.14}$$

where $c_1, c_2, c_3,$ and c_4 are fitting parameters, which are listed in Table 4.2. As shown in Figure 4.4, this correlation provides an excellent fit for the MD results. Note that Eq. 4.14 is only valid for conditions where H_2O is in the liquid phase, and therefore data points for temperatures of 723 K or higher and pressures of 400 bar or higher (supercritical phase) are excluded from the fit.

In Figure 4.4(a) a weak pressure dependence of the self-diffusivities of H_2 is observed . The logarithm of the self-diffusivities decays linearly with respect to variations in pressure, similarly to what is reported by Tsimpanogiannis *et al.* [51]. The pressure dependence of the self-diffusivities of H_2 is more significant at 723 K (Figure 4.4(a)) as the solution is more compressible at these conditions. As shown in Figure 4.4(b), the logarithm of the self-diffusivities is also found to decay linearly with respect to variation in the NaCl molalities. Laliberté. [113] has shown that the viscosities of aqueous NaCl solutions increase exponentially with

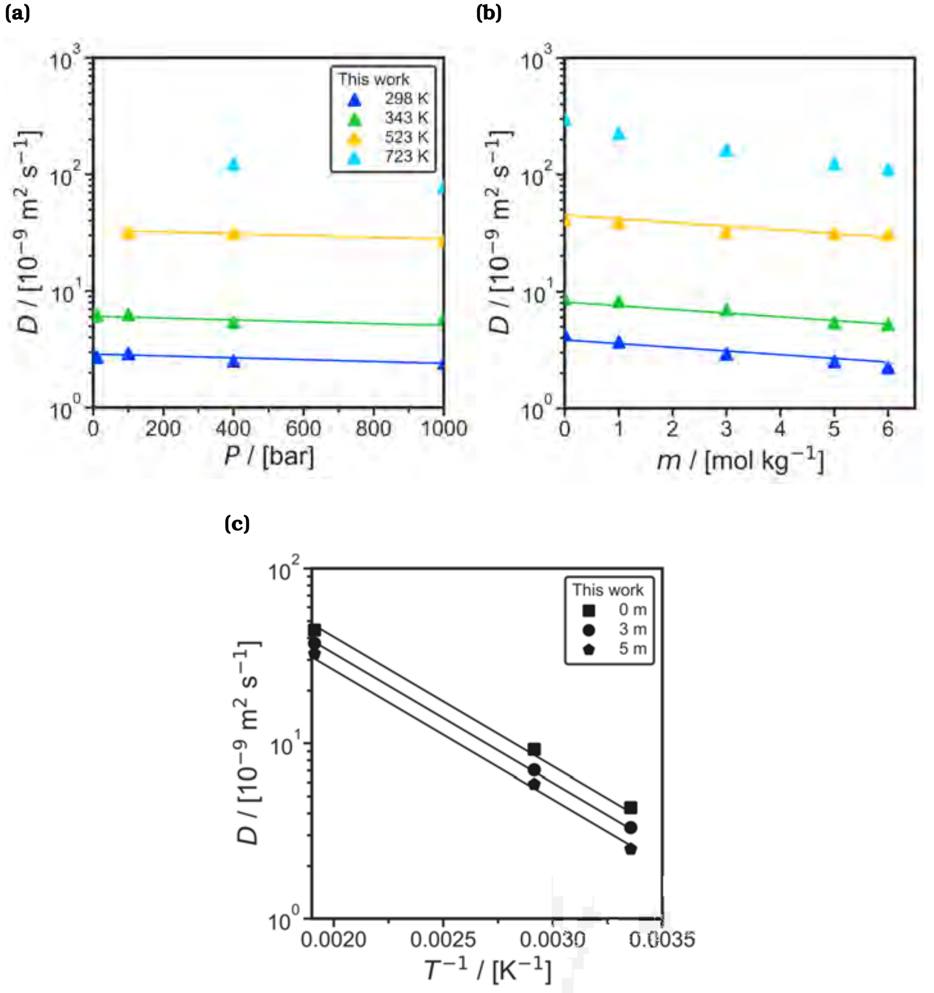

Figure 4.4. Computed finite size corrected self-diffusivities (D) of H_2 in aqueous NaCl solutions (a) with a molality (m) of 5 mol NaCl/kg H_2O solution as a function of pressure P for temperatures of (298 to 723) K, (b) at a pressure of 400 bar as a function of m of the solution for the similar temperatures, and (c) as a function of the reciprocal temperature at a pressure of 100 bar. The results are obtained using the NaCl Madrid-Transport [47, 111] force fields, TIP4P/2005 [100] H_2O force field, and Vrabec [90] H_2 force field. The statistical uncertainties are comparable to or smaller than the symbols and can be found in Table S11 of the Supporting Information of Ref. [48]. The solid lines are fits calculated using Eq. 4.14 for temperatures of (298 to 523) K. Data points at a temperature of 723 K and a pressure of 400 bar are excluded from the fit because H_2O is supercritical at these conditions.

Table 4.2. Parameters of Eq. 4.14 for predicting the computed finite size corrected self-diffusivities D of H_2 in aqueous NaCl solutions obtained using the NaCl Madrid-Transport [47, 111] force fields, the TIP4P/2005 [100] H_2O force field, and the Vrabec [90] H_2 force field. These parameters are valid for NaCl molalities of (0 to 6) mol NaCl/ kg H_2O, temperatures of (298 to 523) K, and pressures of (1 to 1000) bar. Note that Eq. 4.14 should only be used at conditions in which water is in the liquid state.

c_1 / [m^2/s]	1.24×10^{-6}
c_2 / $[(\mathrm{mol_{NaCl}}/\mathrm{kg_{H_2O}})^{-1}]$	-7.29×10^{-2}
c_3 / [K]	-1.70×10^{3}
c_4 / [bar^{-1}]	-1.84×10^{-4}

respect to NaCl molalities. As the self-diffusivities of gases dissolved in liquids are inversely proportional to the viscosities of the solution [115, 197], the self-diffusivities of H_2 are expected to decay exponentially with respect to the NaCl molalities. The computed self-diffusivities of H_2 follow an Arrhenius-type [50] relation with respect to variations in temperature ($D \propto \exp[\frac{c}{T}]$) as shown in Figure 4.4(c). This behavior is also observed in literature for gases (e.g., O_2, H_2) dissolved in aqueous solvents [109, 253, 293–295].

4.3.4. Solubilities of H_2

In Figure 4.5, the solubilities of H_2 computed using CFCMC are shown as a function of (a) NaCl molality, (b) temperature, and (c) pressure. The computed solubilities are compared to the experimental measurements of Chabab *et al.* [211], Torín-Ollarves *et al.* [212], and their corresponding experimental correlations (also shown in Figure 4.5). The correlation of Torín-Ollarves *et al.* [212] is based on the experimental measurements for NaCl molalities of 0 and 2.5 mol NaCl/kg H_2O, the experimental data by Wiebe *et al.*, Wiebe *et al.* [297], Kling *et al.* [298], and Choudhary *et al.* [299] for H_2 solubility in pure H_2O, and the experiments by Crozier *et al.* [217] and Gordon *et al.* [218] for solubility of H_2 in saline solutions. Chabab *et al.* [211] provide an extensive experimental data set and a correlation for H_2 solubilities at temperatures of (323 to 373) K, and NaCl molalities in the range of (0 to 5) mol/kg H_2O. Lopez-Lazaro *et al.* [245] obtained the Henry constants of H_2 in aqueous NaCl solutions for molalities up to 2 mol NaCl/kg H_2O using excess chemical potentials computed using the WTPI method [49, 50, 277, 278]. Using the Henry constants reported by Lopez-Lazaro *et al.* [245], the solubilities of H_2 at a partial pressure of 100 bar are computed and shown in Figures 4.5(a) and 4.5(b). The simulations of Lopez-Lazaro *et al.* [245] show large error bars (ca. 10-20%). This may be due to the use of the WTPI method [49, 50, 277, 278], which

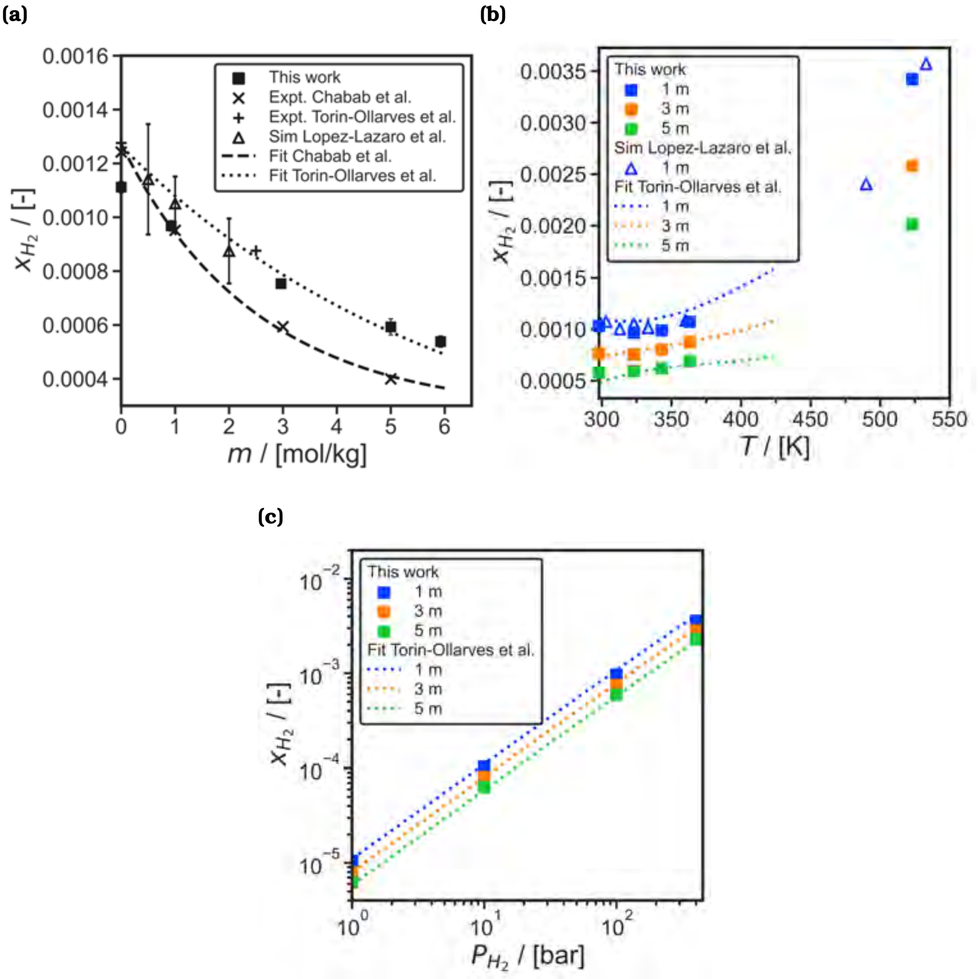

Figure 4.5. Computed solubilities of H_2 in aqueous NaCl solutions using the NaCl Madrid-2019 force field [103], TIP4P/2005 [100] H_2O force field, and Marx [91] H_2 force field as functions of (a) NaCl molality (m) in units of mol NaCl/kg H_2O for a H_2 partial pressure of 100 bar, at 323 K, (b) temperature for a H_2 partial pressure of 100 bar, and (c) H_2 partial pressure at 323 K. The dashed lines represent the experimental correlation provided by Torín-Ollarves *et al.* [212], and the dotted lines represent the experimental correlation results of Chabab et al. [211] The experimental data of Chabab et al. [211], and Torín-Ollarves *et al.* [212], and the simulation results of Lopez-Lazaro *et al.* [245] (converted from Henry constants) are also shown.

requires a large number of MC cycles to obtain low standard deviations for excess chemical potentials in the liquid phase [245, 248]. The solubilities computed in this chapter using CFCMC simulations [55, 56, 249, 250] have uncertainties of less than 5 %.

Figure 4.5(a) shows the decrease of the solubilities of H_2 at increasing molalities of NaCl (i.e., salting-out effect). The salting-out of non-polar gases (e.g., H_2, O_2, and CO_2) in presence of salts such as NaCl, KCl, and KOH is a well observed phenomenon [47, 236, 292]. As shown in Figure 4.5(a), the models by Torín-Ollarves *et al.* [212] and Chabab et al. [211] agree for H_2 solubilities in pure H_2O and at NaCl molalities below 0.5 mol NaCl/kg H_2O. For NaCl concentrations higher than 0.5 mol NaCl/kg H_2O the two models predict different H_2 solubilities. The salting-out effect of H_2 observed in this chapter using the Madrid-2019 [103] Na^+ and Cl^-, TIP4P/2005 [100] H_2O, and the Marx [91] H_2 force fields show better agreement to the salting-out effect observed by Torín-Ollarves *et al.* [212], especially at higher NaCl molalities of 3 and 5 mol NaCl/kg H_2O as shown in Figure 4.5(a). The correlation of Torín-Ollarves *et al.* [212] also shows agreement with our simulations at H_2 partial pressures ranging from (1 to 400) bar in the temperature range (298 to 363) K, as shown in Figures 4.5(b) and 4.5(c). Our simulation results also agree with the MC simulations by Lopez-Lazaro *et al.* [245] both for different NaCl molalities, and for different temperatures in the range of (298 to 523) K, even though the choice of the force fields for Na^+, Cl^-, and H_2 is different. Lopez-Lazaro *et al.* [245] have used the OPLS force field [300] for Na^+, and Cl^-, combined with the model by Darkim et al. [301] for H_2.

In Table S13 of the Supporting Information of Ref. [48], we provide an extensive database for solubilities of H_2 at temperatures of (298 to 363) K, H_2 partial pressures of (1 to 1000) bar, and at NaCl molalities of (0 to 6) mol/kg H_2O. The solubilities of H_2 at partial pressures up to 100 bar are computed for a wider temperature range i.e., (298 to 523) K. These data can be further used to test and train existing machine-learning models [213] or equations of state [302] for predicting H_2 solubilities in saline solutions at conditions relevant to geological H_2 storage.

4.4. Conclusions

Molecular simulations are used to compute (a) interfacial tensions of H_2 and aqueous NaCl solutions for temperatures, pressures, and molalities of (298 to 523) K, (1 to 600) bar, and (0 to 6) mol NaCl/kg H_2O, respectively, (b) self-diffusivities of H_2 in aqueous NaCl solutions for temperatures, pressures, and molalities of (298 to 723) K, (1 to 1000) bar and (0 to 6) mol NaCl/kg H_2O, respectively, and (c) solubilities of H_2 in aqueous NaCl solutions for temperatures, pressures, and molalities of (298 to 363) K, (1 to 1000) bar and (0 to 6) mol NaCl/kg H_2O, respectively. The simulations for computing H_2 self-diffusivities are also used to yield predictions for densities and viscosities of the NaCl solutions. The interfacial tensions and self-diffusivities are computed using MD simulations, and the solubilities are computed using CFCMC simulations. The H_2O TIP4P/2005 [100] force field, the NaCl Madrid-2019 [103] force fields, and H_2 Vrabec [90] and Marx [91] force fields are used. In addition, a modified version of the Madrid-2019 force field (i.e., the Madrid-Transport [47, 111] force field) is used, which is optimized for transport properties of aqueous solutions. Our results are validated against the available experimental data, models, and simulations. Excellent agreement between the results and experimental data is found with deviations smaller than 10% for the vast majority of the data points. The results of the NaCl Madrid-Transport force field were in better agreement with experimental data for transport properties, while the Madrid-2019 force field was sufficiently accurate for interfacial tensions and solubilities. The new data are used to develop engineering equations for interfacial tension and self-diffusion capturing the effect of pressure, temperature, and solution molality.

5

Thermodynamic and Transport Properties of Hydrogen in Aqueous KOH and NaOH Solutions

This chapter is based on the following publication: P. Habibi, A. Rahbari, S. Blazquez, C. Vega, P. Dey, T. J. H. Vlugt, and O. A. Moultos. “A New Force Field for OH^- for Computing Thermodynamic and Transport Properties of H_2 and O_2 in Aqueous NaOH and KOH Solutions”. *Journal of Physical Chemistry B* 126 (2022), 9376–9387.

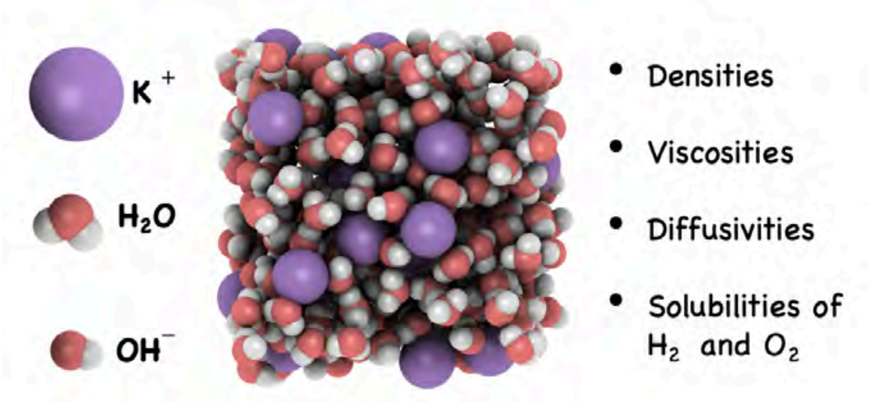

5.1. Introduction

Modelling aqueous alkaline solutions is of interest for a broad array of manufacturing and separation processes [303, 304]. Aqueous alkaline solutions containing KOH and NaOH are often used for electrolysis and in fuel cells due to their high ionic conductivities and low cost [12, 13, 305–307]. NaOH and KOH have solubilities exceeding 18 mol/kg in water at 293 K (and above) [308, 309], and significantly influence the thermophysical properties of the solution [310]. The interplay between different thermophysical properties (e.g. densities, viscosities, ionic conductivities) of aqueous NaOH and KOH solutions influences the product gas purity, and the energy (and Faradaic) efficiency of alkaline-water electrolyzers [7, 16, 311]. Knowledge of the thermodynamic and transport properties of H_2 and O_2 gas in aqueous NaOH and KOH solutions is therefore highly relevant for optimization and process design of electrolyzers [15, 16].

Modelling electrolyte systems is a challenging endeavor because of the strong long-range ionic interactions, which make the solutions highly non-ideal [303, 312–314]. Electrolyte solutions are commonly modelled using semi-empirical equations of state and molecular based simulations [303, 312–323]. Semi-empirical equations provide a rapid and convenient method for the prediction of thermophysical properties [312]. The quality of these equations depends on the availability of accurate experimental and simulation data [315–319]. For aqueous alkaline solutions, experimental data for self-diffusivities and solubilities of H_2 and O_2 at high concentrations (above 4 mol/kg), temperatures (323-373 K), and pressures (above 50 bar) is lacking, especially in the case of aqueous NaOH solutions [15, 324]. These temperatures (ca. 353 K) and concentrations (4-12 mol/kg electrolyte solution) are especially relevant for alkaline electrolyzers [10–14]. MD and MC simulations can be used as a complementary approach to experiments [109] to provide insight at conditions for which experimental data are limited, and difficult to obtain due to high temperatures, pressures, and the corrosivity of the solution (in case of strong alkaline solutions).

Molecular simulations of electrolyte systems can be studied using either ab-initio simulations or force field based methods [303, 325, 326]. Ab-initio simulations have the potential to more accurately describe the structure and solvation of the ions [88, 325], but these simulations are computationally expensive and are limited to systems comprising hundreds of atoms for timescales of the order of pico-seconds. To precisely calculate transport properties of fluids, long simulations of several nanoseconds are essential [321, 327]. To account for ion-ion and ion-water interactions at high electrolyte concentrations, water molecules need to be modelled explicitly [328, 329], which makes the computations more costly. To overcome both the time and system-size restrictions of ab-initio calculations, force field-based methods are usually preferred for large-scale production of thermophysical data.

Force fields for aqueous electrolytes can be polarizable or non-polarizable [101–103]. The non-polarizable TIP4P/2005 water model [100] has proven to be quite suitable for predicting densities, viscosities and self-diffusivities of water [51, 100, 330]. In an attempt to model the effective charge screening that occurs in electrolyte solutions, ions are modelled as scaled charges in non-polarizable force fields [303]. Prior research has demonstrated that the use of scaled charges significantly helps in capturing the correct dynamics of ions [103, 111, 331, 332]. Scaled charge models for ions such as Na^+, K^+, and Cl^- have been developed by Zeron et al. (the so-called Madrid-2019 force field) [103, 111] and used in combination with the TIP4P/2005 water model [103]. These force fields yield reasonable predictions for densities, dynamic viscosities, and self-diffusivities of aqueous electrolytes with a scaled charge of 0.85 for concentrations up to 4 mol/kg salt [103]. However, the dynamic viscosities computed using the Madrid-2019 force field deviate from experiments at higher molalities. To address this, Vega and co-workers have developed a new force field called the Madrid-Transport with a scaled charge of 0.75 [111]. This force field can accurately predict dynamic viscosities of aqueous NaCl, and KCl solutions up to their solubility limit [111]. Despite the importance of alkaline systems, there is no Madrid-force field for OH^- to accurately predict densities and dynamic viscosities of aqueous NaOH and KOH systems. Existing OH^- force fields are often used to simulate the solvation energy [333–335] and structure [336–341], and cannot be used directly in combination with the TIP4P/2005 water model and the Madrid-force fields [103, 111] for Na^+ and K^+ ions as they do not use scaled charges of 0.85 or 0.75.

Here, we propose several non-polarizable two-site OH^- force fields with scaled charges of -0.85 and -0.75, respectively. One of the newly proposed OH^- force fields with a scaled charge of -0.75, yields accurate predictions for both densities and dynamic viscosities of aqueous NaOH and KOH solutions for concentrations ranging from 0 to 8 mol/kg, at temperatures ranging from 298 to 353 K. We use this force field to compute the self-diffusivities of H_2 and O_2 in aqueous NaOH and KOH solutions using MD. Solubilities of these gases as functions of concentrations, and temperatures, and pressures are computed using CFCMC simulations [248–250]. Our data, obtained from molecular simulations, are compared to available experimental data on H_2 and O_2 in KOH solutions. Our simulations can adequately describe the trends observed in experiments for variations in both concentration and temperature. The self-diffusivities and solubilities of H_2 and O_2 in NaOH and KOH solutions are then fitted to semi-empirical engineering equations. These engineering equations can be used for process modelling, and for optimizing electrolyzers and fuel cells [16].

This chapter is organized as follows. In section 5.2, details on the force fields are provided, and the molecular simulation (MD and MC) techniques are explained. In section 5.3, force field optimisation of OH^- is discussed, and the results for viscosities, H_2 and O_2 self-diffusivities and solubilities at temperatures ranging from 298-353 K are provided. Our conclusions are summarized in section 5.4.

5.2. Methodology

5.2.1. Force fields

The four-site TIP4P/2005 water model is used in all simulations [100] in this chapter. The two-site Bohn model [342] is used for modelling O_2. For H_2, the single-site Vrabec model [90], and the three-site Marx model [91] are used similar to Chapter 4. These force fields for H_2 and O_2 have shown to accurately describe gas diffusivities in pure water at various pressures and temperatures [109]. The single-site H_2 Vrabec model is less computationally demanding (no bonds or angles) than the three-site Marx model and yields similar self-diffusivities in pure TIP4P/2005 water (see Figure S1 of the Supporting Information of Ref. [47]). This force field is used for computing self-diffusivities of H_2 in NaOH and KOH solutions. The Marx model yields significantly more accurate H_2 solubilities than the Vrabec model in pure TIP4P/2005 water (see Figure S1 of the Supporting Information of Ref. [47]), and is used for computing H_2 solubilities in NaOH and KOH solutions. For the K^+ and Na^+ ions, the Madrid-Transport (+0.75) [111] and Madrid-2019 (+0.85) [103] force fields are used (parameters listed in Table A.4). For OH^-, several force fields are proposed in this chapter. The details for OH^- force field are discussed in Section 5.3.1. All force fields considered in this chapter are rigid. All interaction parameters for the TIP4P/2005 water, H_2, and O_2 models are provided in Appendix A.2. The Lennard-Jones (LJ) and Coulombic interactions are considered for modelling the intermolecular interactions. The Lorentz-Berthelot mixing rules [49, 50] are applied with the exception of $[\mathrm{Na/K-H_2O}]$ LJ interactions as specified in Table A.4.

5.2.2. MD simulations

The same software (LAMMPS) and methodology used to compute the transport properties in Chapter 4 (i.e., section 4.2.4) is used for the MD simulations [59]. For H_2O, O_2, and OH^-, the SHAKE algorithm in LAMMPS [59, 257] is used to fix the bond lengths (and the bond angle of H_2O). Analytic tail corrections for energies and pressures are applied to the LJ part of the potential. The cut-off radius for both LJ and Coulombic potentials is set to 10 Å. The particle-particle particle-mesh (PPPM) [50, 258] method is used for long-range electrostatic interactions with a relative error of 10^{-5}.

The simulations are initially equilibrated in the NPT and NVT ensembles

Table 5.1. Force field parameters for the Na^+, and K^+ models used (Madrid-2019 [103] and Madrid-Transport [111]). ϵ and σ are the Lennard-Jones parameters and q is the atomic partial charge. O_w refers to the O-atom of water (TIP4P/2005 [100] model). The Lorentz-Berthelot mixing rules [49, 50] are applied for all mixtures, with the exception of $[Na/K-H_2O]$ LJ interactions as specified in this table.

	Madrid-2019		Madrid-Transport	
	Na^+	K^+	Na^+	K^+
q_M/[e]	0.85	0.85	0.75	0.75
ϵ_{MM}/k_B / [K]	177.08	238.83	177.08	238.83
σ_{MM} / [Å]	2.21737	2.30140	2.21737	2.30140
ϵ_{MO_w}/k_B / [K]	95.42	168.43	95.42	168.43
σ_{MO_w} / [Å]	2.60838	2.89040	2.38725	2.89540

for a period of ca. 2 ns. Production runs (in NVT) of 10-50 ns are used to calculate dynamic viscosities and self-diffusivities. To obtain an ensemble mean and a standard deviation, each calculation is repeated 5 times with a different random seed for the initial velocity. The densities and transport properties are calculated in a simulation box containing 700 H_2O molecules. The corresponding numbers of NaOH and KOH molecules, in combination with the respective molarities are provided in Table S4 and S5 of the Supporting Information of Ref. [47]. All initial configurations are created using the PACKMOL software [259]. Two gas molecules (H_2 or O_2) (corresponding to infinite dilution) are used to calculate self-diffusivities of the gasses in the aqueous NaOH and KOH solutions. All self-diffusivities shown in this chapter are corrected for finite size effects using the Yeh-Hummer equation [265–267, 343] (as shown in Eq 4.3). To ensure no precipitation takes place and to calculate RDFs, simulations are also carried out for a larger box size with 4200 H_2O molecules for 10 ns.

5.2.3. CFCMC simulations

The solubilities in this Chapter are calculated using the same approach described in Section 4.2.5, with the exception that 4×10^5 equilibration cycles are carried out followed by 4×10^5 production. All the raw data for the MD and MC simulations are shown in Tables S6-S11 of the Supporting Information of Ref. [47].

5.3. Results and discussion

5.3.1. Force field optimization

To construct accurate models for aqueous NaOH and KOH solutions, four different two-site OH^- (i.e. $O^{\delta-}$, $H^{\delta+}$) force fields are considered (FF1-FF4) combined with the TIP4P/2005 water [100], and the Madrid-2019 [103], or Madrid-Transport [111] force fields for Na^+ and K^+. These force fields and their corresponding parameters are listed in Table 5.2. For all OH^- models, the O−H bond length is set to 0.98 Å, similar to the works of Ref [337, 338]. FF1, FF3 and FF4 have a total scaled charge (q_{OH}) of -0.75 on OH^-, while FF2 has a total scaled charge of -0.85. These force fields are used in combination with the Madrid-Transport (+0.75) [111] and Madrid-2019 (+0.85) [103] Na^+ and K^+ models such that the total charge of NaOH and KOH clusters becomes 0. The charge of OH^- is distributed on the O (q_O) and H (q_H) atom. For FF1 and FF2, the charges on the O and H atoms have the same ratios as in the work by Botti et al. on the structure of concentrated NaOH solutions [337]. The charge distributions of the FF3 and FF4 models are based on Quantum Theory of Atoms in Molecules (QTAIM) calculations for OH^-, which have indicated that the O atom can have an unscaled charge of -1.4 to -1.3 [344]. For this reason, for the FF3 and FF4 models, the charge on the O atom are set to -1.4×0.75 and -1.3×0.75, respectively. The charge on the H atom (q_H) is set such that $q_O + q_H = q_{OH}$. For each force field, the Lennard-Jones σ parameter of the O atom (σ_{OO}) is adjusted based on the experimental densities of aqueous NaOH and KOH solutions [114, 310, 345].

Figure 5.1 shows the variation of densities as functions of electrolyte concentrations for both NaOH and KOH. By adjusting the value of σ_{OO}, it is possible to obtain an excellent agreement for all the different models. All the densities obtained deviate less than 2% from experimental fits found in literature. A larger negative charge on O (q_O) results in a larger optimum σ_{OO} parameter, to counteract the strong attractive Coulombic interactions. The experimental fits of Olsson [345] (for densities and viscosities of aqueous NaOH), Gilliam [114] (densities of aqueous KOH), and Guo [346] (viscosities of aqueous KOH) are used and shown as lines in Figure 5.1.

The dynamic viscosities of aqueous NaOH and KOH solutions calculated using FF1-FF4 are shown in Figure 5.2. It can be observed that the choice of the total charge (q_{OH}), and the resulting σ_{OO} has a significant influence on the viscosities, especially at higher concentrations in which the influence of ion-ion interactions become more important. The influence of ion size on the viscosities and densities is shown in Figure S2 of the Supporting Information of Ref. [47]. In case of FF2 (with $q_{OH} = -0.85$), the dynamic viscosity is overestimated by more than a factor 3 compared to the experimental fit for the highest concentration of NaOH. For aqueous KOH, the FF2 model overestimates the dynamic viscosity by around 40% at the highest concentration of KOH. The FF1, FF3, and FF4 models

Table 5.2. Force field parameters for OH^-. The bond length of O–H is set to 0.98 Å. For all models, the sigma for H (σ_{HH}) is set to 1.443 Å [337]. The Lennard-Jones ϵ parameters for O and H (ϵ_{OO}/k_B, ϵ_{HH}/k_B) are based on Refs. [337, 341] and are set to 30.19, and 22.13 K, respectively, for all the models. The FF1 force field for OH^- is recommended.

Model	q_O / [e]	q_H / [e]	q_{OH}	σ_{OO}/[Å]	ϵ_{OO}/k_B/[K]
FF1	-1.2181	+0.4681	-0.75	3.65	30.19
FF2	-1.3805	+0.5305	-0.85	3.85	30.19
FF3	-1.0500	+0.3000	-0.75	3.55	30.19
FF4	-0.9750	+0.2250	-0.75	3.45	30.19

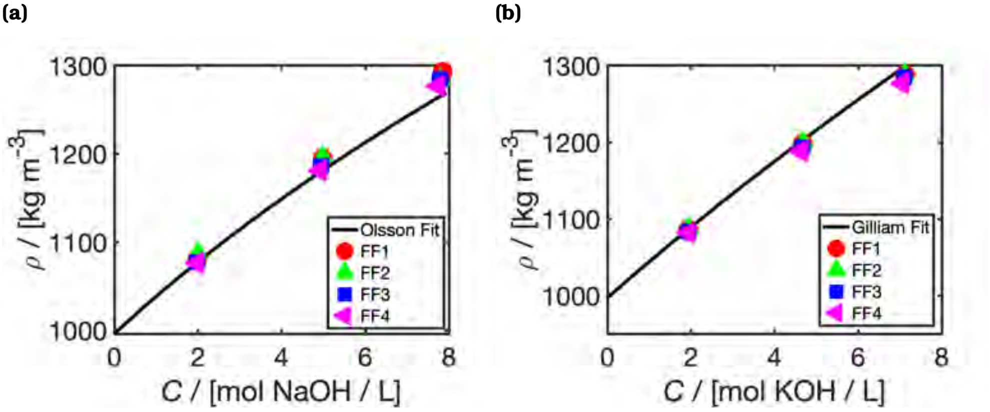

Figure 5.1. Densities (ρ) at 298 K and 1 bar as functions of the electrolyte concentrations (C) for (a) NaOH, (b) KOH. Four different OH^- force fields are considered (FF1-FF4) and compared to experimental fits (shown as lines) of Olsson [345] (for NaOH), and Gillam [114, 310] (for KOH). The different parameters used for all the force fields are listed in Table 5.2.

with $q_{OH} = -0.75$ show a much better agreement with the experimental fit. The findings of the Madrid-Transport model for aqueous NaCl and KCl solutions [111], also show that a scaled charge of 0.75 leads to better predictions of transport properties (especially at concentrations above 4 mol/kg salt) compared to a scaled charge of 0.85. Overall, the FF1 model shows the best agreement with the experimental viscosities and densities. For this reason, only the results of the FF1 model will be used and discussed further in this chapter.

The RDFs for the anion$-O_W$ (O of water) and cation $-O_W$ are shown in Figure 5.3. The RDFs for the anion-anion, anion-cation, and cation-cations are shown in Figure S3 of the Supporting Information of Ref. [47]. Based on the RDFs, the hydration numbers (n_{hyd}) are calculated

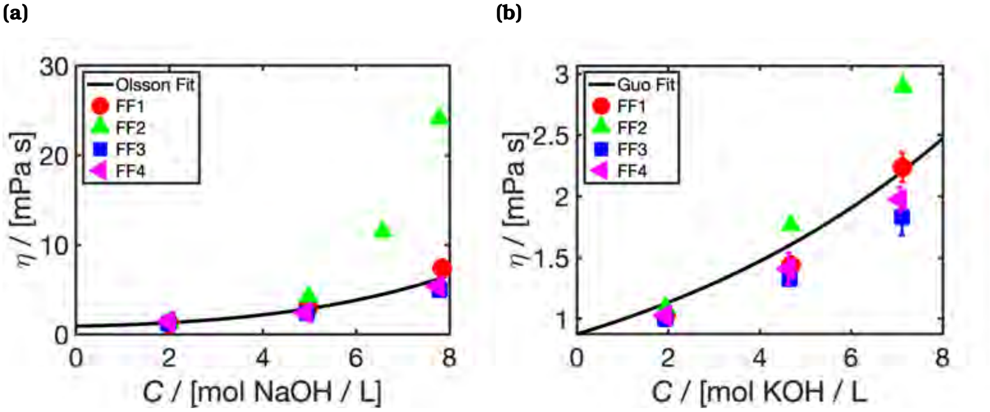

Figure 5.2. Dynamic viscosities (η) at 298 K and 1 bar as functions of the electrolyte concentrations (C) for (a) NaOH, and (b) KOH. Four different OH^- force fields are considered (FF1-FF4) and compared to experimental fits (shown as lines) of Olsson [345](for NaOH), and Guo [346] (for KOH). The different parameters used for all the force fields are listed in Table 5.2.

using [47, 103]

$$n_{\mathrm{hyd}} = 4\pi\rho_{\mathrm{W}} \int_0^{r_{\mathrm{min}}} g_{\mathrm{W}}(r) r^2 dr \tag{5.1}$$

where g_{W} is the anion/cation—$\mathrm{O_W}$ RDF, r is the radial distance, r_{min} is the position of the first minimum in the RDF, and ρ_{W} is the number density of water in the solution. Our results show a first peak at approx. 2.13 and 2.79 Å for Na^+—$\mathrm{O_W}$ and K^+—$\mathrm{O_W}$, respectively. The cation hydration numbers are 4.9 and 7.2 for Na^+ and K^+, respectively, at a molality of 5 mol/kg (corresponding to a molarity of 4.98 mol/L for NaOH, and 4.68 mol/L for KOH). Crystallization of ions is not observed for all our MD simulations of 10-50 ns based on the RDFs. Experimental and simulation results in literature suggest a first RDF peak at approx. 2.4-2.5 Å [326, 337, 340] for Na^+—$\mathrm{O_W}$ and a peak at approx. 2.7-2.8 Å for K^+—$\mathrm{O_W}$ [338]. The reported hydration numbers (in the first shell) are in the range of 4-8 and 6-8 for Na^+ and K^+, respectively [347]. For OH^-, the results show a first peak at approx. 2.75 Å for OH^-—$\mathrm{O_W}$, with hydration numbers of 4.8 and 5.9 for KOH and NaOH, respectively, at a molality of 5 mol/kg. Other molecular simulations in literature report a first peak ranging from 2.3Å to 2.7Å for the first OH^-—$\mathrm{O_W}$ peak [326, 337, 340]. The combined Car-Parrinello MD and x-ray diffraction studies of Megyes et al. for aqueous NaOH report a OH^-—$\mathrm{O_W}$ distance ranging from 2.65Å to 2.70Å, with hydration numbers ranging from 3 to 5 [326]. Overall, our force field results show agreement with other studies, albeit slightly over-predicting

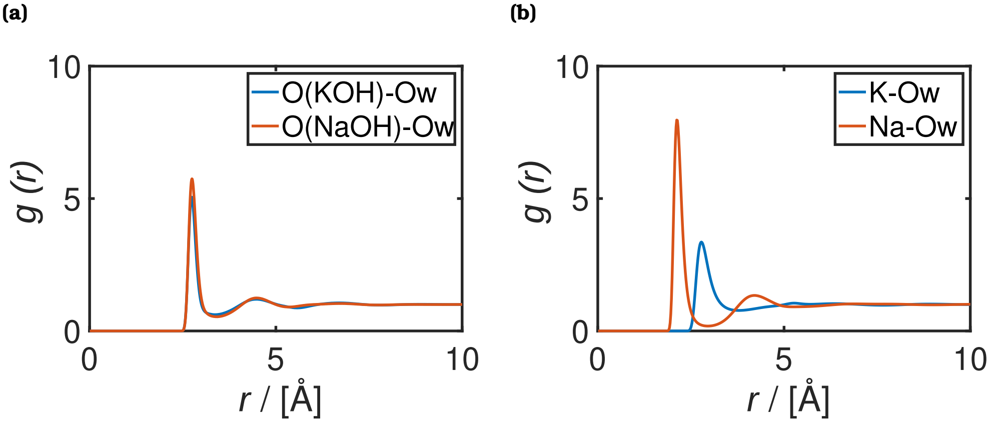

Figure 5.3. Radial distribution functions ($g(r)$) for (a) O(KOH)—O_W (O of water) and O(NaOH)—O_W, and (b) K^+(KOH)—O_W and Na^+(NaOH)—O_W, as a function of radial distance r (Å), at 298 K, 1 bar, and a concentration of 5 mol/kg (corresponding to a molarity of 4.98 mol/L for NaOH, and 4.68 mol/L for KOH). The FF1 OH^- model, in combination with the TIP4P/2005 water model [100], and the Madrid-Transport Na^+, and K^+ models [111] are used for the MD simulations.

the first OH^-—O_W peak and the hydration.

The self-diffusivities of NaOH and KOH are listed in Table 5.3. Even though for Na^+ and K^+ the self-diffusivities at infinite dilution are close, this is not the case for OH^- (underestimated by a factor ca. 5). For reasonable values of σ_{OO}, ϵ_{OO}, and q_O, we could not obtain OH^- self-diffusivities close to the values reported by experiments [348] without causing significant deviations from experimental densities and viscosities. This result is expected as classical OH^- models cannot capture the details of the solvation of OH^- in water and the proton transfer mechanism, which lead to anomalously high OH^- mobilities as discussed by Tuckerman et al. [87, 88]. As such, our model, similarly to other classical force fields, is not suitable for predicting OH^- diffusivities of NaOH and KOH. Since electrical conductivities vastly depend on the mobility of the OH^- ions in the solution, the new OH^- model presented here is unable to accurately predict electrical conductivities of aqueous NaOH and KOH solutions. Although our classical force field cannot capture the proton transfer mechanism, it can correctly predict the dynamic viscosities of the electrolyte solutions. As the aim of this study is to study the transport properties and solubilities of H_2 and O_2 gas in aqueous NaOH and KOH electrolytes, correct predictions of densities and viscosities are sufficient. Developing an OH^- force field by taking into account the proton transfer mechanism and accurate OH^- mobilities is beyond the scope of this

Table 5.3. Finite size corrected (using Equation 4.3) self-diffusivities (in units of $10^{-9}\mathrm{m}^2\mathrm{s}^{-1}$) of cations ($D_{\mathrm{cation}}$) ($\mathrm{Na}^+$, K^+), and OH^- (D_{OH^-}) at different molalities of 1.99 and 0.48 mol/kg calculated using MD. A comparison is made with experimental diffusion coefficients at infinite dilution of ions [348]. The FF1 OH^- model, in combination with the TIP4P/2005 water model [100], and the Madrid-Transport Na^+, and K^+ models [111] are used for the MD simulations.

	$D_{\mathrm{cation}}/[10^{-9}\mathrm{m}^2\mathrm{s}^{-1}]$			$D_{\mathrm{OH}^-}/[10^{-9}\mathrm{m}^2\mathrm{s}^{-1}]$		
	MD		Expt	MD		Expt
Molality (mol/kg)	1.99	0.48	0	1.99	0.48	0
NaOH	1.02	1.36	1.33	0.90	1.17	5.27
KOH	1.59	1.95	1.96	1.09	1.23	5.27

chapter as quantum mechanical based force fields will be required.

5.3.2. Densities and viscosities

It is important that the NaOH and KOH models (FF1 OH^- model, and the Madrid-Transport models of Na^+, and K^+ [111]) can accurately predict the temperature-dependence of densities and viscosities. Figure 5.4 shows the densities and viscosities at different temperatures for both NaOH and KOH solutions. The agreement between MD simulations and experimental fits is excellent for aqueous KOH. For aqueous NaOH solutions, the results of densities are overestimated by ca. 2% and for dynamic viscosities by ca. 20% at the highest concentration (molality 8 mol/kg). Despite this, the trends of densities and viscosities for variations of electrolyte concentration and temperature are well-predicted by the MD simulations using the new force fields. Densities and viscosities show a much weaker dependence on pressure (in the range of 1 to 100 bar) compared to temperature (in the range of 298 to 353 K) due to the incompressibility of the liquid phase. The variations of densities and viscosities as a function of pressure are shown in Figure S4 of the Supporting Information of Ref. [47].

5.3.3. Self-diffusivities of H_2 and O_2

The finite size corrected self-diffusivities (using Equation 4.3) of H_2 and O_2 in aqueous NaOH and KOH solutions calculated using MD simulations at various temperatures are shown in Figure 5.5. The results obtained by our MD simulations for the KOH solution are compared to the experimental data of Tham et al. [324, 349] at different temperatures, i.e, 298 K, 333 K, and 353 K. For H_2 self-diffusivities, our results are in quantitative agreement with the results of Tham et al. [324, 349] The increase in H_2 and O_2 diffusivities at higher temperatures are well-predicted. These

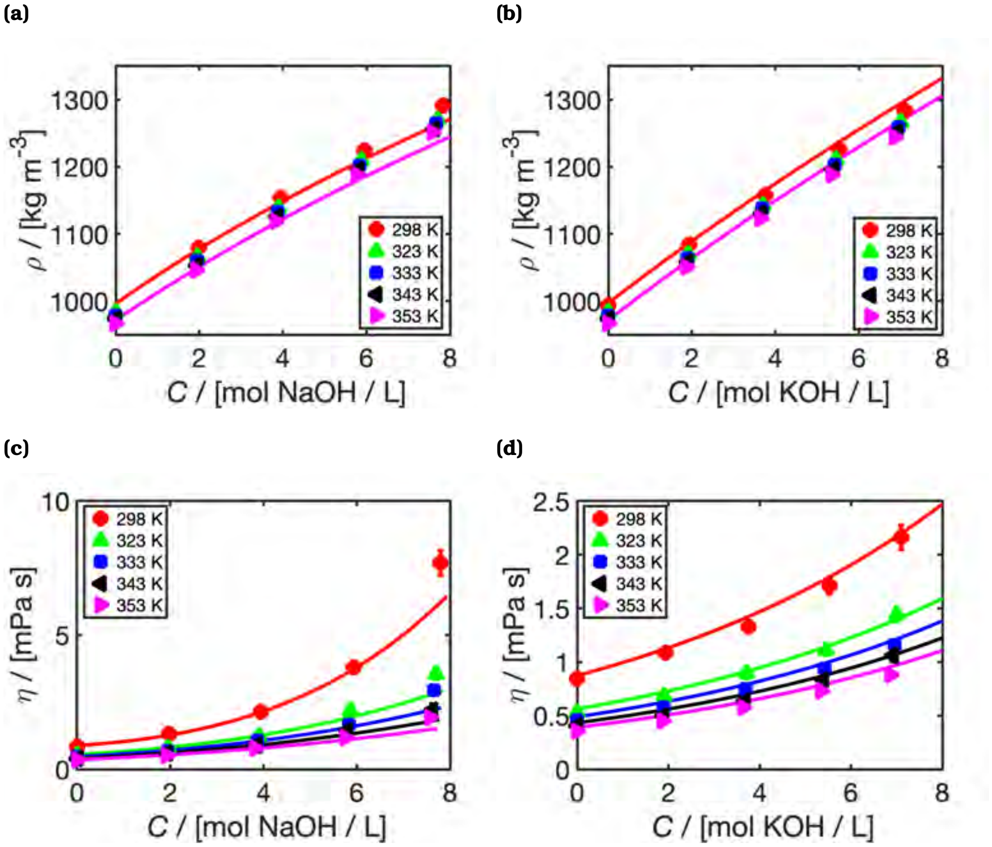

Figure 5.4. Densities (ρ) (a)-(b) and dynamic viscosities (η) (c)-(d) as functions of concentrations (C in units of mol salt / L solution) for aqueous NaOH (a)-(c) and KOH (b)-(d) at 1 bar. The simulations results at temperatures 298 (red), 323 (green), 333 (blue), 343 (black), and 353 (purple) K are shown. The lines represent experimental correlations. For densities, the Olsson [345] and Gilliam correlations [114] at 298 (red) and 353 (purple) K are shown. For viscosities, the Olsson [345] (NaOH) and Guo [346] (KOH) correlations are plotted for all temperatures with the same color scheme as the simulation points. The FF1 OH^- model, in combination with the TIP4P/2005 water model [100], and the Madrid-Transport Na^+, and K^+ models [111] is used for the MD simulations.

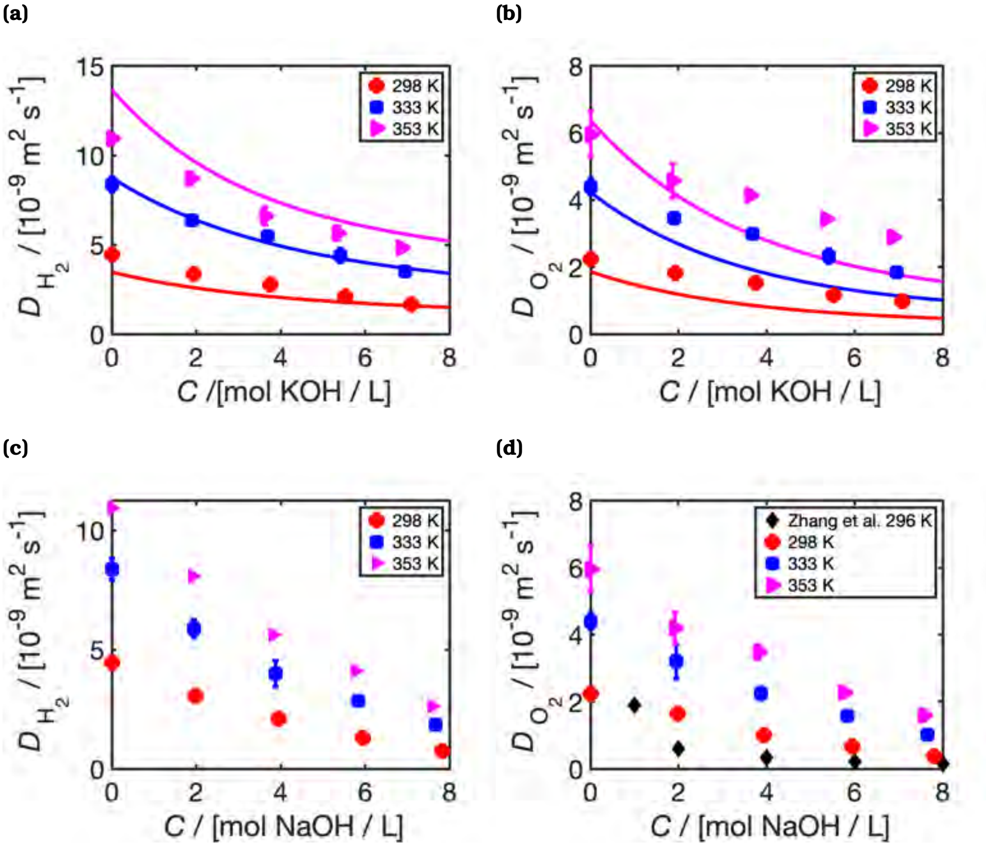

Figure 5.5. H_2 (a)-(c) and O_2 (b)-(d) self-diffusivities (*D*) as functions of KOH (a)-(b) and NaOH (c)-(d) concentrations (*C*) at different temperatures (298, 333, and 353) K at 1 bar. For diffusivities of H_2 and O_2 in the KOH solution, the experimental data of Tham et al. [324, 349] at 298 (red), 333 (blue), and 353 K (purple) are fitted using Equation 5.4 and shown in (a) and (b) as lines. The fitting coefficients of these data are shown in Table 5.4. The experimental diffusivities of O_2 in NaOH solution at 296 K (black) provided by Zhang et al. [15] are plotted as points. The FF1 OH^- model, in combination with the TIP4P/2005 water model [100], the Bohn O_2 model [342], the Vrabec H_2 model [90], and the Madrid-Transport Na^+, and K^+ models [111] is used for the MD simulations.

Table 5.4. Fitting parameters for Equation 5.2 for H_2 and O_2 self-diffusivities in aqueous NaOH and KOH solutions. The values for a_0 (in units of $10^{-11}\mathrm{m}^2/\mathrm{s}$), a_1 (in units of $10^{-12}\mathrm{m}^2/\mathrm{s(L/mol)}$), a_2 (in units of $10^{-13}\mathrm{m}^2/\mathrm{s(L/mol)}^2$), a_3 (in units of $10^{-14}\mathrm{m}^2/\mathrm{s(L/mol)}^3$), and a_4 (in units of $10^{-2}\mathrm{K}^{-1}$) are shown for both the MD simulations obtained in this chapter (range of validity: 0-8 mol/L, 298-353 K), and the experimental work of Tham et al. [324] (at 298, 333, and 353 K) for H_2 and O_2 diffusion in KOH solutions (range of validity: 0-14 mol/L). The FF1 OH^- model, in combination with the TIP4P/2005 water model [100], the Bohn O_2 model [342], the Vrabec H_2 model [90], and the Madrid-Transport Na^+, and K^+ models [111] is used for the MD simulations.

	a_0	a_1	a_2	a_3	a_4
H_2—KOH (Expt)	0.4066	-0.5903	0.4748	-0.1421	2.288
O_2—KOH (Expt)	0.2625	-0.5124	0.4345	-0.1278	2.201
H_2—KOH (MD)	3.844	-5.006	3.686	-1.511	1.606
O_2—KOH (MD)	1.511	-2.092	2.483	-1.743	1.701
H_2—NaOH (MD)	3.344	-5.725	4.649	-2.103	1.648
O_2—NaOH (MD)	1.313	-2.105	1.604	-0.7482	1.743

trends are linked to the decrease of the dynamic viscosities of the solutions, which the MD simulations capture correctly. In our simulations for O_2, the decay in the self-diffusivities with respect to variations of KOH concentrations are underpredicted with respect to the experimental data. Zhang et al. [15] report experimental O_2 diffusivities in aqueous NaOH at 296 K. Although the results of Zhang et al. [15] for O_2 diffusivity at 1 mol/L NaOH is in agreement to ours, at 2 mol/L their results show a sharp decrease of the O_2 diffusivities by approximately a factor $1/3$ with respect to diffusivities at 1 mol/L NaOH [15]. This sharp decline is not observed in our calculations. However, the current force field models have managed to qualitatively predict the trends for a wide concentration (0-8 mol/kg) and temperature (298-353 K) range. For H_2 self-diffusivities in aqueous NaOH no experimental data at these different temperatures are found. Thus, our simulations serve as a first prediction for these data.

The simulations results (at 298, 323, 333, 343, 353 K) in this chapter (shown in Figure S5 of the Supporting Information of Ref. [47]), and the experimental data of Tham et al. (at 298, 333 and 353 K) [324, 349] are fitted to an engineering equation:

$$D_i = (a_0 + a_1 C + a_2 C^2 + a_3 C^3)\exp[a_4 T] \tag{5.2}$$

where D_i is the self-diffusivity of H_2 and O_2 in NaOH and KOH solutions, $a_0 - a_4$ are fitting constants, C is the electrolyte concentration (in $\mathrm{mol/L}$), and T is the temperature (in K). All fitting parameters for H_2 and O_2 in the aqueous NaOH and KOH solutions are listed in Table 5.4. Equation

5.2 provides an excellent fit for both the simulation results found in this chapter and the experimental data of Tham et al. [324] as shown in Figure S5 of the Supporting Information of Ref. [47].

5.3.4. Solubilities of H_2 and O_2

In Figure 5.6, the H_2 and O_2 solubilities obtained using CFCMC calculations are shown as functions of NaOH and KOH concentrations. In this figure, only the results at 298 K and 333 K are shown as solubilities (especially at higher electrolyte concentrations) vary only weakly in the temperature range of 298-353 K. The solubilities of H_2 and O_2 at 298, 323, 333, 343, and 353 K are shown in Figure S7 of the Supporting Information of Ref. [47].

As a comparison the experimental data provided by Walker et al. [349] on the solubilities of H_2 and O_2 in aqueous KOH are fitted and plotted in Figure 5.6(a)-(b). This experimental data are also in agreement with the experiments of Davis et al. [351] for O_2 solubilities (at 298 and 333 K) and with the Sechenov model [292]. The Sechenov model [350] (with the parameters provided by Weisenberger et al. [292]) is an empirical model, which predicts the salting out effect [352, 353] at different temperatures (273-363 K) and electrolyte concentrations [292]. For NaOH, our data are compared to the Sechenov model as direct experimental data at these two temperatures are not available. Zhang et al. [15] report solubilities of O_2 in aqueous NaOH at 296 K. Our simulations show agreement with data and experimental fits for both H_2 and O_2. Both the salting out phenomena and the temperature trends are captured by our simulations. At low electrolyte concentrations (below 2 mol/L), increasing the temperature from 298 to 333 K leads to slightly lower H_2 and O_2 solubilities. At higher molarities, the solubilities become less dependent on the temperature and the concentration of the salts dominate the solubilities. The simulations results and experimental data of Walker et al. [349] for H_2 and O_2 solubilities in aqueous KOH and NaOH are fitted to a Sechenov-based [292] engineering equation:

$$\ln\left(\frac{S_{\mathrm{G}}}{S_{\mathrm{G},0}}\right) = (f_0 + f_1 T)C \tag{5.3}$$

where S_{G} and $S_{\mathrm{G},0}$ are the solubility of the gas in the electrolyte and pure water at 1 bar, respectively. $f_0 - f_1$ are fitting constants. The temperature dependence of the parameter $C_{\mathrm{G},0}$ can be fitted as:

$$S_{\mathrm{G},0} = f_2 + f_3 T + f_4 T^2 \tag{5.4}$$

where $f_2 - f_4$ are additional fitting parameters. The optimized fitting parameters for MC simulations in this chapter and the experimental data of Walker et al. for H_2 and O_2 solubilities are shown in Table 5.5. Equation 5.3 provides an excellent fit for both the simulation results found in this

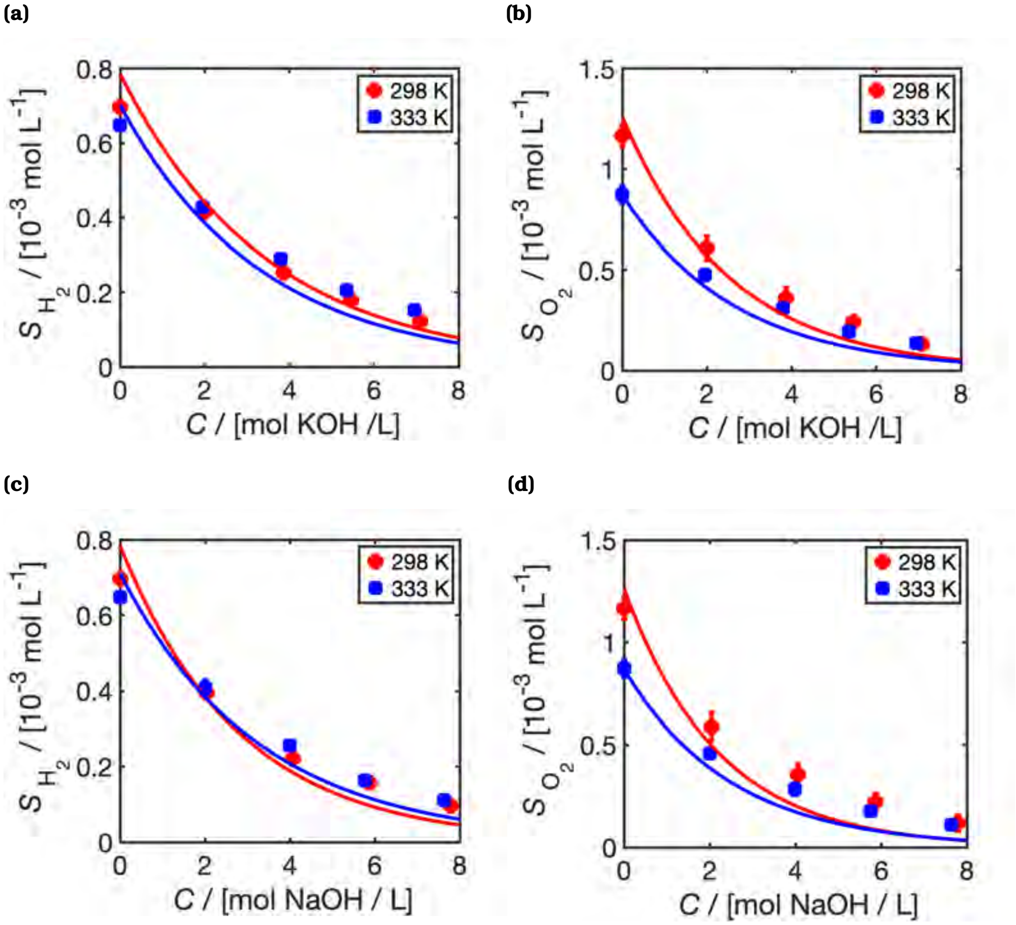

Figure 5.6. H_2 (a)-(c) and O_2 (b)-(d) solubilities (S) as functions of KOH (a)-(b) and NaOH (c)-(d) concentrations (C) at different temperatures of 298, and 333 K at H_2 and O_2 partial pressures of 1 bar. For solubilities of H_2 and O_2 in KOH solutions, the experimental data of Walker et al. [349] at 298 (red), and 333 K (blue) is fitted using Equation 5.3 and shown in (a) and (b) as lines. The fitting coefficients are shown in Table 5.5. For H_2 and O_2 solubilities in NaOH solutions, the Sechenov model [292, 350](using the parameters provided by Weisenberger et al. [292]), and the experimental solubilities in pure water [349] are used to obtain the experimental fits, which are shown as lines. The FF1 OH^- model, in combination with the TIP4P/2005 water model [100], the Bohn O_2 model [342], the Marx H_2 model [91], and the Madrid-Transport Na^+, and K^+ models [111] is used for the MC simulations.

Table 5.5. Fitting parameters for Equation 5.3 for the H_2 and O_2 solubilities (mol/L) in NaOH and KOH solution. The values for f_0 (10^{-1}(L/mol)), f_1 (10^{-4}(L/mol)K^{-1}), f_2 (10^{-3}(mol/L)), f_3 (10^{-5}(mol/L)K^{-1}), and f_4 (10^{-8}(mol/L)K^{-1}) are shown for both the MC simulations obtained in this chapter (range of validity: 0-8 mol/L, 298-353 K), and the experimental work of Walker et al. [349] (at 298, 333, and 353 K) for H_2 and O_2 solubilities in KOH solutions (range of validity: 0-14 mol/L). The FF1 OH^- model, in combination with the TIP4P/2005 water model [100], the Bohn O_2 model [342], the Marx H_2 model [91], and the Madrid-Transport Na^+, and K^+ models [111] is used for the MC simulations.

	f_0	f_1	f_2	f_3	f_4
H_2—KOH (Expt)	-1.944	-3.167	9.517	-5.337	8.078
O_2—KOH (Expt)	-5.712	5.854	16.961	-8.993	12.494
H_2—KOH (MC)	-5.468	10.077	4.874	-2.526	3.773
O_2—KOH (MC)	-5.670	8.889	13.935	-7.331	10.218
H_2—NaOH (MC)	-4.749	7.241	4.874	-2.526	3.773
O_2—NaOH (MC)	-4.093	4.057	13.935	-7.331	10.218

chapter and the experimental data present in the literature, as shown in Figure S7 of the Supporting Information of Ref. [47].

5.4. Conclusions

The self-diffusivities and solubilities of H_2 and O_2 in aqueous NaOH and KOH solutions are modelled using MD and CFCMC simulations. A new two-site non-polarizable OH^- force field (FF1 model) is proposed with a scaled charge of -0.75, which matches with the TIP4P/2005 water and the Madrid-Transport models for Na^+ and K^+. Although our classical force field cannot capture the proton transfer mechanism, which influences the OH^- diffusivities, it can predict the densities, dynamic viscosities and the salting out of H_2 and O_2 in aqueous NaOH and KOH solutions. Excellent agreement is observed between simulation and experimental data for both densities and dynamic viscosities of NaOH and KOH for a concentration range of 0-6 mol/kg and a temperature range of 298-353 K. This model is used to generate self-diffusivity and solubility data for H_2 and O_2 in aqueous NaOH and KOH solutions for a temperature range of 298-353 K and a concentration range of 0-8 mol/kg. The computed data and existing experimental results are used to fit engineering equations. The obtained data and engineering equations can be used for process modelling and optimizing electrolyzers and fuel cells.

6

Thermodynamic and Transport properties of Hydrogen in aqueous $NaB(OH)_4$ solutions

This chapter is based on the following publication: P. Habibi, J. R. T. Postma, J. T. Padding, P. Dey, T. J. H. Vlugt, and O. A. Moultos. "Thermodynamic and Transport Properties of $H_2/H_2O/NaB(OH)_4$ Mixtures Using the Delft Force Field (DFF/$B(OH)_4^-$)". *Industrial and Engineering Chemistry Research* 62 (2023), 11992–12005.

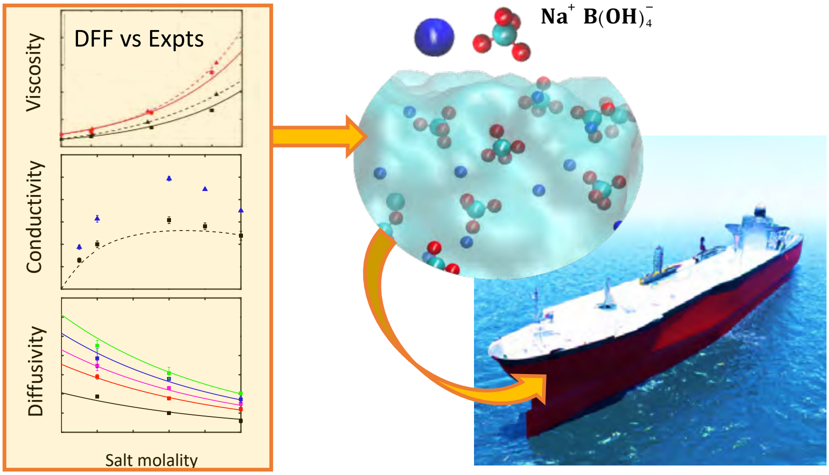

6.1. Introduction

Aqueous borate ions are of relevance to a wide array of industrial applications ranging from nuclear electric power to flame retardants [355–360]. The potential use of $NaBH_4$ for H_2 storage in applications such as maritime shipping, due to its high gravimetric capacity of 10.7 wt%, [120–122, 361–368] has increased the interest for aqueous borate ion chemistry. The hydrolysis reaction of $NaBH_4$ produces H_2 and sodium metaborate ($NaBO_2$) according to [369, 370]:

$$\mathrm{NaBH_4 + 2\,H_2O \longrightarrow NaBO_2 + 4\,H_2} \tag{R1}$$

Sodium metaborate dissolves in water forming aqueous $NaB(OH)_4$ [370–372]:

$$\mathrm{NaBO_2 + 2\,H_2O \longrightarrow Na^+(aq) + B(OH)_4{}^-(aq)} \tag{R2}$$

Other hydroxyl-hydrate borates such as $B(OH)_3$ and $B_3O_3(OH)_4{}^-$ can also be present in the aqueous phase [370, 371, 373, 374], however, previous experimental and theoretical studies of aqueous $NaBO_2$ solutions suggest that more than 95% of borate ions in water are in the form of $B(OH)_4^-$ [371, 373]. Aqueous $B(OH)_4^-$ ions are also formed when boric acid (H_3BO_3), which acts as a Lewis acid, dissolves in water [375–377]. The dissolution of borates in water is discussed in detail in Refs. [373–375, 378]. In this chapter, only hydroxyl-hydrate borate ions of $B(OH)_4^-$ are considered.

The solubility limit of $NaBO_2$ at 298 K is 4.25 mol $NaBO_2$/kg water [379–381], which corresponds to a solubility of 5.02 mol $NaB(OH)_4$/kg water. At the solubility limit (at 298 K), the viscosity of the aqueous $NaB(OH)_4$ solution is ca. 6 times higher than that of pure water [372]. The presence of $NaB(OH)_4$ has a significant influence on the thermophysical properties (e.g., ionic conductivities, viscosities, and densities) of the solution [372] and influences the reaction rates of $NaBH_4$ hydrolysis [382–384]. Uncontrolled crystallization of $NaB(OH)_4$ is one of the major concerns in $NaBH_4$ hydrolysis reactors [380, 385, 386]. Detailed knowledge of the thermophysical properties of aqueous $NaB(OH)_4$ will help in modelling the crystallization rates and the design of $NaBH_4$ hydrolysis reactors.

The densities, viscosities, and ionic conductivities of aqueous $NaB(OH)_4$ solutions (0-5 mol $NaB(OH)_4$/kg water) at 298 K and 323 K have been measured experimentally by Zhou *et al.* [372]. To the best of our knowledge, thermophysical properties of aqueous $NaB(OH)_4$ solutions at temperatures higher than 323 K are not available, despite being relevant for $NaBH_4$ hydrolysis reactors, which usually operate at 298-363 K [387–389]. Data on the solubilities of H_2 and the self-diffusivities of H_2, Na^+, and $B(OH)_4^-$ in $NaB(OH)_4$ solutions are also not available, even though H_2 mass transfer [382] and $NaB(OH)_4$ crystallization [380, 385, 386] are crucial for optimizing the performance of $NaBH_4$ hydrolysis reactors. MD and MC simulations, provide a complementary approach to experiments for investigating thermophysical properties that are difficult to measure experimentally [47, 48, 109, 390, 391] (i.e., self-diffusivities of ions and H_2) at elevated temperatures (ca. 353 K) and salt molalities (ca. 5 mol $NaB(OH)_4$/kg water). MD or MC simulations of aqueous $NaB(OH)_4$ require force fields that are either based on ab-initio calculations or parameterized based on existing experiments [49, 50]. Zhou *et al.* [371] have used ab-initio simulations and empirical potential structure refinement (EPSR) to investigate the structure and hydration of aqueous $NaB(OH)_4$. The EPSR potential of Zhou *et al.* [371] can accurately model RDFs and the hydration numbers of the ions, however, it is not parameterized for viscosities and ionic conductivities of the solution. In fact, despite the significant influence of the $NaB(OH)_4$ concentration on the transport properties of the solution [372], no attempts have been made to develop a classical $B(OH)_4^-$ force field that can describe and predict the densities, viscosities, and ionic conductivities of $NaB(OH)_4$ solutions.

We propose a new classical force field for $B(OH)_4^-$ (the so-called Delft Force Field for $B(OH)_4^-$, which is going to be referred to hereafter as DFF/$B(OH)_4^-$), which combined with the TIP4P/2005 water model [100] and the Madrid-2019 Na^+ model [103] can accurately model densities and viscosities of $NaB(OH)_4$ solutions with a maximum deviation of 2.5% from experimental results up to the solubility limit at 298 K. $B(OH)_4^-$ is modelled as a tetrahedral structure with a scaled charge of -0.85. The OH group in $B(OH)_4^-$ is modelled as a single interaction site. DFF/$B(OH)_4^-$ is an addition to the Delft Force Field family (see DFF/OH^- [47]). The computed ionic conductivities of aqueous $NaB(OH)_4$ solutions using DFF/$B(OH)_4^-$ at 298 K and 323 K are within 10% of available experimental data. The densities, viscosities, and self-diffusivities of H_2, Na^+, and $B(OH)_4^-$ in aqueous $NaB(OH)_4$ solutions at 298-353 K and 0-5 mol $NaB(OH)_4$/kg water are computed using MD simulations. The solubilities of H_2 and activities of water in aqueous $NaB(OH)_4$ solution for the same temperature and concentration range are computed using CFCMC [248–250] simulations. To allow for simple extraction of the computed properties, engineering equations are developed by us [47, 48]. All the computed viscosities, self-diffusivities for H_2, Na^+, and $B(OH)_4^-$, and the solubilities of H_2 are fitted to empirical equations, which can be used to model $NaBH_4$ hydrolysis reactors.

This chapter is organized as follows: In section 6.2, the force fields used for H_2O, Na^+, and H_2 are presented, and the details for the MD and CFCMC simulations [248–250] are explained. In section 6.3.1, a force field for $B(OH)_4^-$ is developed based on experimental densities, viscosities, and RDFs of aqueous $NaB(OH)_4$ at 298 K and 1 bar. The computed densities and viscosities for a temperature range of 298-353 K are discussed in section 6.3.2. The ionic conductivities and the self-diffusivities of ions are reported in section 6.3.3. The self-diffusivities of H_2, solubilities of H_2, and activities of water in aqueous $NaB(OH)_4$ solutions are discussed in sections 6.3.4 and 6.3.5. Our conclusions are outlined in section 6.4.

6.2. Methodology

6.2.1. Force fields

H_2O is modelled using the four-site rigid TIP4P/2005 [100] force field. For Na^+ ions, the Madrid-2019 [103] and Madrid-Transport [111] force fields are used. The three-site Marx [91] model is used for computing the H_2 solubilities and self-diffusion coefficients. A cutoff radius of 10 Å is used for LJ and the real space contribution of electrostatic interactions. Analytic tail corrections for the LJ interactions are applied for computing energies and pressures. The $B(OH)_4{}^-$ force field is developed in this chapter and is discussed in section 6.3.1. All force field parameters for H_2O, Na^+, and H_2 are listed in Appendix A.2. All molecules are considered rigid. The Lorentz-Berthelot mixing rules [49, 50] are used, with the exception of $[\mathrm{Na}^+/\mathrm{B(OH)_4}^- - \mathrm{H_2O}]$ LJ interactions as specified in Table 6.1 and in Table A.3.

6.2.2. MD simulations

MD simulations are carried out using LAMMPS (version August, 2018) [59] and the same methodology used in Section 4.2.4 is used to perform MD simulations and compute transport properties. The OCTP plugin [53] is used to compute RDFs, self-diffusion coefficients of all species (i.e., H_2O, Na^+, $B(OH)_4{}^-$, and H_2), Onsager coefficients [392], and the viscosities of the solutions using Einstein relations. For all details of the OCTP plugin the reader is referred to Ref. [53]. For each state point (temperature, pressure, and salt molality), the volume of the simulation box is obtained using a 5 ns equilibration run (NPT ensemble) and a consequent 5 ns production run (NPT ensemble), in which the average volume is computed. The averaged volume computed in NPT simulations is used in subsequent NVT simulations to compute transport properties and RDFs. In the NVT ensemble, an equilibration run of 1 ns, and a production run of 20-50 ns is used. All self-diffusivities shown here are corrected for finite size effects using the Yeh-Hummer equation [265–267, 343]. The ionic conductivities (κ) in this chapter are computed using the Einstein-Helfand relation [393]:

$$\kappa = \frac{e^2 N}{V k_\mathrm{B} T} \sum_{i,j} z_i z_j \Lambda_{ij} \tag{6.1}$$

where e is the elementary charge, N is the total number of molecules, V is the volume of the simulation box, k_B is the Boltzmann factor, and T is the absolute temperature. z_i and z_j are the charges of ions of type i and j, respectively. It is important to note that z_i represents the ionic charge of the component, e.g., for Na^+ it would be 1. This means that if scaled charges are used in the force field, z_i remains unaffected. Λ_{ij} is the Onsager coefficient between ions of type i and j [295, 394, 395], which is defined here as [392]:

$$\Lambda_{ij} = \frac{1}{N} \lim_{t\to\infty} \frac{1}{6t} \left\langle \left(\sum_{k=1}^{N_i} \sum_{l=1}^{N_j} [\mathbf{r}_{k,i}(t) - \mathbf{r}_{k,i}(0)] \cdot [\mathbf{r}_{l,j}(t) - \mathbf{r}_{l,j}(0)] \right) \right\rangle \tag{6.2}$$

where t is time, N_i is the number of ions of type i, N_j is the number of ions of type j, and $\mathbf{r}_{k,i}(t)$ is the position vector of the $k-$th ion of type i at time t. The exact ionic conductivities including ion-ion correlations, are computed using Eq. 6.1. For dilute electrolyte solutions, the ionic conductivities can be approximated using the Nernst-Einstein (NE) equation (κ_{NE}), which neglects ion-ion correlations [396]:

$$\kappa_{\text{NE}} = \frac{e^2}{V k_{\text{B}} T} \sum_i N_i z_i^2 D_i \tag{6.3}$$

where D_i is the self-diffusivity of ion i.

MD simulations are carried out in systems consisting of 1000 H_2O molecules and 0 – 90 Na^+ and $B(OH)_4{}^-$ ions, depending on the molality. 2 H_2 molecules are added to these systems to compute self-diffusivities of H_2 in aqueous $NaB(OH)_4$ solutions. The exact number of species used for every state point is provided in Table S4 of the Supporting Information of Ref. [354]. The simulations are carried out at 298 K, 323 K, 343 K, and 353 K and 1 bar. For each temperature and molality, 5 independent simulations are carried out each starting with a different set of initial velocities. Based on these 5 independent simulations a mean and a standard deviation for densities, viscosities, self-diffusivities, and ionic conductivities are obtained. All initial configurations are created using the PACKMOL software (v20.3.1) [259]. All the raw data for densities, viscosities, and self-diffusivities of H_2, Na^+, and $B(OH)_4^-$ in aqueous $NaB(OH)_4$ solutions are listed in Table S6 of the Supporting Information of Ref. [354]. The DelftBlue supercomputer [397] is used for performing MD simulations.

6.2.3. CFCMC simulations

The solubilities in this chapter are calculated using the same approach described in Section 4.2.5, with the exception that 5×10^5 equilibration cycles are carried out followed by 1.5×10^6 production cycles. The activity coefficient of H_2O (γ_m) at a molality m of $NaB(OH)_4$ is computed using the excess chemical potential of pure H_2O ($\mu^{\text{ex}}_{\text{H}_2\text{O},0}$) and in solution ($\mu^{\text{ex}}_{\text{H}_2\text{O},m}$) according to [398]:

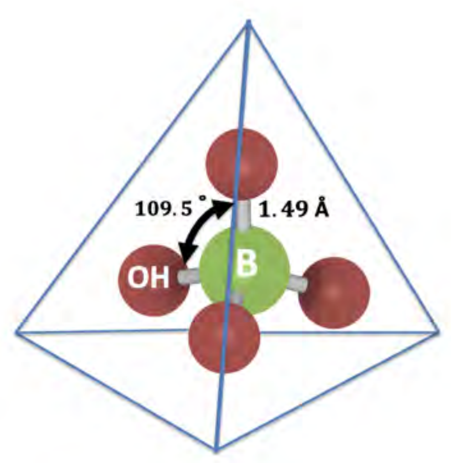

Figure 6.1. B(OH)$_4^-$ is modelled as a rigid tetrahedral structure (OH–B–OH angle of 109.5 degrees) with a single interaction site for OH. The B–(OH) bond length in this model equals 1.49 Å, which is the computed bond length between B–O reported in a prior Density Functional Theory study of aqueous NaB(OH)$_4$ by Zhou *et al.* [371]. iRASPA is used for this visualization [37].

$$\gamma_m = \frac{\langle \rho_\mathrm{w} \rangle}{x_\mathrm{w} \langle \rho_{\mathrm{w},0} \rangle} \exp\left[\frac{\mu^\mathrm{ex}_{\mathrm{H_2O},m} - \mu^\mathrm{ex}_{\mathrm{H_2O},0}}{k_\mathrm{B} T}\right] \tag{6.4}$$

where $\langle \rho_\mathrm{w} \rangle$ and $\langle \rho_{\mathrm{w},0} \rangle$ are the number density of H_2O molecules in a solution with a molality m NaB(OH)$_4$ and in the pure H_2O solution, respectively. x_w is the mole fraction of H_2O in the aqueous solution. $\mu^\mathrm{ex}_{\mathrm{H_2O},m}$ and $\mu^\mathrm{ex}_{\mathrm{H_2O},0}$ are the excess chemical potentials of H_2O in a solution with a molality m NaB(OH)$_4$ and in the pure H_2O solution, respectively. The activity of water (a_w) can be computed by multiplying the activity coefficient and mole fraction of water, i.e., $a_\mathrm{w} = \gamma_m \times x_\mathrm{w}$. To compute $[\mu^\mathrm{ex}_{\mathrm{H_2O},m} - \mu^\mathrm{ex}_{\mathrm{H_2O},0}]$ accurately, long simulations are required [106]. For each state point (concentration, temperature, pressure), 100 independent simulations are performed. The final Boltzmann probability distributions of λ are averaged in blocks of 20 simulations to obtain 5 independent averaged distributions. For all averaged distributions, the excess chemical potentials, activities of H_2O, and solubilities of H_2 are calculated to obtain a mean value and the standard deviation of the 5 independent blocks. All the raw data for excess chemical potentials of H_2 and H_2O, the solubilities of H_2, and the activities of H_2O in aqueous NaB(OH)$_4$ solutions are listed in Table S7 of the Supporting Information of Ref. [354].

6.3. Results and discussion

6.3.1. $B(OH)_4^-$ force field development

To compute the diffusivities of H_2 and ions (Na^+, $B(OH)_4^-$) in aqueous $NaB(OH)_4$ solutions, a force field for $B(OH)_4{}^-$ is required, which can accurately model the densities and viscosities of the solution. To the best of our knowledge, no $B(OH)_4^-$ force field is available for this purpose. In this chapter, the OH group of $B(OH)_4^-$ is modelled using a single interaction site (i.e., H is modelled implicitly, contrary to the DFF/OH^- model in which O and H are two distinct sites [47]). $B(OH)_4^-$ is a tetrahedral structure with B in the center (OH–B–OH angle of 109.5 degrees), as shown in Figure 6.1. The bond length between B and OH is set to 1.49 Å, which equals the bond length between B and O reported in a prior Density Functional Theory study of aqueous $NaB(OH)_4$ [371].

This $B(OH)_4^-$ force field is parameterized based on the TIP4P/2005 water model [100]. There are two distinct interaction sites in $B(OH)_4^-$ (i.e, $(\mathrm{OH})^{\delta-}$ and $\mathrm{B}^{\delta+}$) and the total charge is equal to $q_{\mathrm{B(OH)_4}} = q_{\mathrm{B}} + 4 \times q_{\mathrm{(OH)}}$. The total charge of $B(OH)_4^-$ matches the charge of Na^+ such that $q_{\mathrm{B(OH)_4}} + q_{\mathrm{Na}} = 0$. The B atom in $B(OH)_4$ is not a LJ site as it is surrounded by four OH groups. Two different Na^+ models are considered, i.e., the Madrid-2019 [103] ($q_{\mathrm{Na}} = 0.85$) and the Madrid-Transport ($q_{\mathrm{Na}} = 0.75$). For each Na^+ model, ca. 900 different $B(OH)_4^-$ models are created with varying LJ parameters for the OH group and charge distributions (i.e., different values of q_{B} and q_{OH}). As shown in Figure S1 of the Supporting Information of Ref. [354], for all these models the deviation of computed density versus the experimental density is evaluated at 5 mol $NaB(OH)_4$/kg water at 298 K and 1 bar. Based on these simulations, four different versions of the $B(OH)_4^-$ force field are probed (e.g., V1-V4) and listed in Table 6.1, which accurately model experimental densities with a maximum deviation of 2.5%. Different charge distributions (i.e., $q_{\mathrm{(OH)}}$ and q_{B}) are used for the V1-V4 models. These different charge distributions are probed to investigate which $B(OH)_4^-$ model can accurately model both the densities and viscosities of aqueous $NaB(OH)_4$ solutions. V1, V2, and V4 have a total charge of -0.85 and are based on the Madrid-2019 Na^+ model [103]. V3 has a total charge of -0.75 and is combined with the Madrid-Transport Na^+ model [111]. Details of the four different versions of the $B(OH)_4^-$ model during the force field development phase are listed in Table 6.1.

Figure 6.2 shows the computed densities and viscosities as functions of the $NaB(OH)_4$ molality for the V1-V4 models at 298 K and 1 bar. The experimental data of Zhou *et al.* [372] at the same conditions are also shown in Figure 6.2 as dashed lines. Based on Table 6.1, it can be observed that $B(OH)_4^-$ models with larger absolute values of q_{OH} and q_{B} (comparison between V1, V2, and V4) require larger values of $\sigma_{\mathrm{(OH)(OH)}}$ and $\sigma_{\mathrm{(OH)(Ow)}}$ to reach similar densities as shown in Figure 6.2(a). Despite the accurate density predictions of all models, the viscosities of the V1-V4

Table 6.1. Force field parameters for $B(OH)_4{}^-$. OH is modelled as a single site with a charge of q_{OH}. The B atom has a charge of q_B and is not a LJ site as it is surrounded by four OH. $q_{B(OH)_4}$ is the total charge of $B(OH)_4^-$ and is based on the scaled charges used in Madrid-2019 (0.85) [103] and Madrid-Transport (0.75) [111]. $\epsilon_{(OH)(OH)}$ is the LJ energy parameter for OH—OH interactions and is equal to $\epsilon_{(OH)(OH)}/k_B = 50.32$ K. $\sigma_{(OH)(OH)}$ and $\sigma_{(OH)Ow}$ are the LJ size parameters for OH—OH and OH—O_W (O of water) interactions. For all other LJ interactions with $B(OH)_4^-$ the Lorentz-Berthelot mixing rules [49, 50] are used. The V4 model is recommended as it leads to the best agreement with experimental densities and viscosities of aqueous $NaB(OH)_4$ solutions compared to the V1-V3 models. The parameters of the new DFF/$B(OH)_4^-$ model are the ones of V_4.

Model	q_{OH} / [e]	q_B / [e]	$q_{B(OH)_4}$ / [e]	$\sigma_{(OH)(OH)}$/[Å]	$\sigma_{(OH)(Ow)}$/[Å]
V1	-0.65	1.75	-0.85	2.75	2.91
V2	-0.75	2.15	-0.85	2.85	2.96
V3	-0.85	2.65	-0.75	2.95	3.01
V4	-0.85	2.55	-0.85	2.95	3.01

models differ by more than 50 %. As shown in Figure 6.2(b), reducing the absolute value of the charge on $(OH)^-$ ($q_{(OH)}$) (comparison between V1, V2, and V4) and/or the total charge on $B(OH)_4^-$ ($q_{B(OH)_4}$) (comparison between V3 and V4) leads to lower viscosities.

Overall, the V4 model with a charge scaling of 0.85 leads to optimal agreement with experimentally measured viscosities at 298 K (within 2 % deviation). Zeron *et al.* [103] have also shown that by applying a charge scaling of 0.85 the viscosities of Na_2SO_4 and K_2SO_4 can be computed accurately (less than 1% deviation from experiments). The recent works by Blazquez *et al.* [111] and Habibi *et al.* [47] have shown that the 0.75 charge scaling is optimal for computing the viscosities of aqueous NaCl, KCl, NaOH, and KOH solutions. This indicates that there is a different optimal charge scaling for computing viscosities of electrolyte solutions, depending on the system. Since the V4 model has the best agreement with experimental densities and viscosities, the final parameters of the DFF/$B(OH)_4^-$ model are the ones of V4 (see Table 6.1).

The RDFs ($g(r)$) for B (B of $B(OH)_4^-$)—O_W (O of water), B—B, Na^+—O_W, and Na^+—Na^+ are shown in Figure 6.3. The first RDF peak for B—O_W is at ca. 3.80 Å (Figure 6.3(a)). For Na^+—O_W, a first peak at 2.31 Å is found (Figure 6.3(b)). These results agree with the atomistic simulations of aqueous $NaB(OH)_4$ of Zhou *et al.* [371]. The authors indicated a first peak of 3.72 Å and 2.34 Å for B—O_W and Na^+—O_W, respectively. The first hydration number (n_{hyd}) of B and Na^+ can be computed using Eq. 5.1. The computed hydration numbers of B and Na^+ at 5 mol $NaB(OH)_4$ are 10.9 and 5.6, respectively. Zhou *et al.* [371] report hydration numbers

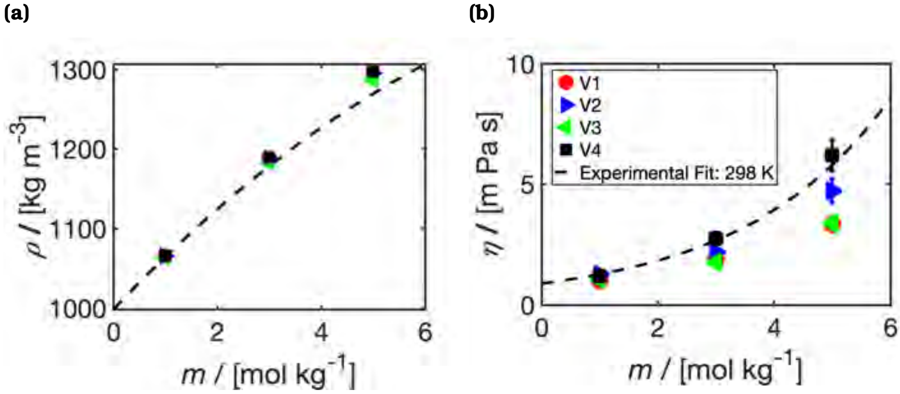

Figure 6.2. Computed (a) densities (ρ) and (b) viscosities (η) as functions of $NaB(OH)_4$ molality (m) at 298 K and 1 bar. The V1-V4 models (details in Table 6.1) are combined with the TIP4P/2005 water model [100], and the Madrid-2019 [103] and the Madrid-Transport [111] Na^+ model. The experimental correlation for densities and viscosities of Zhou *et al.* [372] are shown as dashed lines.

in the ranges from 12.9-15.6 and 3.7-5.4 for B and Na^+, respectively. A prior diffraction study of aqueous $NaB(OH)_4$ solutions by Zhou *et al.* [399] reports hydration numbers in the ranges from 6-12 and 5.8-6.0 for B and Na^+, respectively. In general, the location of the computed first peaks for RDFs of $B{-}O_W$ and $Na^+{-}O_W$ are in excellent agreement with previous works in literature [371, 399], while a reasonable agreement is found for the hydration numbers of B and Na^+ [371, 399]. These results for the structure of aqueous $NaB(OH)_4$ indicate that the hydrodynamic radius of the $B(OH)_4^-$ and Na^+ are modelled reasonably and that no crystallization occurred during the MD simulations.

From this section onwards, the DFF/$B(OH)_4^-$ model is used to compute densities, transport properties (e.g., viscosities, ionic conductivities), solubilities of H_2, and activities of water in aqueous $NaB(OH)_4$ solutions. The $B(OH)_4^-$ model developed in this chapter may also be used to study other systems such as aqueous $KB(OH)_4$ or $LiB(OH)_4$ systems, as K^+ and Li^+ force fields have been developed in Madrid-2019 [103]. Studying the performance of the $B(OH)_4^-$ force field for different cations is beyond the scope of this chapter.

6.3.2. Temperature dependence of viscosities and densities

Figure 6.4 shows the temperature dependence of computed densities and viscosities of aqueous $NaB(OH)_4$ solutions at different molalities

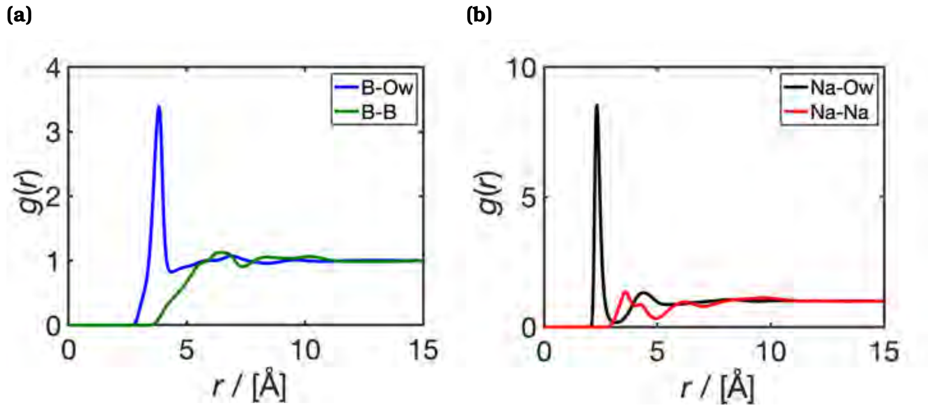

Figure 6.3. Radial distribution functions ($g(r)$) for (a) B(B(OH)$_4{}^-$)—O$_W$ (O of water) and B(B(OH)$_4{}^-$)—B(B(OH)$_4{}^-$), and (b) Na$^+$—O$_W$ and Na$^+$—Na$^+$, as a function of radial distance r (Å), at 298 K, 1 bar, and a concentration of 5 mol NaB(OH)$_4$/kg water. The DFF/B(OH)$_4^-$ model is used and combined with the TIP4P/2005 [100] water and Madrid-2019 [103] Na$^+$ force fields.

of NaB(OH)$_4$. The densities and viscosities shown in Figure 6.4 are computed from MD simulations using the DFF/B(OH)$_4^-$ model of B(OH)$_4^-$, the TIP4P/2005 water model [100], and the Madrid-2019 Na$^+$ model [103]. The experimental data of Zhou *et al.* [372] at 298 K and 323 K are also plotted in Figure 6.4. As shown in Figure 6.4(a), the computed densities in this chapter are in excellent agreement (within 2.5% deviation) with the experimental results of Zhou *et al.* [372] for both temperatures. The viscosities computed in this chapter at 298, 323, 333, 343, and 353 K are fitted to an empirical correlation of the form:

$$\eta = \eta_0 \exp\left[A_1 m + \frac{A_2}{T}\right] \tag{6.5}$$

where η_0, A_1, and A_2 are fitting constants. The values of these fitting constants are listed in Table 6.2. The results of this empirical correlation are shown as solid lines in Figures 6.4(b) and 6.4(c). The viscosity of pure water as a function of temperature is reproduced using Eq. 6.5 with a maximum deviation of 10% for a temperature range of 298-353 K as shown in Figure S2 of the Supporting Information of Ref. [354].

As shown in Figure 6.4 (b), the computed viscosities at 323 K agree with the results of Zhou *et al.* [372]. The viscosities deviate by 2% up to a molality of 3 mol NaB(OH)$_4$/kg water, and by ca. 10% at a molality of 5 mol NaB(OH)$_4$/kg water at 323 K. Overall, it can be concluded that the MD simulations can accurately model both the densities and viscosities at 323 K even though the B(OH)$_4^-$ force field is only fitted to data at 298 K.

Table 6.2. Parameters of Eq. 6.5 for the computed viscosities of aqueous $NaB(OH)_4$ solutions. The viscosities are computed from MD simulations using the DFF/$B(OH)_4^-$ model combined with the TIP4P/2005 [100] water and Madrid-2019 [103] Na^+ force fields. These parameters are valid at a concentration range of 0-5 mol $NaB(OH)_4{}^-$/kg water at 298-353 K.

η_0 / [mPa s]	1.018×10^{-3}
A_1 / $[(\mathrm{mol_{NaB(OH)_4}/kg_{H_2O}})^{-1}]$	3.379×10^{-1}
A_2 / [K]	2.030×10^{3}

In Figure 6.4(c), an exponential increase in the viscosities is observed as a function of the reciprocal temperature ($\eta \propto \exp[A_2/T]$). This behavior has also been observed in other experimental and simulation studies of aqueous electrolyte solutions (e.g., NaCl, NaOH) [47, 48, 320, 321].

6.3.3. Ionic conductivities and self-diffusivities of ions

The computed ionic conductivities of aqueous $NaB(OH)_4$ solutions are shown in Figures 6.5(a) and (b). The finite size corrected [265, 270, 343] self-diffusivities of Na^+ and $B(OH)_4^-$ in aqueous $NaB(OH)_4$ solutions are shown in Figures 6.5(c) and (d), respectively. The computed finite size corrected self-diffusivities (D_s) of Na^+ and $B(OH)_4^-$ are fitted to an empirical function with a functional form of

$$D_s = D_{s,0} \exp\left[-B_1 m - \frac{B_2}{T}\right] \tag{6.6}$$

where $D_{s,0}$, B_1, and B_2 are fitting constants. m is the molality of $NaB(OH)_4$ in units of mol $NaB(OH)_4$/kg water and T is in units of K. The values of these fitting constants for Na^+ and $B(OH)_4^-$ are listed in Table 6.3. The results of the fitting equation are shown in Figures 6.5(c)-(d) as solid lines. The experimentally measured infinite dilution diffusion coefficients at 298 K for Na^+ and $B(OH)_4^-$ are 1.33×10^{-9} m^2/s and 0.96×10^{-9} m^2/s, respectively [103, 371]. The infinite dilution self-diffusivities at 298 K obtained in this chapter by fitting the computed self-diffusivities ($D_{s,0}$) for Na^+ and $B(OH)_4^-$ are 1.2×10^{-9} m^2/s and 0.94×10^{-9} m^2/s, respectively. These values are in excellent agreement with the experimentally measured infinite dilution diffusion coefficients for Na^+ and $B(OH)_4^-$ in water [103, 371].

In Figure 6.5(a), the ionic conductivities at 298 K computed using the Nernst-Einstein approximation (Eq. 6.3) and the exact expression (Eq. 6.1) are compared to the experimental results of Zhou *et al.* [372]. Consistent with what is found for other aqueous electrolyte solutions [393, 396], the NE equation overestimates ionic conductivities with respect to the exact expression (Eq. 6.1). The ion-ion correlations, which are ignored

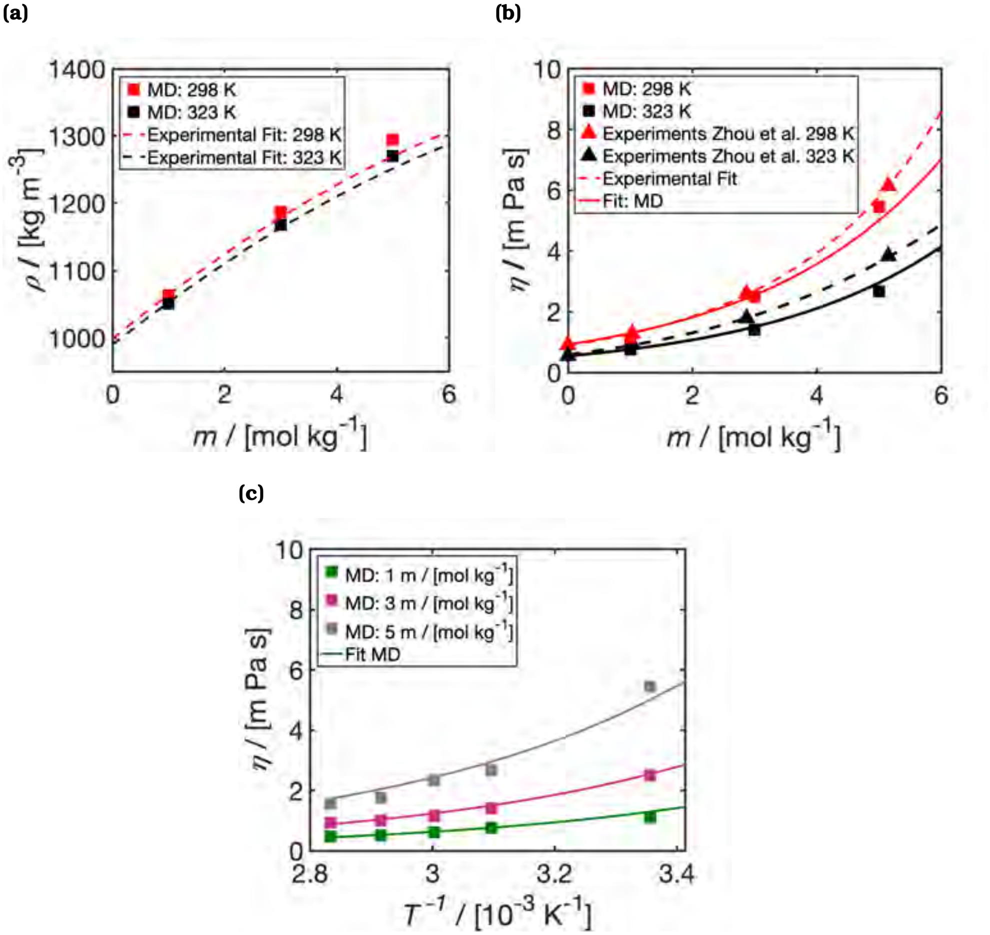

Figure 6.4. Computed (a) densities (ρ) and (b) viscosities (η) as functions of molality m in units of mol NaB(OH)$_4$/kg water at 298 K and 323 K at 1 bar. In (c), η is shown as a function of the reciprocal temperature (T^{-1}) at 1 m, 3 m, and 5 m at 1 bar. The experimental densities and viscosities of Zhou *et al.* [372] at 298 K and 323 K are shown in (a) and (b). The dashed lines are the experimental fits for densities and viscosities based on the results of Zhou *et al.* [372] The solid lines represent Eq. 6.5 based on the parameters shown in Table 6.2. The densities and viscosities are computed from MD simulations using the DFF/B(OH)$_4^-$ model combined with the TIP4P/2005 [100] water and Madrid-2019 [103] Na$^+$ force fields.

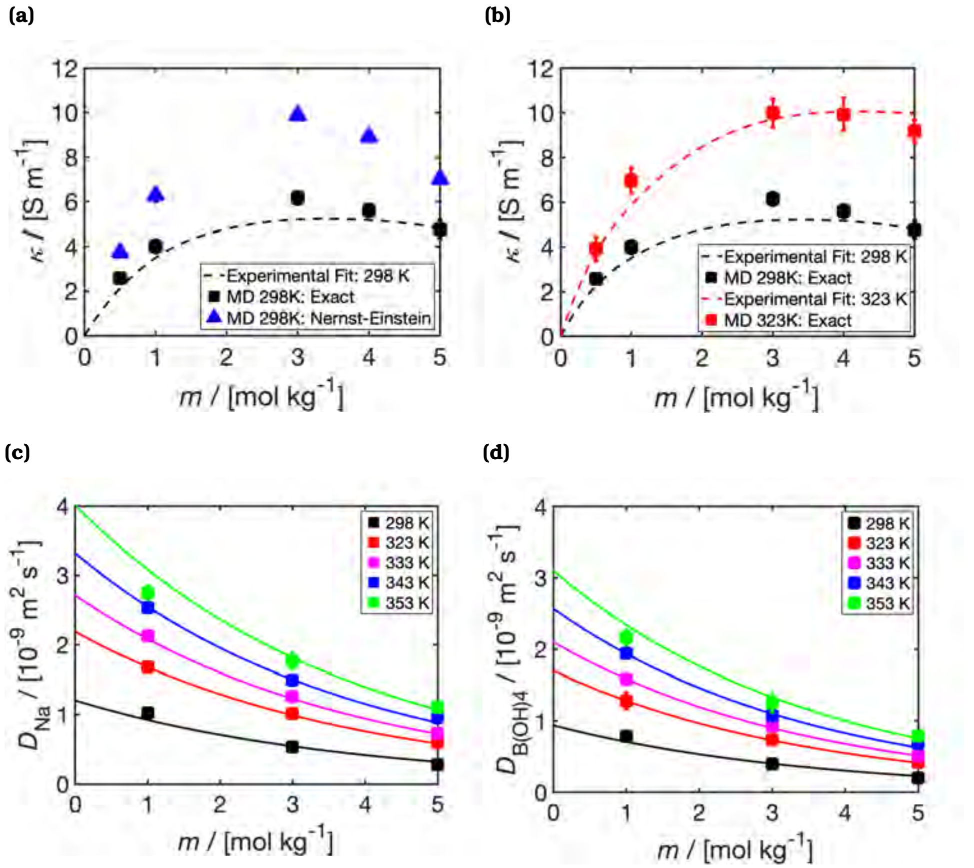

Figure 6.5. Computed ionic conductivities of aqueous NaB(OH)$_4$ as functions of NaB(OH)$_4$ molality (m) are shown in (a) and (b). In (a) the ionic conductivities computed using the exact (Eq. 6.1) and the Nernst-Einstein (Eq. 6.3) equation at 298 K and 1 bar are shown. In (b), the computed exact ionic conductivities are shown at 298 K and 323 K. The experimental fit of Zhou *et al.* [372] for ionic conductivities at 298 K and 323 K are shown in (a) and (b) as dashed lines. The computed finite size corrected self-diffusivities of (c) Na$^+$ (D_{Na}) and (d) B(OH)$_4^-$ ($D_{\mathrm{B(OH)_4}}$) are shown as functions of m at 1 bar and different temperatures (298-353 K). The solid lines represent Eq. 6.6 with the fitting parameters listed in Table 6.3. The DFF/B(OH)$_4^-$ model is used and combined with the TIP4P/2005 [100] water and Madrid-2019 [103] Na$^+$ force fields.

Table 6.3. Parameters of Eq. 6.6 for the computed finite size corrected self-diffusivities of Na^+ and $B(OH)_4^-$ in aqueous $NaB(OH)_4$ solutions.The finite size corrected self-diffusivities are computed from MD simulations using the DFF/$B(OH)_4^-$ model combined with the TIP4P/2005 [100] water and Madrid-2019 [103] Na^+ force fields. These parameters are valid at a concentration range of 0-5 mol $NaB(OH)_4{}^-$/kg water at 298-353 K.

	$B(OH)_4^-$	Na^+
$D_{s,0}$ / [m^2/s]	1.998×10^{-6}	2.736×10^{-6}
B_1 / $[(\mathrm{mol}_{NaB(OH)_4}/\mathrm{kg}_{H_2O})^{-1}]$	2.820×10^{-1}	2.642×10^{-1}
B_2 / [K]	2.283×10^3	2.303×10^3

in the Nernst-Einstein approximation and accounted for in the exact expression, lower the ionic conductivities, and play an important role in accurate predictions of ionic conductivities [396]. This is also observed in literature for other systems such as aqueous NaCl [393, 396]. At the limit of low $NaB(OH)_4$ molalities ($m \rightarrow 0$), the NE expression and the exact expression (Eq. 6.1) are identical by definition. As shown in Figure S3 of the Supporting Information of Ref. [354], this is not the case for exact expression (Eq. 6.1) and the NE expression with Yeh-Hummer corrected [265, 343] ionic diffusivities. At the limit of low $NaB(OH)_4$ molalities ($m \rightarrow 0$), the exact expression (Eq. 6.1) is expected to have the same finite size effects as the NE expression without the Yeh-Hummer corrected diffusivities. As shown in Figure S3 of the Supporting Information of Ref. [354] and briefly discussed in its caption, the finite size effects of the exact ionic conductivities are within the error bars of the values computed with MD simulations (ca. 10%). Thus, no definite conclusion regarding the precise magnitude of these effects can be made here. Also, the derivation of an analytic expression for correcting the finite size effects of ionic conductivities computed using (Eq. 6.1) is beyond the scope of this chapter.

In Figure 6.5(b), the exact ionic conductivities at 298 K and 323 K are compared to the experimental results of Zhou *et al.* [372]. The computed ionic conductivities initially increase as a function of salt molality and then decline at higher concentrations. The initial increase in ionic conductivities is due to the increase in the number of charge carriers, while the subsequent decline is attributed to the increase in the viscosity (and decrease in ion diffusivities) at higher salt molalities [393]. The decrease in the self-diffusivities of Na^+ and $B(OH)_4^-$ as a function of salt molality can be observed in Figures 6.5(c) and 6.5(d), respectively. Overall, the infinite dilution diffusivities of the ions and the ionic conductivities (and their temperature variations) are accurately modelled by the newly fitted DFF/$B(OH)_4^-$ force field developed here, despite the force field being trained only on density, viscosity, and RDF data.

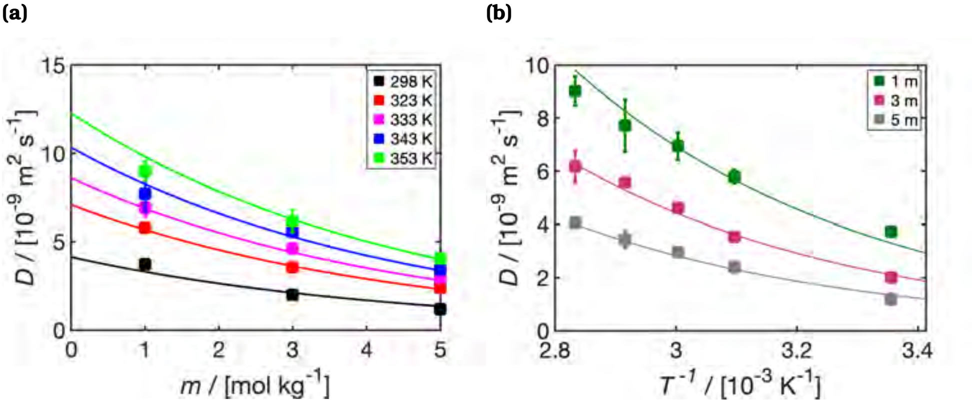

Figure 6.6. Self-diffusivities (D) of H_2 as a function of (a) $NaB(OH)_4$ molality (m in mol $NaB(OH)_4$/kg water) and (b) reciprocal of temperature (T^{-1} in K^{-1}). The DFF/$B(OH)_4^-$ model is used and combined with the TIP4P/2005 [100] water, Madrid-2019 [103] Na^+, and the Marx [91] H_2 force fields. All self-diffusivities are corrected for finite size effects using the Yeh-Hummer equation [265, 343].

6.3.4. Self-diffusivities of H_2

The computed self-diffusivities of H_2 (D_{H_2}) in aqueous $NaB(OH)_4$ solutions are shown in Figure 6.6. To the best of our knowledge, no experimental data are available for diffusivities of H_2 in aqueous $NaB(OH)_4$ solutions. Therefore, our simulations are the first predictions of this property. Similar to the self-diffusivities of Na^+ and $B(OH)_4^-$, the self-diffusivities of H_2 are fitted to Eq. 6.6. The fitting constants of Eq. 6.6 for the self-diffusivities of H_2 are listed in Table 6.4. This empirical correlation has also been used to model the self-diffusivities of H_2 in aqueous NaCl solutions [48] for a wide range of temperatures (298-523 K) and concentrations (0-6 mol NaCl/kg water). In Figure 6.6(a), an exponential decay of the self-diffusivities of H_2 as a function of $NaB(OH)_4$ molalities is observed. This is consistent with the increase of viscosities as a function of $NaB(OH)_4$ molalities as the self-diffusivities of gasses and viscosities of the solution are inversely related [47, 48]. As shown in Figure 6.6(b), the self-diffusivities of H_2 have an Arrhenius relation with respect to the temperature ($D_{H_2} \propto \exp[-A/T]$). These findings are consistent with other simulations and experiments for gas diffusion in aqueous solutions [47, 48].

6.3.5. Solubilities of H_2 and activities of water

Figure 6.7 shows the computed solubilities of H_2 and activities of water in aqueous $NaB(OH)_4$ solutions at 1 bar. The ratio between the solubility of H_2 (expressed as a mole fraction) in the aqueous solution over the

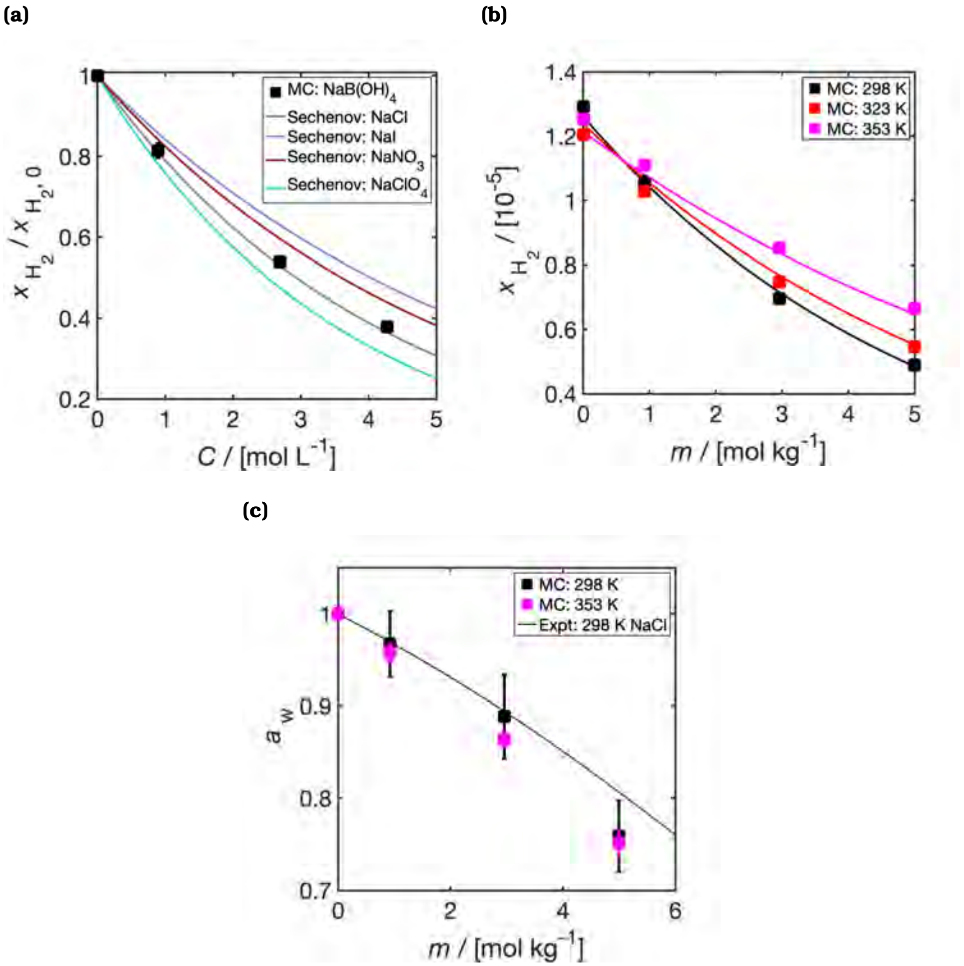

Figure 6.7. Computed (a)-(b) solubilities of H_2 and (c) activities of water (a_w) in aqueous NaB(OH)$_4$ solutions at a H_2 partial pressure of 1 bar. In (a), the mole fractions of H_2 in the solution at 298 K (x_{H_2}) divided by the computed H_2 solubility in pure water ($x_{H_2,0}$) are shown as functions of concentration in units of mol salt/L solution. $x_{H_2}/x_{H_2,0}$ of H_2 in aqueous NaCl, NaI, $NaNO_3$, and $NaClO_4$ is plotted in (a) using the correlations provided by Weisenberger *et al.* [292]. The computed solubilities of H_2 at 298 K, 323 K, and 353 K is shown as a function of molality (m) in units of mol salt/kg water in (b). The computed solubilities are fitted to an engineering equation (Eq. 6.7) and are shown as solid lines in (b). The DFF/B(OH)$_4^-$ model is used and combined with the TIP4P/2005 [100] water, Madrid-2019 [103] Na^+, and the Marx [91] H_2 force fields. In (c), the computed activities of water (a_w) are plotted as a function of m at 298 K and 353 K. The experimental activities of water at 298 K in aqueous NaCl solutions are plotted in (c) using the correlation provided by Tang *et al.* [400].

Table 6.4. Parameters of Eq. 6.6 for the computed finite size corrected self-diffusivities of H_2 in aqueous $NaB(OH)_4$ solutions. The finite size corrected self-diffusivities of H_2 are computed from MD simulations using the DFF/$B(OH)_4^-$ model combined with the TIP4P/2005 [100] water, Madrid-2019 [103] Na^+, and Marx [91] H_2 force fields. These parameters are valid for a concentration range of 0-5 mol $NaB(OH)_4{}^-$/kg water at 298-353 K.

$D_{s,0}$ / [m^2/s]	4.503×10^{-6}
B_1 / $[(\mathrm{mol}_{NaB(OH)_4}/\mathrm{kg}_{H_2O})^{-1}]$	2.240×10^{-1}
B_2 / [K]	2.084×10^{3}

computed solubility in pure water ($x_{H_2}/x_{H_2,0}$) is plotted as a function of $NaB(OH)_4$ concentration in Figure 6.7(a). The reduction of H_2 solubilities in aqueous solutions due to addition of salts (i.e, salting-out effect) is a well-established phenomenon [47, 48, 292]. To the best of our knowledge, no experimental data are available for the solubilities of H_2 in aqueous $NaB(OH)_4$ solutions. The salting-out of H_2 in aqueous solutions is commonly modelled using the Sechenov relation [292]. The Sechenov relation and constants provided by Weisenberger *et al.* [292] are used in this chapter to compute $x_{H_2}/x_{H_2,0}$ for aqueous NaCl, NaI, $NaNO_3$, and $NaClO_4$ as shown in Figure 6.7(a). Similarly to $B(OH)_4^-$, Cl^-, I^-, $NO_3{}^-$, and $ClO_4{}^-$ are monovalent and do not have a dipole moment. The computed salting out of H_2 in aqueous $NaB(OH)_4$ solutions shown in Figure 6.7(a) is in qualitative agreement with other aqueous electrolyte solutions and in quantitative agreement with the salting out of H_2 in aqueous NaCl solutions.

All the computed solubilities of H_2 (x_{H_2}) at a H_2 partial pressure of 1 bar (298 K, 323 K, and 353 K) are fitted to an empirical equation inspired by the Sechenov relation [292]:

$$\ln\left(\frac{x_{H_2}}{x_{H_2,0}}\right) = (f_0 + f_1 T)m \tag{6.7}$$

where f_0 and f_1 are fitting constants. m is the molality of $NaB(OH)_4$ in units of mol $NaB(OH)_4$ / kg water and T is in units of K. $x_{H_2,0}$ is the computed solubility of H_2 in pure water at a H_2 partial pressure of 1 bar and is fitted to:

$$x_{H_2,0} = f_2 \exp\left[\frac{f_3}{T} + f_4 \ln(T)\right] \tag{6.8}$$

where f_3, f_4, and f_5 are additional fitting parameters to capture the temperature dependence of H_2 solubilities in pure water. Eq. 6.8 is also used by Young. [401] to model the experimental solubilities of H_2 in water. The simulated solubilities of H_2 in water using the Marx [91]

Table 6.5. Parameters of Eqs. 6.7-6.8 for the computed solubilities of H_2 in aqueous $NaB(OH)_4$ solutions. The solubilities of H_2 are computed from CFCMC simulations using the DFF/$B(OH)_4^-$ model combined with the TIP4P/2005 [100] water, Madrid-2019 [103] Na^+, and Marx [91] H_2 force fields. These parameters are valid for a concentration range of 0-5 mol $NaB(OH)_4{}^-$/kg water at 298-353 K.

f_0 / $[(mol_{NaB(OH)_4}/kg_{H_2O})^{-1}]$	-5.473×10^{-1}
f_1 / $[(K\ mol_{NaB(OH)_4}/kg_{H_2O})^{-1}]$	1.195×10^{-3}
f_2 / [-]	5.844×10^{-5}
f_3 / [K]	-1.145×10^{1}
f_4 / [ln(K)]	-2.624×10^{-1}

H_2 force field and the TIP4P/2005 water force field deviate by ca. 10% from experimental solubilities [401]. The comparison of the experimental H_2 solubilities in water from 298-353 K with the solubility of Marx H_2 force field in the TIP4P/2005 water model is discussed in more detail in Refs. [47, 48]. All the fitting constants for Eqs. 6.7-6.8 are shown in Table 6.5. The results of Eq. 6.7 for the solubilities of H_2 in aqueous $NaB(OH)_4$ solutions at 298 K, 323 K, and 353 K are shown as solid lines in Figure 6.3.5(c).

The computed activities of water in aqueous $NaB(OH)_4{}^-$ solutions at 298 K and 353 K are compared to the activities of water in aqueous NaCl solutions (based on the activity correlation of Tang *et al.* [400]) in Figure 6.7(c). It can be observed that the computed activities of water in this chapter are not strongly dependent on temperature. This is also observed in other works for activities of water (in the liquid phase) in aqueous NaCl solutions [402]. At lower salt molalities (below 3 mol salt/ kg water), both $NaB(OH)_4{}^-$ and NaCl lead to similar changes to the water activities. At higher salt molalities (5 mol salt/kg water), the water activities start to deviate. Similar to the solubilities of H_2, there are no experimental values for the activities of water in aqueous $NaB(OH)_4$ solutions. The values computed in this chapter can be used as a first estimate for this property, to predict vapor pressures of water in aqueous $NaB(OH)_4$ solutions. All H_2 solubilities and activities of water at 298 K, 323 K, and 353 K computed in this chapter are shown in Table S7 of the Supporting Information of Ref. [354].

6.4. Conclusions

In this chapter, the transport and thermodynamic properties of $H_2/H_2O/NaB(OH)_4$ mixtures are investigated. The Delft Force Field for $B(OH)_4^-$ (DFF/$B(OH)_4^-$) is proposed and parameterized based on the TIP4P/2005 water model [100] and the Madrid-2019 [103] Na^+ models. The combination of the DFF/$B(OH)_4^-$ model with the Madrid-2019 [103] Na^+ model in TIP4P/2005 [100] water can accurately predict the densities and viscosities of aqueous $NaB(OH)_4$ solutions up to the solubility limit at 298 K with 2.5% deviation from experimental results. These force fields are used to compute the viscosities, ionic conductivities, and self-diffusivities of H_2, Na^+, and $B(OH)_4^-$ for a concentration range of 0-5 mol $NaB(OH)_4$/kg water at 298-353 K and 1 bar. CFCMC simulations are used to compute the solubilities of H_2 and activities of water in $NaB(OH)_4$ solutions in the same temperature and concentration ranges as the MD simulations. The salting-out of H_2 in aqueous $NaB(OH)_4$ solutions is observed similar to the salting out of H_2 in other aqueous electrolyte solutions. The viscosities, self-diffusivities of the ions and H_2, and the solubilities of H_2 in aqueous $NaB(OH)_4$ solutions are fitted to engineering equations. These engineering equations can be used for modelling the crystallization of $NaB(OH)_4$ in the aqueous solution and for designing $NaBH_4$ hydrolysis reactors.

An interesting future outlook for expanding this chapter would be to validate the performance of DFF/$B(OH)_4^-$ for different cations and in combination with other water force fields. Such a transferability check may be important because although TIP4P/2005 can accurately model the densities and transport coefficients of water, it is less accurate in capturing properties such as the experimental saturated vapor pressures. [110] When considering the Vapor Liquid Equilibrium of water/salt/H_2 systems, the hydrogen phase will contain a small amount of water [110]. A recent modification of TIP4P/2005 was developed by Rahbari *et al.* [110] (denoted here as TIP4P/μ). TIP4P/μ can accurately model the saturated vapor pressures of water, and thus, it would be interesting to investigate the performance of DFF/$B(OH)_4^-$ + TIP4P/μ. Finally, a possible future extension of this chapter would be to investigate the exact magnitude of the finite size effects of ionic conductivities using the exact expression (Eq. 6.1) in MD simulations.

7

Accurate Free Energies of Aqueous Electrolyte Solutions from Molecular Simulations with Non-polarizable Force Fields

This chapter is based on the following publication: P. Habibi, H. M. Polat, S. Blazquez, C. Vega, P. Dey, T. J. H. Vlugt, and O. A. Moultos. "Accurate Free Energies of Aqueous Electrolyte Solutions from Molecular Simulations with Non-polarizable Force Fields". *Journal of Physical Chemistry Letters* 15 (2024), 4477–4485.

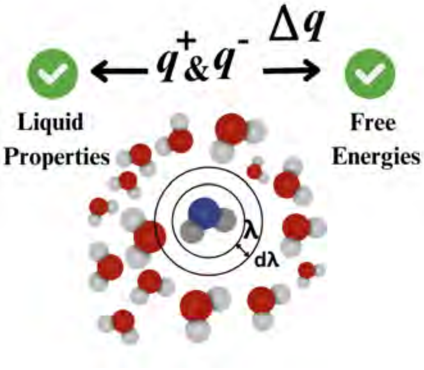

7.1. Introduction

Modeling aqueous electrolytes is a significant challenge due to long-range electrostatic interactions that make solutions highly non-ideal [303, 313]. Significant efforts are made to develop analytical models (i.e., EOS) for aqueous electrolytes [312, 314, 318, 403, 404]. Although these models are computationally efficient, they rely on existing thermophysical data for parameterization and do not offer atomistic insight [313, 314]. Molecular simulation is a powerful tool for atomistic modeling and predicting thermodynamic and transport properties of aqueous electrolyte solutions at different temperatures, pressures, and electrolyte concentrations [47, 48, 51, 405]. The accuracy of molecular simulations depends on the Potential Energy Surface (PES) that is used to compute the interactions between different species [49, 50, 99, 406]. The PES of aqueous electrolyte solutions can be computed from ab-initio calculations or semi-empirical force fields [49, 50, 87].

For this purpose, many classical force fields for water have been developed [95, 96, 98, 100, 110, 407, 408]. TIP4P/2005 [100] is a computationally efficient and popular water force field, which accurately predicts many properties of water such as shear viscosity, diffusivity, density, the temperature of maximum density, and surface tension, despite being rigid and non-polarizable [51, 100, 406, 409]. Clearly, the effective interactions of TIP4P/2005 (dictated by the relative energy differences in the PES [99]) in the liquid phase are well-described [99, 409]. Despite this, the TIP4P/2005 force field does not yield accurate predictions of the VLE of water, as predictions for vaporization enthalpies and saturated vapor pressures are poor [110, 410, 411]. Describing the VLE of water requires accurate modeling of (1) effective interactions between water molecules, and (2) the excess chemical potential (with respect to the ideal gas reference state) of the liquid phase ($\mu_{\mathrm{w}}^{\mathrm{ex}}$) [110] (dictated by the absolute value of the PES [99]), as the coexistence pressures have an exponential dependency on $\mu_{\mathrm{w}}^{\mathrm{ex}}$ [412]. TIP4P/2005 consistently underestimates $\mu_{\mathrm{w}}^{\mathrm{ex}}$ compared to experiments (e.g., by ca. 10% at 300 K), resulting in a significant underestimation of experimental saturated vapor pressures (by a factor of ca. 4 at 300 K) [110]. The second virial coefficients of TIP4P/2005 are also inaccurate compared to experimental data [413, 414].

Rigid non-polarizable water force fields that accurately capture the experimental $\mu_{\mathrm{w}}^{\mathrm{ex}}$ and the vaporization enthalpy of water, e.g., SPC [98], TIP4P [100], and TIP4P/μ [110, 354] (defined in the Supporting Information of Ref. [110]), poorly predict other important properties of the liquid phase (e.g., transport properties) compared to TIP4P/2005 [98–100, 110, 354]. It becomes clear that modeling both transport properties of water and $\mu_{\mathrm{w}}^{\mathrm{ex}}$ is not possible using available non-polarizable force fields [98, 99]. Already in 1987, Berendsen *et al.* [98] discussed this issue: to obtain effective interactions between water molecules in the liquid phase (thereby capturing experimental transport properties), the absolute value of the charges in the water force field needs to be enhanced to account for the polarization energy of water (i.e., "The Missing Term" in non-polarizable force fields mentioned in the title of the famous paper by Berendsen and co-workers [98]). Explicitly accounting for "The Missing Term" in non-polarizable force fields automatically results in an overestimation of the heat of vaporization and hence poor predictions of the VLE of water [98, 99, 410]. Some polarizable force fields (e.g., BK3 [95] and HBP [96]) capture the VLE of water without compromising the transport properties of the liquid phase but at the cost of higher complexity, significantly higher computational time (usually by a factor of ca. 3-10) [96, 97, 410, 415], and lack of transferability [95–97]. Therefore, non-polarizable force fields will likely remain popular for large-scale classical molecular simulations.

Based on TIP4P/2005 water, different force fields for salts (e.g., NaCl, KCl, and KOH) have been developed [47, 103, 111, 354, 416]. The charges of ion force fields are commonly scaled down (usually by a factor of 0.85 [103] or 0.75 [47, 111]) to account for the effective charge screening that occurs in the aqueous medium [103, 417, 418]. Charge scaling follows from the electronic continuum correction and accounts for polarisability of ions in a mean-field way [417, 418]. Using the "scaled charge" force fields of Madrid-2019 [103] (scaled charges of +0.85/-0.85), Madrid-Transport (scaled charges of +0.75/-0.75) [111], and the Delft Force Field of OH^- (DFF/OH^-) [47] (scaled charge of -0.75), many of the properties of aqueous NaCl, KCl, NaOH, and KOH solutions such as densities, viscosities, and interfacial tensions and their temperature dependence can be accurately computed [47, 48, 103, 111, 405]. Force fields with integer charges of ions (e.g., +1/-1 for Na^+/Cl^-), such as the Joung-Cheatam force field [104], significantly overestimate the change in liquid phase viscosities and ion-diffusivities in concentrated solutions (i.e., close to the solubility limit) with respect to the pure solvents [103]. The infinite dilution free energies of hydration of salts can be accurately captured using available integer charge force fields, whereas scaled charge force fields of ions deviate by ca. 20-30 % compared to experiments [236, 256].

Recently, Han *et al.* [409] have successfully simulated the dielectric constant of water using non-polarizable force fields. This study shows that the charges used in TIP4P/2005 water should only be used to model the PES, from which effective interactions between molecules are computed, and a different set of charges (derived from quantum mechanical simulations) should be used to model the dipole moment of the aqueous system, from which the dielectric constant is computed [405, 409]. Similarly Blazquez *et al.* [405] reproduced the experimental electrical conductivities of aqueous NaCl and KCl solutions up to the solubility limit by (1) using non-polarizable scaled charge force fields to describe the PES of ions, and (2) using integer charges to compute the dipole moment of the aqueous solution from which electrical conductivities are calculated.

Here, we introduce a new approach to accurately compute free energies of aqueous electrolyte solutions using non-polarizable force fields without compromising the predictive ability for transport and thermodynamic properties of the liquid phase. The PES is modeled using the TIP4P/2005 [100] force field and the Madrid-2019 [103] scaled charge ions, whereas a different set of charges, hereafter referred to as the Effective Charge Surface (ECS), are used to compute excess chemical potentials in the liquid phase. The ECS corrects for the effect of both polarization energy (i.e., "The Missing Term" of Berendsen *et al.* [98]) and charge scaling [417, 418] on the computed free energies. We show that using an ECS trained for TIP4P/2005 [100] water at 350 K, the experimental excess chemical potential of water along the liquid-vapor coexistence line can be reproduced within ca. 1% at a temperature range of 300-500 K, thereby, yielding accurate predictions for the saturated vapor pressures. Similarly, a single parameter ECS trained on the free energy of hydration of Madrid-2019 NaCl in water at 298 K corrects the free energies of hydration for the Madrid-2019 family of both monovalent and divalent salts such as LiCl, KCl, $MgCl_2$, $CaCl_2$ with ca. 5% accuracy from the experimental data of Marcus. [419]. Based on the computed excess chemical potential of pure water using the ECS, we correct the excess chemical potentials of water/salt mixtures by applying a free energy correction to the partition function of the system. Using this, we compute liquid/vapor coexistence densities of the water/NaCl system at 350 K up to 6 mol NaCl/kg water. Our simulations show an excellent agreement (within error bars) with experiments, in sharp contrast to simulations which do not have this correction (e.g., ca. a factor 4 deviation for saturated vapor densities at 350 K).

7.2. Methodology

The workflow of our method is shown in Figure 7.1. CFCMC [248–250] simulations in the isobaric-isothermal (*NPT*) ensemble are performed to simulate pure water and aqueous electrolyte solutions (i.e., NaCl(aq), KCl (aq), $MgCl_2$(aq), and $CaCl_2$(aq)) using the BRICK-CFCMC open source software [55, 56]. We define charge-neutral "fractional groups", which contain one or more ions or molecules [55]. For water, the fractional group contains a single molecule of water. For salts, it contains all ions in the molecule (e.g., for $MgCl_2$ the fractional group consists of one Mg^{2+} and two Cl^- ions). Details of CFCMC simulations can be found in the Supporting Information of Ref. [105] and in Refs. [55, 248]. We first simulate pure water in the absence of ions. With the exception of the single fractional molecule, all water molecules interact via the TIP4P/2005 [100] force field. The fractional H_2O molecule is a new species (i.e., ECS-TIP4P/2005 with parameters listed in Table S1 of the Supporting Information of Ref. [105])

with the LJ parameters of TIP4P/2005, but with a different set of charges (i.e., q^{+}_{ECS} and q^{-}_{ECS}, which are obtained by multiplying the charges of TIP4P/2005 by a factor of 0.965). This ensures that bulk properties of liquid water (i.e., densities and transport properties) are computed using the TIP4P/2005 water force field, while the ECS charges are used when calculating the excess chemical potential of pure water ($\mu^{\mathrm{ex}}_{\mathrm{w,ECS},m=0}$, i.e., at molality of the salt: $m = 0$ mol salt/kg water). To compute the excess chemical potential of water at finite salt concentrations, $\mu^{\mathrm{ex}}_{\mathrm{w,ECS},m=0}$ is used to compute a free energy correction (ϵ_{w}) for water:

$$\epsilon_{\mathrm{w}} = \mu^{\mathrm{ex}}_{\mathrm{w,ECS},m=0} - \mu^{\mathrm{ex}}_{\mathrm{w,PES},m=0} \tag{7.1}$$

where $\mu^{\mathrm{ex}}_{\mathrm{w,PES},m=0}$ refers to the excess chemical potential of pure water computed using the PES charges (i.e., TIP4P/2005). ϵ_{w} depends only on temperature (T) as it is calculated along the liquid branch of the vapor-liquid coexistence curve (i.e., when evaluating Eq. 7.1, the pressure, P, should be fixed to the saturated vapor pressure). ϵ_{w} is applied as a background energy in the isolated molecule partition function of water and changes the partition function (Q_{NPT}) of the system (here shown for the isobaric-isothermal ensemble):

$$\begin{aligned} Q_{NPT} = \frac{P}{k_{\mathrm{B}}T}\left(\prod_{i}^{n_t}\frac{q_{0,i}^{N_i}}{N_i!\Lambda_i^{3N}}\right)\int \mathrm{d}V V^N \exp\left[\frac{-PV}{k_{\mathrm{B}}T}\right] \\ \int \mathrm{d}\mathbf{s}^N \exp\left[\frac{-U(\mathbf{s}^N)+\sum_i^{n_t} N_i\epsilon_i}{k_{\mathrm{B}}T}\right] \end{aligned} \tag{7.2}$$

where V, N, $\mathbf{s}^N$, k_{B}, Λ_i, and n_t refer to the system volume, total number of molecules, the scaled coordinate vector of all molecules, the Boltzmann constant, the thermal wavelength of species i, and the total number of species types, respectively. $q_{0,i}$, N_i, and ϵ_i refer to isolated molecular partition functions (excluding the translation part), the number of molecules of species i, and the free energy correction for species i, respectively. The derivation of Eq. 7.2 after applying the free energy correction ϵ_i to the isolated molecule partition function of species i is shown in the Appendix A.3. ϵ_i is not a function of V and $\mathbf{s}^N$, and therefore it does not influence the density, virial pressure, liquid structure, or transport properties at a given temperature or pressure. The chemical potential of species i (μ_i) can be computed using:

$$\mu_i = -k_{\mathrm{B}}T\left(\frac{\partial \ln(Q_{NpT})}{\partial N_i}\right)_{T,p,N_{j,j\neq i}} = \mu_i^{\mathrm{id}} + \mu^{\mathrm{ex}}_{i,\mathrm{PES}} + \epsilon_i \tag{7.3}$$

where μ_i^{id} is the ideal gas contribution and $\mu^{\mathrm{ex}}_{i,\mathrm{PES}}$ is the excess chemical potential computed from the PES. The chemical potential, μ_i at $m = 0$

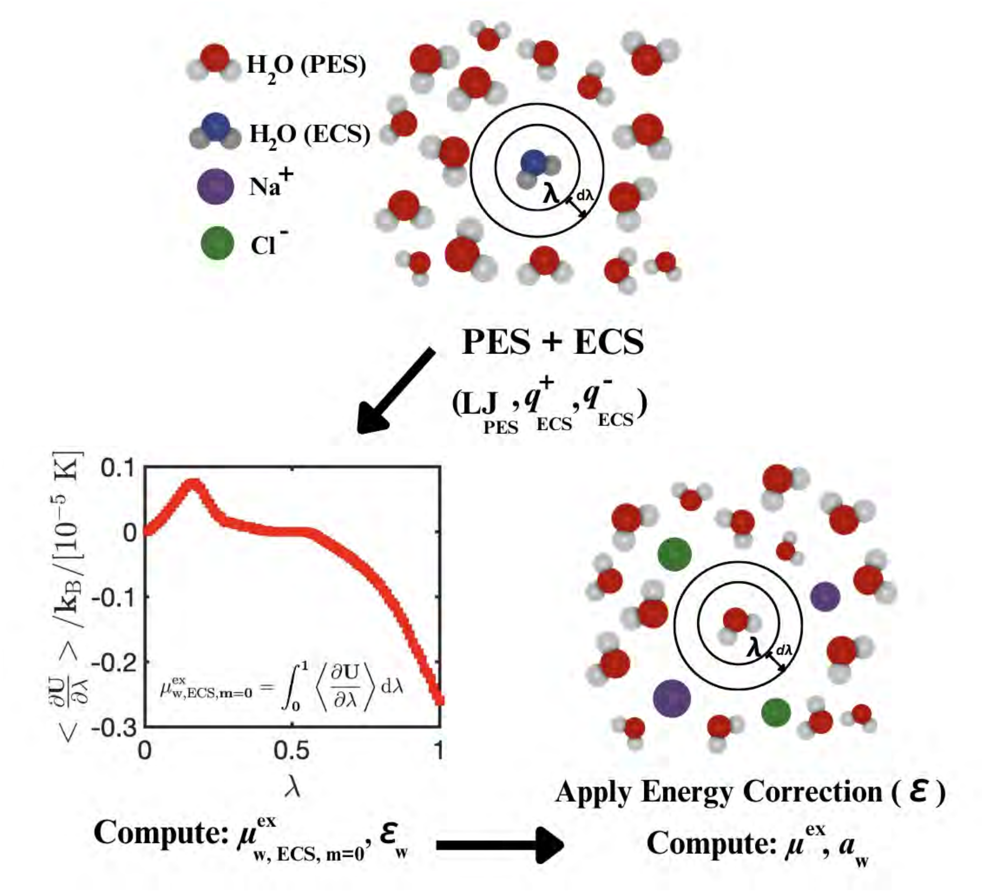

Figure 7.1. Schematic representation of the workflow used in this work [55, 248, 249]. Excess chemical potentials (with respect to the ideal gas reference state) are computed using the BRICK-CFCMC software [55, 56]. The details for computing excess chemical potentials are discussed in the Supporting Information of Ref. [105]. The excess chemical potential of pure water ($\mu^{ex}_{w,ECS,m=0}$) at various temperatures (300-500 K) is computed using a single fractional molecule of water, with the same Lennard-Jones parameters as TIP4P/2005, but with different temperature-independent charges (i.e., q^+_{ECS} and q^-_{ECS}). The computed ($\mu^{ex}_{w,ECS,m=0}$) is used to construct a temperature-dependent free energy correction ($\epsilon_{c,w}$) with which μ^{ex}_{w} of water at different salt concentrations can be computed.

is shifted to equal the values obtained using the ECS. After applying the free energy correction, the charges of TIP4P/2005 [100] can be used to compute excess chemical potentials at finite salt concentrations, as changes in the chemical potential as a function of m can be computed accurately using the PES [416]. Activities ($a_\mathrm{w} = \gamma_\mathrm{w} x_\mathrm{w}$, where γ_w and x_w refer to the activity coefficient and mole fraction of water, respectively) of water at different molalities of salts are computed using [398]:

$$\begin{aligned} a_\mathrm{w} &= \frac{\langle \rho_{\mathrm{w},m} \rangle}{\langle \rho_{\mathrm{w},m=0} \rangle} \exp\left[\frac{(\mu^\mathrm{ex}_{\mathrm{w,PES},m} + \epsilon_\mathrm{w}) - (\mu^\mathrm{ex}_{\mathrm{w,PES},m=0} + \epsilon_\mathrm{w})}{k_\mathrm{B}T}\right] \\ &= \frac{\langle \rho_{\mathrm{w},m} \rangle}{\langle \rho_{\mathrm{w},m=0} \rangle} \exp\left[\frac{\mu^\mathrm{ex}_{\mathrm{w,PES},m} - \mu^\mathrm{ex}_{\mathrm{w,PES},m=0}}{k_\mathrm{B}T}\right] \end{aligned} \tag{7.4}$$

where $\langle \rho_{\mathrm{w},m=0} \rangle$ and $\langle \rho_{\mathrm{w},m} \rangle$ are the ensemble averaged number densities of water at molalities m and 0, respectively. $\mu^\mathrm{ex}_{\mathrm{w,PES},m}$ is the excess chemical potential of water computed using the PES at a molality m [398]. ϵ_w does not depend on m (at constant T), therefore, ϵ_w cancels out for all m (as shown in Eq. 7.4), when computing a_w (i.e., a_w only depends on the PES).

7.3. Results and discussion

To correct the excess chemical potential of the TIP4P/2005 [100] water force field the ECS approach is used. Figure 7.2(a) and 7.2(b) show the computed liquid densities and excess chemical potentials of water at the simulated vapor-liquid coexistence line at 300-500 K for TIP4P/2005 [100], TIP4P/μ [110], and the ECS approach of this chapter. As shown in Figure 7.2(a) and 7.2(b), TIP4P/2005 [100] accurately predicts the liquid densities at coexistence, but it overestimates the attractive electrostatic interactions of water leading to lower excess chemical potentials (and higher vaporization enthalpies) [99]. The overestimation of attractive electrostatic interactions is required to obtain correct intermolecular interactions, as polarization of water can then be modeled in a mean-field way as described by Vega. [99] and Berendsen *et al.* [98].

At 300 K, the excess chemical potential of TIP4P/2005 [100] water in the liquid phase is -30.0 kJ/mol [110], while the experimental value is -26.37 kJ/mol (REFPROP version 10 [420], computed based on IAPWS-95 [421]). This underprediction of the excess chemical potentials for TIP4P/2005 [100] leads to a saturated vapor pressure that is ca. 4 times smaller than experimental value at 300 K [110, 420, 421]. Saturated vapor pressures (P_sat) are related to the excess chemical potential of liquid water using [106, 412]:

$$P_\mathrm{sat} = \frac{k_\mathrm{B} T \rho_\mathrm{L}}{\phi_\mathrm{w}} \exp\left[\frac{\mu^\mathrm{ex}_\mathrm{w}}{k_\mathrm{B}T}\right] \tag{7.5}$$

where ϕ_{w} is the fugacity coefficient of water vapor at a given T and P_{sat}. Eq. 7.5 can be solved iteratively to obtain consistent P_{sat} and ϕ_{w}. The derivation of Eq. 7.5 and the iterative scheme for a multi-component mixture is discussed in Section S2 of the Supporting Information of Ref. [105] and Appendix A.4. When calculating P_{sat} using Eq. 7.5, it is assumed that the liquid phase is incompressible (i.e., ρ_{L} and $\mu_{\text{w}}^{\text{ex}}$ computed in the liquid phase are not influenced by pressure in the range of 1-50 bar). The TIP4P/2005 force field cannot accurately model the virial coefficient of water in the gas phase [413, 414], and hence, it does not correctly describe deviations from the ideal gas behavior, leading to an inaccurate relation between T, P_{sat}, and ϕ_{w}. In this chapter, the Peng-Robinson equation of state (PR-EOS) for water vapor [422, 423], is used to relate T, P_{sat}, and ϕ_{w}. From the PR-EOS, the saturated vapor densities (ρ_{G} as shown in Figure 7.2(c)) are computed for the ECS approach, TIP4P/2005 [100], and TIP4P/μ. The following parameters are used for the PR-EOS of water in the gas phase: critical temperature of 647.3 K, critical pressure of 221.2 bar, and an acentric factor of 0.344 [197]. For TIP4P/2005 [100] and TIP4P/μ, the results provided in Ref. [110] are used for ρ_{L} and $\mu_{\text{w}}^{\text{ex}}$.

The TIP4P/μ force field [110] accurately describes the excess chemical potentials of liquid water (and thereby the saturated vapor pressures and densities), yet it underestimates the liquid densities at $T > 300$ K (as shown in Figure 7.2) as it cannot correctly capture the interactions between liquid water molecules. This also explains the ca. 30% lower viscosities for TIP4P/μ at 298 K and 1 bar compared to experiments [354]. Using the ECS approach for TIP4P/2005, we accurately model the excess chemical potentials of pure liquid water compared to experiments for a wide temperature range (i.e., 300 to 500 K). The ECS charges are computed by multiplying the charges of TIP4P/2005 [100] by a temperature-independent charge scaling parameter equal to 0.965. This charge scaling parameter is obtained by only fitting the simulated excess chemical potential of liquid water at 350 K to the experimental value. As shown in Figure 7.2, the ECS approach leads to accurate modeling of the VLE of pure water without compromising liquid phase densities, and at the same computational expense as TIP4P/2005. The heat of vaporization computed using the ECS at 298 K and 1 bar is 45 ± 2 kJ mol^{-1} (obtained as explained in Section S1 of the Supporting Information of Ref. [105]), and has a much closer agreement with experiments (44.01 kJ mol^{-1}) [251] than the TIP4P/2005 force field (i.e., 50.2 kJ mol^{-1}) [251].

After obtaining the infinite dilution excess chemical potentials of water using the ECS, we compute the free energy correction (ϵ_{w}) for TIP4P/2005 as a function of temperature. ϵ_{w} is fitted as a linear function temperature using:

$$\epsilon_{\text{w}} = \mu_{\text{w,ECS},m=0}^{\text{ex}} - \mu_{\text{w,PES},m=0}^{\text{ex}} = A_0 + A_1 T \tag{7.6}$$

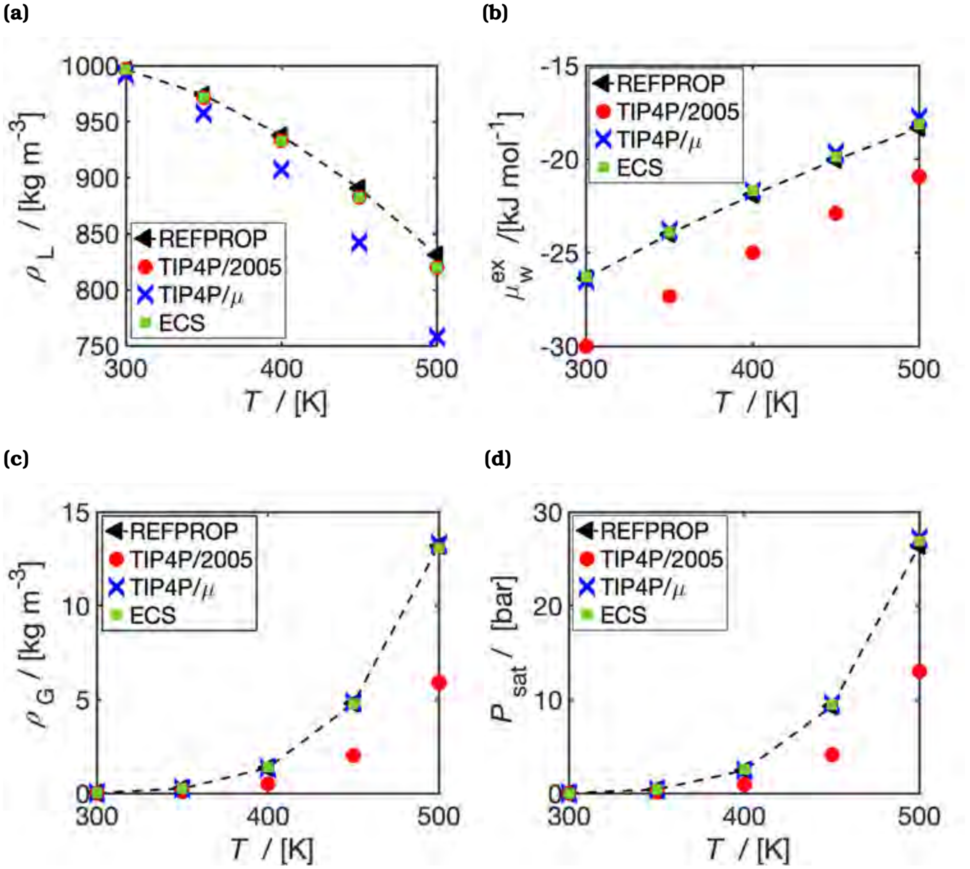

Figure 7.2. Computed (a) liquid densities (ρ_L) and (b) liquid phase excess chemical potentials (μ_w^{ex}), and (c) gas densities (ρ_G) as functions of temperature T along the vapor-liquid coexistence line of H_2O. In (d), the saturated vapor pressure (P_{sat}) of H_2O on the Vapor-Liquid coexistence line is shown as a function of T. The computed results using the ECS developed in this chapter are compared to the results of the TIP4P/2005 [100] and TIP4P/μ [110] water force fields and the experimental data obtained from REFPROP [420, 421]. For TIP4P/2005 [100] and TIP4P/μ, the results provided in Ref. [110] are used for the values of ρ_L and μ_w^{ex}.

where A_0 (5.00 kJ mol^{-1}) and A_1 (-4.36×10^{-3} kJ mol^{-1} K^{-1}) are the fitting parameters. Eq. 7.6 provides an excellent fit for ϵ_w (within the error bars) as shown in Figure S2 of the Supporting Information of Ref. [105].

Figure 7.3 (a) and 7.3 (b) show the computed water activities and densities for TIP4P/2005 [100] combined with the Madrid-2019 [103], Madrid-Transport [111], and the Joung-Cheatam [104] NaCl force fields at 298 K and 1 bar. Activities of water at a molality m (a_w) are computed using Eq. 7.4 and do not depend on ϵ_w. As shown in Figure 7.3, activities of water are predicted best using scaled charge force fields, especially for concentrations higher than 4 mol NaCl/kg water, despite all force fields having accurate density predictions (within 1% agreement with the data of Ref. [112] as shown in Figure 7.3 (b)). The Madrid-2019 [103] NaCl force field combined with TIP4P/2005 [103] predicts the activities of water with deviations smaller than ca. 3 %. Accurate predictions of water activities indicate that the mean activity of the salt is correctly described, due to the Gibbs-Duhem relation (binary mixture) [425]. As the Madrid-2019 [103] NaCl and TIP4P/2005 [100] water combination has the best agreement with the experimental activities of water, these force fields are used with the ECS approach (i.e., using ϵ_w) to simulate the coexistence vapor densities at 350 K at various NaCl molalities. The chemical potential of liquid water at molality m is equal to $\mu_\mathrm{w}(m) = \mu_\mathrm{w}(m=0) + k_\mathrm{B}T\ln(a_\mathrm{w})$, where $\mu_\mathrm{w}(m=0)$ is the chemical potential at $m=0$. In the ECS approach, the value of $\mu_\mathrm{w}(m=0)$ is shifted by ϵ_w (Eq. 7.3), thereby changing P_sat (as computed by Eq. 7.5) and ρ_G. As shown in Figure 7.3(c) and 7.3(d), the ECS approach results in perfect agreement (within the error bars) with the data of Clarke *et al.* [424] for the vapor phase coexistence pressures and densities of water/NaCl mixtures, while TIP4P/2005 [100] at 350 K underpredicts the vapor densities of water/NaCl by a factor of ca. 4. The saturated vapor pressures and densities of aqueous NaCl and $CaCl_2$ solutions are computed at 300-350 K and shown in Figure S3 of the Supporting Information of Ref. [105]. As shown in this figure, the ECS approach combined with TIP4P/2005 and the Madrid-2019 force fields can accurately capture the experimental saturated vapor pressures and densities for aqueous NaCl and $CaCl_2$ solutions (within 5% deviation).

The computed free energies of hydration of several aqueous salts (i.e., NaCl, KCl, LiCl, $MgCl_2$, and $CaCl_2$) in TIP4P/2005 water are shown in Figure 7.4. The free energy of hydration of a salt refers to the free energy change associated with bringing an ion-pair (ions infinitely apart) from a dilute gas phase to the aqueous phase [427]. Even though scaled charge force fields can accurately predict experimental activities in aqueous electrolyte solutions (as shown in Figure 7.3(a)), the free energies of hydration computed using the scaled ion force fields of Madrid-2019 [103](0.85 charge scaling for Na^+, K^+, Li^+, Mg^{2+}, Ca^{2+}, and Cl^-) underestimate the experimental values by ca. 20-30 %. The Joung-Cheatam [104] NaCl force field with integer charges of +1/-1

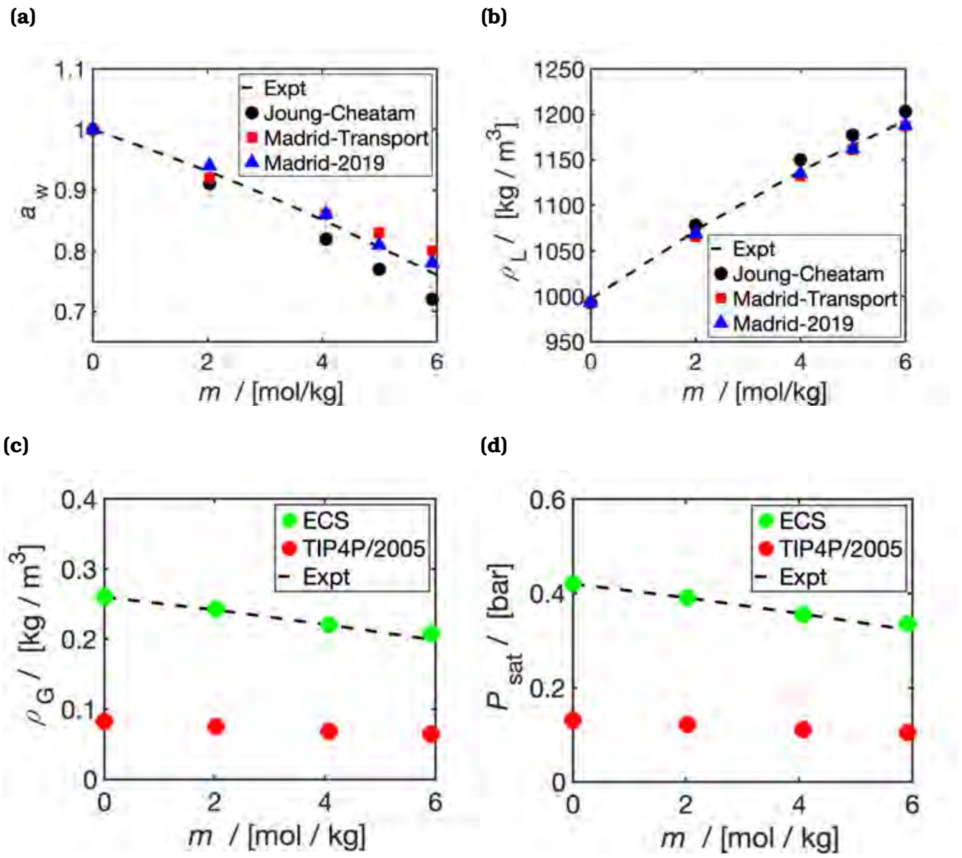

Figure 7.3. Computed (a) activities of water (a_w) and (b) liquid densities (ρ_L) at 298 K and 1 bar as a function of molality (m, in units of mol NaCl/kg water). The Madrid-2019 [103], Madrid-Transport [111], and the Joung-Cheatam [104] NaCl force fields are combined with the TIP4P/2005 [100] water force field. The experimental correlation of Tang *et al.* [400] is used for the activities of water at 298 K and the experimental correlation of Laliberté *et al.* [112] is used for the densities. Computed coexistence (c) vapor densities (ρ_G) and (d) saturated vapor pressures (P_{sat}) of water at 350 K as a function of m. The liquid densities and excess chemical potentials used to calculate ρ_G and P_{sat} from Eq. 7.5 are computed at 1 bar. The ECS approach combined with TIP4P/2005 [100] water and Madrid-2019 NaCl force fields are used to compute ρ_G and the results are compared to the data of Clarke *et al.* [424]. The computed coexistence vapor densities of TIP4P/2005 and Madrid-2019 NaCl force fields without the ECS approach are shown for comparison in (c).

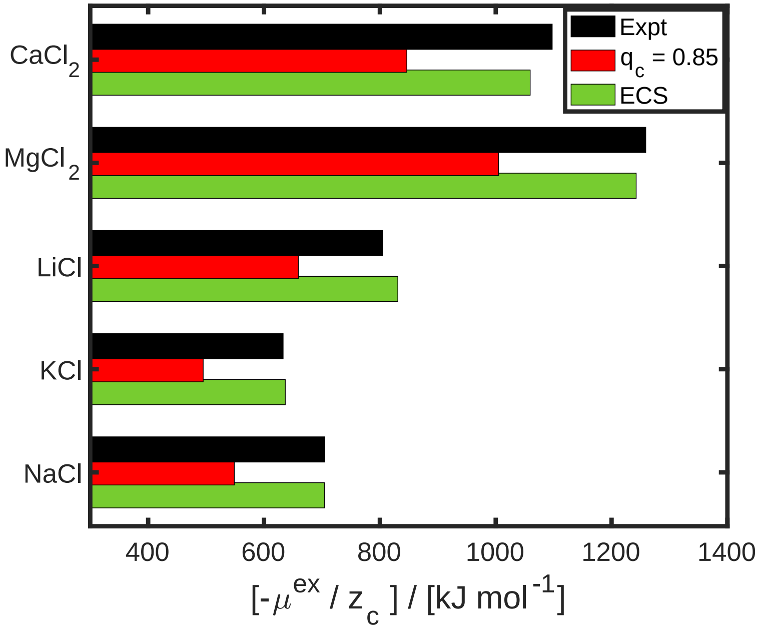

Figure 7.4. Computed infinite dilution excess chemical potentials (μ_{ex}) (i.e., free energies of hydration) at 298 K and 1 bar for aqueous NaCl, KCl, LiCl, $MgCl_2$, and $CaCl_2$ solutions at infinite dilution. μ_{ex} is normalised with respect to the integer cation charge (z_c) (i.e., 1 for Na^+, K^+, and Li and 2 for Ca^{2+} and Mg^{2+}). The ion force fields of Madrid-2019 [103] (scaled charge of 0.85: $q_c = 0.85$ for Na^+, K^+, Li^+, Mg^{2+}, Ca^{2+}, and Cl^-) are considered. The TIP4P/2005 [100] water force field is used for all calculations. In the ECS approach, a single fractional group of cations and anions are used, with the same LJ parameters of Madrid-2019 [103] force fields. ECS charges of +0.95/-0.95 for monovalent ions and +1.90/-1.90 for divalent ions is used to sample the free energies of hydration (fitted only to the free energy of hydration of an aqueous NaCl solution at infinite dilution at 298 K and multiplied by the valency, i.e., 2, for divalent ions). The experimental data of Marcus. [419] are shown in black. All the raw data are listed in Table S6 of the Supporting Information of Ref. [105] (along with the experimental free energy of hydration data of Marcus. [419] and Schmid *et al.* [426]).

reproduces the free energies of hydration within 5% from experimental values [104, 256], however, it largely overestimates the change in viscosities at higher molalities with respect to the pure solvent (i.e., at 298 K and 4 mol NaCl / kg water, the viscosity computed using the Joung-Cheatam NaCl force field combined with TIP4P/2005 [100] deviates by ca. 100% from experiments [103]). The ECS approach can be used to correct the free energies of hydration of these scaled charge ion force fields without influencing the predictive ability for transport properties and activities of salt/water mixtures. For this, a single fractional group (i.e., consisting of a cation and an anion) molecule is introduced to a system with 300 TIP4P/2005 [100] water molecules. This fractional group uses the same LJ parameters as the Madrid-2019 [103] ion force fields, but with different ion charges (i.e., +0.95/-0.95 for monovalent ions and +1.90/-1.90 for divalent ions). This ECS for the ion pair is trained at 298 K based on the free energy of hydration of an aqueous NaCl solution at infinite dilution using a single charge scaling parameter. For divalent ions such as Mg^{2+}, the ECS obtained for Na^{+} is multiplied by 2 (i.e., the ion valency). Figure 7.4 clearly shows that the ECS approach leads to free hydration values that deviate by ca. 5% or less from the experimental data provided by Marcus. [419] for all ionic species considered. The free energies of hydration of Madrid-Transport [111] ions (scaled charges of +0.75/-0.75) and the DFF/OH^{-} (scaled charge of -0.75) [47] can also be corrected using the ECS as discussed in Figure S4 and Table S7 of the Supporting Information of Ref. [105]. This shows the applicability of the ECS approach to different ion force fields. It is important to note that these free energies of hydration of salts are computed at infinite dilution. To simulate the excess chemical potential of salts at finite concentrations, the free energy correction for the salt (ϵ_{s}) needs to be computed using the same workflow followed for water (values of $\epsilon_{\mathrm{s}} = \mu^{\mathrm{ex}}_{\mathrm{s,ECS},m=0} - \mu^{\mathrm{ex}}_{\mathrm{s,PES},m=0}$ at 298 K are listed in Tables S6 and S7 of the Supporting Information of Ref. [105]). This ensures that only the initial free energy offset is corrected while energy differences (i.e., related to activities) are computed using the PES.

7.4. Conclusions

We have shown that TIP4P/2005 can accurately model the vapor-liquid properties of aqueous electrolyte solutions, provided that an additional charge surface, the so-called Effective Charge Surface (ECS), is used to correct the infinite dilution excess chemical potentials of water and salt. The excess chemical potential of water is corrected using the new ECS, and excellent agreement with experiments is obtained for both gas and liquid coexistence densities. A temperature-independent ECS trained at 350 K using a single charge scaling parameter (scaling factor of 0.965 with respect to the charges of TIP4P/2005 [100]) can be used to model the infinite dilution excess chemical potentials of water from 300-500 K with differences smaller than 1% with respect to experiments. The excess chemical potentials of water at infinite dilution computed using the ECS are used to obtain a free energy correction, which corrects the saturated vapor densities of water/NaCl systems. An ECS with charges of +0.95/-0.95 [e] for monovalent ions and +1.90/-1.90 [e] for divalent ions, trained only on an aqueous NaCl solution at infinite dilution (for divalent ions the ECS is multiplied by the valency 2), successfully corrects the free energies of hydration of Madrid-2019 [103] force fields for aqueous KCl, LiCl, $MgCl_2$, and $CaCl_2$ solutions with deviations of ca. 5% or less from the experimental data of Marcus. [419]. The ECS approach enables accurate computation of free energies and VLE in large-scale molecular simulations using simple non-polarizable force fields, without compromising the predictive ability for thermodynamic and transport properties of the liquid phase. This method is transferable and can also be used for other non-polarizable water and ion force fields. An interesting future direction would be to investigate if the same approach can be used to accurately compute free energy differences between water (combined with salts) and ice as these have a profound impact on computed nucleation rates of ice [428].

8

Effect of dissolved KOH and NaCl on the solubility of water in Hydrogen

This chapter is based on the following publication: P. Habibi, P. Dey, T. J. H. Vlugt, and O. A. Moultos. “Effect of dissolved KOH and NaCl on the solubility of water in hydrogen: A Monte Carlo simulation study”. *Journal of Chemical Physics* 161 (2024), 054304.

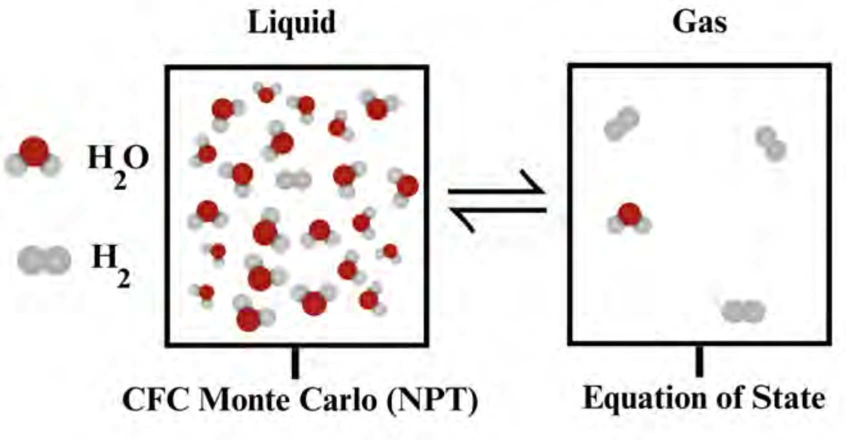

8.1. Introduction

The accurate prediction of the VLE of H_2 and aqueous electrolyte systems (e.g., aqueous NaCl and KOH solutions) is crucial for the design and optimization of environmental and industrial processes such as water electrolysis [7, 12, 16, 305], electrochemical compression of water [106, 110], and underground hydrogen storage [22, 194, 196]. For example, the VLE of H_2 and aqueous KOH solutions influences the product gas purities in alkaline water electrolyzers [7, 9, 10] and the presence of water in compressed hydrogen affects the thermophysical properties (e.g., the Joule-Thompson coefficients) of the gaseous mixture [106]. Excess water can also block porous membranes in PEM fuel cells [430, 431]. All of these factors are relevant for production, storage, and subsequent use of H_2 [10, 16, 106, 430, 431].

The VLE of H_2 and aqueous systems are traditionally measured in experiments [211, 212, 432]. Nevertheless, such experiments at high pressures (up to ca. 700 bar) are costly and time consuming considering the vast range of conditions of interest (i.e., type of aqueous salts, salt molality (m), and temperature) [7, 10, 23, 198]. Alkaline water electrolyzers typically operate at ca. 360 K, 2-8 mol KOH / kg water, and at pressures of 1-100 bar [7, 10, 198]. For underground storage of H_2, H_2 gas is in contact with brine solutions with molalities up to 5 mol NaCl / kg water, pressures up to 300 bar, and temperatures ranging from 348 K to 372 K [23]. As an alternative to experiments, MC simulation, can be used to compute the VLE of H_2 with aqueous electrolyte solutions (i.e., KOH and NaCl) for a wide range of temperatures, pressures, and salt concentrations [47, 48, 411, 422, 433].

Two-body force fields with point chrages (non-polarizable) are widely used for computing the VLE of H_2 and aqueous electrolyte systems due to their computational efficiency, small number of parameters, and accuracy in predicting various thermophysical properties of aqueous solutions [47, 48, 105, 106]. Rahbari *et al.* [106] computed the VLE of H_2 and pure water systems using MC simulations for a temperature range of 298-423 K and pressures up to 1000 bar. Rahbari *et al.* [106] showed that the TIP4P/2005 [100] water force field (which is parameterized based on liquid densities, transport properties, and the temperature of maximum density) can accurately model the solubilities of H_2 in water but fails in predicting the water content in compressed H_2 gas due to incorrect predictions of the saturated vapor pressure of water. Other non-polarizable water force fields such as TIP3P (which is trained on the vaporization energy of water) [99, 255] do not predict the solubilities of H_2 in water, but correctly capture the water content in H_2 gas [106]. TIP4P/2005 and TIP3P also cannot correctly predict the second virial coefficient (and hence the non-idealities) of water in the gas phase [413, 434]. In other molecular simulation studies in literature (such as in Refs. [47, 48, 245, 354, 422, 433]) the solubilities of H_2 in the aqueous phase are calculated, without computing the solubility of water in compressed H_2. This is done by either assuming an ideal H_2 gas phase (for pressures below 100 bar) and computing the Henry constants of H_2, or by neglecting the water content in the gas phase at higher pressures (as the experimental water content is below 1% for temperatures below 363 K and pressures above 100 bar) [47, 48, 106, 245, 354, 422, 433].

Despite the importance of the VLE data for H_2 and aqueous electrolyte (i.e., KOH and NaCl) solutions, none of the existing molecular simulation studies have reported both the equilibrium water composition in H_2 and the solubilities of H_2 in aqueous solutions at different KOH and NaCl concentrations. In this chapter, the excess chemical potentials (i.e., with respect to the ideal gas reference state [248]) of H_2 and water in the liquid phase are computed using CFCMC [248–250] simulations. As derived in Ref. [105], a temperature-dependent free energy correction is used to shift the excess chemical potential of the TIP4P/2005 water force field (at a molality of 0 mol salt / kg water). A constant free energy correction for the infinite dilution excess chemical potential of Marx H_2 force field [91] in TIP4P/2005 [100] is also applied. This results in an accurate prediction of H_2 solubilities in water (and the temperature of minimum H_2 solubility in water) for 298-363 K at a H_2 fugacity of 1 bar (within 5% deviation from experiments [212]). The Madrid-Transport K^+ [111] and the Delft Force Field of OH^- (DFF/OH^-) [47] are used to model KOH, and the Madrid-2019 force fields [103] of Na^+ and Cl^- are used to model NaCl. These ion force fields are shown to accurately model the densities and activities of water (and their temperature-dependence) with respect to experiments (within 2% deviation). The equilibrium compositions of H_2 and water are computed from the liquid phase excess chemical potentials and densities using an iterative scheme in which the gas phase fugacities and densities are computed using the GERG-2008 Equation of State (EoS) [123]. This approach accurately predicts the scarcely available experimental equilibrium compositions of water and H_2 for H_2/aqueous NaCl systems [212, 432] (within 5%) without any refitting of force fields or modifying the Lorentz-Berthelot [50] (LB) mixing rules. The CFCMC simulations are then performed for a wide range of conditions to simulate the VLE of H_2 and aqueous electrolyte solutions at 298-423 K, 10-400 bar, 0-8 mol KOH / kg water, and 0-6 mol NaCl/kg water.

This chapter is organized as follows. In Section 8.2, details are provided for force fields, the CFCMC simulations, the free energy correction, and the iterative scheme for computing the VLE of H_2 and aqueous KOH/NaCl solutions. In Section 8.3, the computed densities and activities of water (and their temperature dependence) for aqueous KOH and NaCl solutions are shown, the influence of the free energy correction on the saturated vapor pressure of water and solubility of H_2 in pure water is discussed, and the VLE data for H_2 and aqueous KOH and NaCl solutions are provided. Conclusions and recommendations are outlined in Section 8.4

8.2. Computational methods

8.2.1. Force fields

Water is modeled using the four-site rigid TIP4P/2005 [100] force field. For aqueous NaCl solutions, the Na^+ and Cl^- force fields of Madrid-2019 [103] are used. For aqueous KOH solutions, the K^+ ions are modeled using the Madrid-Transport force field [111] and OH^- ions are modeled using the Delft Force Field of OH^- (DFF/OH^-) [47]. H_2 is modeled using the three-site Marx [91] force field. The combination of Marx [91] H_2 and TIP4P/2005 water has performed accurately in prior studies in predicting the diffusivities and solubilities of H_2 in water [47, 48, 109, 354, 433]. The force field choices are justified in the Results section of this chapter. Ion charges are commonly scaled in non-polarizable models [103, 111, 418]. In Madrid-2019 [103], the unit charge of ions is scaled by a factor of 0.85, and in the Madrid-Transport [111] and DFF/OH^- [47], charges are scaled by a factor of 0.75. Charge scaling leads to accurate density, viscosity, electrical conductivities, and water activity predictions for aqueous electrolyte solutions (e.g., NaCl and KOH) compared to using unscaled charges [47, 48, 103, 354, 405]. Charge scaling is discussed in detail in Refs. [103, 111, 303]. All force field parameters for H_2O, Na^+, Cl^-, K^+, OH^-, and H_2 are listed in Tables S1-S5 of the Supplementary Material of Ref. [429] and Appendix A.2. The LB mixing rules [49, 50] are used in all simulations, with the exception of $[\mathsf{Na}^+/\mathsf{K}^+/\mathsf{Cl}^- - \mathsf{H_2O}]$ and $[\mathsf{Na}^+ - \mathsf{Cl}^-]$ Lennard-Jones (LJ) interactions as specified in Appendix A.2. The Ewald summation [50] is used for electrostatic interactions (relative precision of 10^{-6}). A cut off radius of 10Å is used for the LJ interactions and the real space contribution of the Ewald-Summation. Analytical tail corrections for energies and pressures are applied for the LJ part of the interactions.

8.2.2. MC simulations

A schematic of our computational methodology is shown in Figure 8.1. To compute the VLE of H_2 and aqueous electrolyte solutions of NaCl and KOH, the chemical potentials of H_2O and H_2 in the liquid phase are equated to the gas phase chemical potentials at constant T and P. The liquid phase chemical potentials are computed using CFCMC simulations [248–250], which are carried out using the open-source BRICK-CFCMC software package [55, 56] in the Continuous Fractional Component isobaric-isothermal (CFCNPT) ensemble [248–250]. The gas phase is modelled using the GERG-2008 EoS [123] as the TIP4P/2005 water force field is a poor EoS of water in the vapor phase [413]. For all CFCNPT simulations, periodic boundary conditions are applied in all directions of the cubic simulation box. The simulations consist of 300 water molecules and 0-43 molecules of KOH (corresponding to 0-8 mol KOH/ kg water) or 0-32 molecules of NaCl (corresponding to 0-6 mol NaCl/ kg water), depending on the molalities of the solution. The exact numbers of KOH and NaCl molecules and the corresponding molalities are provided in Table S6-S7 of the Supplementary Material of Ref. [429]. The VLE of H_2 and aqueous NaCl/KOH solutions are calculated at the following temperatures: 298 K, 323 K, 363 K, 393 K, and 423 K. The pressures considered are 10 bar, 50 bar, 100 bar, 200 bar, and 500 bar.

To compute the chemical potentials of H_2O and H_2, the excess chemical potentials of H_2 and H_2O (i.e., with respect to the ideal gas reference state [248]) in the aqueous phase are required. The excess chemical potentials of H_2 and H_2O are computed by introducing a single fractional molecule of H_2 and H_2O. The same methodology used in Section 4.2.5 is used in this Chapter to compute excess chemical potentials of H_2 and water.

The computed excess chemical potentials of water and H_2 at a salt molality of 0 mol salt / kg water are corrected using a free energy correction ϵ_i. Details on this free energy correction are given in Ref. [105]. The TIP4P/2005 force field can accurately model the change in the free energy as a function of pressure or salt molality but not the absolute values of the excess chemical potentials [105]. To correct for the initial offset of the excess chemical potentials of water and H_2 at $m = 0$, the computed excess chemicals are shifted using:

$$\mu^{\mathrm{ex}}_{\mathrm{L},i} = \mu^{\mathrm{ex}}_{\mathrm{L,MC},i} + \epsilon_i \tag{8.1}$$

where $\mu^{\mathrm{ex}}_{\mathrm{L},i}$ refers to the corrected excess chemical potential of species i in the liquid phase. The free energy correction for TIP4P/2005 [100]($\epsilon_{\mathrm{H_2O}}$) is derived in Ref. [105] and is a weak function of temperature:

$$\epsilon_{\mathrm{H_2O}} = A_0 + A_1 T \tag{8.2}$$

where $A_0 = 5.00$ kJ mol^{-1} and $A_1 = -4.36 \times 10^{-3}$ kJ mol^{-1} K^{-1}. A_0 and A_1 are fitted parameters (i.e., for TIP4P/2005 [100]) and differ for different water force fields [105]. Using the free energy correction term $\epsilon_{\mathrm{H_2O}}$, the computed excess chemical potentials of water in the liquid phase using the TIP4P/2005 [100] force field match the experimental values [105]. The free energy correction for the infinite dilution excess chemical potential of Marx H_2 ($\epsilon_{\mathrm{H_2}}$) in TIP4P/2005 water is independent of temperature and is equal to $\epsilon_{\mathrm{H_2}} = -0.27$ kJ mol^{-1} (computed in this chapter based on the solubilities of H_2 in water at 298 K and a H_2 fugacity of 1 bar).

Equating the chemical potential of water in the liquid phase with the gas phase results in [105]:

$$y_{\mathrm{H_2O}} = \frac{k_{\mathrm{B}} T \rho_{\mathrm{L,H_2O}}}{P \phi_{\mathrm{H_2O}}} \exp\left[\frac{\mu^{\mathrm{ex}}_{\mathrm{L,H_2O}}}{k_{\mathrm{B}} T}\right] \tag{8.3}$$

where $y_{\mathrm{H_2O}}$ is the gas phase mole fraction of water, $\phi_{\mathrm{H_2O}}$ is the fugacity coefficient of water, and $\rho_{\mathrm{L,H_2O}}$ is the number density of water in the

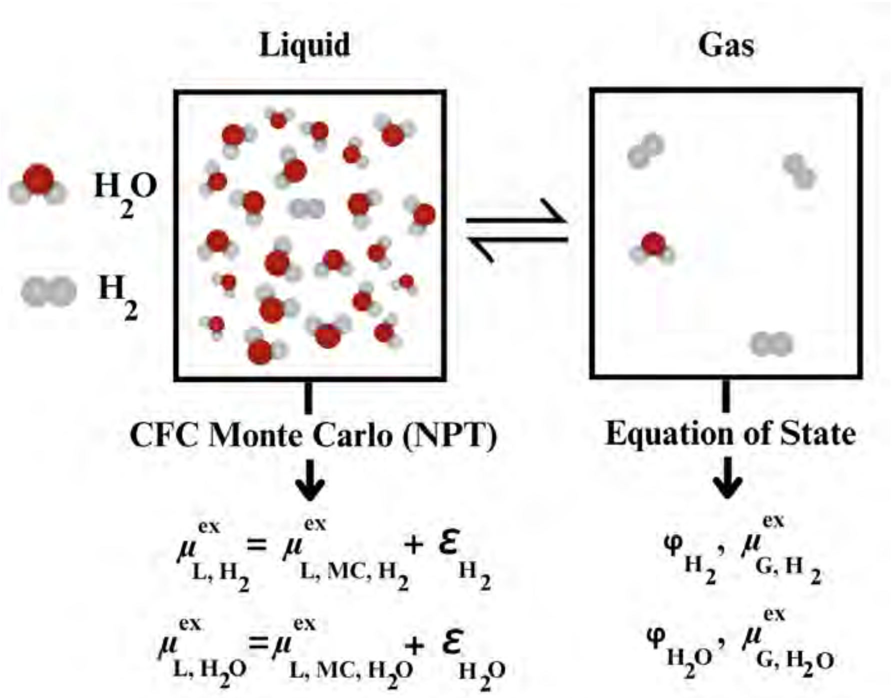

Figure 8.1. Schematic representation of the methodology used in this chapter. To compute the Vapor-Liquid Equilibrium of H_2 and aqueous electrolyte (i.e., KOH and NaCl) systems, the chemical potentials of water and H_2 in the liquid phase are equated with the gas phase chemical potentials at constant temperature and pressure. Continuous Fractional Component Monte Carlo [248–250] simulations are used to compute the excess chemical potentials ($\mu^{ex}_{L,MC,i}$ for species i) of water and H_2 in the liquid phase. These excess chemical potentials are then shifted using the free energy correction, ϵ_i, (as described in Ref. [105] and Eq. 8.1 in this chapter) to yield the final $\mu^{ex}_{L,i}$. The compositions of water and H_2 are computed using an iterative scheme as discussed in Section 8.2, in which the gas phase excess chemical potentials ($\mu^{ex}_{G,i}$) and fugacity coefficients (ϕ_i) are obtained from the GERG-2008 equation of state [123].

liquid phase (in units of molecules / m^3). Eq. 8.3 is derived in the Supplementary Material of Ref. [105]. Here, the gas phase consists of only H_2 and H_2O (i.e., $y_{H_2} + y_{H_2O} = 1$) since salts such as NaCl and KOH are not volatile. y_{H_2O}, y_{H_2}, and ρ_{L,H_2} (i.e., solubility of H_2 in the liquid phase) are unknowns. Eq. 8.3 is solved iteratively by initially assuming that $\phi_{H_2O} = 1$. Starting from an initial value of y_{H_2O} (and y_{H_2} as we have a binary gas mixture), the value of ϕ_{H_2O} is updated at the given composition, T, and P using the GERG-2008 EoS [123]. The new value of ϕ_{H_2O} is then used to update y_{H_2O}. This is repeated until y_{H_2O} is changed by less than 0.1 %. The non-ideality of gaseous H_2-H_2O mixtures are captured using GERG-2008 EoS [123] instead of using the TIP4P/2005 water and Marx H_2 force fields, as TIP4P/2005 cannot accurately model the virial coefficients of gaseous water [413, 414] and hence neither the non-idealities of the gas phase. After obtaining y_{H_2O} and y_{H_2}, the number density of H_2 in the liquid phase ρ_{L,H_2} can be computed using:

$$\rho_{L,H_2} = \frac{P\phi_{H_2}y_{H_2}}{k_BT}\exp\left[-\frac{\mu^{ex}_{L,H_2}}{k_BT}\right] \tag{8.4}$$

Eq. 8.4 is a rearrangement of Eq. 8.3 for H_2. Eq. 8.4 assumes that the excess chemical potential of H_2 in the liquid phase μ^{ex}_{L,H_2} is independent of the H_2 density in the aqueous phase i.e., that μ^{ex}_{L,H_2} is equal to the infinite dilution excess chemical potential, computed using a single fractional molecule of H_2 plus the correction term ϵ_{H_2}. This assumption is valid, as the mole fraction (i.e., solubility) of H_2 in the aqueous phase is well below 1% for all the conditions considered in this chapter [106]. ρ_{L,H_2} is converted to the unit of mole fraction in the aqueous phase using:

$$x_{H_2} = \frac{\rho_{L,H_2}\langle V\rangle}{n_{H_2O} + n_s + \rho_{L,H_2}\langle V\rangle}, \tag{8.5}$$

where $\langle V\rangle$ is the ensemble averaged volume of the simulation box, computed in the CFCNPT ensemble. n_{H_2O} and n_s are the number of moles of H_2O and salt (i.e., NaCl or KOH) in the simulation box, respectively. The activity of water (a_{H_2O}) can be computed using Eq. 7.4 (as discussed in chapter 7).

In all simulations, 2×10^5 equilibration cycles are carried out followed by 1×10^6 production cycles. A cycle refers to N trial moves, with N corresponding to the total number of molecules, with a minimum of 20. Trial moves are selected with the following probabilities: 29% rotations, 35% translations, 1% volume changes, 25% λ changes, and 10% reinsertions of fractional molecules at random locations inside the simulation box. The maximum displacements for volume changes, molecule translations, rotations, and λ changes are adjusted to obtain an acceptance probability of ca. 50%. For a detailed discussion on the CFCMC simulations the reader is referred to Refs. [55, 56]. For each pressure, temperature, and salt concentration, 100 independent simulations are performed. The Boltzmann probability distributions are averaged from blocks of 20 simulations to obtain 5 independent distributions for the order parameter λ of water and H_2, from which the uncertainties are computed. For all averaged distributions, the excess chemical potentials, activities of water, and solubilities of H_2 are calculated to obtain a mean value and the standard deviation of the 5 independent blocks. All raw data are listed in Table S8-S13 of the Supplementary Material of Ref. [429].

8.3. Results and discussion

8.3.1. Liquid phase densities and activities of water

Before computing the VLE of aqueous KOH/NaCl solutions and H_2, the densities and activities of water in the liquid phase are validated with respect to experimental data. Figure 8.2(a) and 8.2(b) show the liquid densities as functions of the salt molality for aqueous KOH and NaCl solutions, respectively, at 298 K and 363 K at 50 bar. The experimental correlations of Laliberté *et al.* [112] for aqueous NaCl and KOH solutions are used for comparison. These correlations can accurately model the densities of various aqueous salts (e.g., NaCl, KOH, LiCl, and $AlCl_3$) with average deviations of 0.1 kg m^{-3} compared to experiments. As shown in Figure 8.2(a) and 8.2(b), the MC results computed using the Madrid-Transport K^+ [111], the DFF/OH^- [47], and Madrid-2019 Na^+/Cl^- force fields [103] combined with TIP4P/2005 [100] can accurately model the variations of the liquid density with respect to KOH/NaCl molality and temperature compared to the experimental correlations (deviations smaller than 1%).

Figure 8.2(c) and 8.2(d) show the computed activities of water as functions of KOH/NaCl molalities at 298 K and 363 K at 50 bar. The experimental correlation of Balej. [435] and Clarke *et al.* [424] for activities of aqueous KOH and NaCl solutions are shown as solid lines in Figure 8.2(c) and 8.2(d), respectively. As shown in Figure 8.2(c), the activities of aqueous KOH solutions can be computed accurately with respect to experiments (within error bars) using the non-polarizable Madrid-Transport K^+ [111], DFF/OH^- [47] (with scaled charges of +0.75 [e] / -0.75 [e]), and TIP4P/2005 water. To the best of our knowledge, this is the first time that the activities of water in aqueous KOH solutions have been computed using molecular simulations. The experimental activities of water in aqueous KOH solutions show a small temperature dependence (i.e., ca. 3% deviation between a_{H_2O} at 298 K and 363, at 8 mol KOH / kg water). The slight increase of a_{H_2O} as a function of temperature is also observed in the MC simulations (Figure 8.2(c)), despite the fact that the error bars are of the same order of magnitude as the variations in temperature. As discussed by Resnik *et al.* [436] for aqueous NaCl,

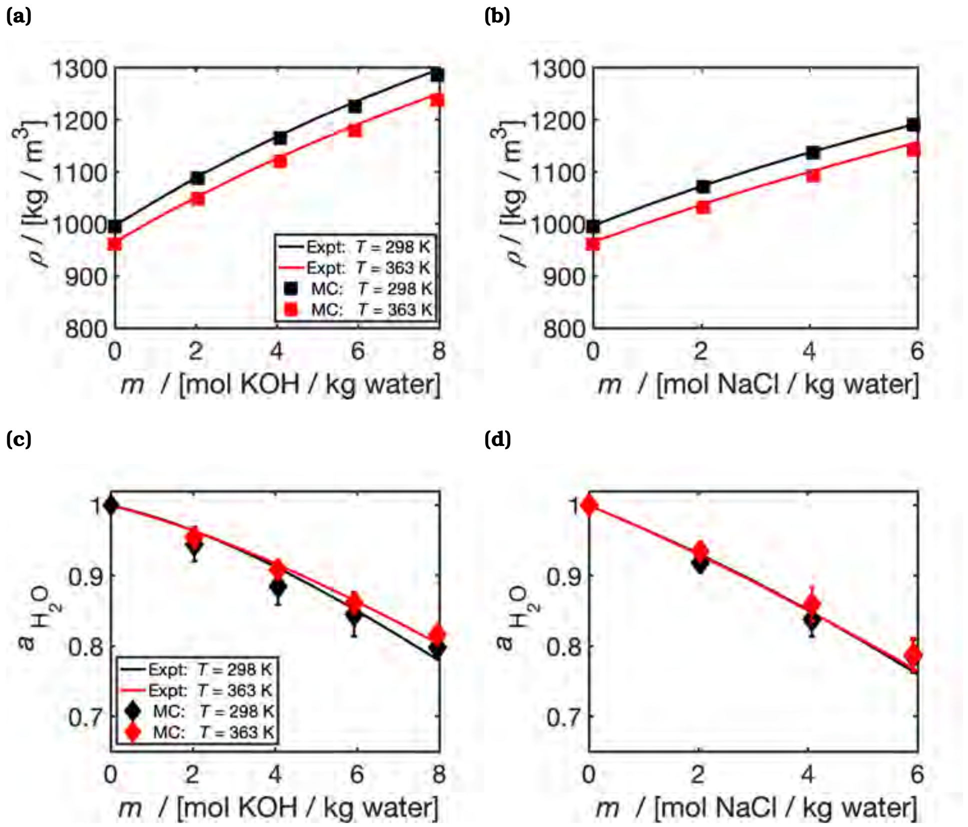

Figure 8.2. Computed liquid densities (ρ) in units of kg / m^3 solution for aqueous (a) KOH and (b) NaCl solutions as functions of salt molality (m) in units of mol salt / kg water. Computed activities of water for aqueous (c) KOH and (d) NaCl solutions as functions of m. ρ and a_{H_2O} are computed at 298 K and 363 K at 50 bar. The experimental correlation of Laliberté *et al.* [112] for densities of aqueous KOH and NaCl solutions is shown in (a) and (b) at 298 K and 363 K as solid lines. The experimental correlation of Balej. [435] and the data of Clarke *et al.* [424] for a_{H_2O} of aqueous KOH and NaCl solutions are used, respectively.

LiCl, and H_2SO_4 solutions, the temperature dependence of water activities depends on the specific salt type, and are mainly present at higher salt concentrations (i.e., up to 4 mol salt/kg water barely any temperature dependence is experimentally observed).

As shown in Figure 8.2(d), the non-polarizable Madrid-2019 Na^+/Cl^- force fields (with scaled charges of +0.85 / -0.85 [e]) combined with the TIP4P/2005 force field can accurately capture the experimental activities of water in aqueous NaCl solutions. These results are in line with the findings of Ref. [105]. Accurate modeling of the activities of water entails that the change in the chemical potential of water (i.e., $\mu^{\mathrm{ex}}_{\mathrm{H_2O},m} - \mu^{\mathrm{ex}}_{\mathrm{H_2O},0}$) and the liquid densities as a function of m are well-captured in the MC simulations. This also ensures that the variation of the water content in the gas phase ($y_{\mathrm{H_2O}}$) as a function of KOH/NaCl can be correctly predicted.

8.3.2. Gas phase fugacity coefficients

Accurate calculations for the VLE of water and H_2 systems require models that can model both the densities and excess chemical potentials of the liquid phase and the fugacity coefficients of the gas phase (as shown in Eq. 8.3 of the methodology section). Figure 8.3(a) shows the computed (using CFCMC simulations) excess chemical potentials of gaseous TIP4P/2005 ($\mu^{\mathrm{ex}}_{\mathrm{G,H_2O}}$) at 350 K as a function of P. The MC simulations are compared to data from REFPROP [421] and the GERG-2008 EoS [123]. $\mu^{\mathrm{ex}}_{\mathrm{G,H_2O}}$ is also approximated using the second virial coefficients of both gaseous water (experimental) and TIP4P/2005 water force field reported by Harvey *et al.* [437] and Rouha *et al.* [413], respectively. The relation between the fugacity coefficient of water, excess chemical potentials of water, and the second virial coefficient are shown in Appendix A.5. As shown in Figure 8.3(a), TIP4P/2005 overestimates the non-ideality of the gas phase (i.e., more negative excess chemical potentials) compared to the data of REFPROP [421]. The results of Figure 8.3(a) show that the TIP4P/2005 force field, which is trained on the liquid phase properties, should not be used to make predictions for the gas phase (e.g., for fugacities and $\mu^{\mathrm{ex}}_{\mathrm{G,H_2O}}$).

8

Instead of using classical non-polarizable force fields to model the gas phase, the GERG-2008 EoS [123] is used to model the relation between composition, T, P, ϕ, and the gas phase densities. The GERG-2008 EoS [123] is the ISO-standard for natural gasses and is trained based on 21 natural gasses (including H_2 and water vapor) and their binary mixtures. This EoS can model the excess chemical potentials of pure gaseous water with deviations of ca. 0.005 kJ/mol at 350 K and 0.3 bar (shown in Figure 8.3(a)). The computed fugacity coefficients (using the GERG-2008 EoS [123]) of water and H_2 as functions of pressure are shown in Figure 8.3(b) and 8.3(c). As shown in Figure 8.3, at pressures of already ca. 100 bar the fugacity coefficients of water and H_2 deviate by

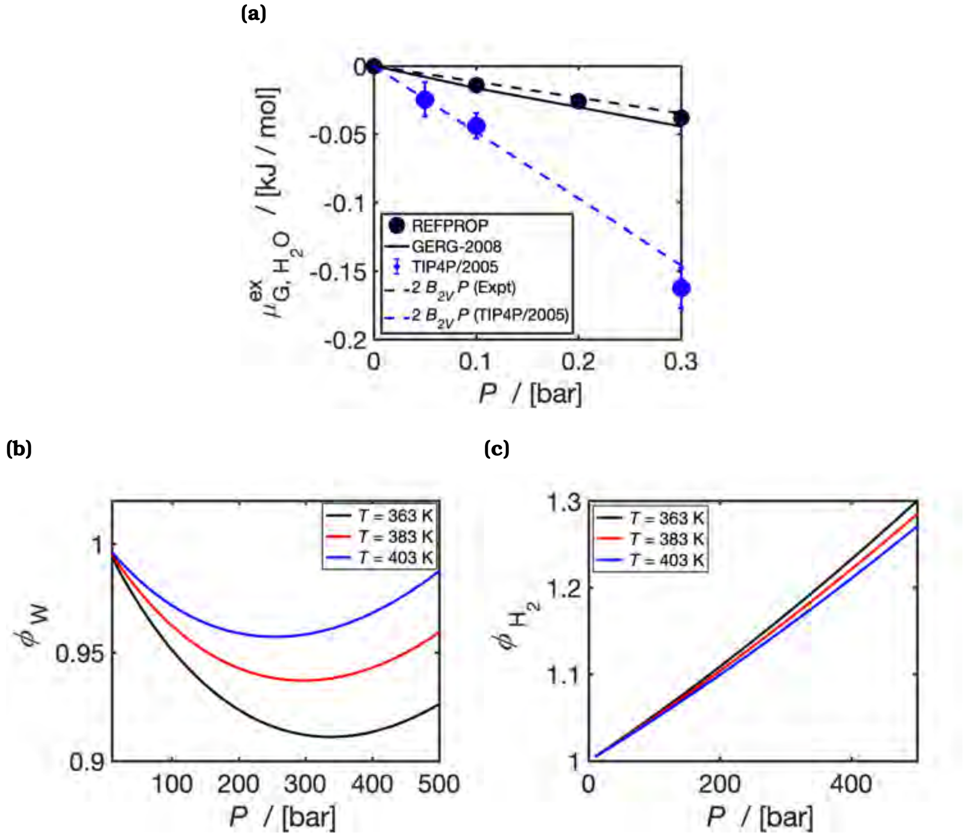

Figure 8.3. Computed (a) excess chemical potentials (i.e., μ^{ex}_{G,H_2O} with respect to the ideal gas reference state) of pure gaseous TIP4P/2005 water [100] as a function of pressure (P) at 350 K. The computed μ^{ex}_{G,H_2O} values are compared to the data from REFPROP [421] and GERG-2008 equation of state [123] for pure water. μ^{ex}_{G,H_2O} can be estimated from the second virial coefficients (B_{2V}) of water vapor (derivation is shown in Appendix A.5). Values of B_{2V} for water vapor (experimental) and TIP4P/2005 at 350 K are obtained from Harvey *et al.* [437] and Rouha *et al.* [413], respectively. Computed fugacity coefficients of (b) water (ϕ_{H_2O}) and (c) H_2 (ϕ_{H_2}) in the gas phase as functions of total pressure (P) at 363 K, 383 K, and 403 K. The fugacity coefficients are computed at a water mole fraction (y_{H_2O}) of 0.001 and a H_2 mole fraction (y_{H_2}) of 0.999 using the GERG-2008 equation of state [123].

more than 5% from ideality in a binary gas mixture with a water mole fraction of 0.001. Simple cubic EoS such as Peng-Robinson [423] (without optimizing the mixing rules) are not suitable for water and H_2 mixtures due to the polar nature of water as discussed by Rahbari *et al.* [106].

8.3.3. VLE of pure water and solubilities of H_2 in water

In this section, the computed VLE of pure water and solubilities H_2 in water are validated against experiments. Figures 8.4(a) and 8.4(b) show the computed saturated vapor pressures of water (P_{H_2O}) and solubilities of H_2 (x_{H_2O}) in water, respectively, as functions of temperature. The experimental correlation of Sako *et al.* [438] for the saturated vapor pressure of water and the correlation of Torín-Ollarves *et al.* [212] for the solubilities of H_2 in water are also shown in Figure 8.4(a) and 8.4(b), respectively. The results obtained with and without the free energy correction (as introduced in Eq. 8.1 and in Ref. [105]) are compared in Figure 8.4 . The free energy correction shifts the excess chemical potentials of water at infinite salt dilution, and allows for accurate modeling of the saturated vapor pressures of water using TIP4P/2005 [100]. Without the free energy correction, the saturated vapor pressures of TIP4P/2005 are underpredicted with respect to the experiments as shown in Figure 8.4(a) (i.e., by a factor of 4 at 298 K).

As shown in Figure 8.4(b), the solubilities of H_2 in water for a temperature range of 298-363 K can be accurately modeled using the Marx H_2 force field combined with TIP4P/2005 [100] water provided that a constant (temperature-independent) free energy correction (trained at 298 K) is applied to the infinite dilution excess chemical potential of H_2 in water. Kerkache *et al.* [433] have also accurately modeled the solubilities of H_2 in water using the Marx- TIP4P/2005 combination by modifying the LB [50] mixing rules. Kerkache *et al.* [433] state that deviating from LB [50] mixing rules (by a factor 1.05) indirectly corrects the influence of polarizability on the free energies leading to accurate excess chemical potentials of H_2. The Marx H_2 force field combined with the TIP4P/μ [110] water force field can accurately model the solubilities of H_2 in water at 298 K as shown in Figure S1 of the Supplementary Material of Ref. [429]. However, the variation of the H_2 solubilities with respect to temperature is not correctly captured (no minimum in H_2 solubility as observed experimentally [212]), resulting to an inaccurate prediction of H_2 solubilities in water at 363 K (by ca. 20%). As shown in this section, applying a free energy correction for H_2 and water is an alternative method to account for polarizability when using non-polarizable force fields which can lead to an accurate computation of both P_{H_2O} and x_{H_2}, and their temperature dependence.

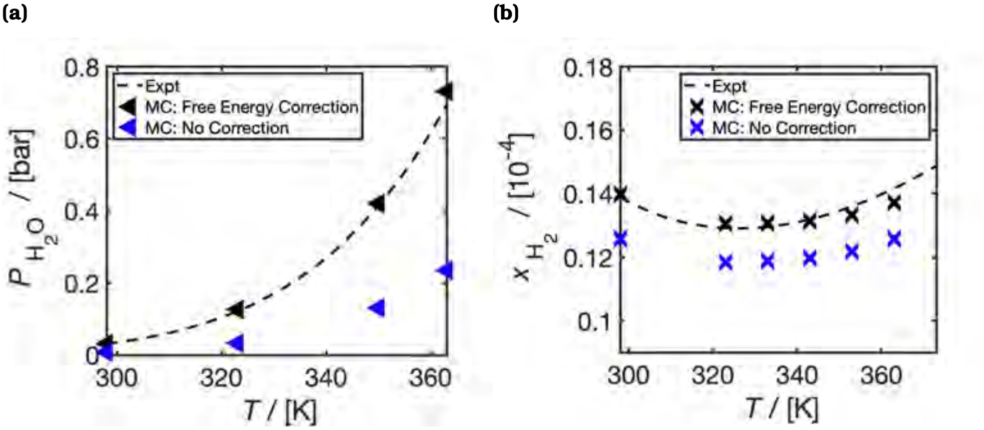

Figure 8.4. Computed (a) saturated vapor pressures of pure water (P_{H_2O}) as a function of temperature T at 1 bar, and (b) solubilities of H_2 (x_{H_2}) in units of mole fraction in the liquid phase at a H_2 fugacity of 1 bar. The experimental correlation of Sako *et al.* [438] is used for the saturated vapor pressures of water and the correlation of Torín-Ollarves *et al.* [212] is used for the solubilities of H_2 in water. The results computed using the free energy correction (as discussed in Eq. 8.1 and Ref. [105])) for both water and H_2 are compared with the results without the free energy correction.

8.3.4. VLE of aqueous KOH and NaCl solutions and H_2

Figure 8.5(a) and 8.5(b) show the equilibrium compositions for water vapor (y_{H_2O}) in H_2 and solubilities of H_2 (x_{H_2}), respectively, for H_2/H_2O/salt (i.e., KOH and NaCl) systems at 323 K. At $m = 0$ mol salt / kg water, the experimental data for y_{H_2O} in H_2 of Bartlett. [432], which are listed in the Supplementary Material of Ref. [106] are plotted for comparison. The experimental correlations of Torín-Ollarves *et al.* [212] for x_{H_2} in aqueous NaCl (for $m = 0$ and $m = 6$ mol NaCl / kg water) solutions are shown in Figure 8.5(b).

Obtaining both y_{H_2O} and x_{H_2} accurately for H_2/H_2O systems using molecular simulations is a difficult endeavour. As discussed by Rahbari *et al.* [106], the TIP4P/2005 water force field (without the free energy correction defined in Eq. 8.1]) cannot accurately capture y_{H_2O} because the saturated water vapor pressures are inaccurate, but can capture the experimental values of x_{H_2}. Other water force fields such as TIP3P can accurately predict y_{H_2O} and the saturated water vapor pressures but fail to yield precise x_{H_2} because the liquid water interactions are not correctly captured [106]. For this reason, prior studies [47, 48, 245] on molecular simulations of H_2/H_2O/salt (e.g., NaCl) systems mainly focus on the

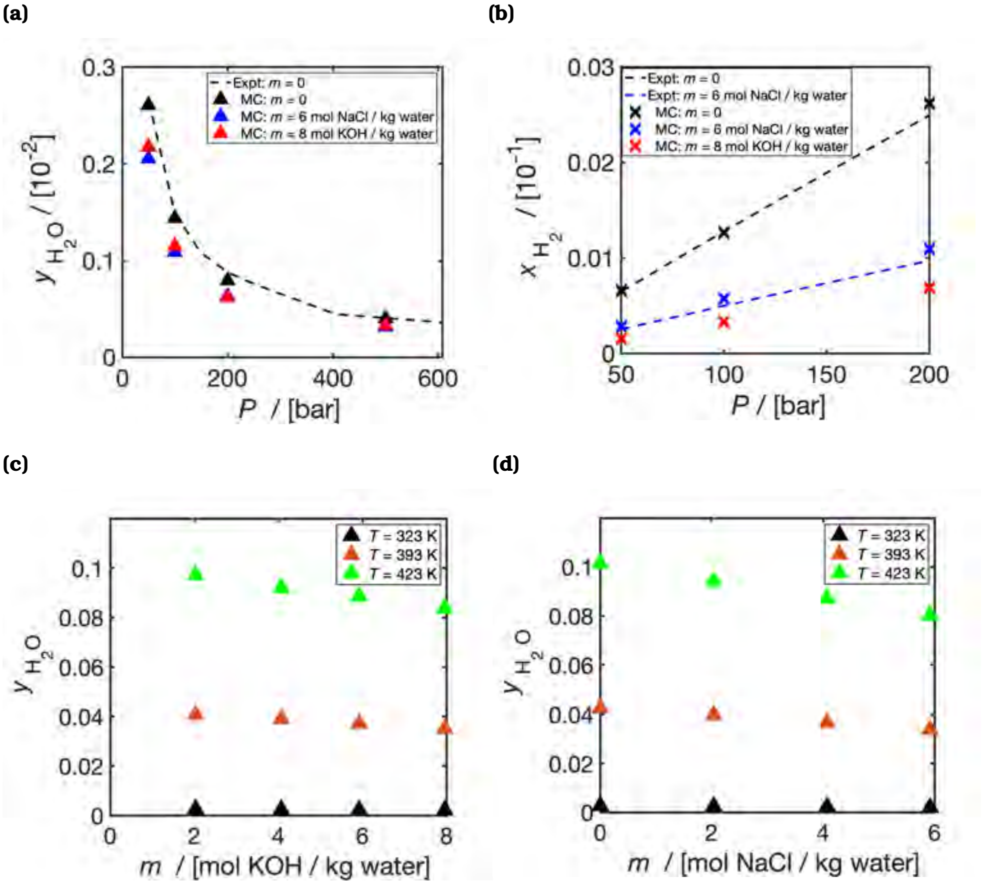

Figure 8.5. Computed Vapor-Liquid Equilibrium (VLE) composition of (a) water vapor (y_{H_2O}) in H_2 and of (b) H_2 (x_{H_2})in aqueous NaCl and KOH solutions as functions of pressure at 323 K. The experimental data listed in Ref. [106] at 323 K for y_{H_2O} of pure water (i.e., salt molality of m = 0 mol salt / kg water)-H_2 system are also shown (a). The experimental correlation of Torín-Ollarves *et al.* [212] for x_{H_2} in aqueous NaCl solutions is shown in (b) for $m = 0$ and $m = 6$ mol NaCl / kg water. The VLE composition of water vapor in H_2 as functions of m for (c) aqueous KOH and (d) NaCl solutions at 50 bar are shown for 298 K, 393 K, and 423 K.

solubilities of H_2 in the aqueous phase and do not consider the amount of water in the gas phase. Here, both y_{H_2O} and x_{H_2} are modeled accurately with respect to the experiments. As shown in Figure 8.5(a), the computed y_{H_2O} as a function of P shows an excellent agreement with the available experimental data at $m = 0$ and 323 K. The computed values of x_{H_2} at $m = 0$ and $m = 6$ mol NaCl/kg water also show an excellent agreement with respect to the experimental correlation (within 5% deviations).

As shown in Figure 8.5(a), the values for y_{H_2O} at $m = 6$ mol NaCl/kg water are quantitatively in line with the values computed at $m = 8$ mol KOH/kg water (both lower by ca. 20% from the data at $m = 0$). This is consistent with the fact that the activities of water for aqueous KOH at $m = 8$ mol KOH/kg water, and for aqueous NaCl at $m = 6$ mol NaCl/kg water are both ca. 0.80 (as shown in Figure 8.2(c) and 8.2(d)). The solubility of H_2 in the aqueous solution exhibits a stronger decrease as a function of the salt molalities (Figure 8.5(b)). This decrease of H_2 (which is a non-polar gas) solubilities is due to the salting-out effect [292] and is discussed in Refs. [47, 48, 212, 352, 433] for aqueous KOH and NaCl solutions.

Figure 8.5(c) and 8.5(d) show y_{H_2O} as a function of m for aqueous KOH and NaCl solutions, respectively, at 323 K, 393 K, and 423 K at 50 bar. Temperature has the strongest influence on y_{H_2O} (as discussed in Eq. 8.3, there is an exponential dependence to $1/T$). The salt molality changes the computed values of y_{H_2O} by ca. $10-25\%$ for a molality of 4-8 mol salt / kg water as shown in Figure 8.5, with NaCl having a stronger effect on y_{H_2O} values at a given molality compared to KOH. To the best of our knowledge, no other molecular simulation result is available for y_{H_2O} for H_2/H_2O/salt (i.e., KOH and NaCl) systems. The computed y_{H_2O} values for H_2/H_2O/salt systems can be used to model alkaline electrolyzers, electrochemical compression processes, and underground hydrogen storage. All raw data for the computed y_{H_2O} and x_{H_2} values for aqueous KOH / NaCl solutions at 10-500 bar and 298-423 K are shown in Tables S8-S13 of the Supplementary Material of Ref. [429].

8.4. Conclusions

In this chapter, for the first time the VLE of H_2 and aqueous KOH/NaCl solutions are computed at 298-423 K, 10-400 bar, 0-8 mol KOH/kg water, and at 0-6 mol NaCl/kg water using molecular simulations. The excess chemical potentials of water and H_2 are computed using CFCMC simulations. Free energy corrections are applied to the computed excess chemical potentials of water and H_2 to accurately model the experimental saturated vapor pressures of water and solubilities of H_2 in water using the TIP4P/2005 water force field and the Marx H_2 force field. Applying a constant free energy correction to the excess chemical potentials of Marx H_2 in TIP4P/2005 water (at salt molality of 0) results in accurate predictions for H_2 solubilities for a temperature range of 298-373 K. The densities and activities of water (and their temperature dependence) in the aqueous phase for aqueous KOH and NaCl solutions are modeled accurately using the non-polarizable Madrid-2019 force field of Na^+/Cl^-, Madrid-Transport force field of K^+, and the DFF/OH^- force field combined with TIP4P/2005 water (2% deviation with respect to experimental densities and water activities). The compositions of water and H_2 are computed using an iterative scheme from the liquid phase excess chemical potentials and densities, in which the gas phase fugacities are computed using the GERG-2008 EoS. For the first time, the equilibrium compositions of both water and H_2 (and their pressure dependence) for systems of H_2 and aqueous KOH/NaCl solutions are modeled with excellent agreement with respect to the available experimental data (within 5%) without any additional refitting of force fields or changing the LB mixing rules. The VLE data provided in this chapter can be used to model the water content in the H_2 stream of alkaline electrolyzers (for aqueous KOH solutions) and for underground hydrogen storage (for aqueous NaCl solutions).

9

Conclusions & Outlook

Molecular simulations are a versatile tool for screening of new materials for hydrogen storage and for predicting the thermophysical properties of H_2 in aqueous systems at high pressures and temperatures.

In this thesis, we use Density Functional Theory (DFT), Born-Oppenheimer Molecular Dynamics (BOMD), and Nudged Elastic Band (NEB) calculations to optimize H_2 storage capacities and adsorption/desorption kinetics for hydrogen storage in 2D boron based materials. We show that in their pristine form (i.e., without any addition of metal dopants or structural engineering), borophene, borophene hydride, and borophene oxide based materials are not suitable for H_2 storage. The physical adsorption energy of H_2 with the 2D substrate is too weak (i.e., ca. -0.10 eV / H_2) to allow for any practical H_2 capacity at ambient conditions. Different metal atoms such as Li, Na, and K enhance the adsorption energy of H_2 with the 2D substrate. Li atoms are particularly promising as dopants due to their low mass and strong adsorption energy (with respect to the cohesion energy in bulk Li) on the 2D boron based substrate. A Li doped borophene oxide structure is designed, which has a theoretical gravimetric capacity of 8.3 wt% H_2 (exceeding the US DOE target of 5.5 wt% H_2). Li decorating atoms are shown to also influence the chemisorption properties (i.e., hydrogenation and dehydrogenation reaction pathways) of H_2 in 2D boron structures. In this work, a Li doped borophene hydride structure with low energy barriers for hydrogenation and dehydrogenation was designed, suitable for chemisorption of hydrogen.

A major shortcoming of DFT and NEB calculations is that predictions are made at 0 K. To optimize the adsorption and desorption conditions, it is essential to compute the storage capacity of H_2 at finite temperatures and pressures. In this thesis, empirical equations are used to calculate H_2 capacities under adsorption conditions of 298 K and 30 atm, and desorption conditions of 373 K and 3 atm. For this calculation, it is assumed that the average adsorption energy of H_2 with the 2D substrate (computed at 0 K) is the same at 298-373 K and is independent of site-site interactions for the adsorption/desorption processes. To calculate the adsorption and desorption capacities at finite temperatures and pressures without these assumptions, the computational expense of ab-initio based MD simulations needs to be reduced to simulate longer time scales. This is because the length scales and time scales achievable with ab-initio MD (typically around ca. 100 atoms for 5-50 ps) are insufficient for modeling adsorption and desorption processes. To accelerate ab-initio calculations, further simulations are encouraged using machine-learned interaction potentials trained using DFT simulations. Experimental studies are also required to validate the H_2 capacities in Li-decorated boron structures and to find low-cost synthesis routes.

To calculate thermodynamic and transport properties of H_2 in aqueous electrolyte systems, non-polarizable force fields are used here. The simplicity and computational efficiency of non-polarizable force fields allows to reach time scales required for computing thermodynamic and transport properties. We show that the interfacial tensions of $H_2/H_2O/NaCl$ systems and the salting out of H_2 in aqueous NaCl solutions can be accurately computed (i.e., with respect to experiments) using the Madrid-2019 Na^+ and Cl^- force fields (with ion charges of +0.85 and -0.85 [e]) combined with the TIP4P/2005 water force field. The same force field combination results in ca. 100 % deviation from experiments when computing the shear viscosities of aqueous NaCl solutions at 298 K and 5 mol NaCl/kg water. To accurately compute the shear viscosities and self-diffusivities of H_2 in concentrated aqueous NaCl solutions (i.e., above 2 mol NaCl/kg water), a different Na^+ and Cl^- model, namely the Madrid-Transport force field, with charges of +0.75 and -0.75 [e]) force field is required. This entails that the simplicity of non-polarizable force fields introduces a fundamental inaccuracy that results in requiring different force fields depending on the property of interest. This limitation can affect the coherence of simulation results, particularly when generating comprehensive data sets for both thermodynamic and transport properties.

The thermophysical properties of H_2 in aqueous electrolyte solutions such as aqueous KOH, NaOH (for alkaline electrolyzers) and $NaB(OH)_4$ (for $NaBH_4$ hydrolysis) solutions are also computed. We parameterized new non-polarizable force fields for OH^- and $B(OH)_4{}^-$, which can accurately (within 5% deviation from experiments) predict densities and viscosities of aqueous KOH, NaOH, and $NaB(OH)_4$ solutions. The new classical OH^- force field cannot describe the unusually high self-diffusivity of OH^-, which originates from the proton transfer mechanism in the aqueous solution. To capture this proton transfer mechanism, reactive force fields or machine-learned potentials based on quantum chemical calculations could be used. Despite this, the newly parameterized OH^- force field (with an overall charge of -0.75 [e]) can be used to predict self-diffusivities and solubilities of H_2 in aqueous KOH and NaOH solutions at molalities up to 8 mol salt / kg water, as the viscosities and densities of the solutions are accurately modeled. For $B(OH)_4^-$, an ion charge of -0.85 [e] resulted in more accurate estimations of both viscosities and ionic conductivities compared to an ion charge of -0.75 [e]. This indicates that depending on the type of salt (e.g., NaOH or $NaB(OH)_4$), a different optimum charge scaling can be found for modeling the transport properties of the aqueous solution, and that the charge scaling remains a 'fitting' parameter that changes depending on the type of system that is modeled. The need for different force field combinations for different mixtures emphasizes the importance of consistently validating simulations with experimental data, as scaled charge ion force fields are not fully transferable. Development of machine-learned force fields based on ab-initio simulations [439, 440] can potentially mitigate these issues, as these force field can naturally capture the polarizability of aqueous systems, thereby addressing the inaccuracy of simpler non-polarizable force fields.

Another fundamental issue of non-polarizable force fields is that force fields fitted to the free energies cannot accurately predict transport properties of aqueous electrolyte solutions as these force fields exclude the self-polarization energy of water (i.e., the "missing term" mentioned in the title of the paper by Berendsen et al. [98]). Force fields of water such as the TIP4P/2005 and scaled charge ion force fields such as Madrid-2019 and Madrid-Transport, which are trained on liquid phase transport properties, cannot accurately describe the free energy of water in the liquid phase and the second virial coefficients of water vapor. This leads to inaccurate predictions for the Vapor-Liquid Equilibria of H_2/H_2O/salt systems. In this thesis, we developed a new approach in which an additional temperature-independent charge surface is used to correct the free energy of liquid water in the absence of salts, to obtain a free energy correction which can be used in the presence of salts. The compositions of water and H_2 at equilibrium are accurately computed from the liquid phase free energies using an iterative scheme in which the gas phase non-idealities are described using the GERG-2005 EoS instead of using the TIP4P/2005 water force field (as the same dipole moment used to model liquid water cannot describe water vapor). Similar issues are observed in literature for modeling the free energy difference of the liquid water-ice phase transition [428, 441]. Further research is required to investigate if a similar approach can be used to accurately compute free energy differences between water (combined with salts) and ice as free energy differences have a significant influence on computed nucleation rates of ice.

A

Appendix

A.1. Sample simulation input and output files

Sample simulation input and output files for each chapter in this thesis (except the Introduction and Conclusions) are available in the 4TU data repository to ensure clarity and reproducibility of the data. The corresponding DOI link for each chapter is provided below:

- Chapter 2: `https://doi.org/10.4121/19391945.v1`
- Chapter 3: `https://doi.org/10.4121/19391960.v1`
- Chapter 4: `https://doi.org/10.4121/22211650.v1`
- Chapter 5: `https://doi.org/10.4121/21941327.v1`
- Chapter 6: `https://doi.org/10.4121/55e208e7-32ea-4beb-9234-596086884092.v1`
- Chapter 7: `https://doi.org/10.4121/00da62fc-9204-435c-a627-1ba2bde58bc1.v1`
- Chapter 8: `https://doi.org/10.4121/79ef09f1-b5c4-45ff-8bc7-648426be6e7b.v1`

A.2. Force field details

Table A.1. Parameters for TIP4P/2005 [100] and TIP4P/μ water force fields (discussed in the Supporting Information of Ref. [110]). σ and ϵ are the Lennard-Jones parameters, q are atomic partial charges, and l is the bond length. σ and l are in units of Å, ϵ is in units of kJ/mol, and q is in units of the elementary charge e. In all force fields, the charge on O is on a massless site M, which is equidistant from both H atoms.

	TIP4P/2005 [100]	TIP4P/μ [110]
$\mathsf{H-\widehat{O}-H}$ (°)	104.52	104.52
$l_{\mathsf{O-H}}$	0.9572	0.9572
$l_{\mathsf{O-M}}$	0.1546	0.1546
σ_{OO}	3.1589	3.1589
σ_{HH}	0	0
ϵ_{OO}	0.774908	0.663989
ϵ_{HH}	0	0
q_{O}	0	0
q_{M}	−1.1128	−1.06272
q_{H}	0.5564	0.53136

Table A.2. Parameters for the three-site Marx [91] H_2 force field. σ and ϵ are the Lennard-Jones parameters, q is the atomic partial charge, dummy site L is the geometric center of mass, and l is the bond length. σ and l are in units of Å, ϵ is in units of kJ/mol, and q is in units of the elementary charge e.

σ_{LL}	2.958
ϵ_{LL}	0.305141
q_{H}	0.468
q_{L}	−0.936
$l_{\mathsf{H-H}}$	0.74

Table A.3. Parameters for the Madrid-2019 [103] Na^+/Cl^- force field. σ and ϵ are the Lennard-Jones parameters and q is the atomic partial charge. σ is units of Å, ϵ is in units of kJ/mol, and q is in units of the elementary charge e. O_w refers to the O-atom of water (TIP4P/2005 [100] force field).

$\sigma_{Na^+Na^+}$	2.21737
$\sigma_{Na^+Cl^-}$	3.00512
$\sigma_{Cl^-Cl^-}$	4.69906
$\sigma_{Na^+O_w}$	2.60838
$\sigma_{Cl^-O_w}$	4.23867
$\epsilon_{Na^+Na^+}$	1.472356
$\epsilon_{Na^+Cl^-}$	1.438894
$\epsilon_{Cl^-Cl^-}$	0.076923
$\epsilon_{Na^+O_w}$	0.793388
$\epsilon_{Cl^-O_w}$	0.061983
q_{Na^+}	0.85
q_{Cl^-}	-0.85

Table A.4. Parameters for the Madrid-Transport [111] K^+ force field. σ and ϵ are the Lennard-Jones parameters and q is the atomic partial charge. σ is units of Å, ϵ is in units of kJ/mol, and q is in units of the elementary charge e. O_w refers to the O-atom of water (TIP4P/2005 [100] force field).

$\sigma_{K^+O_w}$	2.89540
$\sigma_{K^+K^+}$	2.30140
$\epsilon_{K^+K^+}$	1.985740
$\epsilon_{K^+O_w}$	1.400430
q_{K^+}	0.75

A.3. The partition function and the ECS free energy correction

We derive an expression for the partition function in the isobaric-isothermal ensemble (Q_{NPT}) after applying the free energy correction to the isolated molecule partition function of water in the liquid phase (as discussed in chapter 7).

A schematic representation of the simulation box is shown in Figure A.1. In the simulation box (liquid phase), molecules are subjected to a background potential that adds an additional temperature-dependent energy contribution (ϵ_i) to the isolated molecule partition function (q_i) of molecule type i. We will derive how this background energy changes the partition function of the system. The partition function in the isobaric-isothermal ensemble (Q_{NPT}) for a mixture of n_t components is equal to [50, 54]:

$$Q_{\mathrm{NPT}} = \frac{P}{k_{\mathrm{B}}T}\left(\prod_{i=1}^{n_t}\frac{q_i^{N_i}}{N_i!\Lambda_i^{3N}}\right)\int \mathrm{d}V V^N \exp\left[\frac{-PV}{k_{\mathrm{B}}T}\right]\int \mathrm{d}\mathbf{s}^N \exp\left[\frac{-U(\mathbf{s}^N)}{k_{\mathrm{B}}T}\right] \tag{A.1}$$

where P, V, k_{B}, T, Λ_i , N, $\mathbf{s}^N$, and $U(\mathbf{s}^N)$ refer to pressure, volume, Boltzmann constant, temperature, the thermal wavelength of component i, total number of molecules, the scaled position vector of all molecules, and the internal energy of the system (which is a function of $\mathbf{s}^N$). q_i and N_i are the isolated molecule partition function (excluding the translational part) and the number of molecules of type i, respectively. q_i can be expressed as [54]:

$$q_i = \sum_j \exp\left[-\frac{\epsilon_{\mathrm{el},j} + \epsilon_{\mathrm{rot},j} + \epsilon_{\mathrm{vib},j} + \epsilon_i}{k_{\mathrm{B}}T}\right] \tag{A.2}$$

$\epsilon_{\mathrm{el},j}$, $\epsilon_{\mathrm{rot},j}$, $\epsilon_{\mathrm{vib},j}$, are the electronic, rotational, and vibrational energy of intramolecular system state j. As these do not depend on the free energy correction ϵ_i, we can group these terms together in a term $q_{0,i}$. ϵ_i is not a function of the intramolecular system state j and can be factored out of the summation:

$$q_i = q_{0,i} \exp\left[\frac{\epsilon_i}{k_{\mathrm{B}}T}\right] \tag{A.3}$$

By combining Eq. A.3 and Eq. A.1, we obtain:

$$Q_{\mathrm{NPT}} = \frac{P}{k_{\mathrm{B}}T}\left(\prod_{i=1}^{n_t}\frac{q_{0,i}^{N_i}\exp\left[\frac{N_i\epsilon_i}{k_B T}\right]}{N_i!\Lambda_i^{3N}}\right)\int \mathrm{d}V V^N \exp\left[\frac{-PV}{k_{\mathrm{B}}T}\right]\int \mathrm{d}\mathbf{s}^N \exp\left[\frac{-U(\mathbf{s}^N)}{k_{\mathrm{B}}T}\right] \tag{A.4}$$

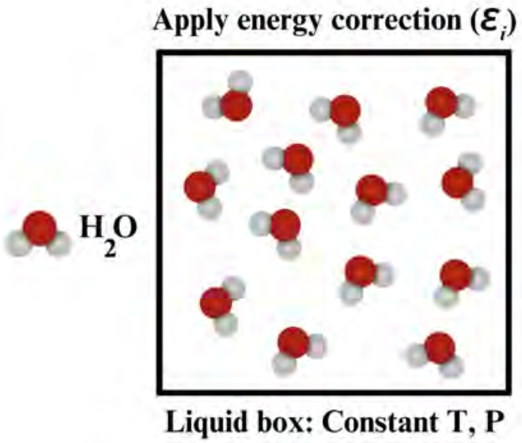

Figure A.1. Simulation box of liquid water at constant temperature (T) and pressure (P). A background energy for component i (ϵ_i) is applied to modify the free energies computed from the Potential Energy Surface (PES).

As multiplying exponential functions is equivalent to summing the exponents, we have:

$$\prod_{i=1}^{n_t} \exp\left[\frac{N_i \epsilon_i}{k_\mathrm{B} T}\right] = \exp\left[\sum_{i}^{n_t} \frac{N_i \epsilon_i}{k_\mathrm{B} T}\right] \tag{A.5}$$

Note that ϵ_i (a function of T) is not a function of V or $\mathbf{s}^N$. Therefore, Eq. A.4 can be reformulated as:

$$Q_\mathrm{NPT} = \frac{P}{k_\mathrm{B} T}\left(\prod_{i=1}^{n_t} \frac{q_{0,i}^{N_i}}{N_i! \Lambda_i^{3N}}\right) \int \mathrm{d}V V^N \exp\left[\frac{-PV}{k_\mathrm{B} T}\right] \int \mathrm{d}\mathbf{s}^N \exp\left[\frac{-U(\mathbf{s}^N) + \sum_i^{n_t} N_i \epsilon_i}{k_\mathrm{B} T}\right] \tag{A.6}$$

The ensemble averaged volume ($\langle V \rangle$) can be computed by taking the partial derivative of $\ln(Q_\mathrm{NPT})$ with respect to P at constant T and N (for all molecular species) [54]:

$$\langle V \rangle = -k_\mathrm{B} T \left(\frac{\partial \ln(Q_{NPT})}{\partial P}\right)_{T,N} \tag{A.7}$$

The chemical potential of species i (μ_i) can be computed by taking the partial derivative of $\ln(Q_\mathrm{NPT})$ with respect to N_i at constant T, P, and N_j (for $j \neq i$):

$$\mu_i = -k_{\mathrm{B}}T\left(\frac{\partial \ln(Q_{NPT})}{\partial N_i}\right)_{T,P,N_{j,j\neq i}} \tag{A.8}$$

For computing $\langle V\rangle$ and μ_i, we first need to evaluate $\ln(Q_{NPT})$. Considering that multiplication inside the natural logarithm is equal to the summation of the natural logarithms (i.e., $\ln(AB) = \ln(A) + \ln(B)$) and that ϵ_i is not a function of $\mathbf{s}^N$, we can express $\ln(Q_{NPT})$ as:

$$\ln(Q_{\mathrm{NPT}}) = \ln\left(\frac{P}{k_{\mathrm{B}}T}\left(\prod_i^{n_t}\frac{q_{0,i}^{N_i}}{N_i!\Lambda_i^{3N}}\right)\int \mathrm{d}VV^N\exp\left[\frac{-PV}{k_{\mathrm{B}}T}\right]\int \mathrm{d}\mathbf{s}^N\exp\left[\frac{-U(\mathbf{s}^N)}{k_{\mathrm{B}}T}\right]\right) + \sum_i^{n_t}\frac{N_i\epsilon_i}{k_{\mathrm{B}}T} \tag{A.9}$$

Taking the partial derivative of $\ln(Q_{NPT})$ with respect to P results in cancellation of the terms containing ϵ_i, as these are not functions of P (and only a weak function of T, as explained in chapter 7). This means that $\langle V\rangle$ does not depend on the correction term ϵ_i and hence the pressure of the system is unaltered. Evaluating Eq. A.8 results in three seperate terms for the chemical potential of species i:

$$\mu_i = \mu_i^{\mathrm{id}} + \mu_{i,\mathrm{PES}}^{\mathrm{ex}} + \epsilon_i \tag{A.10}$$

The first term is the ideal gas term (μ_i^{id}), which depends on the isolated molecule partition function (excluding the contribution of ϵ_i) and the density. $\mu_{i,\mathrm{PES}}^{\mathrm{ex}}$ is determined by the force field used to describe the PES. The third term is the correction term which shifts the chemical potential of species i obtained using the PES by ϵ_i. This adjustment to the partition function ensures that the excess chemical potentials are corrected without changing the average volume $\langle V\rangle$, transport properties, the liquid structure, and the pressure P.

A.4. Relation between pressure and excess chemical potential

We derive an equation relating the pressure and composition of a multi-component gas mixture to the excess chemical potentials in the liquid phase (Eq. 7.5) at VLE. At a given temperature (T) and pressure (P), chemical equilibrium dictates that chemical potentials of each species i in the gas phase are equal to the chemical potential of the same species in the liquid phase [54, 106]:

$$k_\mathrm{B}T\ln\left(\frac{\rho_{\mathrm{G},i}}{\rho_0}\right)+\mu^\mathrm{ex}_{\mathrm{G},i}=k_\mathrm{B}T\ln\left(\frac{\rho_{\mathrm{L},i}}{\rho_0}\right)+\mu^\mathrm{ex}_{\mathrm{L},i} \tag{A.11}$$

where k_B, $\rho_{\mathrm{G},i}$, $\rho_{\mathrm{L},i}$, $\mu^\mathrm{ex}_{\mathrm{G},i}$, and $\mu^\mathrm{ex}_{\mathrm{L},i}$ refer to the Boltzmann constant, gas phase number density of species i, liquid phase number density of species i, excess chemical potential (with respect to the ideal gas reference state) in the gas phase for species i, and the excess chemical potential in the liquid phase for species i, respectively. ρ_0 is a reference number density (equal to 1 m^{-3}) to make the arguments of the natural logarithm unitless. $\mu^\mathrm{ex}_{\mathrm{G},i}$ is related to the fugacity coefficient of species i (ϕ_i) in the gas phase [106]:

$$\mu^\mathrm{ex}_{\mathrm{G},i}=k_\mathrm{B}T\ln\left(\frac{y_iP\phi_i}{k_\mathrm{B}T\rho_{\mathrm{G},i}}\right) \tag{A.12}$$

where y_i is the mole fraction of species i in the gas phase. This equation is derived in the Supporting Information of Ref. [106]. After substituting $\mu^\mathrm{ex}_{\mathrm{G},i}$ in Eq. A.11 by Eq. A.12, we obtain:

$$y_iP=\frac{k_\mathrm{B}T\rho_{\mathrm{L},i}}{\phi_i}\exp\left[\frac{\mu^\mathrm{ex}_{\mathrm{L},i}}{k_\mathrm{B}T}\right] \tag{A.13}$$

For a multi-component mixture with n_t number of species, we have n_t+1 number of unknowns (i.e., P and n_t values for y_i) and n_t+1 number of equations (i.e., n_t different versions of Eq. A.13 for each species, and $\sum_i^{n_t} y_i = 1$). This set of equations can be solved iteratively using an equation of state for the gas phase, which is often available. In chapter 7, we only consider a single species (i.e., water) in the gas phase (i.e., $y_\mathrm{w} = 1$). In chapter 8, we have binary H_2-H_2O gas mixtures. Eq. A.13 is solved iteratively by initially starting with $\phi_\mathrm{w} = 1$. After computing a first estimate of P using Eq. A.13, an improved estimate for ϕ_w is computed using an equation of state for the gas phase. In chapter 7, the Peng-Robinson equation of state [422, 423] is used. In chapter 8, the GERG-2008 equation of state [123] is used, as this equation is more accurate for modeling binary H_2-H_2O gas mixtures. This iterative scheme is stopped after the values of P and ϕ_w change by less than 0.1%.

A.5. Relation between the second virial coefficient and the excess chemical potentials of dilute gasses

We derive an equation relating the excess chemical potential of species i in the gas phase ($\mu^{\text{ex}}_{\text{G},i}$) to the second virial coefficient (pressure expansion) of the pure gas of species i ($B_{2P,i}$). In chapter 8, the equation derived in this section is applied to a single (pure) component system of water vapor. The excess chemical potential of component i in the gas phase, $\mu^{\text{ex}}_{\text{G},i}$, is related to the the fugacity coefficient (ϕ_i) of species i via Eq. A.12. As $y_i = N_i/N_\text{t}$ (where N_t and N_i are the total number of molecules and the number of molecules of type i in the gas phase, respectively), Eq. A.12 can be reformulated:

$$\mu^{\text{ex}}_{\text{G},i} = k_\text{B}T\ln\left(\frac{N_i\phi_iPV}{N_\text{t}RTN_i}\right) = k_\text{B}T\ln\left(Z_\text{mix}\phi_i\right) = k_\text{B}T(\ln(Z_\text{mix}) + \ln(\phi_i)) \quad \text{(A.14)}$$

where $Z_\text{mix} = (PV)/(k_\text{B}TN_\text{t})$ is the compressibility factor of the total gas mixture. For the gas mixture at relatively low pressure P, the Lewis-Randall rule [69] can be applied to approximate the fugacity of species i (f_i) in the mixture in terms of the fugacity of the pure gas of species i ($f_{\text{pure},i}$) at the same total pressure:

$$f_i \approx y_i f_{\text{pure},i} = \phi_{\text{pure},i} y_i P \quad \text{(A.15)}$$

where $\phi_{\text{pure},i}$ is the fugacity coefficient of the pure gas of species i at a given T and P. The compressibility factor of the pure solution of species i ($Z_{\text{pure},i}$) can be approximated using the virial expansion (in terms of pressure P) [69]:

$$Z_{\text{pure},i} = \frac{PV}{N_i k_\text{B}T} \approx 1 + B_{2P,i}P \quad \text{(A.16)}$$

where $B_{2P,i}$ is the second virial coefficient of species i (in the pressure expansion) in units of Pa^{-1}. $\phi_{\text{pure},i}$ is related to $Z_{\text{pure},i}$ and $B_{2P,i}$ via [69]:

$$\ln(\phi_{\text{pure},i}) = \int_0^P \frac{Z_{\text{pure},i} - 1}{p}\,\text{d}p \approx B_{2P,i}P \quad \text{(A.17)}$$

Combining Eq. A.17 and Eq. A.14 results in:

$$\mu^{\text{ex}}_{\text{G},i} \approx k_\text{B}T(\ln(Z_\text{mix}) + B_{2P,i}P) \quad \text{(A.18)}$$

Eq. A.18 relates the excess chemical potential of species i to the second virial coefficient of the pure system of species i and the compressibility factor of the mixture, which can be easily computed using molecular simulations. For small values of $\mu^{\text{ex}}_{\text{G},i}$ (i.e., ca. 0.01 kJ/mol), computing $\mu^{\text{ex}}_{\text{G},i}$ directly using molecular simulations is not efficient. This is because long simulations are required to reduce the relative error of $\mu^{\text{ex}}_{\text{G}}$. Eq. A.18 can be used as an alternative for predicting $\mu^{\text{ex}}_{\text{G},i}$ as it is easy to compute the second virial coefficient in the gas phase from NPT simulations (i.e., by plotting $\left[\frac{P\langle V\rangle}{Nk_{\text{B}}T} - 1\right]/P$ as a function of applied pressure P and extrapolating to $P \to 0$) [54].

The excess chemical potential of the pure gas of species i ($\mu^{\text{ex}}_{\text{G,Pure},i}$) can be calculated using $Z_{\text{pure},i}$ and $B_{2P,i}$ using:

$$\mu^{\text{ex}}_{\text{G,Pure},i} \approx k_{\text{B}}T(\ln(1 + B_{2P,i}P) + B_{2P,i}P) \approx 2k_{\text{B}}TB_{2P,i}P \tag{A.19}$$

in which the Taylor series expansion of the natural logarithm is used to approximate $\ln(1 + B_{2P,i}P)$ as $B_{2P,i}P$. Note that in this section, we have derived a relation in terms of the pressure-based second virial coefficient. The density-based second virial coefficient (i.e., $B_{2V,i}$ in units of volume per molecule) can also be used to predict $\mu^{\text{ex}}_{\text{G,Pure},i}$. The relation $B_{2P,i} = B_{2V,i}/(k_{\text{B}}T)$ can be used [69] to rewrite Eq. A.19 in terms of $B_{2V,i}$:

$$\mu^{\text{ex}}_{\text{G,Pure},i} \approx 2B_{2V,i}P \tag{A.20}$$

In chapter 8, we use Eq. A.20 to compare excess chemical potentials in the gas phase of TIP4P/2005 [100] computed in this work (using Monte Carlo simulations) with the reported density-based second virial coefficients of TIP4P/2005 by Rouha *et al.* [413].

It is instructive to show that for a pure component system with pair interactions, Eq. A.20 is consistent with the low density approximations for the excess energy ($U^{\text{ex}}_{\text{Pure},i}$) and excess entropy ($S^{\text{ex}}_{\text{Pure},i}$) of species i. For the excess energy, $U^{\text{ex}}_{\text{Pure},i}$ we have [50, 442]:

$$U^{\text{ex}}_{\text{Pure},i} = \frac{2\pi N_i^2}{V} \int_0^{\infty} u(r)g(r)r^2\,\text{d}r \tag{A.21}$$

in which $u(r)$ is the pair interaction potential for two molecules (of species i) at distance r. For excess entropy, $S^{\text{ex}}_{\text{Pure},i}$ we have the following low density approximation [443]:

$$S^{\text{ex}}_{\text{Pure},i} \approx \frac{-2\pi N_i^2 k_{\text{B}}}{V} \int_0^{\infty} (g(r)\ln[g(r)] - g(r) + 1)\, r^2\,\text{d}r \tag{A.22}$$

Note that to compute Eqs. A.24 and A.25 for finite-size systems one may need to consider finite-size effects for both $g(r)$ [444] and the integrals over volume [445]. $\mu^{\text{ex}}_{\text{Pure},i}$ is related to the excess entropy, $S^{\text{ex}}_{\text{Pure},i}$ and excess energy, $U^{\text{ex}}_{\text{G,Pure},i}$ using the definition [442]:

$$\mu^{\text{ex}}_{\text{G,Pure},i} = \left(\frac{\partial A^{\text{ex}}_{\text{Pure},i}}{\partial N_i}\right)_{T,V} = \left(\frac{\partial U^{\text{ex}}_{\text{Pure},i}}{\partial N_i}\right)_{T,V} - T\left(\frac{\partial S^{\text{ex}}_{\text{Pure},i}}{\partial N_i}\right)_{T,V} \tag{A.23}$$

where $A^{\text{ex}}_{\text{Pure},i}$ is the excess Helmholtz energy of the pure component system of species i. At low density, the derivative of excess energy, $U^{\text{ex}}_{\text{G,Pure},i}$, with respect to N_i at constant T and V is equal to:

$$\left(\frac{\partial U^{\text{ex}}_{\text{Pure},i}}{\partial N_i}\right)_{T,V} = \frac{4\pi N_i}{V}\int_0^\infty u(r)g(r)r^2\text{d}r \tag{A.24}$$

Similarly, at low density the derivative of excess entropy, $S^{\text{ex}}_{\text{G,Pure},i}$, with respect to N_i at constant T and V is equal to:

$$\left(\frac{\partial S^{\text{ex}}_{\text{Pure},i}}{\partial N_i}\right)_{T,V} = \frac{4\pi N_i k_B}{V}\int_0^\infty \left(g(r)\ln[g(r)] - g(r) + 1\right)r^2\text{d}r \tag{A.25}$$

We can express $g(r)$ in terms of $u(r)$ at low density [50, 442]:

$$g(r) \approx \exp\left[\frac{-u(r)}{k_\text{B}T}\right] \tag{A.26}$$

By combining Eq. A.24 and A.26, we obtain [50, 442]:

$$\left(\frac{\partial U^{\text{ex}}_{\text{Pure},i}}{\partial N_i}\right)_{T,V} \approx \frac{4\pi N_i}{V}\int_0^\infty \left(u(r)\exp\left[\frac{-u(r)}{k_\text{B}T}\right]\right)r^2\text{d}r \tag{A.27}$$

Similarly, we can formulate an expression for $S^{\text{ex}}_{\text{Pure},i}$ in terms of $u(r)$ by combining Eqs. A.25 and A.26:

$$\begin{aligned}\left(\frac{\partial S^{\text{ex}}_{\text{Pure},i}}{\partial N_i}\right)_{T,V} &\approx \\ \frac{-4\pi N_i k_\text{B}}{V}\int_0^\infty &\left(\exp\left[\frac{-u(r)}{k_\text{B}T}\right]\frac{-u(r)}{k_\text{B}T} - \exp\left[\frac{-u(r)}{k_\text{B}T}\right] + 1\right)r^2\text{d}r\end{aligned} \tag{A.28}$$

Using Eq. A.23 an expression can be found for $\mu^{\text{ex}}_{\text{G,Pure},i}$ in terms of $u(r)$ by combining Eqs. A.27 and A.28:

$$\mu^{\text{ex}}_{\text{G,Pure},i} \approx \frac{4\pi N_i k_\text{B}T}{V}\int_0^\infty \left(1 - \exp\left[\frac{-u(r)}{k_\text{B}T}\right]\right)r^2\text{d}r \tag{A.29}$$

The second virial coefficient $B_{2V,i}$ can be obtained from [50, 442]:

$$B_{2V,i} \approx 2\pi \int_0^\infty \left(1 - \exp\left[\frac{-u(r)}{k_\mathrm{B}T}\right]\right) r^2 \mathrm{d}r \tag{A.30}$$

By combining Eq. A.30 with Eq. A.20 and $P = N_i k_\mathrm{B} T/V$ (valid at low densities), we again obtain the same expression for the excess chemical potential shown in Eq. A.29. This shows that the low density expressions for $\mu^\mathrm{ex}_{\mathrm{G,Pure},i}$ (Eq. A.29) is consistent with the expressions for excess energy (Eq. A.27) and excess entropy (Eq. A.28) [50, 442].

References

[1] W. Lubitz and W. Tumas. “Hydrogen: An Overview”. *Chemical Reviews* 107 (2007), 3900–3903.

[2] G. Qing, R. Ghazfar, S. T. Jackowski, F. Habibzadeh, M. M. Ashtiani, C.-P. Chen, M. R. I. Smith, and T. W. Hamann. “Recent Advances and Challenges of Electrocatalytic N_2 Reduction to Ammonia”. *Chemical Reviews* 120 (2020), 5437–5516.

[3] M. Ribeiro Gomes, T. Leber, T. Tillmann, D. Kenn, D. Gavagnin, T. Tonnesen, and J. Gonzalez-Julian. “Towards H_2 implementation in the iron- and steelmaking industry: State of the art, requirements, and challenges for refractory materials”. *Journal of the European Ceramic Society* 44 (2024), 1307–1334.

[4] M. D. Johnson, S. A. May, M. E. Kopach, J. M. Groh, T. Braden, V. Shankarraman, and J. M. Merritt. “Design and Selection of Continuous Reactors for Pharmaceutical Manufacturing”. *Chemical Engineering in the Pharmaceutical Industry*. John Wiley & Sons, Ltd, 2019. Chap. 16, 367–385.

[5] N. Armaroli, E. Bandini, and A. Barbieri. “Hydrogen as an energy carrier: constraints and opportunities”. *Pure and Applied Chemistry* 96 (2024), 479–485.

[6] H. Nazir, C. Louis, S. Jose, J. Prakash, N. Muthuswamy, M. E. Buan, C. Flox, S. Chavan, X. Shi, P. Kauranen, T. Kallio, G. Maia, K. Tammeveski, N. Lymperopoulos, E. Carcadea, E. Veziroglu, A. Iranzo, and A. M. Kannan. “Is the H_2 economy realizable in the foreseeable future? Part I: H_2 production methods”. *International Journal of Hydrogen Energy* 45 (2020), 13777–13788.

[7] P. Haug, M. Koj, and T. Turek. “Influence of Process Conditions on Gas Purity in Alkaline Water Electrolysis”. *International Journal of Hydrogen Energy* 42 (2017), 9406–9418.

[8] S. A. Grigoriev, V. N. Fateev, D. G. Bessarabov, and P. Millet. “Current status, research trends, and challenges in water electrolysis science and technology”. *International Journal of Hydrogen Energy* 45 (2020), 26036–26058.

[9] S. Oikonomidis, M. Ramdin, O. A. Moultos, A. Bos, T. J. H. Vlugt, and A. Rahbari. “Transient modelling of a multi-cell alkaline electrolyzer for gas crossover and safe system operation”. *International Journal of Hydrogen Energy* 48 (2023), 34210–34228.

[10] G. Tjarks, J. Mergel, and D. Stolten. “Dynamic Operation of Electrolyzers – Systems Design and Operating Strategies”. *Hydrogen Science and Engineering : Materials, Processes, Systems and Technology*. John Wiley & Sons, Ltd, 2016. Chap. 14, 309–330.

[11] A. Manabe, M. Kashiwase, T. Hashimoto, T. Hayashida, A. Kato, K. Hirao, I. Shimomura, and I. Nagashima. “Basic study of alkaline water electrolysis”. *Electrochimica Acta* 100 (2013), 249–256.

[12] M. Bodner, A. Hofer, and V. Hacker. “H_2 generation from alkaline electrolyzer”. *Wiley Interdisciplinary Reviews: Energy and Environment* 4 (2015), 365–381.

[13] G. Merle, M. Wessling, and K. Nijmeijer. “Anion exchange membranes for alkaline fuel cells: A review”. *Journal of Membrane Science* 377 (2011), 1–35.

[14] F. Bidault, D. Brett, P. Middleton, and N. Brandon. “Review of gas diffusion cathodes for alkaline fuel cells”. *Journal of Power Sources* 187 (2009), 39–48.

[15] C. Zhang, F.-R. F. Fan, and A. J. Bard. “Electrochemistry of oxygen in concentrated NaOH solutions: solubility, diffusion coefficients, and superoxide formation”. *Journal of the American Chemical Society* 131 (2009), 177–181.

[16] P. Haug, B. Kreitz, M. Koj, and T. Turek. “Process modelling of an alkaline water electrolyzer”. *International Journal of Hydrogen Energy* 42 (2017), 15689–15707.

[17] D. Durbin and C. Malardier-Jugroot. “Review of Hydrogen Storage Techniques for on Board Vehicle Applications”. *International Journal of Hydrogen Energy* 38 (2013), 14595–14617.

[18] U. Eberle, M. Felderhoff, and F. Schueth. “Chemical and Physical Solutions for Hydrogen Storage”. *Angewandte Chemie International Edition* 48 (2009), 6608–6630.

[19] A. Züttel. “Materials for Hydrogen Storage”. *Materials Today* 6 (2003), 24–33.

[20] J. M. Ogden. “Hydrogen: The Fuel of the Future?” *Physics Today* 55 (2002), 69–75.

[21] H. Nazir, N. Muthuswamy, C. Louis, S. Jose, J. Prakash, M. E. Buan, C. Flox, S. Chavan, X. Shi, P. Kauranen, T. Kallio, G. Maia, K. Tammeveski, N. Lymperopoulos, E. Carcadea, E. Veziroglu, A. Iranzo, and A. M. Kannan. “Is the H_2 economy realizable in the foreseeable future? Part II: H_2 storage, transportation, and distribution”. *International Journal of Hydrogen Energy* 45 (2020), 20693–20708.

[22] B. Pan, X. Yin, Y. Ju, and S. Iglauer. “Underground hydrogen storage: Influencing parameters and future outlook”. *Advances in Colloid and Interface Science* 294 (2021), 102473.

[23] D. Zivar, S. Kumar, and J. Foroozesh. “Underground hydrogen storage: A comprehensive review”. *International Journal of Hydrogen Energy* 46 (2021), 23436–23462.

[24] P. Carden and L. Paterson. “Physical, chemical and energy aspects of underground hydrogen storage”. *International Journal of Hydrogen Energy* 4 (1979), 559–569.

[25] P. Jena. “Materials for Hydrogen Storage: Past, Present, and Future”. *Journal of Physical Chemistry Letters* 2 (2011), 206–211.

[26] *DOE Technical Targets for Onboard Hydrogen Storage for Light-Duty Vehicles*. `https://www.energy.gov/eere/fuelcells/doe-technical-targets-onboard-hydrogen-storage-light-duty-vehicles`, (Accessed Jun. 30, 2023).

[27] P. Habibi, T. J. H. Vlugt, P. Dey, and O. A. Moultos. “Reversible Hydrogen Storage in Metal-Decorated Honeycomb Borophene Oxide”. *ACS Applied Materials & Interfaces* 13 (2021), 43233–43240.

[28] H. Nishino, T. Fujita, A. Yamamoto, T. Fujimori, A. Fujino, S.-i. Ito, J. Nakamura, H. Hosono, and T. Kondo. “Formation Mechanism of Boron-Based Nanosheet through the Reaction of MgB_2 with Water”. *Journal of Physical Chemistry C* 121 (2017), 10587–10593.

[29] R. Kawamura, N. T. Cuong, T. Fujita, R. Ishibiki, T. Hirabayashi, A. Yamaguchi, I. Matsuda, S. Okada, T. Kondo, and M. Miyauchi. “Photoinduced Hydrogen Release From Hydrogen Boride Sheets”. *Nature Communications* 10 (2019), 25523–25528.

[30] T. A. Abtew and P. Zhang. “Charging-Assisted Hydrogen Release Mechanism in Layered Boron Hydride”. *Physical Review B* 84 (2011), 094303.

[31] A. M. P. Peedikakkal and I. H. Aljundi. “Mixed-Metal Cu-BTC Metal–Organic Frameworks as a Strong Adsorbent for Molecular Hydrogen at Low Temperatures”. *ACS Omega* 5 (2020), 28493–28499.

[32] O. Khvostikova, B. Assfour, G. Seifert, H. Hermann, A. Horst, and H. Ehrenberg. “Novel experimental methods for assessment of hydrogen storage capacity and modelling of sorption in Cu-BTC”. *International Journal of Hydrogen Energy* 35 (2010), 11042–11051.

[33] I. Diaz, E. Kokkoli, O. Terasaki, and M. Tsapatsis. “Surface Structure of Zeolite (MFI) Crystals”. *Chemistry of Materials* 16 (2004), 5226–5232.

[34] N. Torres, J. Galicia, Y. Plasencia, A. Cano, F. Echevarría, L. Desdin-Garcia, and E. Reguera. “Implications of structural differences between Cu-BTC and Fe-BTC on their hydrogen storage capacity”. *Colloids and Surfaces A: Physicochemical and Engineering Aspects* 549 (2018), 138–146.

[35] H. Wang, X. Dong, and Y. Lin. “Highly stable bilayer MFI zeolite membranes for high temperature hydrogen separation”. *Journal of Membrane Science* 450 (2014), 425–432.

[36] X. Gu, Z. Tang, and J. Dong. “On-stream modification of MFI zeolite membranes for enhancing hydrogen separation at high temperature”. *Microporous and Mesoporous Materials* 111 (2008), 441–448.

[37] D. Dubbeldam, S. Calero, and T. J. H. Vlugt. “iRASPA: GPU-accelerated visualization software for materials scientists”. *Molecular Simulation* 44 (2018), 653–676.

[38] N. S. Bobbitt and R. Q. Snurr. “Molecular modelling and machine learning for high-throughput screening of metal-organic frameworks for hydrogen storage”. *Molecular Simulation* 45 (2019), 1069–1081.

[39] J. Zhang, T. S. Fisher, P. V. Ramachandran, J. P. Gore, and I. Mudawar. “A Review of Heat Transfer Issues in Hydrogen Storage Technologies”. *Journal of Heat Transfer* 127 (2005), 1391–1399.

[40] M. Felderhoff, C. Weidenthaler, R. von Helmolt, and U. Eberle. “Hydrogen storage: the remaining scientific and technological challenges”. *Physical Chemistry Chemical Physics* 9 (2007), 2643–2653.

[41] M. Visaria, I. Mudawar, T. Pourpoint, and S. Kumar. “Study of heat transfer and kinetics parameters influencing the design of heat exchangers for hydrogen storage in high-pressure metal hydrides”. *International Journal of Heat and Mass Transfer* 53 (2010), 2229–2239.

[42] A. Ahmed, S. Seth, J. Purewal, A. G. Wong-Foy, M. Veenstra, A. J. Matzger, and D. J. Siegel. “Exceptional hydrogen storage achieved by screening nearly half a million metal-organic frameworks”. *Nature Communications* 10 (2019), 1568.

[43] D. Broom, C. Webb, G. Fanourgakis, G. Froudakis, P. Trikalitis, and M. Hirscher. “Concepts for improving hydrogen storage in nanoporous materials”. *International Journal of Hydrogen Energy* 44 (2019), 7768–7779.

[44] A. J. Mannix, Z. Zhang, N. P. Guisinger, B. I. Yakobson, and M. C. Hersam. “Borophene as a Prototype for Synthetic 2D Materials Development”. *Nature Nanotechnology* 13 (2018), 444–450.

[45] V. Tozzini and V. Pellegrini. “Prospects for hydrogen storage in graphene”. *Physical Chemistry Chemical Physics* 15 (2013), 80–89.

[46] C. San Marchi, E. Hecht, I. Ekoto, K. Groth, C. LaFleur, B. Somerday, R. Mukundan, T. Rockward, J. Keller, and C. James. “Overview of the DOE hydrogen safety, codes and standards program, part 3: Advances in research and development to enhance the scientific basis for hydrogen regulations, codes and standards”. *International Journal of Hydrogen Energy* 42 (2017), 7263–7274.

[47] P. Habibi, A. Rahbari, S. Blazquez, C. Vega, P. Dey, T. J. H. Vlugt, and O. A. Moultos. “A New Force Field for OH^- for Computing Thermodynamic and Transport Properties of H_2 and O_2 in Aqueous NaOH and KOH Solutions”. *Journal of Physical Chemistry B* 126 (2022), 9376–9387.

[48] W. A. van Rooijen, P. Habibi, K. Xu, P. Dey, T. J. H. Vlugt, H. Hajibeygi, and O. A. Moultos. “Interfacial Tensions, Solubilities, and Transport Properties of the $H_2/H_2O/NaCl$ System: A Molecular Simulation Study”. *Journal of Chemical & Engineering Data* 69 (2024), 307–319.

[49] M. Allen, D. Tildesley, and D. Tildesley. *Computer Simulation of Liquids*. 2nd ed. Oxford Science Publications. New York: Oxford University Press, 2017.

[50] D. Frenkel and B. Smit. *Understanding molecular simulation: from algorithms to applications*. 3rd ed. San Diego: Elsevier, 2023.

[51] I. N. Tsimpanogiannis, O. A. Moultos, L. F. M. Franco, M. B. M. Spera, M. Erdős, and I. G. Economou. “Self-diffusion coefficient of bulk and confined water: a critical review of classical molecular simulation studies”. *Molecular Simulation* 45 (2019), 425–453.

[52] S. Haldar, S. Mukherjee, and C. V. Singh. “Hydrogen Storage in Li, Na and Ca Decorated and Defective Borophene: a First Principles Study”. *RSC Advances* 8 (2018), 20748–20757.

[53] S. H. Jamali, L. Wolff, T. M. Becker, M. De Groen, M. Ramdin, R. Hartkamp, A. Bardow, T. J. H. Vlugt, and O. A. Moultos. “OCTP: A tool for on-the-fly calculation of transport properties of fluids with the order-n algorithm in LAMMPS”. *Journal of Chemical Information and Modeling* 59 (2019), 1290–1294.

[54] S. I. Sandler. *An Introduction to Applied Statistical Thermodynamics*. 1st ed. Hoboken, New Jersey: John Wiley & Sons, 2011.

[55] R. Hens, A. Rahbari, S. Caro-Ortiz, N. Dawass, M. Erdős, A. Poursaeidesfahani, H. S. Salehi, A. T. Celebi, M. Ramdin, O. A. Moultos, D. Dubbeldam, and T. J. H. Vlugt. “Brick-CFCMC: Open Source Software for Monte Carlo Simulations of Phase and Reaction Equilibria Using the Continuous Fractional Component

Method". *Journal of Chemical Information and Modeling* 60 (2020), 2678–2682.

[56] H. M. Polat, H. S. Salehi, R. Hens, D. O. Wasik, A. Rahbari, F. de Meyer, C. Houriez, C. Coquelet, S. Calero, D. Dubbeldam, O. A. Moultos, and T. J. H. Vlugt. "New Features of the Open Source Monte Carlo Software Brick-CFCMC: Thermodynamic Integration and Hybrid Trial Moves". *Journal of Chemical Information and Modeling* 61 (2021), 3752–3757.

[57] N. Metropolis, A. W. Rosenbluth, M. N. Rosenbluth, A. H. Teller, and E. Teller. "Equation of state calculations by fast computing machines". *Journal of Chemical Physics* 21 (1953), 1087–1092.

[58] E. J. Maginn, R. A. Messerly, D. J. Carlson, D. R. Roe, and J. R. Elliot. "Best Practices for Computing Transport Properties 1. Self-Diffusivity and Viscosity from Equilibrium Molecular Dynamics [Article v1.0]". *Living Journal of Computational Molecular Science* 1 (2018), 6324.

[59] S. Plimpton. "Fast Parallel Algorithms for Short-Range Molecular Dynamics". *Journal of Computational Physics* 117 (1995), 1–19.

[60] S. Plimpton. *LAMMPS Documentation (15 Sep 2022 version)*. Accessed: 26/10/2022. 2015. URL: `https://docs.lammps.org/Manual.html`.

[61] H. Berendsen, D. van der Spoel, and R. van Drunen. "GROMACS: A message-passing parallel molecular dynamics implementation". *Computer Physics Communications* 91 (1995), 43–56.

[62] M. J. Abraham, T. Murtola, R. Schulz, S. Páll, J. C. Smith, B. Hess, and E. Lindahl. "GROMACS: High performance molecular simulations through multi-level parallelism from laptops to supercomputers". *SoftwareX* 1-2 (2015), 19–25.

[63] D. A. Case, H. M. Aktulga, K. Belfon, D. S. Cerutti, G. A. Cisneros, V. W. D. Cruzeiro, N. Forouzesh, T. J. Giese, A. W. Götz, H. Gohlke, S. Izadi, K. Kasavajhala, M. C. Kaymak, E. King, T. Kurtzman, T.-S. Lee, P. Li, J. Liu, T. Luchko, R. Luo, M. Manathunga, M. R. Machado, H. M. Nguyen, K. A. O'Hearn, A. V. Onufriev, F. Pan, S. Pantano, R. Qi, A. Rahnamoun, A. Risheh, S. Schott-Verdugo, A. Shajan, J. Swails, J. Wang, H. Wei, X. Wu, Y. Wu, S. Zhang, S. Zhao, Q. Zhu, T. E. I. Cheatham, D. R. Roe, A. Roitberg, C. Simmerling, D. M. York, M. C. Nagan, and K. M. J. Merz. "AmberTools". *Journal of Chemical Information and Modeling* 63 (2023), 6183–6191.

[64] R. Salomon-Ferrer, D. A. Case, and R. C. Walker. "An overview of the Amber biomolecular simulation package". *WIREs Computational Molecular Science* 3 (2013), 198–210.

[65] D. Dubbeldam, S. Calero, D. E. Ellis, and R. Q. Snurr. “RASPA: molecular simulation software for adsorption and diffusion in flexible nanoporous materials”. *Molecular Simulation* 42 (2016), 81–101.

[66] D. Dubbeldam, A. Torres-Knoop, and K. S. Walton. “On the inner workings of Monte Carlo codes”. *Molecular Simulation* 39 (2013), 1253–1292.

[67] Y. Nejahi, M. Soroush Barhaghi, J. Mick, B. Jackman, K. Rushaidat, Y. Li, L. Schwiebert, and J. Potoff. “GOMC: GPU Optimized Monte Carlo for the simulation of phase equilibria and physical properties of complex fluids”. *SoftwareX* 9 (2019), 20–27.

[68] J. K. Shah, E. Marin-Rimoldi, R. G. Mullen, B. P. Keene, S. Khan, A. S. Paluch, N. Rai, L. L. Romanielo, T. W. Rosch, B. Yoo, and E. J. Maginn. “Cassandra: An open source Monte Carlo package for molecular simulation”. *Journal of Computational Chemistry* 38 (2017), 1727–1739.

[69] J. M. Prausnitz, R. N. Lichtenthaler, and E. G. De Azevedo. *Molecular thermodynamics of fluid-phase equilibria*. 3rd ed. Pearson Education, 1998.

[70] M. E. Tuckerman. *Statistical mechanics: theory and molecular simulation*. 1st ed. New York: Oxford university press, 2023.

[71] G. Kresse and J. Furthmüller. “Efficient Iterative Schemes for Ab-Initio Total-Energy Calculations Using a Plane-Wave Basis Set”. *Physical Review B* 54 (1996), 11169–11186.

[72] G. Kresse and J. Furthmüller. “Efficiency of Ab-Initio Total Energy Calculations for Metals and Semiconductors Using a Plane-Wave Basis Set”. *Computational Materials Science* 6 (1996), 15–50.

[73] J. Pokluda, M. Černý, M. Šob, and Y. Umeno. “Ab initio calculations of mechanical properties: Methods and applications”. *Progress in Materials Science* 73 (2015), 127–158.

[74] S. Haldar, S. Mukherjee, F. Ahmed, and C. V. Singh. “A First Principles Study of Hydrogen Storage in Lithium Decorated Defective Phosphorene”. *International Journal of Hydrogen Energy* 42 (2017), 23018–23027.

[75] N. Khossossi, Y. Benhouria, S. R. Naqvi, P. K. Panda, I. Essaoudi, A. Ainane, and R. Ahuja. “Hydrogen Storage Characteristics of Li and Na Decorated 2D Boron Phosphide”. *Sustainable Energy & Fuels* 4 (2020), 4538–4546.

[76] G. Henkelman, B. P. Uberuaga, and H. Jónsson. “A Climbing Image Nudged Elastic Band Method for Finding Saddle Points and Minimum Energy Paths”. *Journal of Chemical Physics* 113 (2000), 9901–9904.

[77] G. Henkelman and H. Jónsson. “Improved Tangent Estimate in the Nudged Elastic Band Method for Finding Minimum Energy Paths and Saddle Points”. *Journal of Chemical Physics* 113 (2000), 9978–9985.

[78] P. Habibi, T. H. G. Saji, T. J. H. Vlugt, O. A. Moultos, and P. Dey. “Hydrogen dissociation in Li-decorated borophene and borophene hydride: An ab-initio study”. *Applied Surface Science* 603 (2022), 154323.

[79] G. K. Sunnardianto, G. Bokas, A. Hussein, C. Walters, O. A. Moultos, and P. Dey. “Efficient Hydrogen Storage in Defective Graphene and its Mechanical Stability: A Combined Density Functional Theory and Molecular Dynamics Simulation Study”. *International Journal of Hydrogen Energy* 46 (2021), 5485–5494.

[80] P. Giannozzi, S. Baroni, N. Bonini, M. Calandra, R. Car, C. Cavazzoni, D. Ceresoli, G. L. Chiarotti, M. Cococcioni, I. Dabo, A. D. Corso, S. de Gironcoli, S. Fabris, G. Fratesi, R. Gebauer, U. Gerstmann, C. Gougoussis, A. Kokalj, M. Lazzeri, L. Martin-Samos, N. Marzari, F. Mauri, R. Mazzarello, S. Paolini, A. Pasquarello, L. Paulatto, C. Sbraccia, S. Scandolo, G. Sclauzero, A. P. Seitsonen, A. Smogunov, P. Umari, and R. M. Wentzcovitch. “QUANTUM ESPRESSO: a modular and open-source software project for quantum simulations of materials”. *Journal of Physics: Condensed Matter* 21 (2009), 395502.

[81] P. Giannozzi, O. Andreussi, T. Brumme, O. Bunau, M. B. Nardelli, M. Calandra, R. Car, C. Cavazzoni, D. Ceresoli, M. Cococcioni, N. Colonna, I. Carnimeo, A. D. Corso, S. de Gironcoli, P. Delugas, R. A. DiStasio, A. Ferretti, A. Floris, G. Fratesi, G. Fugallo, R. Gebauer, U. Gerstmann, F. Giustino, T. Gorni, J. Jia, M. Kawamura, H.-Y. Ko, A. Kokalj, E. Küçükbenli, M. Lazzeri, M. Marsili, N. Marzari, F. Mauri, N. L. Nguyen, H.-V. Nguyen, A. Otero-de-la-Roza, L. Paulatto, S. Poncé, D. Rocca, R. Sabatini, B. Santra, M. Schlipf, A. P. Seitsonen, A. Smogunov, I. Timrov, T. Thonhauser, P. Umari, N. Vast, X. Wu, and S. Baroni. “Advanced capabilities for materials modelling with Quantum ESPRESSO”. *Journal of Physics: Condensed Matter* 29 (2017), 465901.

[82] P. Blaha, K. Schwarz, F. Tran, R. Laskowski, G. K. H. Madsen, and L. D. Marks. “WIEN2k: An APW+lo program for calculating the properties of solids”. *The Journal of Chemical Physics* 152 (2020), 074101.

[83] M. J. Frisch, G. W. Trucks, H. B. Schlegel, G. E. Scuseria, M. A. Robb, J. R. Cheeseman, G. Scalmani, V. Barone, G. A. Petersson, H. Nakatsuji, X. Li, M. Caricato, A. V. Marenich, J. Bloino, B. G. Janesko, R. Gomperts, B. Mennucci, H. P. Hratchian, J. V. Ortiz, A. F. Izmaylov, J. L. Sonnenberg, D. Williams-Young, F. Ding, F.

Lipparini, F. Egidi, J. Goings, B. Peng, A. Petrone, T. Henderson, D. Ranasinghe, V. G. Zakrzewski, J. Gao, N. Rega, G. Zheng, W. Liang, M. Hada, M. Ehara, K. Toyota, R. Fukuda, J. Hasegawa, M. Ishida, T. Nakajima, Y. Honda, O. Kitao, H. Nakai, T. Vreven, K. Throssell, J. A. Montgomery Jr., J. E. Peralta, F. Ogliaro, M. J. Bearpark, J. J. Heyd, E. N. Brothers, K. N. Kudin, V. N. Staroverov, T. A. Keith, R. Kobayashi, J. Normand, K. Raghavachari, A. P. Rendell, J. C. Burant, S. S. Iyengar, J. Tomasi, M. Cossi, J. M. Millam, M. Klene, C. Adamo, R. Cammi, J. W. Ochterski, R. L. Martin, K. Morokuma, O. Farkas, J. B. Foresman, and D. J. Fox. *Gaussian~16 Revision C.01*. Gaussian Inc. Wallingford CT. 2016.

[84] D. A. McQuarrie. *Quantum chemistry*. 2nd ed. California: University Science Books, 2008.

[85] K. S. Deeg, J. J. Gutiérrez-Sevillano, R. Bueno-Pérez, J. B. Parra, C. O. Ania, M. Doblaré, and S. Calero. “Insights on the Molecular Mechanisms of Hydrogen Adsorption in Zeolites”. *The Journal of Physical Chemistry C* 117 (2013), 14374–14380.

[86] M. C. Andrade, R. Car, and A. Selloni. “Probing the self-ionization of liquid water with ab initio deep potential molecular dynamics”. *Proceedings of the National Academy of Sciences* 120 (2023), e2302468120.

[87] M. Tuckerman, K. Laasonen, M. Sprik, and M. Parrinello. “Ab Initio Molecular Dynamics Simulation of the Solvation and Transport of H_3O^+ and OH^- Ions in Water”. *Journal of Physical Chemistry* 99 (1995), 5749–5752.

[88] M. E. Tuckerman, A. Chandra, and D. Marx. “Structure and dynamics of $OH^-(aq)$”. *Accounts of Chemical Research* 39 (2006), 151–158.

[89] J. O. Hirschfelder, C. F. Curtiss, and R. B. Bird. *Molecular theory of gases and liquids*. 1st ed. New York: John Wiley, 1964.

[90] A. Köster, M. Thol, and J. Vrabec. “Molecular Models for the Hydrogen Age: Hydrogen, Nitrogen, Oxygen, Argon, and Water”. *Journal of Chemical and Engineering Data* 63 (2018), 305–320.

[91] D. Marx and P. Nielaba. “Path-integral Monte Carlo techniques for rotational motion in two dimensions: Quenched, annealed, and no-spin quantum-statistical averages”. *Physical Review A* 45 (1992), 8968.

[92] M. Śmiechowski. “Molecular hydrogen solvated in water–A computational study”. *Journal of Chemical Physics* 143 (2015).

[93] V. Buch. “Path integral simulations of mixed para-D_2 and ortho-D_2 clusters: The orientational effects”. *Journal of Chemical Physics* 100 (1994), 7610–7629.

[94] S. Wang, K. Hou, and H. Heinz. “Accurate and Compatible Force Fields for Molecular Oxygen, Nitrogen, and Hydrogen to Simulate Gases, Electrolytes, and Heterogeneous Interfaces”. *Journal of Chemical Theory and Computation* 17 (2021), 5198–5213.

[95] P. T. Kiss and A. Baranyai. “A Systematic Development of a Polarizable Potential of Water”. *Journal of Chemical Physics* 138 (2013), 204507.

[96] H. Jiang, O. A. Moultos, I. G. Economou, and A. Z. Panagiotopoulos. “Hydrogen-Bonding Polarizable Intermolecular Potential Model for Water”. *Journal of Physical Chemistry B* 120 (2016), 12358–12370.

[97] C. Zhang, C. Lu, Z. Jing, C. Wu, J.-P. Piquemal, J. W. Ponder, and P. Ren. “AMOEBA Polarizable Atomic Multipole Force Field for Nucleic Acids”. *Journal of Chemical Theory and Computation* 14 (2018), 2084–2108.

[98] H. J. C. Berendsen, J. R. Grigera, and T. P. Straatsma. “The missing term in effective pair potentials”. *Journal of Physical Chemistry* 91 (1987), 6269–6271.

[99] C. Vega. “Water: One Molecule, Two Surfaces, One Mistake”. *Molecular Physics* 113 (2015), 1145–1163.

[100] J. L. Abascal and C. Vega. “A general purpose model for the condensed phases of water: TIP4P/2005”. *Journal of Chemical Physics* 123 (2005), 234505.

[101] H. Jiang, O. A. Moultos, I. G. Economou, and A. Z. Panagiotopoulos. “Gaussian-Charge Polarizable and Nonpolarizable Models for CO_2”. *Journal of Physical Chemistry B* 120 (2016), 984–994.

[102] P. T. Kiss and A. Baranyai. “A new polarizable force field for alkali and halide ions”. *Journal of Chemical Physics* 141 (2014), 114501.

[103] I. M. Zeron, J. L. F. Abascal, and C. Vega. “A Force Field of Li^+, Na^+, K^+, Mg^{2+}, Ca^+, Cl^-, and SO_4^{2-} in Aqueous Solution Based on the TIP4P/2005 Water Model and Scaled Charges for the Ions”. *Journal of Chemical Physics* 151 (2019), 104501.

[104] I. S. Joung and T. E. I. Cheatham. “Determination of Alkali and Halide Monovalent Ion Parameters for Use in Explicitly Solvated Biomolecular Simulations”. *Journal of Physical Chemistry B* 112 (2008), 9020–9041.

[105] P. Habibi, H. M. Polat, S. Blazquez, C. Vega, P. Dey, T. J. H. Vlugt, and O. A. Moultos. “Accurate Free Energies of Aqueous Electrolyte Solutions from Molecular Simulations with Non-polarizable Force Fields”. *Journal of Physical Chemistry Letters* 15 (2024), 4477–4485.

[106] A. Rahbari, J. Brenkman, R. Hens, M. Ramdin, L. J. P. van den Broeke, R. Schoon, R. Henkes, O. A. Moultos, and T. J. H. Vlugt. “Solubility of water in hydrogen at high pressures: A molecular simulation study”. *Journal of Chemical & Engineering Data* 64 (2019), 4103–4115.

[107] D. T. Kallikragas, A. Y. Plugatyr, and I. M. Svishchev. “High temperature diffusion coefficients for O_2, H_2, and OH in water, and for pure water”. *Journal of Chemical & Engineering Data* 59 (2014), 1964–1969.

[108] X. Zhao and H. Jin. “Investigation of hydrogen diffusion in supercritical water: A molecular dynamics simulation study”. *International Journal of Heat and Mass Transfer* 133 (2019), 718–728.

[109] I. N. Tsimpanogiannis, S. Maity, A. T. Celebi, and O. A. Moultos. “Engineering Model for Predicting the Intradiffusion Coefficients of Hydrogen and Oxygen in Vapor, Liquid, and Supercritical Water based on Molecular Dynamics Simulations”. *Journal of Chemical and Engineering Data* 66 (2021), 3244.

[110] A. Rahbari, J. C. Garcia-Navarro, M. Ramdin, L. J. P. van den Broeke, O. A. Moultos, D. Dubbeldam, and T. J. H. Vlugt. “Effect of Water Content on Thermodynamic Properties of Compressed Hydrogen”. *Journal of Chemical & Engineering Data* 66 (2021), 2071–2087.

[111] S. Blazquez, M. M. Conde, and C. A. Vega. “Scaled Charges for Ions: An Improvement but not the Final Word for Modeling Electrolytes in Water”. *Journal of Chemical Physics* 158 (2023), 054505.

[112] M. Laliberté and W. E. Cooper. “Model for Calculating the Density of Aqueous Electrolyte Solutinos”. *Journal of Chemical & Engineering Data* 49 (2004), 1141–1151.

[113] M. Laliberté. “Model for calculating the viscosity of aqueous solutions”. *Journal of Chemical and Engineering Data* 52 (2007), 321–335.

[114] R. Gilliam, J. Graydon, D. Kirk, and S. Thorpe. “A review of specific conductivities of potassium hydroxide solutions for various concentrations and temperatures”. *International Journal of Hydrogen Energy* 32 (2007), 359–364.

[115] I. N. Tsimpanogiannis and O. A. Moultos. “Is Stokes-Einstein relation valid for the description of intra-diffusivity of hydrogen and oxygen in liquid water?” *Fluid Phase Equilibria* 563 (2022), 113568.

[116] M. de Lucas, S. Blazquez, J. Troncoso, C. Vega, and F. Gámez. “Dressing a Nonpolarizable Force Field for OH^- in TIP4P/2005 Aqueous Solutions with Corrected Hirshfeld Charges”. *Journal of Physical Chemistry Letters* 15 (2024), 9411–9418.

[117] C. Zhong, W. Wu, J. He, G. Ding, Y. Liu, D. Li, S. A. Yang, and G. Zhang. “Two-Dimensional Honeycomb Borophene Oxide: Strong Anisotropy and Nodal Loop Transformation”. *Nanoscale* 11 (2019), 2468–2475.

[118] S. Grimme. “Semiempirical GGA-type Density Functional Constructed with a Long-Range Dispersion Correction”. *Journal of Computational Chemistry* 27 (2006), 1787–1799.

[119] D. Sheppard, R. Terrell, and G. Henkelman. “Optimization Methods for Finding Minimum Energy Paths”. *Journal of Chemical Physics* 128 (2008), 134106.

[120] L. Van Hoecke, L. Laffineur, R. Campe, P. Perreault, S. W. Verbruggen, and S. Lenaerts. “Challenges in the use of hydrogen for maritime applications”. *Energy & Environmental Science* 14 (2021), 815–843.

[121] Q. Zhang, Y. Wu, X. Sun, and J. Ortega. “Kinetics of Catalytic Hydrolysis of Stabilized Sodium Borohydride Solutions”. *Industrial & Engineering Chemistry Research* 46 (2007), 1120–1124.

[122] P. A. Mosier-Boss, C. A. Becker, G. W. Anderson, and B. J. Wiedemeier. “Feasibility Studies of the $NaBH_4/H_2O$ Hydrolysis to Generate Hydrogen Gas to Inflate Lighter than Air (LTA) Vehicles”. *Industrial & Engineering Chemistry Research* 54 (2015), 7706–7714.

[123] O. Kunz and W. Wagner. “The GERG-2008 Wide-Range Equation of State for Natural Gases and Other Mixtures: An Expansion of GERG-2004”. *Journal of Chemical & Engineering Data* 57 (2012), 3032–3091.

[124] J. Joseph, V. S. Sivasankarapillai, S. Nikazar, M. S. Shanawaz, A. Rahdar, H. Lin, and G. Z. Kyzas. “Borophene and Boron Fullerene Naterials in Hydrogen Storage: Opportunities and challenges”. *ChemSusChem* 13 (2020), 3754–3765.

[125] A. Hashmi, M. U. Farooq, I. Khan, J. Son, and J. Hong. “Ultra-High Capacity Hydrogen Storage in a Li Decorated Two-Dimensional C_2N Layer”. *Journal of Materials Chemistry A* 5 (2017), 2821–2828.

[126] X. Tan, H. A. Tahini, and S. C. Smith. “Conductive Boron-Doped Graphene as an Ideal Material for Electrocatalytically Switchable and High-Capacity Hydrogen Storage”. *ACS Applied Materials & Interfaces* 8 (2016), 32815–32822.

[127] X. Li, X. Tan, Q. Xue, and S. Smith. “Charge-Controlled Switchable H_2 Storage on Conductive Borophene Nanosheet”. *International Journal of Hydrogen Energy* 44 (2019), 20150–20157.

[128] L. Li, H. Zhang, and X. Cheng. “The High Hydrogen Storage Capacities of Li-Decorated Borophene”. *Computational Materials Science* 137 (2017), 119–124.

[129] A. J. Mannix, X.-F. Zhou, B. Kiraly, J. D. Wood, D. Alducin, B. D. Myers, X. Liu, B. L. Fisher, U. Santiago, J. R. Guest, M. J. Yacaman, A. Ponce, A. R. Oganov, M. C. Hersam, and N. P. Guisinger. “Synthesis of Borophenes: Anisotropic, Two-Dimensional Boron Polymorphs”. *Science* 350 (2015), 1513–1516.

[130] W. Li, L. Kong, C. Chen, J. Gou, S. Sheng, W. Zhang, H. Li, L. Chen, P. Cheng, and K. Wu. “Experimental Realization of Honeycomb Borophene”. *Science Bulletin* 63 (2018), 282–286.

[131] B. Kiraly, X. Liu, L. Wang, Z. Zhang, A. J. Mannix, B. L. Fisher, B. I. Yakobson, M. C. Hersam, and N. P. Guisinger. “Borophene Synthesis on Au(111)”. *ACS Nano* 13 (2019), 3816–3822.

[132] S. Er, G. A. de Wijs, and G. Brocks. “DFT Study of Planar Boron Sheets: A New Template for Hydrogen Storage”. *Journal of Physical Chemistry C* 113 (2009), 18962–18967.

[133] Y. Liu, V. I. Artyukhov, M. Liu, A. R. Harutyunyan, and B. I. Yakobson. “Feasibility of Lithium Storage on Graphene and its Derivatives”. *Journal of Physical Chemistry Letters* 4 (2013), 1737–1742.

[134] Y. Zhang and X. Cheng. “Hydrogen Adsorption Property of Na-Decorated Boron Monolayer: A First Principles Investigation”. *Physica E: Low-dimensional Systems and Nanostructures* 107 (2019), 170–176.

[135] J. Wang, Y. Du, and L. Sun. “Ca-Decorated Novel Boron Sheet: A Potential Hydrogen Storage Medium”. *International Journal of Hydrogen Energy* 41 (2016), 5276–5283.

[136] T. Wen, A. Xie, J. Li, and Y. Yang. “Novel Ti-Decorated Borophene $\chi 3$ as Potential High-Performance for Hydrogen Storage Medium”. *International Journal of Hydrogen Energy* 45 (2020), 29059–29069.

[137] Q. Li, V. S. C. Kolluru, M. S. Rahn, E. Schwenker, S. Li, R. G. Hennig, P. Darancet, M. K. Chan, and M. C. Hersam. “Synthesis of Borophane Polymorphs Through Hydrogenation of Borophene”. *Science* 371 (2021), 1143–1148.

[138] Y. Mu and S.-D. Li. “First-Principles Study on the Oxidation of Supported β_{12}-Borophene”. *Journal of Physical Chemistry C* 124 (2020), 28145–28151.

[139] L. Yan, P.-F. Liu, H. Li, Y. Tang, J. He, X. Huang, B.-T. Wang, and L. Zhou. “Theoretical dissection of superconductivity in two-dimensional honeycomb borophene oxide B_2O crystal with a high stability”. *npj Computational Materials* 6 (2020), 1–7.

[140] R. Zhang, Z. Li, and J. Yang. “Two-Dimensional Stoichiometric Boron Oxides as a Versatile Platform for Electronic Structure Engineering”. *Journal of Physical Chemistry Letters* 8 (2017), 4347–4353.

[141] J. Hu, C. Zhong, W. Wu, N. Liu, Y. Liu, S. A. Yang, and C. Ouyang. “2D Honeycomb Borophene Oxide: a Promising Anode Material Offering Super High Capacity for Li/Na-ion Batteries”. *Journal of Physics: Condensed Matter* 32 (2019), 065001.

[142] Y. Wang, Y. Park, L. Qiu, I. Mitchell, and F. Ding. “Borophene with Large Holes”. *Journal of Physical Chemistry Letters* 11 (2020), 6235–6241.

[143] E. S. Penev, Y. Liu, T. Altalhi, A. Kutana, and B. I. Yakobson. “Stable Low-Dimensional Boron Chalcogenides from Planar Structural Motifs”. *Journal of Physical Chemistry A* 125 (2021), 6059–6063.

[144] J. P. Perdew, K. Burke, and M. Ernzerhof. “Generalized Gradient Approximation Made Simple”. *Physical Review Letters* 77 (1996), 3865.

[145] L. Chen, X. Chen, C. Duan, Y. Huang, Q. Zhang, and B. Xiao. “Reversible Hydrogen Storage in Pristine and Li Decorated 2D Boron Hydride”. *Physical Chemistry Chemical Physics* 20 (2018), 30304–30311.

[146] Z. Liu, S. Liu, and S. Er. “Hydrogen Storage Properties of Li-Decorated B_2S Monolayers: A DFT Study”. *International Journal of Hydrogen Energy* 44 (2019), 16803–16810.

[147] R. Varunaa and P. Ravindran. “Potential Hydrogen Storage Materials From Metal Decorated 2D-C_2N: an Ab Initio Study”. *Physical Chemistry Chemical Physics* 21 (2019), 25311–25322.

[148] B. Chakraborty, P. Ray, N. Garg, and S. Banerjee. “High Capacity Reversible Hydrogen Storage in Titanium Doped 2D Carbon Allotrope Ψ-Graphene: Density Functional Theory Investigations”. *International Journal of Hydrogen Energy* 46 (2021), 4154–4167.

[149] R. Y. Sathe and T. Dhilip Kumar. “Electronic Structure Calculations of Reversible Hydrogen Storage in Nanoporous Ti Cluster Frameworks”. *ACS Applied Nano Materials* 3 (2020), 5575–5582.

[150] S. Nosé. “A Unified Formulation of the Constant Temperature Molecular Dynamics Methods”. *Journal of Chemical Physics* 81 (1984), 511–519.

[151] W. G. Hoover. “Canonical Dynamics: Equilibrium Phase-Space Distributions”. *Physical Review A* 31 (1985), 1695.

[152] L. Verlet. “Computer "Experiments" on Classical Fluids. I. Thermodynamical Properties of Lennard-Jones molecules”. *Physical Review* 159 (1967), 98–103.

[153] K. Momma and F. Izumi. “VESTA 3 for Three-Dimensional Visualization of Crystal, Volumetric and Morphology Data”. *Journal of Applied Crystallography* 44 (2011), 1272–1276.

[154] K. S. Chan, M. A. Miller, and X. Peng. “First-Principles Computational Study of Hydrogen Storage in Silicon Clathrates”. *Materials Research Letters* 6 (2018), 72–78.

[155] S. K. Bhatia and A. L. Myers. “Optimum Conditions for Adsorptive Storage”. *Langmuir* 22 (2006), 1688–1700.

[156] H. Lee, W. I. Choi, M. C. Nguyen, M.-H. Cha, E. Moon, and J. Ihm. “Ab Initio Study of Dihydrogen Binding in Metal-Decorated Polyacetylene for Hydrogen Storage”. *Physical Review B* 76 (2007), 195110.

[157] L. Wang, X. Chen, H. Du, Y. Yuan, H. Qu, and M. Zou. “First-Principles Investigation on Hydrogen Storage Performance of Li, Na and K Decorated Borophene”. *Applied Surface Science* 427 (2018), 1030–1037.

[158] S. Kumar and T. J. Dhilip Kumar. “Electronic Structure Calculations of Hydrogen Storage in Lithium-Decorated Metal–Graphyne Framework”. *ACS Applied Materials & Interfaces* 9 (2017), 28659–28666.

[159] D. R. Lide. *CRC Handbook of Chemistry and Physics*. 75th ed. New York: CRC Press, 1994.

[160] J. Ren, N. M. Musyoka, H. W. Langmi, M. Mathe, and S. Liao. “Current research trends and perspectives on materials-based hydrogen storage solutions: A critical review”. *International Journal of Hydrogen Energy* 42 (2017), 289–311.

[161] A. Schneemann, J. L. White, S. Kang, S. Jeong, L. F. Wan, E. S. Cho, T. W. Heo, D. Prendergast, J. J. Urban, B. C. Wood, M. D. Allendorf, and V. Stavila. “Nanostructured Metal Hydrides for Hydrogen Storage”. *Chemical Reviews* 118 (2018), 10775–10839.

[162] S. Er, G. A. de Wijs, and G. Brocks. “Tuning the Hydrogen Storage in Magnesium Alloys”. *Journal of Physical Chemistry Letters* 1 (2010), 1982–1986.

[163] L. Zang, W. Sun, S. Liu, Y. Huang, H. Yuan, Z. Tao, and Y. Wang. “Enhanced Hydrogen Storage Properties and Reversibility of $LiBH_4$ Confined in Two-Dimensional Ti_3C_2”. *ACS Applied Materials & Interfaces* 10 (2018), 19598–19604.

[164] G. Liu, Y. Wang, L. Jiao, and H. Yuan. “Understanding the Role of Few-Layer Graphene Nanosheets in Enhancing the Hydrogen Sorption Kinetics of Magnesium Hydride”. *ACS Applied Materials & Interfaces* 6 (2014), 11038–11046.

[165] A. Yadav, A. Dashora, N. Patel, A. Miotello, M. Press, and D. Kothari. “Study of 2D MXene Cr_2C material for hydrogen storage using density functional theory”. *Applied Surface Science* 389 (2016), 88–95.

[166] X. Liang, S.-P. Ng, N. Ding, and C.-M. L. Wu. “Strain-Induced Switch for Hydrogen Storage in Cobalt-Decorated Nitrogen-Doped Graphene”. *Applied Surface Science* 473 (2019), 174–181.

[167] D. Kag, N. Luhadiya, N. D. Patil, and S. Kundalwal. “Strain and Defect Engineering of Graphene for Hydrogen Storage Via Atomistic Modelling”. *International Journal of Hydrogen Energy* 46 (2021), 22599–22610.

[168] V. Surya, K. Iyakutti, H. Mizuseki, and Y. Kawazoe. “Modification of Graphene as Active Hydrogen Storage Medium by Strain Engineering”. *Computational Materials Science* 65 (2012), 144–148.

[169] Y. Wang, G. Xu, S. Deng, Q. Wu, Z. Meng, X. Huang, L. Bi, Z. Yang, and R. Lu. “Lithium and sodium decorated graphdiyne as a candidate for hydrogen storage: First-principles and grand canonical Monte Carlo study”. *Applied Surface Science* 509 (2020), 144855.

[170] T. Liu, Y. Chen, H. Wang, M. Zhang, L. Yuan, and C. Zhang. “Li-Decorated β_{12}-Borophene as Potential Candidates for Hydrogen Storage: A First-Principle Study”. *Materials* 10 (2017).

[171] Y. Zhang, L. Zhang, H. Pan, H. Wang, and Q. Li. “Li-decorated porous hydrogen substituted graphyne: A new member of promising hydrogen storage medium”. *Applied Surface Science* 535 (2021), 147683.

[172] D. John, B. Nharangatt, S. Madhav Kastuar, and R. Chatanathodi. “Blue phosphorene nanosheets with point defects: Electronic structure and hydrogen storage capability”. *Applied Surface Science* 551 (2021), 149363.

[173] S. Goler, C. Coletti, V. Tozzini, V. Piazza, T. Mashoff, F. Beltram, V. Pellegrini, and S. Heun. “Influence of Graphene Curvature on Hydrogen Adsorption: Toward Hydrogen Storage Devices”. *Journal of Physical Chemistry C* 117 (2013), 11506–11513.

[174] V. Tozzini and V. Pellegrini. “Reversible Hydrogen Storage by Controlled Buckling of Graphene Layers”. *Journal of Physical Chemistry C* 115 (2011), 25523–25528.

[175] M. Makaremi, B. Mortazavi, and C. V. Singh. “2D Hydrogenated Graphene-Like Borophene as a High Capacity Anode Material for Improved Li/Na Ion Batteries: A First Principles Study”. *Materials Today Energy* 8 (2018), 22–28.

[176] Y. Jiao, F. Ma, J. Bell, A. Bilic, and A. Du. “Two-Dimensional Boron Hydride Sheets: High Stability, Massless Dirac Fermions, and Excellent Mechanical Properties”. *Angewandte Chemie International Edition* 128 (2016), 10448–10451.

[177] V. Shukla, R. B. Araujo, N. K. Jena, and R. Ahuja. “Borophene’s Tryst With Stability: Exploring 2D Hydrogen Boride as an Electrode for Rechargeable Batteries”. *Physical Chemistry Chemical Physics* 20 (2018), 22008–22016.

[178] I. Cabria, A. Lebon, M. Torres, L. Gallego, and A. Vega. “Hydrogen storage capacity of Li-decorated borophene and pristine graphene slit pores: A combined ab initio and quantum-thermodynamic study”. *Applied Surface Science* 562 (2021), 150019.

[179] B. Peng, H. Zhang, H. Shao, Z. Ning, Y. Xu, G. Ni, H. Lu, D. W. Zhang, and H. Zhu. “Stability and strength of atomically thin borophene from first principles calculations”. *Materials Research Letters* 5 (2017), 399–407.

[180] B. Mortazavi, M. Makaremi, M. Shahrokhi, M. Raeisi, C. V. Singh, T. Rabczuk, and L. F. C. Pereira. “Borophene hydride: a stiff 2D material with high thermal conductivity and attractive optical and electronic properties”. *Nanoscale* 10 (2018), 3759–3768.

[181] Z.-Q. Wang, T.-Y. Lü, H.-Q. Wang, Y. P. Feng, and J.-C. Zheng. “Review of borophene and its potential applications”. *Frontiers of Physics* 14 (2019), 1–20.

[182] T. A. Abtew, B.-c. Shih, P. Dev, V. H. Crespi, and P. Zhang. “Prediction of a Multicenter-Bonded Solid Boron Hydride for Hydrogen Storage”. *Physical Review B* 83 (2011), 094108.

[183] N. K. Jena, R. B. Araujo, V. Shukla, and R. Ahuja. “Borophane as a Benchmate of Graphene: A Potential 2D Material for Anode of Li and Na-Ion Batteries”. *ACS Applied Materials & Interfaces* 9 (2017), 16148–16158.

[184] S. Grimme, J. Antony, S. Ehrlich, and H. Krieg. “A consistent and Accurate Ab Initio Parametrization of Density Functional Dispersion Correction (DFT-D) for the 94 Elements H-Pu”. *Journal of Chemical Physics* 132 (2010), 154104.

[185] G. Henkelman, A. Arnaldsson, and H. Jónsson. “A Fast and Robust Algorithm for Bader Decomposition of Charge Density”. *Computational Materials Science* 36 (2006), 354–360.

[186] W. Tang, E. Sanville, and G. Henkelman. “A Grid-Based Bader Analysis Algorithm Without Lattice Bias”. *Journal of Physics: Condensed Matter* 21 (2009), 084204.

[187] E. Sanville, S. D. Kenny, R. Smith, and G. Henkelman. “Improved grid-based algorithm for Bader charge allocation”. *Journal of Computational Chemistry* 28 (2007), 899–908.

[188] M. Yu and D. R. Trinkle. “Accurate and efficient algorithm for Bader charge integration”. *Journal of Chemical Physics* 134 (2011), 064111.

[189] X. Chen, J. Liu, W. Zhang, B. Xiao, P. Zhang, and L. Li. “First-Principles Study on the Mechanism of Hydrogen Decomposition and Spillover on Borophene”. *Journal of Physical Chemistry C* 121 (2017), 17314–17320.

[190] G. Qin, A. Du, and Q. Sun. “A Theoretical Insight Into a Feasible Strategy for the Fabrication of Borophane”. *Physical Chemistry Chemical Physics* 20 (2018), 16216–16221.

[191] P. Liang, Y. Cao, B. Tai, L. Zhang, H. Shu, F. Li, D. Chao, and X. Du. “Is borophene a suitable anode material for sodium ion battery?” *Journal of Alloys and Compounds* 704 (2017), 152–159.

[192] D. Zivar, S. Kumar, and J. Foroozesh. “Underground hydrogen storage: A comprehensive review”. *International Journal of Hydrogen Energy* 46 (2021), 23436–23462.

[193] R. Tarkowski. “Underground hydrogen storage: Characteristics and prospects”. *Renewable and Sustainable Energy Reviews* 105 (2019), 86–94.

[194] L. Hashemi, M. Blunt, and H. Hajibeygi. “Pore-scale modelling and sensitivity analyses of hydrogen-brine multiphase flow in geological porous media”. *Sci. Rep.* 11 (2021), 1–13.

[195] A. Ursúa, L. M. Gandía, and P. Sanchis. “Hydrogen production from water electrolysis: Current status and future trends”. *Proceedings of the IEEE* 100 (2012), 410–426.

[196] A. Zarghami, N. Deen, and A. Vreman. “CFD modeling of multiphase flow in an alkaline water electrolyzer”. *Chemical Engineering Science* 227 (2020), 115926.

[197] B. E. Poling, J. M. Prausnitz, and J. P. O’Connell. *The Properties of gases and liquids*. 5th ed. New York: McGraw-Hill Education, 2001.

[198] J. Hnát, M. Paidar, K. Bouzek, A. Iulianelli, and A. Basile. *Current Trends and Future Developments on (Bio-) Membranes*. 1st ed. Amsterdam: Elsevier, 2020.

[199] A. Hauch, S. D. Ebbesen, S. H. Jensen, and M. Mogensen. “Highly efficient high temperature electrolysis”. *Journal of Materials Chemistry* 18 (2008), 2331–2340.

[200] D. Todd, M. Schwager, and W. Mérida. “Thermodynamics of high-temperature, high-pressure water electrolysis”. *Journal of Power Sources* 269 (2014), 424–429.

[201] T. Holm, T. Borsboom-Hanson, O. E. Herrera, and W. Mérida. "Hydrogen costs from water electrolysis at high temperature and pressure". *Energy Conversion and Management* 237 (2021), 114106.

[202] E. J. Slowinski, E. E. Gates, and C. E. Waring. "The effect of pressure on the surface tensions of liquids". *Journal of Physical Chemistry* 61 (1957), 808–810.

[203] L. Braun. "Über die Absorption von Stickstoff und von Wasserstoff in wässerigen Lösungen verschieden dissociierter Stoffe". *Zeitschrift für Physikalische Chemie* 33U (1900), 721–739.

[204] K. Gertz and H. Loeschcke. "Bestimmung der Diffusions-Koeffizienten von H_2, O_2, N_2, und He in Wasser und Blutserum bei konstant gehaltener Konvektion". *Zeitschrift für Naturforschung B* 9 (1954), 1–9.

[205] Y. T. Chow, G. C. Maitland, and J. P. Trusler. "Interfacial tensions of (H_2O + H_2) and (H_2O + CO_2 + H_2) systems at temperatures of (298–448) K and pressures up to 45 MPa". *Fluid Phase Equilibria* 475 (2018), 37–44.

[206] R. Massoudi and A. D. King Jr. "Effect of pressure on the surface tension of water. Adsorption of low molecular weight gases on water at 25 °C". *Journal of Physical Chemistry* 78 (1974), 2262–2266.

[207] M. Hosseini, J. Fahimpour, M. Ali, A. Keshavarz, and S. Iglauer. "H_2-brine interfacial tension as a function of salinity, temperature, and pressure; implications for hydrogen geo-storage". *Journal of Petroleum Science and Engineering* 213 (2022), 110441.

[208] S. Higgs, Y. Da Wang, C. Sun, J. Ennis-King, S. J. Jackson, R. T. Armstrong, and P. Mostaghimi. "In-situ hydrogen wettability characterisation for underground hydrogen storage". *International Journal of Hydrogen Energy* 47 (2022), 13062–13075.

[209] T. W. Richards and E. K. Carver. "A critical study of the capillary rise method of determining surface tension, with data for water, benzene, toluene, chloroform, carbon tetrachloride, ether and dimethyl aniline. [second paper.]" *Journal of the American Chemical Society* 43 (1921), 827–847.

[210] J. Drelich, C. Fang, and C. White. "Measurement of interfacial tension in fluid-fluid systems". *Encyclopedia of surface and colloid science* 3 (2002), 3158–3163.

[211] S. Chabab, P. Théveneau, C. Coquelet, J. Corvisier, and P. Paricaud. "Measurements and predictive models of high-pressure H_2 solubility in brine (H_2O+NaCl) for underground hydrogen storage application". *International Journal of Hydrogen Energy* 45 (2020), 32206–32220.

[212] G. A. Torín-Ollarves and J. M. Trusler. “Solubility of hydrogen in sodium chloride brine at high pressures”. *Fluid Phase Equilibria* 539 (2021), 113025.

[213] S. Ansari, M. Safaei-Farouji, S. Atashrouz, A. Abedi, A. Hemmati-Sarapardeh, and A. Mohaddespour. “Prediction of hydrogen solubility in aqueous solutions: Comparison of equations of state and advanced machine learning-metaheuristic approaches”. *International Journal of Hydrogen Energy* 47 (2022), 37724–37741.

[214] P. Steiner. “Ueber die Absorption des Wasserstoffs im Wasser und in wässerigen Lösungen”. *Annalen der Physik* 288 (1894), 275–299.

[215] W. Knopp. “Über die Löslichkeitsbeeinflussung von Wasserstoff und Stickoxydul in wässerigen Lösungen verschieden dissoziierter Stoffe”. *Zeitschrift für Physikalische Chemie* 48U (1904), 97–108.

[216] J. Gerecke and H. Bittrich. “The solubility of H_2, CO_2 and NH_3 in an aqueous electrolyte solution”. *Wiss Z Tech Hochsch Chem Carl Shorlemmer Leuna Merseburg* 13 (1971), 115–122.

[217] T. E. Crozier and S. Yamamoto. “Solubility of Hydrogen in Water, Seawater, and NaCl Solutions”. *Journal of Chemical and Engineering Data* 19 (1974), 242–244.

[218] L. I. Gordon, Y. Cohen, and D. R. Standley. “The solubility of molecular hydrogen in seawater”. *Deep Sea Research* 24 (1977), 937–941.

[219] J. Winkelmann. *Landolt-Bornstein: Numerical Data and Functional Relationships in Science and Technology, Group IV*. 1st ed. Vol. 15A. New York: Springer-Verlag, 2007.

[220] M. Baird and J. Davidson. “Annular jets—II: Gas absorption”. *Chemical Engineering Science* 17 (1962), 473–480.

[221] G. Houghton and D. Wise. “The diffusion coefficients of ten slightly soluble gases in water at 10–60° C”. *Chemical Engineering Science* 21 (1966), 999–1010.

[222] A. Akgerman and J. L. Gainer. “Predicting gas-liquid diffusivities”. *Journal of Chemical and Engineering Data* 17 (1972), 372–377.

[223] D. Himmelblau. “Diffusion of dissolved gases in liquids”. *Chemical Reviews* 64 (1964), 527–550.

[224] P. Verhallen, L. Oomen, A. Elsen, J. Kruger, and J. Fortuin. “The diffusion coefficients of helium, hydrogen, oxygen and nitrogen in water determined from the permeability of a stagnant liquid layer in the quasi-s”. *Chemical Engineering Science* 39 (1984), 1535–1541.

[225] B. Jähne, G. Heinz, and W. Dietrich. “Measurement of the diffusion coefficients of sparingly soluble gases in water”. *Journal of Geophysical Research: Oceans* 92 (1987), 10767–10776.

[226] W. De Blok and J. Fortuin. “Method for determining diffusion coefficients of slightly soluble gases in liquids”. *Chemical Engineering Science* 36 (1981), 1687–1694.

[227] L. C. Nielsen, I. C. Bourg, and G. Sposito. “Predicting CO_2–water interfacial tension under pressure and temperature conditions of geologic CO_2 storage”. *Geochimica et Cosmochimica Acta* 81 (2012), 28–38.

[228] X. Li, D. A. Ross, J. P. Trusler, G. C. Maitland, and E. S. Boek. “Molecular dynamics simulations of CO_2 and brine interfacial tension at high temperatures and pressures”. *Journal of Physical Chemistry B* 117 (2013), 5647–5652.

[229] S. Tsuji, Y. Liang, M. Kunieda, S. Takahashi, and T. Matsuoka. “Molecular Dynamics Simulations of the CO_2-Water-silica Interfacial Systems”. *Energy Procedia* 37 (2013), 5435–5442.

[230] S. Knauer, M. R. Schenk, T. Koddermann, D. Reith, and P. Jaeger. “Interfacial tension and related properties of ionic liquids in CH_4 and CO_2 at elevated pressures: experimental data and molecular dynamics simulation”. *Journal of Chemical and Engineering Data* 62 (2017), 2234–2243.

[231] Y. Hosseinzadeh Dehaghani, M. Assareh, and F. Feyzi. “Simultaneous Prediction of Equilibrium, Interfacial, and Transport Properties of CO_2-Brine Systems Using Molecular Dynamics Simulation: Applications to CO_2 Storage”. *Industrial & Engineering Chemistry Research* 61 (2022), 15390–15406.

[232] L. Zhao, J. Ji, L. Tao, and S. Lin. “Ionic effects on supercritical CO_2–brine interfacial tensions: Molecular dynamics simulations and a universal correlation with ionic strength, temperature, and pressure”. *Langmuir* 32 (2016), 9188–9196.

[233] Y. Yang, A. K. Narayanan Nair, and S. Sun. “Molecular dynamics simulation study of carbon dioxide, methane, and their mixture in the presence of brine”. *Journal of Physical Chemistry B* 121 (2017), 9688–9698.

[234] K. D. Papavasileiou, O. A. Moultos, and I. G. Economou. “Predictions of water/oil interfacial tension at elevated temperatures and pressures: A molecular dynamics simulation study with biomolecular force fields”. *Fluid Phase Equilibria* 476 (2018), 30–38.

[235] A. Aminian and B. ZareNezhad. “Molecular dynamics simulations study on the shear viscosity, density, and equilibrium interfacial tensions of CO_2 + brines and brines + CO_2 + n-decane systems”. *Journal of Physical Chemistry B* 125 (2021), 2707–2718.

[236] S. Blazquez, I. Zeron, M. Conde, J. Abascal, and C. Vega. “Scaled Charges at Work: Salting out and Interfacial Tension of Methane with Electrolyte Solutions from Computer Simulations”. *Fluid Phase Equilibria* 513 (2020), 112548.

[237] X. Zhao and H. Jin. “Correlation for self-diffusion coefficients of H_2, CH_4, CO, O_2 and CO_2 in supercritical water from molecular dynamics simulation”. *Applied Thermal Engineering* 171 (2020), 114941.

[238] X. Zhao, H. Jin, Y. Chen, and Z. Ge. “Numerical study of H_2, CH_4, CO, O_2 and CO_2 diffusion in water near the critical point with molecular dynamics simulation”. *Computers & Mathematics with Applications* 81 (2021), 759–771.

[239] R. F. Cracknell. “Molecular simulation of hydrogen adsorption in graphitic nanofibres”. *Physical Chemistry Chemical Physics* 3 (2001), 2091–2097.

[240] S. Alavi, J. Ripmeester, and D. Klug. “Molecular-dynamics study of structure II hydrogen clathrates”. *Journal of Chemical Physics* 123 (2005), 024507.

[241] M. Garcia-Ratés, J.-C. de Hemptinne, J. B. Avalos, and C. Nieto-Draghi. “Molecular Modeling of Diffusion Coefficient and Ionic Conductivity of CO_2 in Aqueous Ionic Solutions”. *Journal of Physical Chemistry B* 116 (2012), 2787–2800.

[242] C. G. Aimoli, E. J. Maginn, and C. R. Abreu. “Transport properties of carbon dioxide and methane from molecular dynamics simulations”. *Journal of Chemical Physics* 141 (2014), 134101.

[243] H. Zhong, S. Lai, J. Wang, W. Qiu, H.-D. Ludemann, and L. Chen. “Molecular dynamics simulation of transport and structural properties of CO_2 using different molecular models”. *Journal of Chemical and Engineering Data* 60 (2015), 2188–2196.

[244] H. Jiang, I. G. Economou, and A. Z. Panagiotopoulos. “Molecular modeling of thermodynamic and transport properties for CO_2 and aqueous brines”. *Accounts of Chemical Research* 50 (2017), 751–758.

[245] C. Lopez-Lazaro, P. Bachaud, I. Moretti, and N. Ferrando. “Predicting the phase behavior of hydrogen in NaCl brines by Molecular Simulation for geological applications”. *BSGF-Earth Sci. Bulletin* 190 (2019), 7.

[246] Y. Liu, A. Z. Panagiotopoulos, and P. G. Debenedetti. “Monte Carlo simulations of high-pressure phase equilibria of CO_2–H_2O mixtures”. *Journal of Physical Chemistry B* 115 (2011), 6629–6635.

[247] Y. Liu, T. Lafitte, A. Z. Panagiotopoulos, and P. G. Debenedetti. “Simulations of vapor–liquid phase equilibrium and interfacial tension in the CO_2–H_2O–NaCl system”. *AIChE Journal* 59 (2013), 3514–3522.

[248] A. Rahbari, R. Hens, M. Ramdin, O. A. Moultos, D. Dubbeldam, and T. J. H. Vlugt. “Recent Advances in the Continuous Fractional Component Monte Carlo Methodology”. *Mol. Simulat.* 47 (2021), 804–823.

[249] W. Shi and E. J. Maginn. “Continuous Fractional Component Monte Carlo: an Adaptive Biasing Method for Open System Atomistic Simulations”. *Journal of Chemical Theory and Computation* 3 (2007), 1451–1463.

[250] W. Shi and E. J. Maginn. “Improvement in molecule exchange efficiency in Gibbs ensemble Monte Carlo: Development and implementation of the Continuous Fractional Component move”. *Journal of Computational Chemistry* 29 (2008), 2520–2530.

[251] C. Vega and J. L. Abascal. “Simulating water with rigid non-polarizable models: a general perspective”. *Physical Chemistry Chemical Physics* 13 (2011), 19663–19688.

[252] M. A. González and J. L. Abascal. “The shear viscosity of rigid water models”. *Journal of Chemical Physics* 132 (2010), 096101.

[253] O. A. Moultos, I. N. Tsimpanogiannis, A. Z. Panagiotopoulos, and I. G. Economou. “Atomistic Molecular Dynamics Simulations of CO_2 Diffusivity in H_2O for a Wide Range of Temperatures and Pressures”. *Journal of Physical Chemistry B* 118 (2014), 5532–5541.

[254] R. Sakamaki, A. K. Sum, T. Narumi, R. Ohmura, and K. Yasuoka. “Thermodynamic properties of methane/water interface predicted by molecular dynamics simulations”. *Journal of Chemical Physics* 134 (2011), 144702.

[255] C. Vega and E. D. Miguel. “Surface tension of the most popular models of water by using the test-area simulation method”. *Journal of Chemical Physics* 126 (2007), 154707.

[256] M. F. Döpke, O. A. Moultos, and R. Hartkamp. “On the transferability of ion parameters to the TIP4P/2005 water model using molecular dynamics simulations”. *Journal of Chemical Physics* 152 (2020), 024501.

[257] J. Ryckaert, G. Ciccotti, and H. J. Berendsen. “Numerical integration of the cartesian equations of motion of a system with constraints: molecular dynamics of n-alkanes”. *Journal of Computational Physics* 23 (1977), 327–341.

[258] R. Hockney and J. Eastwood. *Computer Simulation Using Particles.* 1st ed. New York: CRC Press, 1988.

[259] L. Martínez, R. Andrade, E. G. Birgin, and J. M. Martínez. “PACKMOL: A package for building initial configurations for molecular dynamics simulations”. *Journal of Computational Chemistry* 30 (2009), 2157–2164.

[260] R. E. Isele-Holder, W. Mitchell, and A. E. Ismail. “Development and application of a particle-particle particle-mesh Ewald method for dispersion interactions”. *Journal of Chemical Physics* 137 (2012), 174107.

[261] H. S. Salehi, O. A. Moultos, and T. J. H. Vlugt. “Interfacial Properties of Hydrophobic Deep Eutectic Solvents with Water”. *Journal of Physical Chemistry B* 125 (2021), 12303–12314.

[262] J. S. Rowlinson and B. Widom. *Molecular theory of capillarity*. 1st ed. Oxford: Courier Corporation, 1982.

[263] S. H. Jamali, L. Wolff, T. M. Becker, M. D. Groen, M. Ramdin, R. Hartkamp, A. Bardow, T. J. H. Vlugt, and O. A. Moultos. “OCTP: A Tool for On-the-Fly Calculation of Transport Properties of Fluids with the Order- n Algorithm in LAMMPS”. *Journal of Chemical Information and Modeling* 59 (2019), 1290–1294.

[264] D. Dubbeldam, D. C. Ford, D. E. Ellis, and R. Q. Snurr. “A new perspective on the order-n algorithm for computing correlation functions”. *Molecular Simulation* 35 (2009), 1084–1097.

[265] I. Yeh and G. Hummer. “System-size dependence of diffusion coefficients and viscosities from molecular dynamics simulations with periodic boundary conditions”. *Journal of Physical Chemistry B* 108 (2004), 15873–15879.

[266] A. T. Celebi, S. H. Jamali, A. Bardow, T. J. H. Vlugt, and O. A. Moultos. “Finite-size effects of diffusion coefficients computed from molecular dynamics: a review of what we have learned so far”. *Molecular Simulation* 47 (2021), 831–845.

[267] S. H. Jamali, A. Bardow, T. J. H. Vlugt, and O. A. Moultos. “Generalized form for finite-size corrections in mutual diffusion coefficients of multicomponent mixtures obtained from equilibrium molecular dynamics simulation”. *Journal of Chemical Theory and Computation* 16 (2020), 3799–3806.

[268] O. A. Moultos, Y. Zhang, I. N. Tsimpanogiannis, I. G. Economou, and E. J. Maginn. “System-size corrections for self-diffusion coefficients calculated from molecular dynamics simulations: The case of CO_2, n-alkanes, and poly(ethylene glycol) dimethyl ethers”. *Journal of Chemical Physics* 145 (2016), 074109.

[269] S. H. Jamali, R. Hartkamp, C. Bardas, J. Sohl, T. J. H. Vlugt, and O. A. Moultos. “Shear viscosity computed from the finite-size effects of self-diffusivity in equilibrium molecular dynamics”. *Journal of Chemical Theory and Computation* 14 (2018), 5959–5968.

[270] S. H. Jamali, L. Wolff, T. M. Becker, A. Bardow, T. J. H. Vlugt, and O. A. Moultos. “Finite-size effects of binary mutual diffusion coefficients from molecular dynamics”. *Journal of Chemical Theory and Computation* 14 (2018), 2667–2677.

[271] A. Poursaeidesfahani, R. Hens, A. Rahbari, M. Ramdin, D. Dubbeldam, and T. J. H. Vlugt. “Efficient application of Continuous Fractional Component Monte Carlo in the reaction ensemble”. *Journal of Chemical Theory and Computation* 13 (2017), 4452–4466.

[272] A. Rahbari, R. Hens, D. Dubbeldam, and T. J. H. Vlugt. “Improving the accuracy of computing chemical potentials in CFCMC simulations”. *Molecular Physics* 117 (2019), 3493–3508.

[273] A. Rahbari, R. Hens, S. Jamali, M. Ramdin, D. Dubbeldam, and T. J. H. Vlugt. “Effect of truncating electrostatic interactions on predicting thermodynamic properties of water–methanol systems”. *Molecular Simulation* 45 (2019), 336–350.

[274] F. Wang and D. P. Landau. “Efficient multiple-range random walk algorithm to calculate the density of states”. *Physical Review Letters* 86 (2001), 2050.

[275] F. Wang and D. P. Landau. “Determining the density of states for classical statistical models: A random walk algorithm to produce a flat histogram”. *Physical Review E* 64 (2001), 056101.

[276] H. S. Salehi, R. Hens, O. A. Moultos, and T. J. H. Vlugt. “Computation of gas solubilities in choline chloride urea and choline chloride ethylene glycol deep eutectic solvents using Monte Carlo simulations”. *Journal of Molecular Liquids* 316 (2020), 113729.

[277] B. Widom. “Potential-distribution theory and the statistical mechanics of fluids”. *Journal of Physical Chemistry* 86 (1982), 869–872.

[278] B. Widom. “Some Topics in the Theory of Fluids”. *Journal of Chemical Physics* 39 (1963), 2808–2812.

[279] A. Rahbari, R. Hens, I. K. Nikolaidis, A. Poursaeidesfahani, M. Ramdin, I. G. Economou, O. A. Moultos, D. Dubbeldam, and T. J. H. Vlugt. “Computation of partial molar properties using continuous fractional component Monte Carlo”. *Molecular Physics* 116 (2018), 3331–3344.

[280] A. Georgiadis, G. Maitland, J. M. Trusler, and A. Bismarck. “Interfacial tension measurements of the (H_2O+ CO_2) system at elevated pressures and temperatures”. *Journal of Chemical and Engineering Data* 55 (2010), 4168–4175.

[281] S. Bachu and D. B. Bennion. “Interfacial tension between CO_2, freshwater, and brine in the range of pressure from (2 to 27) MPa, temperature from (20 to 125) °C, and water salinity from (0 to 334 000) mg $\cdot$ L^{-1}”. *Journal of Chemical and Engineering Data* 54 (2009), 765–775.

[282] A. Hebach, A. Oberhof, N. Dahmen, A. Kögel, H. Ederer, and E. Dinjus. “Interfacial tension at elevated pressures measurements and correlations in the water+ carbon dioxide system”. *Journal of Chemical and Engineering Data* 47 (2002), 1540–1546.

[283] Q.-Y. Ren, G.-J. Chen, W. Yan, and T.-M. Guo. “Interfacial tension of (CO_2+ CH_4)+ water from 298 K to 373 K and pressures up to 30 MPa”. *Journal of Chemical and Engineering Data* 45 (2000), 610–612.

[284] P. Naeiji, T. K. Woo, S. Alavi, and R. Ohmura. “Molecular dynamics simulations of interfacial properties of the CO_2–water and CO_2–CH_4–water systems”. *Journal of Chemical Physics* 153 (2020), 044701.

[285] X. Li, E. Boek, G. C. Maitland, and J. M. Trusler. “Interfacial Tension of (Brines+ CO_2):(0.864 NaCl+ 0.136 KCl) at Temperatures between (298 and 448) K, Pressures between (2 and 50) MPa, and Total Molalities of (1 to 5) mol$\cdot$ kg^{-1}”. *Journal of Chemical and Engineering Data* 57 (2012), 1078–1088.

[286] C. Aggelopoulos, M. Robin, and O. Vizika. “Interfacial tension between CO_2 and brine (NaCl+ $CaCl_2$) at elevated pressures and temperatures: The additive effect of different salts”. *Advances in Water Resources* 34 (2011), 505–511.

[287] G. R. Jerauld and A. Kazemi. “An improved simple correlation for accurate estimation of CO_2-Brine interfacial tension at reservoir conditions”. *Journal of Petroleum Science and Engineering* 208 (2022), 109537.

[288] M. Manciu and E. Ruckenstein. “Specific ion effects via ion hydration: I. Surface tension”. *Advances in Colloid and Interface Science* 105 (2003), 63–101.

[289] Y. Marcus. “Effect of ions on the structure of water: Structure making and breaking”. *Chemical Reviews* 109 (2009), 1346–1370.

[290] L. M. Pegram and M. T. Record. “Hofmeister salt effects on surface tension arise from partitioning of anions and cations between bulk water and the air-water interface”. *Journal of Physical Chemistry B* 111 (2007), 5411–5417.

[291] Y. Levin, A. P. D. Santos, and A. Diehl. “Ions at the air-water interface: An end to a hundred-year-old mystery?” *Physical Review Letters* 103 (2009), 257802.

[292] S. Weisenberger and A. Schumpe. “Estimation of gas solubilities in salt solutions at temperatures from 273 K to 363 K”. *AIChE Journal* 42 (1996), 298–300.

[293] E. L. Cussler. “Diffusion Coefficients and Diffusion of Interacting Species”. *Diffusion: Mass Transfer in Fluid Systems* (2009), 126–171.

[294] R. Taylor and R. Krishna. *Multicomponent mass transfer*. 1st ed. Vol. 2. John Wiley & Sons, 1993.

[295] R. Krishna and J. Wesselingh. “The Maxwell-Stefan approach to mass transfer”. *Chemical Engineering Science* 52 (1997), 861–911.

[296] R. Wiebe and V. L. Gaddy. “The Solubility of Hydrogen in Water at 0, 50, 75 and 100° from 25 to 1000 Atmospheres”. *Journal of the American Chemical Society* 56 (1934), 76–79.

[297] R. Wiebe, V. Gaddy, and C. Heins. “Solubility of Hydrogen in Water at 25° C. from 25 to 1000 Atmospheres”. *Industrial and Engineering Chemistry* 24 (1932), 823–825.

[298] G. Kling and G. Maurer. “The solubility of hydrogen in water and in 2-aminoethanol at temperatures between 323 K and 423 K and pressures up to 16 MPa”. *Journal of Chemical Thermodynamics* 23 (1991), 531–541.

[299] V. R. Choudhary, M. G. Parande, and P. H. Brahme. “Simple apparatus for measuring solubility of gases at high pressures”. *Industrial & Engineering Chemistry Fundamentals* 21 (1982), 472–474.

[300] J. Chandrasekhar, D. C. Spellmeyer, and W. L. Jorgensen. “Energy component analysis for dilute aqueous solutions of lithium (1+), sodium (1+), fluoride (1-), and chloride (1-) ions”. *Journal of the American Chemical Society* 106 (1984), 903–910.

[301] F. Darkrim, J. Vermesse, P. Malbrunot, and D. Levesque. “Monte Carlo simulations of nitrogen and hydrogen physisorption at high pressures and room temperature. Comparison with experiments”. *Journal of Chemical Physics* 110 (1999), 4020–4027.

[302] Z. Zhu, Y. Cao, Z. Zheng, and D. Chen. “An Accurate Model for Estimating H_2 Solubility in Pure Water and Aqueous NaCl Solutions”. *Energies* 15 (2022), 5021.

[303] A. Z. Panagiotopoulos. “Simulations of activities, solubilities, transport properties, and nucleation rates for aqueous electrolyte solutions”. *Journal of Chemical Physics* 153 (2020), 010903.

[304] M. Hellström and J. Behler. “Structure of aqueous NaOH solutions: insights from neural-network-based molecular dynamics simulations”. *Physical Chemistry Chemical Physics* 19 (2017), 82–96.

[305] M. David, C. Ocampo-Martínez, and R. Sánchez-Peña. “Advances in alkaline water electrolyzers: A review”. *J. Energy Storage* 23 (2019), 392–403.

[306] V. Solovey, A. Shevchenko, M. Zipunnikov, A. Kotenko, N. T. Khiem, B. D. Tri, and T. T. Hai. “Development of high pressure membraneless alkaline electrolyzer”. *International Journal of Hydrogen Energy* 47 (2022), 6975–6985.

[307] Ø. Ulleberg. “Modeling of advanced alkaline electrolyzers: a system simulation approach”. *International Journal of Hydrogen Energy* 28 (2003), 21–33.

[308] *Solubility table of compounds in water at temperature*. `https://www.sigmaaldrich.com/NL/en/support/calculators-and-apps/solubility-table-compounds-water-temperature`, (Accessed Sep. 6, 2022).

[309] *Potassium hydroxide*. `https://webwiser.nlm.nih.gov/substance?substanceId=401&catId=44`, Accessed Sep. 6, 2022).

[310] D. Le Bideau, P. Mandin, M. Benbouzid, M. Kim, and M. Sellier. “Review of necessary thermophysical properties and their sensivities with temperature and electrolyte mass fractions for alkaline water electrolysis multiphysics modelling”. *International Journal of Hydrogen Energy* 44 (2019), 4553–4569.

[311] A. Zarghami, N. Deen, and A. Vreman. “CFD modeling of multiphase flow in an alkaline water electrolyzer”. *Chemical Engineering Science* 227 (2020), 115926.

[312] D. Rowland, E. Königsberger, G. Hefter, and P. M. May. “Aqueous electrolyte solution modelling: Some limitations of the Pitzer equations”. *Applied Geochemistry* 55 (2015), 170–183.

[313] G. M. Kontogeorgis, B. Maribo-Mogensen, and K. Thomsen. “The Debye-Hückel theory and its importance in modeling electrolyte solutions”. *Fluid Phase Equilibria* 462 (2018), 130–152.

[314] P. J. Walker, X. Liang, and G. M. Kontogeorgis. “Importance of the Relative Static Permittivity in electrolyte SAFT-VR Mie Equations of State”. *Fluid Phase Equilibria* 551 (2022), 113256.

[315] M. C. Reis. “Current Trends in Predictive Methods and Electrolyte Equations of State”. *ACS Omega* 7 (2022), 16847.

[316] B. Maribo-Mogensen, K. Thomsen, and G. M. Kontogeorgis. “An electrolyte CPA equation of state for mixed solvent electrolytes”. *AIChE Journal* 61 (2015), 2933–2950.

[317] I. K. Nikolaidis, N. Novak, G. M. Kontogeorgis, and I. G. Economou. "Rigorous Phase Equilibrium Calculation Methods for Strong Electrolyte Solutions: The Isothermal Flash". *Fluid Phase Equilibria* 558 (2022), 113441.

[318] G. M. Kontogeorgis, A. Schlaikjer, M. D. Olsen, B. Maribo-Mogensen, K. Thomsen, N. von Solms, and X. Liang. "A Review of Electrolyte Equations of State with Emphasis on Those Based on Cubic and Cubic-Plus-Association (CPA) Models". *International Journal of Thermophysics* 43 (2022), 1–68.

[319] N. Novak, G. M. Kontogeorgis, M. Castier, and I. G. Economou. "Modeling of Gas Solubility in Aqueous Electrolyte Solutions with the eSAFT-VR Mie Equation of State". *Industrial & Engineering Chemistry Research* 60 (2021), 15327–15342.

[320] H. Jiang, Z. Mester, O. A. Moultos, I. G. Economou, and A. Z. Panagiotopoulos. "Thermodynamic and Transport Properties of H_2O + NaCl from Polarizable Force Fields". *Journal of Chemical Theory and Computation* 11 (2015), 3802–3810.

[321] G. A. Orozco, O. A. Moultos, H. Jiang, I. G. Economou, and A. Z. Panagiotopoulos. "Molecular simulation of thermodynamic and transport properties for the H_2O+NaCl system". *Journal of Chemical Physics* 141 (2014), 234507.

[322] S. H. Saravi and A. Z. Panagiotopoulos. "Activity Coefficients and Solubilities of NaCl in Water–Methanol Solutions from Molecular Dynamics Simulations". *Journal of Physical Chemistry B* 126 (2022), 2891–2898.

[323] C. Zhang, S. Yue, A. Z. Panagiotopoulos, M. L. Klein, and X. Wu. "Dissolving salt is not equivalent to applying a pressure on water". *Nature Communications* 13 (2022), 1–6.

[324] M. J. Tham, R. D. Walker Jr, and K. E. Gubbins. "Diffusion of oxygen and hydrogen in aqueous potassium hydroxide solutions". *Journal of Physical Chemistry* 74 (1970), 1747–1751.

[325] B. Chen, I. Ivanov, J. M. Park, M. Parrinello, and M. L. Klein. "Solvation Structure and Mobility Mechanism of OH-: A Car-Parrinello Molecular Dynamics Investigation of Alkaline Solutions". *Journal of Physical Chemistry B* 106 (2002), 12006–12016.

[326] T. Megyes, S. Bálint, T. Grósz, T. Radnai, I. Bakó, and P. Sipos. "The structure of aqueous sodium hydroxide solutions: A combined solution x-ray diffraction and simulation study". *Journal of Chemical Physics* 128 (2008), 044501.

[327] G. Guevara-Carrion, C. Nieto-Draghi, J. Vrabec, and H. Hasse. "Prediction of Transport Properties by Molecular Simulation: Methanol and Ethanol and their Mixture". *Journal of Physical Chemistry B* 112 (2008), 16664–16674.

[328] A. Ghaffari and A. Rahbar-Kelishami. “MD simulation and evaluation of the self-diffusion coefficients in aqueous NaCl solutions at different temperatures and concentrations”. *Journal of Molecular Liquids* 187 (2013), 238–245.

[329] S. H. Saravi and A. Z. Panagiotopoulos. “Individual Ion Activity Coefficients in Aqueous Electrolytes from Explicit-Water Molecular Dynamics Simulations”. *Journal of Physical Chemistry B* 125 (2021), 8511–8521.

[330] J. L. Abascal and C. Vega. “Widom line and the liquid–liquid critical point for the TIP4P/2005 water model”. *Journal of Chemical Physics* 133 (2010), 234502.

[331] S. Blazquez, M. M. Conde, J. L. F. Abascal, and C. Vega. “The Madrid-2019 force field for electrolytes in water using TIP4P/2005 and scaled charges: Extension to the ions F^-, Br^-, I^-, Rb^+, and Cs^+”. *Journal of Chemical Physics* 156 (2022), 044505.

[332] Z. Kann and J. Skinner. “A scaled-ionic-charge simulation model that reproduces enhanced and suppressed water diffusion in aqueous salt solutions”. *Journal of Chemical Physics* 141 (2014), 104507.

[333] D. J. Bonthuis, S. I. Mamatkulov, and R. R. Netz. “Optimization of classical nonpolarizable force fields for OH^- and H_3O^+”. *Journal of Chemical Physics* 144 (2016), 104503.

[334] J. S. Hub, M. G. Wolf, C. Caleman, P. J. van Maaren, G. Groenhof, and D. van der Spoel. “Thermodynamics of hydronium and hydroxide surface solvation”. *Chemical Science* 5 (2014), 1745–1749.

[335] J. R. Pliego and J. M. Riveros. “On the Calculation of the Absolute Solvation Free Energy of Ionic Species: Application of the Extrapolation Method to the Hydroxide Ion in Aqueous Solution”. *Journal of Physical Chemistry B* 104 (2000), 5155–5160.

[336] I. S. Ufimtsev, A. G. Kalinichev, T. J. Martinez, and R. J. Kirkpatrick. “A charged ring model for classical OH^-(aq) simulations”. *Chemical Physics Letters* 442 (2007), 128–133.

[337] A. Botti, F. Bruni, S. Imberti, M. A. Ricci, and A. K. Soper. “Ions in water: The microscopic structure of concentrated NaOH solutions”. *Journal of Chemical Physics* 120 (2004), 10154–10162.

[338] S. Imberti, A. Botti, F. Bruni, G. Cappa, M. A. Ricci, and A. K. Soper. “Ions in water: The microscopic structure of concentrated hydroxide solutions”. *Journal of Chemical Physics* 122 (2005), 194509.

[339] R. Vácha, T. Megyes, I. Bakó, L. Pusztai, and P. Jungwirth. "Benchmarking Polarizable Molecular Dynamics Simulations of Aqueous Sodium Hydroxide by Diffraction Measurements". *Journal of Physical Chemistry A* 113 (2009), 4022–4027.

[340] A. Coste, A. Poulesquen, O. Diat, J.-F. Dufrêche, and M. Duvail. "Investigation of the Structure of Concentrated NaOH Aqueous Solutions by Combining Molecular Dynamics and Wide-Angle X-ray Scattering". *Journal of Physical Chemistry B* 123 (2019), 5121–5130.

[341] M. Zapałowski and W. M. Bartczak. "Structural and dynamical properties of concentrated aqueous NaOH solutions: a computer simulation study". *Computers & Chemistry* 24 (2000), 459–468.

[342] M. Bohn, R. Lustig, and J. Fischer. "Description of polyatomic real substances by two-center Lennard-Jones model fluids". *Fluid Phase Equilibria* 25 (1986), 251–262.

[343] B. Dünweg and K. Kremer. "Molecular dynamics simulation of a polymer chain in solution". *Journal of Chemical Physics* 99 (1993), 6983–6997.

[344] F. Heidar-Zadeh, P. W. Ayers, T. Verstraelen, I. Vinogradov, E. Vöhringer-Martinez, and P. Bultinck. "Information-Theoretic Approaches to Atoms-in-Molecules: Hirshfeld Family of Partitioning Schemes". *Journal of Physical Chemistry A* 122 (2018), 4219–4245.

[345] J. Olsson, Å. Jernqvist, and G. Aly. "Thermophysical properties of aqueous NaOH-H_2O solutions at high concentrations". *International Journal of Thermophysics* 18 (1997), 779–793.

[346] Y. Guo, H. Xu, F. Guo, S. Zheng, and Y. Zhang. "Density and viscosity of aqueous solution of K_2CrO_4/KOH mixed electrolytes". *Transactions of Nonferrous Metals Society of China* 20 (2010), s32–s36.

[347] Y. Marcus. "Ionic radii in aqueous solutions". *Chemical Reviews* 88 (1988), 1475–1498.

[348] L. Yuan-Hui and S. Gregory. "Diffusion of ions in sea water and in deep-sea sediments". *Geochimica et Cosmochimica Acta* 38 (1974), 703–714.

[349] R. D. Walker Jr. *Study of gas solubilities and transport properties in fuel cell electrolytes*. Technical Report. Florida Univ., Gainesville (USA), 1971, `https://www.osti.gov/biblio/5044425`, (Accessed Jun. 10, 2022).

[350] I. M. Sechenov. "Über die konstitution der salzlö sungen auf grund ihres verhaltens zu kohlensäure". *Zeitschrift für Physikalische Chemie* 4 (1889), 117–125.

[351] R. Davis, G. Horvath, and C. Tobias. “The solubility and diffusion coefficient of oxygen in potassium hydroxide solutions”. *Electrochimica Acta* 12 (1967), 287–297.

[352] S. Shoor, R. D. Walker Jr, and K. Gubbins. “Salting out of nonpolar gases in aqueous potassium hydroxide solutions”. *Journal of Physical Chemistry* 73 (1969), 312–317.

[353] P. Ruetschi and R. Amlie. “Solubility of hydrogen in potassium hydroxide and sulfuric acid. Salting-out and hydration”. *Journal of Physical Chemistry* 70 (1966), 718–723.

[354] P. Habibi, J. R. T. Postma, J. T. Padding, P. Dey, T. J. H. Vlugt, and O. A. Moultos. “Thermodynamic and Transport Properties of $H_2/H_2O/NaB(OH)_4$ Mixtures Using the Delft Force Field (DFF/$B(OH)_4^-$)”. *Industrial and Engineering Chemistry Research* 62 (2023), 11992–12005.

[355] W. Gu, F. Li, X. Liu, Q. Gao, S. Gong, J. Li, and S. Q. Shi. “Borate chemistry inspired by cell walls converts soy protein into high-strength, antibacterial, flame-retardant adhesive”. *Green Chemistry* 22 (2020), 1319–1328.

[356] B. Li, X. Ling, X. Liu, Q. Li, and W. Chen. “Hydration of Portland cements in solutions containing high concentration of borate ions: Effects of LiOH”. *Cement and Concrete Composites* 102 (2019), 94–104.

[357] W. Xu, X. Wang, Y. Wu, W. Li, and C. Chen. “Functionalized graphene with Co-ZIF adsorbed borate ions as an effective flame retardant and smoke suppression agent for epoxy resin”. *Journal of Hazardous Materials* 363 (2019), 138–151.

[358] T. J. Stockmann, P. D. Boyle, and Z. Ding. “Preparation and crystal structure of tetraoctylphosphonium tetrakis(pentafluorophenyl)borate ionic liquid for electrochemistry at its interface with water”. *Catalysis Today* 295 (2017), 89–94.

[359] S. K. Gulsoy and H. Eroglu. “Influence of Sodium Borohydride on Kraft Pulping of European Black Pine as a Digester Additive”. *Industrial & Engineering Chemistry Research* 50 (2011), 2441–2444.

[360] J. P. Ferguson, H. Arcis, G. H. Zimmerman, and P. R. Tremaine. “Ion-Pair Formation Constants of Lithium Borate and Lithium Hydroxide under Pressurized Water Nuclear Reactor Coolant Conditions”. *Industrial & Engineering Chemistry Research* 56 (2017), 8121–8132.

[361] K. Manoharan, V. K. Palaniswamy, K. Raman, and R. Sundaram. “Investigation of solid state hydrogen storage performances of novel $NaBH_4$/Ah-BN nanocomposite as hydrogen storage medium for fuel cell applications”. *Journal of Alloys and Compounds* 860 (2021), 158444.

[362] C. Tarhan and M. A. Çil. “A study on hydrogen, the clean energy of the future: Hydrogen storage methods”. *Journal of Energy Storage* 40 (2021), 102676.

[363] P. Brack, S. E. Dann, and K. G. U. Wijayantha. “Heterogeneous and homogenous catalysts for hydrogen generation by hydrolysis of aqueous sodium borohydride ($NaBH_4$) solutions”. *Energy Science & Engineering* 3 (2015), 174–188.

[364] U. B. Demirci, A. Ouardia, J. Andrieux, J. Hannauer, R. Chamoun, and P. Miele. “Sodium borohydride hydrolysis as hydrogen generator: issues, state of the art and applicability upstream from a fuel cell”. *Fuel Cells* 10 (2010).

[365] Q. Zhang and R. M. Mohring. “Reaction Chemistry Between Aqueous Sulfuric Acid and Solid Sodium Borohydride”. *Industrial & Engineering Chemistry Research* 48 (2009), 1603–1607.

[366] E. Y. Marrero-Alfonso, A. M. Beaird, T. A. Davis, and M. A. Matthews. “Hydrogen Generation from Chemical Hydrides”. *Industrial & Engineering Chemistry Research* 48 (2009), 3703–3712.

[367] A. Hojjati-Najafabadi, A. Aygun, R. N. E. Tiri, F. Gulbagca, M. I. Lounissaa, P. Feng, F. Karimi, and F. Sen. “Bacillus thuringiensis Based Ruthenium/Nickel Co-Doped Zinc as a Green Nanocatalyst: Enhanced Photocatalytic Activity, Mechanism, and Efficient H_2 Production from Sodium Borohydride Methanolysis”. *Industrial & Engineering Chemistry Research* 62 (2023), 4655–4664.

[368] E. S. van Rheenen, J. T. Padding, J. C. Slootweg, and K. Visser. *A review of the potential of hydrogen carriers for zero emission, low signature ship propulsion systems*. `https://library.imarest.org/record/10649`, (Accessed 10 Dec. 2023). 2022.

[369] A.-J. Hung, S.-F. Tsai, Y.-Y. Hsu, J.-R. Ku, Y.-H. Chen, and C.-C. Yu. “Kinetics of sodium borohydride hydrolysis reaction for hydrogen generation”. *International Journal of Hydrogen Energy* 33 (2008), 6205–6215.

[370] A. M. Beaird, P. Li, H. S. Marsh, W. A. Al-Saidi, J. K. Johnson, M. A. Matthews, and C. T. Williams. “Thermal Dehydration and Vibrational Spectra of Hydrated Sodium Metaborates”. *Industrial & Engineering Chemistry Research* 50 (2011), 7746–7752.

[371] Y. Zhou, S. Higa, C. Fang, Y. Fang, W. Zhang, and T. Yamaguchi. “$B(OH)_4^-$ hydration and association in sodium metaborate solutions by X-ray diffraction and empirical potential structure refinement”. *Physical Chemistry Chemical Physics* 19 (2017), 27878–27887.

[372] Y. Zhou, C. Fang, Y. Yang, and F. Zhu. “Volumetric and Transport Properties of Aqueous $NaB(OH)_4$ Solutions”. *Chinese Journal of Chemical Engineering* 21 (2013), 1048–1056.

[373] Y. Zhou, C. Fang, Y. Fang, and F. Zhu. “Polyborates in aqueous borate solution: A Raman and DFT theory investigation”. *Spectrochimica Acta Part A: Molecular and Biomolecular Spectroscopy* 83 (2011), 82–87.

[374] R. K. Momii and N. H. Nachtrieb. “Nuclear magnetic resonance study of borate-polyborate equilibria in aqueous solution”. *Inorganic Chemistry* 6 (1967), 1189–1192.

[375] A. Lopalco, A. A. Lopedota, V. Laquintana, N. Denora, and V. J. Stella. “Boric Acid, a Lewis Acid With Unique and Unusual Properties: Formulation Implications”. *Journal of Pharmaceutical Sciences* 109 (2020), 2375–2386.

[376] J. R. Rustad, E. J. Bylaska, V. E. Jackson, and D. A. Dixon. “Calculation of boron-isotope fractionation between $B(OH)_3$(aq) and $B(OH)_4^-$(aq)”. *Geochimica et Cosmochimica Acta* 74 (2010), 2843–2850.

[377] Y. P. Perelygin and D. Y. Chistyakov. “Boric acid”. *Russian Journal of Applied Chemistry* 79 (2006), 2041–2042.

[378] L. M. S. G. A. Applegarth, C. C. Pye, J. S. Cox, and P. R. Tremaine. “Raman Spectroscopic and ab Initio Investigation of Aqueous Boric Acid, Borate, and Polyborate Speciation from 25 to 80 °C”. *Industrial & Engineering Chemistry Research* 56 (2017), 13983–13996.

[379] U. B. Demirci, O. Akdim, J. Andrieux, J. Hannauer, R. Chamoun, and P. Miele. “Sodium Borohydride Hydrolysis as Hydrogen Generator: Issues, State of the Art and Applicability Upstream from a Fuel Cell”. *Fuel Cells* 10 (2010), 335–350.

[380] U. Demirci, O. Akdim, and P. Miele. “Ten-year efforts and a no-go recommendation for sodium borohydride for on-board automotive hydrogen storage”. *International Journal of Hydrogen Energy* 34 (2009), 2638–2645.

[381] H. K. Atiyeh and B. R. Davis. “Separation of sodium metaborate from sodium borohydride using nanofiltration membranes for hydrogen storage application”. *International Journal of Hydrogen Energy* 32 (2007), 229–236.

[382] T. Sousa, V. Fernandes, P. Pinto, Y. Slavkov, L. Bosukov, and C. Rangel. “A sodium borohydride hydrogen generation reactor for stationary applications: Experimental and reactor simulation studies”. *Chemical Engineering Science* 84 (2012), 70–79.

[383] A. F. Baye, M. W. Abebe, R. Appiah-Ntiamoah, and H. Kim. “Engineered iron-carbon-cobalt (Fe_3O_4 C-Co) core-shell composite with synergistic catalytic properties towards hydrogen generation via $NaBH_4$ hydrolysis”. *Journal of Colloid and Interface Science* 543 (2019), 273–284.

[384] L. Yu, P. Pellechia, and M. A. Matthews. “Kinetic models of concentrated $NaBH_4$ hydrolysis”. *International Journal of Hydrogen Energy* 39 (2014), 442–448.

[385] B. Liu and Z. Li. “Hydrogen generation from borohydride hydrolysis reaction”. *Journal of Power Sources* 187 (2009), 527–534.

[386] “Hydrogen production from $NaBH_4$ hydrolysis via Co-ZIF-9 catalyst”. *Fuel Processing Technology* 100 (2012), 43–48.

[387] V. Fernandes, A. Pinto, and C. Rangel. “Hydrogen production from sodium borohydride in methanol–water mixtures”. *International Journal of Hydrogen Energy* 35 (2010), 9862–9868.

[388] S. Shabunya, V. Minkina, V. Kalinin, N. Sankir, and C. Altaf. “Kinetics of the catalytic hydrolysis of concentrated aqueous solutions of $NaBH_4$ on Co/TiO_2 powder”. *Kinetics and Catalysis* 62 (2021), 350–359.

[389] R. Oronzio, G. Monteleone, A. Pozio, M. De Francesco, and S. Galli. “New reactor design for catalytic sodium borohydride hydrolysis”. *International Journal of Hydrogen Energy* 34 (2009), 4555–4560.

[390] X. Liu, A. Martín-Calvo, E. McGarrity, S. K. Schnell, S. Calero, J.-M. Simon, D. Bedeaux, S. Kjelstrup, A. Bardow, and T. J. H. Vlugt. “Fick Diffusion Coefficients in Ternary Liquid Systems from Equilibrium Molecular Dynamics Simulations”. *Industrial & Engineering Chemistry Research* 51 (2012), 10247–10258.

[391] B. Zhang, X. Zhao, Y. Chen, Z. Ge, and H. Jin. “Investigation of H_2S Diffusion in Transcritical and Supercritical Water: A Molecular Dynamics Simulation Study”. *Industrial & Engineering Chemistry Research* 62 (2023), 3026–3037.

[392] S. H. Jamali, L. Wolff, T. M. Becker, A. Bardow, T. J. H. Vlugt, and O. A. Moultos. “Finite-Size Effects of Binary Mutual Diffusion Coefficients from Molecular Dynamics”. *Journal of Chemical Theory and Computation* 14 (2018), 2667–2677.

[393] Ø. Gullbrekken, I. T. Røe, S. M. Selbach, and S. K. Schnell. “Charge Transport in Water–NaCl Electrolytes with Molecular Dynamics Simulations”. *Journal of Physical Chemistry B* 127 (2023), 2729–2738.

[394] L. Onsager. “Theories and Problems of Liquid Diffusion”. *Annals of the New York Academy of Sciences* 46 (1945), 241–265.

[395] R. Krishna and J. M. van Baten. “The Darken Relation for Multicomponent Diffusion in Liquid Mixtures of Linear Alkanes: An Investigation Using Molecular Dynamics (MD) Simulations”. *Industrial & Engineering Chemistry Research* 44 (2005), 6939–6947.

[396] P. Kubisiak and A. Eilmes. “Estimates of Electrical Conductivity from Molecular Dynamics Simulations: How to Invest the Computational Effort”. *Journal of Physical Chemistry B* 124 (2020), 9680–9689.

[397] Delft High Performance Computing Centre (DHPC),*DelftBlue Supercomputer (Phase 2)*. `https://www.tudelft.nl/dhpc/ark:/44463/DelftBluePhase2`. 2024.

[398] S. Hempel, J. Fischer, D. Paschek, and G. Sadowski. “Activity coefficients of complex molecules by molecular simulation and Gibbs-Duhem integration”. *Soft Materials* 10 (2012), 26–41.

[399] F. Zhou Yongquanand Chunhui, F. Yan, Z. Fayan, T. Song, and X. Sha. “Structure of aqueous sodium metaborate solutions: X-ray diffraction study”. *Russian Journal of Physical Chemistry A* 86 (2012), 1236–1244.

[400] I. Tang, H. Munkelwitz, and N. Wang. “Water activity measurements with single suspended droplets: The NaCl-H_2O and KCl-H_2O systems”. *Journal of Colloid and Interface Science* 114 (1986), 409–415.

[401] C. L. Young. *Solubility Data Series: Hydrogen and Deuterium*. 1st ed. Vol. 5/6. Oxford: Pergamon Press, 1981.

[402] J. G. Reynolds. “Salt Solubilities in Aqueous Solutions of $NaNO_3$, $NaNO_2$, NaCl, and NaOH: A Hofmeister-like Series for Understanding Alkaline Nuclear Waste”. *ACS Omega* 3 (2018), 15149–15157.

[403] S. Naseri Boroujeni, X. Liang, B. Maribo-Mogensen, and G. M. Kontogeorgis. “Comparison of Models for the Prediction of the Electrical Conductivity of Electrolyte Solutions”. *Industrial and Engineering Chemistry Research* 61 (2022), 3168–3185.

[404] S. Naseri Boroujeni, B. Maribo-Mogensen, X. Liang, and G. M. Kontogeorgis. “New Electrical Conductivity Model for Electrolyte Solutions Based on the Debye–Hückel–Onsager Theory”. *Journal of Physical Chemistry B* 127 (2023), 9954–9975.

[405] S. Blazquez, J. L. F. Abascal, J. Lagerweij, P. Habibi, P. Dey, T. J. H. Vlugt, O. A. Moultos, and C. Vega. “Computation of Electrical Conductivities of Aqueous Electrolyte Solutions: Two Surfaces, One Property”. *Journal of Chemical Theory and Computation* 19 (2023), 5380–5393.

[406] L.-P. Wang, T. J. Martinez, and V. S. Pande. “Building Force Fields: An Automatic, Systematic, and Reproducible Approach”. *Journal of Physical Chemistry Letters* 5 (2014), 1885–1891.

[407] Y. Xiong, S. Izadi, and A. V. Onufriev. “Fast Polarizable Water Model for Atomistic Simulations”. *Journal of Chemical Theory and Computation* 18 (2022), 6324–6333.

[408] H. Jiang, Z. Mester, O. A. Moultos, I. G. Economou, and A. Z. Panagiotopoulos. “Thermodynamic and Transport Properties of H_2O + NaCl from Polarizable Force Fields”. *Journal of Chemical Theory and Computation* 11 (2015), 3802–3810.

[409] B. Han, C. M. Isborn, and L. Shi. “Incorporating Polarization and Charge Transfer into a Point-Charge Model for Water Using Machine Learning”. *Journal of Physical Chemistry Letters* 14 (2023), 3869–3877.

[410] A. W. Milne and M. Jorge. “Polarization Corrections and the Hydration Free Energy of Water”. *Journal of Chemical Theory and Computation* 15 (2019), 1065–1078.

[411] C. Vega, J. L. F. Abascal, and I. Nezbeda. “Vapor-Liquid Equilibria from the Triple Point up to the Critical Point for the New Generation of TIP4P-like Models: TIP4P/Ew, TIP4P/2005, and TIP4P/Ice”. *Journal of Chemical Physics* 125 (2006), 034503.

[412] N. Dawass, R. R. Wanderley, M. Ramdin, O. A. Moultos, H. K. Knuutila, and T. J. H. Vlugt. “Solubility of Carbon Dioxide, Hydrogen Sulfide, Methane, and Nitrogen in Monoethylene Glycol; Experiments and Molecular Simulation”. *Journal of Chemical & Engineering Data* 66 (2021), 524–534.

[413] M. Rouha, I. Nezbeda, J. Hrubŷ, and F. Moučka. “Higher Virial Coefficients of Water”. *Journal of Molecular Liquids* 270 (2018), 81–86.

[414] A. A. Chialvo, A. Bartók, and A. Baranyai. “On the Re-Engineered TIP4P Water Models for the Prediction of Vapor–Liquid Equilibrium”. *Journal of Molecular Liquids* 129 (2006), 120–124.

[415] C. M. Baker and R. B. Best. “Matching of Additive and Polarizable Force Fields for Multiscale Condensed Phase Simulations”. *Journal of Chemical Theory and Computation* 9 (2013), 2826–2837.

[416] A. L. Benavides, M. A. Portillo, V. C. Chamorro, J. R. Espinosa, J. L. F. Abascal, and C. Vega. “A potential model for sodium chloride solutions based on the TIP4P/2005 water model”. *Journal of Chemical Physics* 147 (2017), 104501.

[417] V. Kostal, P. Jungwirth, and H. Martinez-Seara. “Nonaqueous Ion Pairing Exemplifies the Case for Including Electronic Polarization in Molecular Dynamics Simulations”. *Journal of Physical Chemistry Letters* 14 (2023), 8691–8696.

[418] I. V. Leontyev and A. A. Stuchebrukhov. “Electronic Continuum Model for Molecular Dynamics Simulations of Biological Molecules”. *Journal of Chemical Theory and Computation* 6 (2010), 1498–1508.

[419] Y. Marcus. “A Simple Empirical Model Describing the Thermodynamics of Hydration of Ions of Widely Varying Charges, Sizes, and Shapes”. *Biophysical Chemistry* 51 (1994), 111–127.

[420] E. W. Lemmon, I. H. Bell, M. L. Huber, and M. O. McLinden. *NIST Standard Reference Database 23: Reference Fluid Thermodynamic and Transport Properties-REFPROP, Version 10.0, National Institute of Standards and Technology*. 2018.

[421] W. Wagner and A. Pruß. “The IAPWS Formulation 1995 for the Thermodynamic Properties of Ordinary Water Substance for General and Scientific Use”. *Journal of Physical and Chemical Reference Data* 31 (2002), 387–535.

[422] J. S. Lopez-Echeverry, S. Reif-Acherman, and E. Araujo-Lopez. “Peng-Robinson Equation of State: 40 years Through Cubics”. *Fluid Phase Equilibria* 447 (2017), 39–71.

[423] D.-Y. Peng and D. B. Robinson. “A New Two-Constant Equation of State”. *Industrial & Engineering Chemistry Fundamentals* 15 (1976), 59–64.

[424] E. C. W. Clarke and D. N. Glew. “Evaluation of the Thermodynamic Functions for Aqueous Sodium Chloride from Equilibrium and Calorimetric Measurements below 154°C”. *Journal of Physical and Chemical Reference Data* 14 (1985), 489–610.

[425] Z. Mester and A. Z. Panagiotopoulos. “Mean Ionic Activity Coefficients in Aqueous NaCl Solutions From Molecular Dynamics Simulations”. *Journal of Chemical Physics* 142 (2015), 044507.

[426] R. Schmid, A. M. Miah, and V. N. Sapunov. “A New Table of the Thermodynamic Quantities of Ionic Hydration: Values and Some Applications (Enthalpy–Entropy Compensation and Born Radii)”. *Physical Chemistry Chemical Physics* 2 (2000), 97–102.

[427] Y. Marcus. “Thermodynamics of Solvation of Ions. Part 5.—Gibbs Free Energy of Hydration at 298.15 K”. *Journal of the Chemical Society, Faraday Transactions* 87 (1991), 2995–2999.

[428] E. Sanz, C. Vega, J. R. Espinosa, R. Caballero-Bernal, J. L. F. Abascal, and C. Valeriani. “Homogeneous Ice Nucleation at Moderate Supercooling from Molecular Simulation”. *Journal of the American Chemical Society* 135 (2013), 15008–15017.

[429] P. Habibi, P. Dey, T. J. H. Vlugt, and O. A. Moultos. “Effect of dissolved KOH and NaCl on the solubility of water in hydrogen: A Monte Carlo simulation study”. *Journal of Chemical Physics* 161 (2024), 054304.

[430] W. Schmittinger and A. Vahidi. “A review of the main parameters influencing long-term performance and durability of PEM fuel cells”. *J. Power Sources* 180 (2008), 1–14.

[431] X. Wang, Y. Ma, J. Gao, T. Li, G. Jiang, and Z. Sun. “Review on water management methods for proton exchange membrane fuel cells”. *International Journal of Hydrogen Energy* 46 (2021), 12206–12229.

[432] E. P. Bartlett. “The Concentration of Water Vapor in Compressed Hydrogen, Nitrogen and a Mixture of These Gases in The Presence of Condensed Water”. *Journal of the American Chemical Society* 49 (1927), 65–78.

[433] H. Kerkache, H. Hoang, P. Cézac, G. Galliéro, and S. Chabab. “The solubility of H_2 in NaCl brine at high pressures and high temperatures: Molecular simulation study and thermodynamic modeling”. *Journal of Molecular Liquids* 400 (2024), 124497.

[434] K. M. Benjamin, J. K. Singh, A. J. Schultz, and D. A. Kofke. “Higher-Order Virial Coefficients of Water Models”. *Journal of Physical Chemistry B* 111 (2007), 11463–11473.

[435] J. Balej. “Water vapour partial pressures and water activities in potassium and sodium hydroxide solutions over wide concentration and temperature ranges”. *International Journal of Hydrogen Energy* 10 (1985), 233–243.

[436] S. L. Resnik and J. Chirife. “Proposed Theoretical Water Activity Values at Various Temperatures for Selected Solutions to be Used as Reference Sources in the Range of Microbial Growth”. *J. Food Prot.* 51 (1988), 419–423.

[437] A. H. Harvey and E. W. Lemmon. “Correlation for the Second Virial Coefficient of Water”. *Journal of Physical and Chemical Reference Data* 33 (2004), 369–376.

[438] T. Sako, T. Hakuta, and H. Yoshitome. “Vapor Pressures of Binary (Water-Hydrogen Chloride, -Magnesium Chloride, and -Calcium Chloride) and Ternary (Water-Magnesium Chloride-Calcium Chloride) Aqueous Solutions”. *Journal of Chemical & Engineering Data* 30 (1985), 224–228.

[439] R. Jinnouchi, F. Karsai, and G. Kresse. “On-the-fly machine learning force field generation: Application to melting points”. *Physical Review B* 100 (2019), 014105.

[440] L. Zhang, H. Wang, M. C. Muniz, A. Z. Panagiotopoulos, R. Car, and W. E. “A deep potential model with long-range electrostatic interactions”. *Journal of Chemical Physics* 156 (2022), 124107.

[441] J. L. F. Abascal, E. Sanz, R. García Fernández, and C. Vega. “A potential model for the study of ices and amorphous water: TIP4P/Ice”. *The Journal of Chemical Physics* 122 (2005), 234511.

[442] D. A. McQuarrie. *Statistical Mechanics*. 1st ed. New York: Harper and Row, 1976.

[443] S. A. Ghaffarizadeh and G. J. Wang. “Excess Entropy Scaling in Active-Matter Systems”. *Journal of Physical Chemistry Letters* 13 (2022), 4949–4954.

[444] P. Ganguly and N. F. A. van der Vegt. “Convergence of Sampling Kirkwood–Buff Integrals of Aqueous Solutions with Molecular Dynamics Simulations”. *Journal of Chemical Theory and Computation* 9 (2013), 1347–1355.

[445] P. Krüger, S. K. Schnell, D. Bedeaux, S. Kjelstrup, T. J. H. Vlugt, and J.-M. Simon. “Kirkwood–Buff Integrals for Finite Volumes”. *Journal of Physical Chemistry Letters* 4 (2013), 235–238.

[446] B. Fang, P. Habibi, O. A. Moultos, T. Lü, F. Ning, and T. J. H. Vlugt. “Solubilities and Self-Diffusion Coefficients of Light n-Alkanes in NaCl Solutions at the Temperature Range (278.15–308.15) K and Pressure Range (1–300) bar and Thermodynamics Properties of Their Corresponding Hydrates at (150–290) K and (1–7000) bar”. *Journal of Chemical & Engineering Data* (2023). in press, `doi.org/10.1021/acs.jced.3c00225`.

[447] R. Fan, P. Habibi, J. T. Padding, and R. Hartkamp. “Coupling mesoscale transport to catalytic surface reactions in a hybrid model”. *Journal of Chemical Physics* 156 (2022), 084105.

Summary

In this thesis, molecular simulations are performed to design and assess novel 2D materials for H_2 storage applications (chapters 2-3) and to predict thermodynamic and transport properties of H_2 in aqueous electrolyte solutions for storage and production of H_2 (chapters 4-8). Both ab-initio and force field-based methods are used in this thesis.

Novel 2D boron based materials (i.e., borophene, borophene oxide, and borophene hydride) are assessed for physisorption (chapter 2) and chemisorption (chapter 3) storage of H_2 using ab-initio calculations. In their pristine form (i.e., without any addition of metal dopants or structural engineering), 2D boron based materials are not suitable for H_2 storage. The physical adsorption energy of H_2 with the 2D substrate is too weak (i.e., ca. -0.10 eV / H_2) to allow for any practical H_2 capacity at ambient conditions. In chapter 2, we consider the addition of different metal atoms such as Li, Na, and K to the 2D boron structure to enhance the adsorption energy of H_2. Li atoms are particularly promising as dopants on the 2D boron based substrate due to their low mass and strong adsorption energy (with respect to the cohesion energy in bulk Li). We discovered a Li doped borophene oxide structure with a theoretical gravimetric capacity of 8.3 wt% H_2 (exceeding the US DOE target of 5.5 wt% H_2). Born-Oppenheimer Molecular Dynamics (BOMD) simulations at 100-500 K indicate the structural stability of the 2D structure. The average adsorption energy of H_2 on the 2D structure in the presence of Li-atoms is ca. -0.24 eV/H_2, which results in a practical gravimetric capacity of 5.2 wt% H_2 at adsorption conditions of 298 K and 30 atm and desorption conditions of 373 K and 3 atm. In chapter 3, Li decorating atoms are shown to also influence chemisorption (i.e., hydrogenation and dehydrogenation reaction pathways) of H_2 in 2D boron structures. In borophene hydride (i.e., BH, which contains 8.2 wt% H_2 in its pristine form), the presence of Li atoms weakens the 3-center 2-electron B–H–B bonds. We show that the energy barriers (computed using Nudged Elastic Band calculations) for H_2 release (i.e., dehydrogenation) in borophene hydride are reduced by more than 50% in presence of Li decorating atoms, thereby significantly increasing the H_2 desorption kinetics.

H_2 can also be stored in underground reservoirs. Designing reservoirs for H_2 storage requires detailed knowledge of the thermophysical properties of H_2 in brine (i.e., aqueous solutions primarily consisting of water and NaCl) that are present in aquifers underground. The interfacial tension between H_2 and brine influences the stability of the storage reservoir. The

phase equilibria of H_2 and brine (i.e., water content in gaseous H_2, and H_2 solubility in brine) influences the hydrogen purity. In chapter 4, MD and MC simulations using non-polarizable force fields are used to compute interfacial tensions, solubilities, and self-diffusivities of $H_2/H_2O/NaCl$ systems for high pressures (up to 1000 bar) and temperatures (up to 723 K). The non-polarizable Madrid-2019 force field of NaCl (with scaled charges of +0.85/-0.85 [e] for Na^+/Cl^-) combined with the TIP4P/2005 water force field and the Vrabec force field for H_2 can accurately model interfacial tensions of H_2/brine systems and the salting out (i.e., reduction of solubility of H_2 in the presence of salts) of H_2 at different NaCl molalities. A different non-polarizable force field for NaCl, namely the Madrid-Transport force field (with scaled charges of +0.75/-0.75 [e] for Na^+/Cl^-) is required for accurately predicting transport properties (i.e., viscosities and H_2 self-diffusivities) of H_2 in aqueous NaCl solutions. In this thesis, non-polarizable force fields are also used to predict the solubilities and diffusivities of H_2 in aqueous KOH, NaOH, and $NaB(OH)_4$ solutions. The self-diffusivities and solubilities of H_2 influence the product gas purities and the Faradaic efficiency of in alkaline water electrolyzers. In chapter 5, we develop a new force field for OH^- with a scaled charge of -0.75 [e] that can accurately predict (within 2% from experiments) the densities and viscosities of aqueous KOH and NaOH solutions up to 8 mol salt / kg water. The newly developed classical OH^- force field cannot capture proton transfer between H_2O and OH^-. This proton transfer strongly influences the self-diffusivities of OH^-. The developed force field for OH^- can be used to accurately model (1) the self-diffusivities of H_2 (as the viscosities of the alkaline solution are correctly captured), and (2) the salting out of H_2 in aqueous KOH and NaOH solutions. In chapter 6, a new force field for $B(OH)_4{}^-$ is developed based on the densities and viscosities of aqueous $NaB(OH)_4$ solutions at 298 K. Aqueous $NaB(OH)_4$ is formed as a byproduct of the hydrolysis reaction of $NaBH_4$ with water along with H_2. $NaBH_4$ is a promising H_2 storage medium for maritime applications with a gravimetric capacity of 10.7 wt% H_2. $NaB(OH)_4$ strongly influences the thermophysical properties of the aqueous mixture and thereby the hydrolysis of $NaBH_4$. In the newly developed $B(OH)_4{}^-$ force field, OH^- is modeled as a single interaction site. Scaled charges of +0.85 [e] and -0.85 [e] for Na^+ and $B(OH)_4{}^-$, respectively, are found to accurately predict the viscosities and densities of aqueous $NaB(OH)_4$ solutions at 298 K up to 5 mol salt / kg water.

To calculate the water content in gaseous H_2 using non-polarizable force fields, a new approach is developed and used in chapters 7 and 8. Non-polarizable force fields of water, such as the TIP4P/2005 force field, that accurately capture the densities and transport properties of the liquid phase cannot accurately predict the free energies of water and thereby the vapor pressures of water. Already in 1987, it was discovered by Berendsen et al. that non-polarizable force fields that are parameterized based on the free energies of water exclude the self-polarization energy of water (i.e., the "missing term in effective pair potentials" mentioned in the title of the paper by Berendsen et al.), thereby resulting in inaccurate predictions for transport properties of water. In chapter 7, a new approach is presented in which (1) the TIP4P/2005 water force field and scaled charge ion force fields are used to describe effective interactions between molecules and ions, and (2) an additional (temperature-independent) effective charge surface is used to sample the excess chemical potentials of salts and water at infinite salt dilution. At finite salt dilution, a free energy correction is applied to the partition function of the system to correct for the free energy offset at a molality of 0 mol salt / kg water (i.e., the "missing term"). Using this approach, the VLE of water and the infinite dilution free energies of hydration of salts (e.g., NaCl, KCl, LiCl) are accurately modeled (within 5% from experiments). In chapter 8, the free energy correction that is obtained in chapter 7 is used to compute the compositions of water and H_2 gas in equilibrium with aqueous KOH and NaCl solutions. The equilibrium compositions of water and H_2 are accurately computed (compared to experiments) from liquid phase excess chemical potentials of water and H_2 (computed using Continuous Fractional Component Monte Carlo simulations), using an iterative scheme in which fugacity coefficients in the gas phase are computed using the GERG-2008 equation of state. The VLE data presented in chapter 8 can be used for modeling the water content in the H_2 product stream of alkaline electrolyzers (for aqueous KOH solutions) and in underground hydrogen storage systems (for aqueous NaCl solutions).

Samenvatting

In dit proefschrift werden moleculaire simulaties uitgevoerd om nieuwe 2D-materialen te ontwerpen voor opslag van H_2 (hoofdstukken 2-3) en om thermodynamische en transporteigenschappen van H_2 in waterige elektrolytoplossingen te voorspellen voor de opslag en productie van H_2 (hoofdstukken 4-8). Zowel ab-initio als krachtveld-gebaseerde methoden werden in dit proefschrift gebruikt.

Nieuwe 2D-boron gebaseerde materialen (d.w.z., borofeen, borofeenoxide en borofeenhydride) werden beoordeeld voor fysiosorptie (hoofdstuk 2) en chemisorptie (hoofdstuk 3) van H_2 met behulp van ab-initio berekeningen. Zonder toevoeging van metaal dopanten of aanpassingen van de oppervlaktestructuur zijn 2D-boron gebaseerde materialen niet geschikt voor H_2 opslag. De fysieke adsorptie-energie van H_2 met het 2D-substraat is te zwak (ca. -0,10 eV / H_2) om een zekere mate van praktische H_2 capaciteit toe te staan. In hoofdstuk 2 werden verschillende metaal atomen zoals Li, Na en K toegevoegd aan de 2D-boronstructuur om de adsorptie-energie van H_2 te verhogen. Li-atomen zijn bijzonder veelbelovend als dopanten vanwege hun geringe massa en sterke adsorptie-energie (ten opzichte van de cohesie-energie in bulk Li) met het 2D-boron gebaseerde substraat. We hebben een Li-gedopeerde borofeenoxide-structuur gevonden met een theoretische gravimetrische capaciteit van 8,3 wt% H_2 (groter dan de US DOE-doelstelling van 5,5 wt% H_2). Born-Oppenheimer Moleculaire Dynamica (BOMD) simulaties bij 100-500 K duiden op de structurele stabiliteit van de 2D-structuur. De gemiddelde adsorptie-energie van H_2 op de 2D-structuur in aanwezigheid van Li-atomen is -0,24 eV/H_2. Dit resulteert in een praktische gravimetrische capaciteit van 5,2 wt% H_2 bij adsorptie bij 298 K en 30 atm, en desorptie bij 373 K en 3 atm. In hoofdstuk 3 wordt aangetoond dat Li-decorerende atomen ook de chemisorptie (d.w.z., hydrogeneringsreactie en dehydrogeneringsreactie) van H_2 in 2D-boronstructuren beïnvloeden. In borofeenhydride (d.w.z., BH, dat 8,2 wt% H_2 bevat in zijn pure vorm), verzwakken de 3-center 2-elektron B–H–B bindingen in aanwezigheid van Li. We tonen aan dat de energie-barriéres (berekend met Nudged Elastic Band-berekeningen) voor H_2 afgifte in borofeenhydride met meer dan 50% werden verminderd in aanwezigheid van Li-decorerende atomen, waardoor de H_2 desorptie snelheid aanzienlijk toeneemt.

H_2 kan ook worden opgeslagen in ondergrondse reservoirs. Het ontwerpen van reservoirs voor H_2 opslag vereist gedetailleerde kennis van de thermofysische eigenschappen van H_2 in zoutoplossingen (d.w.z., systemen die voornamelijk bestaan uit water en NaCl) die aanwezig zijn in aquifers onder de grond. De oppervlaktespanning tussen H_2 en de zoutoplossing beïnvloedt de stabiliteit van het opslagreservoir en de fase-evenwichten (d.w.z., het watergehalte in H_2 en de oplosbaarheid van H_2 in de zoutoplossing) beïnvloeden de zuiverheid van waterstof. In hoofdstuk 4 werden MD- en MC-simulaties met behulp van niet-polariseerbare krachtvelden gebruikt om oppervlaktespanningen, oplosbaarheden en diffusiecoëfficiënten van $H_2/H_2O/NaCl$ systemen voor hoge drukken (tot 1000 bar) en temperaturen (tot 723 K) te berekenen. De niet-polariseerbare Madrid-2019 krachtvelden van NaCl (met geschaalde ladingen van +0,85/-0,85 [e] voor Na^+/Cl^-), in combinatie met het TIP4P/2005 waterkrachtveld en het Vrabec krachtveld van H_2, kunnen nauwkeurig de oppervlaktespanningen van H_2/zoutoplossingen en de salting out (d.w.z., vermindering van oplosbaarheden van gassen in aanwezigheid van zouten) van H_2 bij verschillende NaCl molaliteiten modelleren. Een ander niet-polariseerbaar krachtveld voor NaCl, namelijk het Madrid-Transport krachtveld (met geschaalde ladingen van +0,75/-0,75 [e] voor Na^+/Cl^-) is nodig voor het nauwkeurig voorspellen van de transporteigenschappen (d.w.z., viscositeiten en H_2 diffusiecoëfficiënten) van H_2 in waterige NaCl oplossingen. In dit proefschrift werden ook niet-polariseerbare krachtvelden gebruikt om de oplosbaarheden en diffusiecoëfficiënten van H_2 in waterige KOH, NaOH en $NaB(OH)_4$ oplossingen te voorspellen. De diffusiecoëfficiënten en oplosbaarheden van H_2 beïnvloeden de zuiverheden van gasvormige producten en de Faraday efficiëntie van alkalische (d.w.z., KOH-oplossingen) water-elektrolyzers. In hoofdstuk 5 ontwikkelen we een nieuw krachtveld voor OH^- met een geschaalde lading van -0,75 [e] dat de dichtheden en viscositeiten van waterige KOH en NaOH oplossingen tot 8 mol zout / kg water nauwkeurig kan voorspellen (binnen 2% van experimenten). Het nieuw ontwikkelde klassieke OH^- krachtveld kan de protonoverdracht tussen H_2O en H_2 niet beschrijven, hetgeen de berekende OH^- diffusiecoëfficiënten beïnvloedt. Het krachtveld kan worden gebruikt om de diffusiecoëfficiënten van H_2 en de salting out van H_2 in aanwezigheid van waterige KOH en NaOH oplossingen te modelleren. In hoofdstuk 6 wordt een nieuw krachtveld voor $B(OH)_4{}^-$ ontwikkeld op basis van de dichtheden en viscositeiten van waterige $NaB(OH)_4$ oplossingen bij 298 K. $NaB(OH)_4$ wordt samen met H_2 gevormd in water als bijproduct van de hydrolysereactie van $NaBH_4$ en water. $NaBH_4$ is een veelbelovend H_2 opslagmedium voor maritieme toepassingen met een gravimetrische capaciteit van 10,7 wt% H_2. Opgelost $NaB(OH)_4$ beïnvloedt de thermofysische eigenschappen van de waterige oplossing sterk en daarmee de hydrolyse van $NaBH_4$. Het nieuw ontwikkelde $B(OH)_4{}^-$ krachtveld heeft een tetraëdrische structuur en OH^- wordt gemodelleerd als een enkele interactie site. Een geschaalde lading van +0,85 / -0,85 [e] blijkt de viscositeiten en dichtheden van waterige $NaB(OH)_4$ oplossingen bij 298 K tot 5 mol zout / kg water nauwkeurig te voorspellen.

Om het watergehalte in gasvormig H_2 te berekenen met behulp van niet-polariseerbare krachtvelden, ontwikkelen en gebruiken we een nieuwe aanpak in hoofdstukken 7 en 8. Niet-polariseerbare krachtvelden van water, zoals het TIP4P/2005 krachtveld, die de dichtheden en transporteigenschappen van de vloeibare fase nauwkeurig voorspellen, kunnen de vrije energieën van water en daarmee de dampdrukken van water niet nauwkeurig voorspellen. In hoofdstuk 7 wordt een nieuwe aanpak gepresenteerd waarbij (1) het TIP4P/2005 waterkrachtveld en geschaalde lading ion krachtvelden worden gebruikt om de effectieve interacties tussen moleculen en ionen te beschrijven, en (2) een extra (temperatuur-onafhankelijke) effectieve lading-oppervlak wordt gebruikt om de excess chemische potentialen van zouten en water bij oneindige zoutverdunning te berekenen. Bij eindige zoutverdunning wordt een vrije-energiecorrectie toegepast op de partitiefunctie van het systeem om de vrije energie-offset bij molaliteit van 0 mol zout / kg water te corrigeren. Met deze aanpak werden de VLE van water en de vrije-energieën van hydratatie van zouten (bijv. NaCl, KCl, LiCl) bij oneindige verdunning nauwkeurig gemodelleerd (binnen 5% van experimenten). In hoofdstuk 8 wordt de vrije-energiecorrectie die in hoofdstuk 7 is verkregen gebruikt om de evenwichtsamenstelling van water en H_2 gas in evenwicht met waterige KOH en NaCl oplossingen te berekenen. De evenwichtsamenstelling van water en H_2 werden nauwkeurig berekend (in vergelijking met experimenten) op basis van de excess chemische potentialen van water en H_2 (berekend met Continuous Fractional Component Monte Carlo-simulaties), met behulp van een iteratief schema waarin de fugaciteitscoëfficiënten in de gasfase werden berekend met de GERG-2008 toestandsvergelijking. De VLE-gegevens in hoofdstuk 8 kunnen worden gebruikt voor het modelleren van het watergehalte in de H_2-stroom van alkalische elektrolyzers (voor waterige KOH-oplossingen) en in ondergrondse waterstofopslagsystemen (voor waterige NaCl-oplossingen).

Curriculum Vitæ

Parsa Habibi was born on 30 January 1997 in Tehran, Iran. In 2015, he started his BSc. in Molecular Science and Technology at Leiden University and Delft University of Technology (joint degree), the Netherlands. After completing his BSc studies with distinction (Cum Laude) in 2018, he continued his MSc. studies in Chemical Engineering at Delft University of Technology. In his MSc. thesis, supervised by Prof. J. T. Padding and Dr. R. Hartkamp, he simulated compressible flows in heterogeneously catalyzed systems using a mesoscopic particle-based technique called Stochastic Rotation Dynamics. After graduating his MSc program with distinction (Cum Laude and honors) in 2020, he joined the Mechanical Engineering Faculty of the Delft University of Technology as a PhD candidate, under the supervision of promoters Prof. Dr. Ir. Thijs J. H. Vlugt and Dr. Othonas Moultos, and copromoter Dr. Poulumi Dey. To investigate hydrogen storage and production, he used various molecular simulation techniques, such as Density Functional Theory, Monte Carlo, and Molecular Dynamics simulations. His research focused on optimizing hydrogen storage in 2D materials and predicting various thermophysical properties (e.g., solubilities and self-diffusivities) of hydrogen in aqueous electrolyte systems relevant for underground hydrogen storage, maritime shipping fuel, and alkaline electrolyzers. This dissertation presents the results of these studies.

List of Publications

Publications included in this thesis:

1. P. Habibi, T. J. H. Vlugt, P. Dey, and O. A. Moultos. "Reversible Hydrogen Storage in Metal-Decorated Honeycomb Borophene Oxide". *ACS Applied Materials & Interfaces* 13 (2021), 43233–43240.
2. P. Habibi, T. H. G. Saji, T. J. H. Vlugt, O. A. Moultos, and P. Dey. "Hydrogen dissociation in Li-decorated borophene and borophene hydride: An ab-initio study". *Applied Surface Science* 603 (2022), 154323.
3. W. A. van Rooijen[1], P. Habibi[1], K. Xu, P. Dey, T. J. H. Vlugt, H. Hajibeygi, O. A. Moultos, "Interfacial Tensions, Solubilities, and Transport Properties of the $H_2/H_2O/NaCl$ system stems: A Molecular Simulation Study". *Journal of Chemical & Engineering Data* 69 (2024) 307-319.
4. P. Habibi, A. Rahbari, S. Blazquez, C. Vega, P. Dey, T. J. H. Vlugt, and O. A. Moultos. "A New Force Field for OH^- for Computing Thermodynamic and Transport Properties of H_2 and O_2 in Aqueous NaOH and KOH Solutions". *Journal of Physical Chemistry B* 126 (2022), 9376–9387.
5. P. Habibi, J. R. T. Postma, J. T. Padding, P. Dey, T. J. H. Vlugt, and O. A. Moultos. "Thermodynamic and Transport Properties of $H_2/H_2O/NaB(OH)_4$ Mixtures Using the Delft Force Field ($DFF/B(OH)_4^-$)". *Industrial and Engineering Chemistry Research* 62 (2023), 11992–12005.
6. P. Habibi, H. M. Polat, S. Blazquez, C. Vega, P. Dey, T. J. H. Vlugt, and O. A. Moultos. "Accurate Free Energies of Aqueous Electrolyte Solutions from Molecular Simulations with Non-polarizable Force Fields". *Journal of Physical Chemistry Letters* 15 (2024), 4477–4485.
7. P. Habibi, P. Dey, T. J. H. Vlugt, and O. A. Moultos. "Effect of dissolved KOH and NaCl on the solubility of water in hydrogen: A Monte Carlo simulation study". *Journal of Chemical Physics* 161 (2024), 054304.

---

[1] These authors contributed equally to this work.

Publications not included in this thesis:

1. B. Fang, P. Habibi, O. A. Moultos, T. Lü, F. Ning, and T. J. H. Vlugt. "Solubilities and Self-Diffusion Coefficients of Light n-Alkanes in NaCl Solutions at the Temperature Range (278.15–308.15) K and Pressure Range (1–300) bar and Thermodynamics Properties of Their Corresponding Hydrates at (150–290) K and (1–7000) bar". *Journal of Chemical & Engineering Data* (2023). in press, doi.org/10.1021/acs.jced.3c00225
2. S. Blazquez, J. L. F. Abascal, J. Lagerweij, P. Habibi, P. Dey, T. J. H. Vlugt, O. A. Moultos, and C. Vega. "Computation of Electrical Conductivities of Aqueous Electrolyte Solutions: Two Surfaces, One Property". *Journal of Chemical Theory and Computation* 19 (2023), 5380–5393
3. R. Fan, P. Habibi, J. T. Padding, and R. Hartkamp. "Coupling mesoscale transport to catalytic surface reactions in a hybrid model". *Journal of Chemical Physics* 156 (2022), 084105

Acknowledgements

I would like to thank all my colleagues and friends in the Process & Energy department and the Material Science and Engineering department who have helped during my PhD. Mert has been the colleague that I did most of my travels and daily walks with. I thank you for being a great company and a nice colleague who I could always talk to. I would like to thank Shrinjay, Darshan, Georgia, Thejas, and Saurabh for all the support, coffee talks, and discussions during meetings. During my PhD, I had the pleasure of supervising and being part of four different MSc thesis projects with Tijin, Prateek, Ke, and Jelle. Each project taught me a lot and contributed to my PhD, and for that I am grateful. I would like to especially thank Jelle, as you have also been an amazing colleague and friend for the last year. Additionally, I would like to thank Julien and Pepijn. I was excited when both of you joined our department as we have been friends since our BSc and MSc studies. All the scientific and political talks that we have had over the last years have been a highlight.

I would like to express my deepest gratitude to my promoters and co-promoter, Thijs Vlugt, Othonas Moultos, and Poulumi Dey. Their guidance and mentorship over the past four years have been invaluable. They provided opportunities for collaboration, conference travel, and scientific development. I always felt comfortable expressing my doubts and received timely, excellent advice. It has been a pleasure working with them. I sincerely thank all the co-authors of the scientific publications that have shaped this thesis: Ahmadreza Rahbari, Carlos Vega, Samuel Blazquez, Julien Postma, Johan Padding, Willemijn van Rooijen, and Hadi Hajibeygi. All the publications in this work are sponsored by NWO Domain Science for the use of supercomputer facilities. I would like to acknowledge the use of computational resources of DelftBlue supercomputer, provided by Delft High Performance Computing Centre.

Finally, I would like to express my appreciation to my parents, Mehrad and Homeira, and my partner, Nina. Their unwavering support and constant encouragement have been pivotal throughout this journey. They have always been there to motivate me and provide a reassuring presence. Without their love and belief in me, this achievement would not have been possible.